WAVEFIELD INVERSION AND TOMOGRAPHY USING THE ENERGY NORM

by

Daniel Carvalho Rocha Jr

© Copyright by Daniel Carvalho Rocha Jr, 2018

All Rights Reserved

A thesis submitted to the Faculty and the Board of Trustees of the Colorado School of Mines in partial fulfillment of the requirements for the degree of Doctor of Philosophy (Geophysics).

Golden, Colorado

Date _____

Signed: _____
Daniel Carvalho Rocha Jr

Signed: _____
Dr. Paul C. Sava
Thesis Advisor

Golden, Colorado

Date _____

Signed: _____
Dr. John Bradford
Professor and Head
Department of Geophysics

ABSTRACT

Wavefield migration and tomography are the most precise methods for subsurface imaging and characterization in complex settings. Tomography provides an accurate earth model of physical properties, usually seismic wave velocities, so that migration can deliver an image with the correct position of geological interfaces. Although these methods, which are based on robust wavefield extrapolation, are considered to be state-of-art technology, both suffer from large computational cost, slow convergence to accurate earth models, ambiguity and crosstalk contamination between model parameters, and imaging artifacts caused by improper correlation between wavefields, among other problems. Considering the interest of the geophysical community in improving these methods and the theoretical framework already developed in wave physics, I propose solutions to wavefield imaging problems based on a powerful measure of wavefield energy called *energy norm*. Since this measure emerges from the differential equations that govern wave propagation, it naturally leads to computational tools that can exploit important wavefield features, such as propagation and polarization directions. Using the energy norm, I propose techniques to attenuate spurious artifacts and expedite convergence to more geologically-plausible earth models, as well as to improve source location estimation for passive seismic methods. The energy norm also enables us to implement correlation of different wave modes without computationally intensive wave-mode separation.

Overall, the energy norm facilitates a whole range of techniques suited for wavefield imaging, since it is a general concept applicable to various problems involving acoustic or elastic propagation in isotropic or anisotropic media. Here, I present solutions to these problems persistent in exploration seismology, including passive- and active-source seismic experiments. Numerical experiments show the efficacy of these applications for models that emulate complex subsurface structures, such as salt bodies, diffractors, dipping layers and

faults. With available field datasets, I validate the methodology for various challenging scenarios currently employed in exploration seismology: 3D, multicomponent, active or passive acquisition, ocean-bottom nodes, etc. Developing novel, accurate and efficient techniques for wavefield imaging, as well as their validation with field data, serves as my main contribution for improving seismic exploration efficiency. The techniques developed in this thesis can potentially be applied to non-exploration problems that involve other types of wave phenomena different from seismic.

TABLE OF CONTENTS

ABSTRACT iii

LIST OF FIGURES x

LIST OF ABBREVIATIONS xviii

ACKNOWLEDGMENTS xix

DEDICATION xxi

CHAPTER 1 INTRODUCTION 1

1.1 Thesis Outline 4

CHAPTER 2 ANISOTROPIC ELASTIC WAVEFIELD IMAGING USING THE ENERGY NORM 8

2.1 Introduction 9

2.2 Theory 11

2.2.1 Elastic wave equation 11

2.2.2 Elastic wavefield energy 12

2.2.3 Physical interpretation 13

2.2.4 Imaging condition 14

2.2.5 Backscattering attenuation 15

2.3 Examples 17

2.4 Discussion 19

2.5 Conclusions 21

2.6 Acknowledgments 27

2.7 Appendices 27

2.7.1 Frobenius product and norm 27

2.7.2 Strain-energy function in isotropic media 28

2.7.3 Imaging conditions for orthorhombic and vertical transverse isotropic (VTI) media 29

CHAPTER 3 3D PASSIVE WAVEFIELD IMAGING USING THE ENERGY NORM . 31

3.1 Introduction 32

3.2 Theory 35

3.2.1 Elastic modeling 35

3.2.2 Passive imaging conditions: autocorrelation 36

3.2.3 Passive imaging conditions: cross-correlation 37

3.2.4 Energy norm imaging conditions 38

3.2.5 Passive imaging conditions: extended domain 40

3.3 Methodology 41

3.4 3-D numerical examples 43

3.4.1 Experiment 1: focusing with correct velocity 43

3.4.2 Experiment 2: sensitivity to changes in velocity and extended images . 45

3.4.3 Experiment 3: SEG/EAGE 3-D overthrust model 48

3.4.4 Experiment 4: field data example 54

3.5 Discussion 60

3.6 Conclusions 61

3.7 Acknowledgments 62

3.8 Appendix 62

3.8.1 Hamilton's Principle 63

CHAPTER 4 3D ACOUSTIC LEAST-SQUARES REVERSE TIME MIGRATION USING THE ENERGY NORM 65

4.1 Introduction 65

4.2 Theory 67

4.2.1 Conventional imaging condition and linearized modeling 68

4.2.2 Energy imaging condition and linearized modeling 69

4.2.3 Least-squares migration and preconditioning with an approximation of the Hessian 71

4.3 Examples 72

4.4 Discussion 76

4.5 Conclusions 83

4.6 Acknowledgments 83

4.7 Appendices 83

4.7.1 Conventional migration and modeling operators 84

4.7.2 Energy migration and modeling operators 85

CHAPTER 5 ELASTIC LEAST-SQUARES REVERSE TIME MIGRATION USING THE ENERGY NORM 87

5.1 Introduction 87

5.2 Theory 90

5.2.1 Energy-norm linearized modeling and migration operators 90

5.2.2 Physical interpretation of energy imaging operators 93

5.2.3 Energy-norm elastic least-squares migration 95

5.3 Examples 96

5.3.1 Single-reflector linearized modeling 96

5.3.2 Single-reflector LSRTM 97

5.3.3 2007 BP TTI anisotropic benchmark model 100

5.3.4 Volve OBC real dataset 103

5.4 Conclusions 107

5.5 Acknowledgments 110

5.6 Appendices 110

5.6.1 Energy-based modeling and migration operators 110

5.6.2 Multicomponent virtual source for 2D VTI linearized modeling 112

5.6.3 Perturbation of model parameters in energy migration and linearized modeling 113

CHAPTER 6 ELASTIC REFLECTION WAVEFORM INVERSION WITH PETROPHYSICAL MODEL CONSTRAINTS 116

6.1 Introduction 117

6.2 Theory 120

6.2.1 Single-scattering and migration operators based on earth model perturbations 121

6.2.2 Waveform inversion with background and scattered wavefields 122

6.2.3 Physical constraints 124

6.3 Examples 126

6.3.1 Single-reflector with a Gaussian anomaly 126

6.3.2 Marmousi II 131

6.4 Conclusions 133

6.5 Acknowledgments 137

6.6 Appendices 139

6.6.1 Single-scattering and migration operators based on model perturbations 139

6.6.2 Waveform inversion gradients in isotropic elastic media based on adjoint-state method 140

CHAPTER 7 CONCLUSION 141

REFERENCES CITED 143

APPENDIX - PERMISSIONS FOR CHAPTERS 160

A.1 Permission from journal 160

A.2 Permission for field datasets 161

A.3 Permission from co-authors 163

LIST OF FIGURES

Figure 2.1 Model parameters used for the experiments in Figure 2.2: (a) P and (b) S velocity along the symmetry axis. The anisotropy parameters $\epsilon = 0.4$, $\delta = 0.3$ and $\nu = 26^\circ$ are constant for the entire model. 19

Figure 2.2 Imaging conditions using displacement components for a horizontal reflector with a vertical displacement source at $x = 5$ km: (a) U_xV_x, (b) U_zV_x, and (c) U_zV_z image, where $\{U_x, U_z\}$ and $\{V_x, V_z\}$ are the horizontal and vertical components of the source and receiver wavefields, respectively. Artifacts present in all images occur due to the "fake" modes (caused by injection of vector fields). Polarity reversal at normal incidence occurs for the image in (b), and backscattering artifacts occur for images in (a)-(c). Comparing to the other images, the energy image in (d) is the only one with attenuated backscattering artifacts and without polarity reversal at normal incidence. 20

Figure 2.3 Acquisition geometry used in the Marmousi II experiment (Figures 2.4-2.6). The white dots indicate the positions of the seventy-six pressure sources ($z = 0.05$ km), and the white line at the water bottom indicates multicomponent receivers that record the displacement field ($z = 0.5$ km). 21

Figure 2.4 Migration model parameters used for the Marmousi II experiment. (a) P- and (b) S-wave velocity along the local symmetry axis (V_{P0} and V_{S0}, in km/s). (c) Stratigraphic density model used to generate synthetic data (in g/cm^3). 22

Figure 2.5 Migration anisotropy parameters used for the Marmousi II experiment. (a) ϵ, (b) δ, and (c) local tilt angle ν (in degrees). 23

Figure 2.6 Images obtained from the Marmousi II experiment: conventional images using the correlation between displacement components (a) U_xV_x, (b) U_xV_z, and (c) U_zV_z; (d) energy image using the imaging condition in equation 2.35. Polarity reversal effects are visible in (b) by the change in polarity from the low-wavenumber artifacts. The energy image in (d) is the only one without low-wavenumber backscattering artifacts. 24

Figure 2.7 Schematic representation of the 3D TTI model used in the experiment of Figure 2.8. The black arrow indicates the tilted symmetry axis. The gray arrows indicate the projections of this vector onto the vertical axis and onto the reflection plane. Model parameters in the original system are $V_{P0} = 2.3$ km/s,$V_{S0} = 1.3$ km/s, $\rho = 2.0$ g/cm^3, $\epsilon = 0.4$, $\delta = 0.1$, and $\gamma = 0.0$. 25

Figure 2.8 Images using the correlation between displacement components: (a) U_xV_y, (b) U_xV_z, and (c) U_zV_z; and an image using the energy imaging condition in (d). Artifacts due to the "fake" modes are present in all images. Backscattering artifacts and polarity reversal occur in the conventional images in (a)-(c) but not in the energy image in (d). 26

Figure 3.1 Constant-velocity experiment that consists of (a) an earth model with $4\times4\times4$ km^3 and multicomponent receivers (black dots) spaced by 0.25km at the surface. (b) PP, (c) SS, (d) PS and energy images using equation 3.12 (e) and equation 3.13 (f). The PS and energy images have strong and focused peaks at the source location compared to all other images that exhibit strong low-wavenumber artifacts. 46

Figure 3.2 Schematic representation of (a) P- and S-waves backpropagated with truncation events (dashed lines). Close to their focus points, (b) P- and S- waves correlate with their respective truncation events, which have the polarity of their original wave but different propagation directions. (c) Snapshot of the vertical component from the back-propagated elastic wavefield. As indicated by the arrows, note the true backpropagated events and the associated artificial extrapolated events. (d) Energy image with the strong artifact caused by the truncation, as opposed to the energy image without such artifact (Figure 3.1(f)). 47

Figure 3.3 PS images with incorrect velocities with respect to a $V_P = 3.0$km/s and $V_S = 1.8$km/s. Top, middle and bottom rows correspond to -8%, 0%, $+8\%$ changes in the P-wave velocity; and left, middle and right columns correspond to -8%, 0%, $+8\%$ changes in the S-wave velocity. Note the unfocused events with respect to the focused correlation in the central image (which uses the correct velocity). 49

Figure 3.4 Energy images with incorrect velocities, computed and displayed as in Figure 3.3. Compared to the PS images in Figure 3.3, the energy correlation produces unfocused imaged events that are more straightforward to interpret and without zero crossings. 50

Figure 3.5 Extended PS images with incorrect velocities. Top, middle and bottom rows correspond to -8%, 0%, $+8\%$ changes in the P-wave velocity; and left, middle and right columns correspond to -8%, 0%, $+8\%$ changes in the S-wave velocity. Note the unfocused events with respect to the focused correlation in the central image (which uses the correct velocity). . 51

Figure 3.6 Extended energy images with incorrect velocities, organized similarly to Figure 3.5. Compared to the PS images in Figure 3.5, the energy correlation produces unfocused images that are more straightforward to interpret, are symmetric with respect to the λ_z axis, and contain no zero crossings. 52

Figure 3.7 SEG/EAGE overthrust experiment: (a) P-wave velocity from the 3D overthrust model and (b) PS velocity ratio. (c) Receiver coordinates used for the overthrust and field acquisition experiments shown in Figures 3.9 and 3.11. 55

Figure 3.8 SEG/EAGE overthrust experiment: (a) PS and (b) energy images for a stress source with $\tau_{xx} = -2, \tau_{yy} = 1, \tau_{zz} = 1$. Zoomed (c) PS and (d) energy images, as well as extended (e) PS and (f) energy images. The energy correlation exhibits peak amplitudes (in red) that are closer to the source location in (d) when compared to (c), and are more focused in the extended domain in (f) when compared to (e). 56

Figure 3.9 Field data experiment: (a) P- and (b) S-wave velocity models. 57

Figure 3.10 Field data experiment: x (top), y (middle) and z (bottom) components from the processed dataset containing a single microseismic event. Note the P- (from $t = 0$s to $t = 0.6$s) and S- (from $t = 0.6$ to $t = 1.5$s) arrivals, and how the P-wave arrival is stronger in the vertical (z) component. 58

Figure 3.11 Field data experiment: (a) PS and (b) energy images for the field dataset. Zoomed (c) PS and (d) energy images, as well as extended (e) PS and (f) energy images. The energy correlation has peak amplitudes (in red) that are closer to the source location in (d) when compared to (c), and are more centralized in the extended domain in (f) when compared to (e). 59

Figure 4.1 GOM 2D dataset: (a) conventional RTM image and (b) LSRTM image with the energy modeling and migration operators. (c) Normalized objective functions for conventional LSRTM (blue), LSRTM with Laplacian (red) and based on the energy norm (green). Note suppression of low-wavenumber artifacts above the salt and the convergence speed-up obtained by the alternative LSRTMs. 74

Figure 4.2 GOM 3D dataset: (a) 37 nodes spaced by approximately 800m, and sources densely distributed at the surface of the model. (b) Velocity model. (c) Normalized objective functions for conventional (blue), Laplacian-based (red), energy-based (green), and preconditioned energy-based (black and then green at iteration 2) LSRTMs. The energy LSRTM has best performance if we apply preconditioning at the first two iterations. 77

Figure 4.3 GOM 3D dataset: depth slices at $z = 1.55$km and $z = 1.77$km, respectively, for (a)/(b) RTM, (c)/(d) conventional LSRTM, and (e)/(f) energy LSRTM with preconditioning. In the LSRTM images, note the improvement in focusing of the diffractors and in delineation of the reflectors. 78

Figure 4.4 GOM 3D dataset: inline sections for energy RTM (left) and LSRTM with preconditioning (right) at $y = 44.9$km. Note the increase in frequency content and illumination for the LSRTM image compared to RTM. 79

Figure 4.5 GOM 3D dataset: wavenumber-domain RTM (a)/(c) and energy LSRTM (b)/(d) images from Figure 4.3 (at $z = 1.55$km and $z = 1.77$km, respectively). Note the stronger amplitudes recovered by LSRTM at the high wavenumbers (near the corners of the plot). 80

Figure 4.6 GOM 3D dataset: depth slices for RTM (left) and LSRTM (right) at the water bottom ($z = 1.20$km). Note the artifact suppression in some locations indicated by the white circles. 81

Figure 4.7 GOM 3D dataset: Node gather at $x = 214.5$km and $y = 44.9$km sorted by increasing offset: (a) observed, final (b) predicted and (c) residual data. (d) Offset values for each trace. Note that the main reflection events are predicted and eliminated in the data residual, especially for events at near- and mid-offsets. Linear moveout is applied on these plots for display purposes. 82

Figure 5.1 Snapshots of the vertical components of (a) background and (b) scattered wavefields at $t = 0.52$s. The black line at $z = 0.55$km indicates the position of the reflector. Using the scattered wavefield in place of the receiver wavefield, we obtain (c) PP, (d) PS, (e) SP, (f) SS, and (g) energy images. The incomplete wave-mode decomposition creates artifacts in PP, PS, SP and SS images, and crosstalk correlation creates artifacts in all images. The space-time diagram in (h) shows all wave events associated with this experiment: solid and dashed lines indicate P and S waves, respectively, and the horizontal gray line indicates the reflector. With this diagram, we can note that (e) SP and (f) SS images contain additional crosstalk artifacts due to the correlation of the incident S wave with the the decomposed PP and PS reflections, respectively, as seen by the intersections between these events indicated by the unfilled circles in the diagram. 98

Figure 5.2 (a) Density model used in full-wavefield modeling, and (b) reflectivity model used in linearized modeling. The acquisition geometry consists of 10 sources and a line of receivers (black dots and gray line at the top). Elastic energy RTM image with (c) full-modeled data and with (d) linearized-modeled data. Elastic energy LSRTM image with (e) full-modeled data and with (f) linearized-modeled data. Note how LSRTM attenuates artifacts caused by sparse acquisition. 100

Figure 5.3 Vertical- (left) and horizontal- (right) component data from (a) full modeling and from (b) linearized modeling. Data residuals from the LSRTM images using (c) full modeling and from (d) linearized modeling. (e) Normalized objective functions for inversion using full-modeled data (dashed) and linearized data (solid). The far-offset amplitudes from full-modeled data are not correctly predicted by the linearized modeling operator. 101

Figure 5.4 BP TTI model parameters: (a) P-wave and (b) S-wave velocities along the symmetry axis; Thomsen parameters (c) δ and (d) ϵ along the symmetry axis; (e) tilt of the symmetry axis (ν); (f) density with contrasts for full-wavefield modeling experiment. 104

Figure 5.5 RTM images using (a) linearized-modeled data and (b) full-modeled data. LSRTM images after 20 iterations using (c) linearized-modeled data and (d) full-modeled data. (e) True reflectivity model for linearized-modeled data and (f) Laplacian operator applied on the density model in Figure 5.4(f) in order to show contrasts that create reflections in the full-wavefield modeling. 105

Figure 5.6 Vertical component of observed data at a $x_s = 41.4$km obtained by (a) linearized modeling using the reflectivity model in Figure 5.5(e), and (b) full-wavefield modeling using density model in Figure 5.4(f). Vertical component data residuals after 20 iterations for (c) linearized and (d) full-wavefield modeling experiments. (e) Normalized objective function for experiments using (dashed) full-modeled and (solid) linearized data. 106

Figure 5.7 Volve 2D model parameters: (a) P-wave and (b) S-wave velocities along the vertical symmetry axis; Thomsen parameters (c) δ and (d) ϵ. 107

Figure 5.8 Volve experiment: (a) observed, (b) residual and (c) modeled (after 15 iterations) pressure shot gathers for a source at $x = 6.4$km. The main reflections are correctly predicted by our modeling operator. (c) Normalized objective function for LSRTM. 108

Figure 5.9 Volve experiment: energy (a) RTM and (b) LSRTM images. Reflectors around $z = 3.0$km become sharper, especially at the edges of the image. The arrows indicate reflectors that become more visible in the LSRTM image relative to RTM. 109

Figure 6.1 True (top), unconstrained (middle), and constrained (bottom) inverted models for (a) λ and (b) μ. The top panels also show the 11 sources (red) and the line of multicomponent receivers (yellow), and the reflector (black). Adding the physical constraint term into the inversion mitigates the spurious artifacts from inter-parameter crosstalk and sparse acquisition, delivering a more plausible earth model. 128

Figure 6.2 Crossplot in λ-μ space of inverted models: unconstrained (left) and constrained (right). The black line corresponds to the true model. The logarithmic barrier function used in the constrained inversion is plotted in the background. The unconstrained inverted model is spread throughout the model space without following a trend, while the constrained model is restricted to the region delimited by the barriers. . 129

Figure 6.3 Objective functions in decibel scale for unconstrained (dashed) and constrained (solid) ERWIs, which alternate between least-squares migration of model perturbations (red) and waveform inversion of background model (blue). Note how constrained ERWI performs better at the final iterations for both smooth model (at iteration 32) and image (final) inversions. 129

Figure 6.4 RTM (top) and LSRTM (middle) images obtained with the initial velocity, and LSRTM (bottom) images obtained with constrained inverted velocities for (a) $\delta\lambda$ and (b) $\delta\mu$. The faint dashed cyan line corresponds to the true reflector. Note the sparse acquisition artifacts in RTM, the irregularity of the imaged flat reflector for RTM and LSRTM as imprint of wrong velocity, and the improved reflector flatness and focusing for LSRTM with the constrained inverted velocity. 130

Figure 6.5 Lamé parameters λ (a) and μ (b) from the Marmousi II model. The acquisition geometry, which consists of 17 pressure sources (red) near the water surface and a line (yellow) of multicomponent receivers, is also shown in (a). The locations for the three wells used as prior information are indicated by green lines in (b). 133

Figure 6.6 Lamé parameters λ (blue) and μ (red) well-log profiles at the three locations shown in Figure 6.5. This information is used for the reference model ($\mathcal{J}_M$) and to define the petrophysical constraints ($\mathcal{J}_C$) implemented in the ERWI experiments. 134

Figure 6.7 Initial (top), reference (middle) and low-pass true (bottom) models. The green lines indicate the three well locations used as input for the image-guided interpolation among wells to create the reference model. . 135

Figure 6.8 Inverted models using the objective functions $\mathcal{J}_D$ (top), $\mathcal{J}_D + \mathcal{J}_M$ (middle), and $\mathcal{J}_D + \mathcal{J}_M + \mathcal{J}_C$. Note the attenuation of spurious artifacts with addition of reference model term (middle), and further improvement with petrophysical constraint term (bottom). 135

Figure 6.9 Crossplots in $\lambda - \mu$ space of (a) well-log samples, whose apparent slope is used to construct the barriers; (b) unconstrained inverted model; (c) constrained inverted model; and (d) true model. As opposed to the model points in (b), which do not follow a trend, the model pairs in (c) obey the imposed constrained constructed from (a) and conforms with the true model in (d). 136

Figure 6.10 Objective functions in decibel scale for unconstrained (dashed) and constrained (solid) ERWIs, which alternate between least-squares migration of model perturbations (red) and waveform inversion of background model (blue). Note how constrained ERWI performs better at the final iterations for both the smooth model (at iteration 44) and the image (final) inversions. Also, the constrained ERWI objective function for waveform inversion (solid blue) exhibits less variation when compared to its unconstrained counterpart (dashed blue). 137

Figure 6.11 From top to bottom: (1) RTM images with the initial velocity, LSRTM images with (2) initial velocity, (3) unconstrained, (4) constrained and (5) true models, for $\delta\lambda$ (a) and energy (b) imaging conditions. Note how the energy images are higher-quality and do not show low-wavenumber artifacts. Also note how improving the velocity model leads to better focused reflectors, and how least-squares migration is superior to conventional migration. 138

Figure A.1 Permission from **Geophysics** 160

Figure A.2 Permission for the 3D microseismic field dataset used in Chapter 3: anonymous company and ESG/Spectraseis 161

Figure A.3 Permission for the 3D GOM field dataset used in Chapter 4: Shell Exploration and Production Company 162

Figure A.4 Permission for the 2D Volve field dataset used in Chapter 5: Statoil ASA and the Volve license partners ExxonMobil E&P Norway AS and Bayerngas Norge AS 163

Figure A.5 Permission from Nicolay Tanushev 164

Figure A.6 Permission from Jeffrey Shragge 165

Figure A.7 Permission from Ben Witten 165

Figure A.8 Permission from Antoine Guitton 166

LIST OF ABBREVIATIONS

Center for Wave Phenomena . . . . . CWP

Conventional Imaging Condition CIC

Elastic Reverse Time Migration . . . . . ERTM

Energy Passive Imaging Condition . . . . . EPIC

Extended Imaging Condition . . . . . EIC

Full Waveform Inversion . . . . . FWI

Gulf of Mexico . . . . . GOM

Least-Squares Migration . . . . . LSM

Least-Squares Reverse Time Migration . . . . . LSRTM

P-S Imaging Condition . . . . . PSIC

Reflection Waveform Inversion . . . . . ERWI

Reflection Waveform Inversion . . . . . RWI

Reverse Time Migration . . . . . RTM

Signal-to-Noise Ratio . . . . . S/N

Wave-Equation Migration Velocity Analysis . . . . . WEMVA

ACKNOWLEDGMENTS

This thesis is a product of many people who have assisted me throughout my graduate studies. The greatest contribution comes Dr. Paul Sava, my research advisor, with his insights and knowledge that were essential for the vast majority of this research. By knowing my potential, he pushed me to addressing challenging research problems that have fostered my development as a scientist. I am very grateful and proud for having him as my advisor. By believing that I would be successful in my research enterprise, Paul is also responsible for bringing me to Colorado School of Mines for PhD studies. Aside from research, he has helped me in personal matters since the beginning of my graduate studies.

Some chapters of this thesis include authors besides myself and Paul. Nicolay Tanushev suggested applying the energy norm to wavefield imaging methods and has given a great input into the energy norm formulation. Jeffrey Shragge provided the insight of applying the energy imaging condition to the passive seismic case. Ben Witten helped me familiarizing with the passive field dataset and associated velocity model. Antoine Guitton assisted me with least-squares migration implementation and field data processing, as well as great suggestions and discussions that improved the technical content of most chapters. Besides all of that, my co-authors also provided assistance with manuscript writing.

I would like to thank the members of my graduate committee, Ilya Tsvankin, Paul Martin, Brandon Dugan and Michael Mooney, for having found time in their busy schedules and accepted to be part of my committee. The faculty, staff and students from Center for Wave Phenomena (CWP), the research center of which I belong to, helped me significantly in various ways. Regarding administrative issues, Pam Kraus, Shingo Ishida and Dawn Umpleby have been always accessible and helpful during the time that I have been at CWP. Michelle Szobody, from the Geophysics Department, has been acessible and helpful to me since my graduate application until the thesis defense. My writing and communication skills

have improved notably since my first days at CWP, thanks to Diane, the writing consultant in our research center. The other members in CWP faculty: Jeffrey Shragge, Roel Snieder and Ilya Tsvankin, taught me relevant subjects that I incorporated in this thesis. A retired CWP faculty member, Ken Larner, has taught me valuable lessons for presenting to an audience effectively in his Professional Oral Communication course. The members of the iTeam (group in CWP focused on wavefield imaging) gave me valuable insights from the many discussions that we had in our seminars: Esteban Diaz, Yuting Duan, Ivan Lim Chen Ning, Thomas Rapstine, Odette Aquino, Iga Pawelec, among others. Special thanks to members from aTeam (group in CWP focused on anisotropy) for helpful discussions: Vladimir Li, Oscar Jarillo and Nishant Kamath. Also, my friends in the department: Samir Jreij, Aline Melo, Paul El Khoury, among others.

The consortium of companies which sponsors CWP funds my research and stipends. I am very grateful for the people who make this thesis research topic possible by funding. They also give relevant feedback in visits and in every CWP consortium meeting, which occurs yearly. One of the sponsor companies, Shell Exploration and Production Company, granted me with two internships and a full time offer. I am grateful for Shell offering me a great opportunity of professional experience and start of a promising career. In addition, I have been awarded a scholarship from Chevron during my last semester, for which I am really grateful.

Finally, I would like to thank my family and friends for the personal support in my stay here in Colorado. These include my parents (Daniel and Ivete Rocha), my beloved sister (Carol Rocha), Igor Vieira, Lorna Crawford, Alisha Bradshaw, and many others.

For my nephew, Mateus Rocha.

CHAPTER 1

INTRODUCTION

Observations of physical phenomena occurring inside the Earth enable geophysicists to extract valuable information about the subsurface. Such information aids natural resources mapping and mitigation of natural hazards. In particular, seismology and its robust imaging methodology serves as a crucial tool for oil and gas exploration and for comprehension of earthquake initiation and behavior.

Although the research work presented here is readily applicable to earthquake seismology, I have dedicated my attention to seismic imaging applications for oil and gas exploration, which is still essential for society despite recent advances in alternative sources of energy. Not only a large proportion of current energy usage is based on fossil fuels, but a great variety of everyday products are manufactured utilizing oil as raw material. Such secondary usage of oil will remain a reality even when clean energy sources become mainstream in the future. Given this importance, many imaging-related challenges persist in the oil exploration industry and new ones appear, such as low oil prices requiring exploration costs to reduce by significant margins. Innovative ideas from geophysics that improve exploration technology, and particularly seismic imaging, represent a significant contribution to addressing this global challenge. Additionally, cutting-edge technology emerging from seismic imaging often yields applications to other fields also relevant to society, such as medical imaging (Manduca et al., 2001), planetary research (Sava and Asphaug, 2018), and non-destructive damage monitoring (He et al., 2017).

Among diverse techniques for exploring hydrocarbon resources, seismic imaging performed by wavefield extrapolation brings the best image quality for complex geological settings, despite its higher computational cost relative to more conventional methods based on traveltime calculation (Yoon et al., 2003; Cerveny, 2005; Guitton et al., 2007b; Dussaud

et al., 2008; Farmer et al., 2009; Liu and Gu, 2012). In this framework, methods for estimating the earth model are categorized as wavefield tomography (Lailly, 1983; Tarantola, 1984; Gauthier et al., 1986; Sava and Biondi, 2004a; Albertin et al., 2005; Plessix, 2006; Symes, 2008; Yang and Sava, 2011; Yang et al., 2013; Diaz et al., 2013; Yang and Sava, 2015), while the methods for locating geological interfaces or a subsurface seismic source are described as wavefield migration (Baysal et al., 1983; McMechan, 1983; Whitmore, 1983; Levin, 1984; Zhang and Sun, 2009; Artman et al., 2010; Nakata and Beroza, 2016).

In both domains, inversion is the theoretical and computational framework that provides plausible earth models matching field observations and potentially conforming with prior geological and petrophysical knowledge. This framework consists of exploring earth models that predict geophysical data through a quantitative comparison with observations based on a data-misfit metric (Tarantola, 2005). Limiting the range of explored models by imposing geological or structural information is crucial (Guitton et al., 2012; Asnaashari et al., 2013; Baumstein, 2013; Peters et al., 2015; Duan and Sava, 2016), especially for seismic tomography which is highly dependent on the proper conditioning of input parameters to deliver reasonable models. Wavefield tomography is intrinsically an inversion problem; however, wavefield migration is called least-squares migration (LSM) when the image is refined through inversion (Chavent and Plessix, 1999; Nemeth et al., 1999; Kuehl and Sacchi, 2003; Aoki and Schuster, 2009; Dai et al., 2010; Yao and Jakubowicz, 2012; Dai and Schuster, 2012; Dong et al., 2012). Both wavefield tomography and least-squares migration are currently feasible given the rapid increase in computational capacity (Chavent and Plessix, 1999; Nemeth et al., 1999; Kuehl and Sacchi, 2003; Jiang and Schuster, 2005; Luo and Hale, 2014). The computational cost of inversion for both migration and tomography can be further reduced with robust techniques (e.g., approximate Hessian preconditioning) that speed up the convergence to the final model (Kiyashchenko et al., 2007; Aoki and Schuster, 2009; Huang et al., 2016c; Liu et al., 2016).

My research covers a variety of topics in both wavefield tomography and migration with increasing degrees of physical complexity (acoustic, elastic, anisotropic, etc.). The current imaging state of the art relies on migration and tomography methods that do not properly take into consideration important features of seismic wavefields, specifically their directionality and polarization, and also disregard prior geological knowledge, such as petrophysical relationships among earth model parameters. As a result, commonly-applied methodology often leads to images and models corrupted by strong artifacts, such as low-wavenumber, polarity-reversed events, inter-parameter crosstalk, among others that degrade our ability to identify features of the geological structure (Balch and Erdemir, 1994; Youn and Zhou, 2001; Yoon and Marfurt, 2006; Guitton et al., 2007a; Denli and Huang, 2008; Yan and Sava, 2008; Zhang and Sun, 2009; Operto et al., 2013; Chen and Huang, 2014; Du et al., 2014a; Duan and Sava, 2015; Diaz and Sava, 2015; Pan and Innanen, 2016). During inversion, these artifacts impede convergence to an accurate earth model, posing a persistent problem for wavefield imaging and subsurface characterization.

I address the shortcomings of conventional wavefield imaging by using a measure of wavefield energy, known as the *energy norm*. The motivation for applying this type of measure to problems in wavefield imaging is that such measure arises from the differential equations that govern wavefield propagation, and therefore it is fundamentally based on our understanding of wave phenomena. One can define the energy norm for any type of wavefield, but for illustration purposes, here is the energy norm for acoustic wavefields in isotropic media:

$$\|U(\mathbf{x},t)\|_E^2 = \left|\frac{1}{v}\frac{\partial U}{\partial t}\right|^2 + |\nabla U|^2 \ , \tag{1.1}$$

where $U(\mathbf{x},t)$ represents an acoustic wavefield as a function of space $\mathbf{x}$ and time t, and $v(\mathbf{x})$ is the wave speed. Equation 1.1 directly follows from the acoustic wave equation

$$\frac{1}{v^2}\frac{\partial^2 U}{\partial t^2} = \nabla^2 U \tag{1.2}$$

that governs wave propagation for the isotropic acoustic case. Based on the energy norm, I define imaging conditions for one or more wavefields in order to generate a better representation of subsurface interfaces. Under the energy norm formulation, migration acquires special properties that effectively highlight desired features of the earth structure and attenuate unwanted ones. I have introduced this subject and shown its merits in wavefield migration during my Master of Science (M.Sc.) studies:

- Rocha, D., Tanushev, N., Sava, P.C., 2015, Acoustic wavefield imaging using the energy norm, Proceedings of the 85th Annual International Meeting, Society of Exploration Geophysicists.
- Rocha, D., Tanushev, N., Sava, P.C., 2015, Elastic wavefield imaging using the energy norm, Proceedings of the 85th Annual International Meeting, Society of Exploration Geophysicists.
- Rocha, D., Tanushev, N., Sava, P.C., 2016, Acoustic wavefield imaging using the energy norm, **Geophysics**, v. 81, pp S151-S163.
- Rocha, D., Tanushev, N., Sava, P.C., 2016, Isotropic elastic wavefield imaging using the energy norm, **Geophysics**, v. 81, pp. S207-S219.

Since then, I have gone beyond and posed energy wavefield imaging in the least-squares migration framework. This naturally extends the research previously conducted during my M.Sc. studies. As I show in this thesis, incorporating the energy norm into the inversion formulation leads to more geological-plausible models, improves source estimation for passive methods, and accelerates inversion convergence. Furthermore, to strengthen energy wavefield migration inversion by providing more accurate earth models, I also explore wavefield tomography that takes into account petrophysical relationships among model parameters.

1.1 Thesis Outline

This thesis is structured into chapters that are based on published or submitted articles to peer-reviewed journals. Each chapter contains relevant literature review, an explanation of a

specific migration and/or tomography method, and numerical examples with synthetic and field datasets; except for Chapter 7 that consists of conclusion remarks and ideas worth exploring in the future. Different physics of wave propagation (acoustic or elastic), acquisition configuration (passive or active), assumptions about the medium (isotropic or anisotropic), or whether one searches for an earth model (tomography) or geological interfaces (migration) are grouped into the following chapters:

- Chapter 2, titled "Anisotropic elastic wavefield imaging using the energy norm", covers wavefield migration using an imaging condition based on the energy norm for one of the most general formulations of seismic wave propagation (i.e., anisotropic elastic). To prove that the method delivers better quality images compared to its conventional counterparts, I show examples with synthetic but realistic earth models. This chapter was presented at an European Association of Geoscientists and Engineers (EAGE) annual meeting, and was also published in **Geophysics**:

  - Rocha, D., Tanushev, N., Sava, P.C., 2016, Anisotropic elastic wavefield imaging using the energy norm, Proceedings of the 78th Annual International Meeting, European Association of Geoscientists and Engineers.

  - Rocha, D., Tanushev, N., Sava, P.C., 2017, Anisotropic elastic wavefield imaging using the energy norm, **Geophysics**, May 2017, Vol. 82, No. 3, pp. S225-S234.

- Chapter 3, titled "3D passive wavefield imaging using the energy norm", covers an imaging condition based on the energy norm that estimates source location for passive multicomponent seismic acquisition without costly wave-mode decomposition. I demonstrate the effectiveness of the method by comparison with conventional cross-correlation between separated wave modes in complicated earth models. I present 3D synthetic and field data examples. A Society of Exploration Geophysicists (SEG) expanded abstract was presented, an EAGE expanded abstract about the subject has been accepted, and this chapter has been submitted to **Geophysics**.

- Rocha, D., Sava, P.C., Shragge, J., 2016, Passive wavefield imaging using the energy norm, Proceedings of the 86th Annual International Meeting, Society of Exploration Geophysicists.
- Rocha, D., Sava, P.C., Shragge, J., Witten, B., 2018, 3D microseismic wavefield imaging using the energy image, Proceedings of the 80th Annual International Meeting, European Association of Geoscientists and Engineers.
- Rocha, D., Sava, P.C., Shragge, J., Witten, B., 2018, 3D passive wavefield imaging using the energy norm, **Geophysics** (submitted).

- Chapter 4, titled "3D acoustic least-squares reverse time migration with the energy norm", exploits the energy norm in least-squares reverse time migration (LSRTM) for acoustic wavefields, coupled with preconditioning based on matching filters between two images. As I show with synthetic and 3D field data examples, this new technique expedites convergence rates for acoustic LSRTM compared to its conventional counterpart. Expedited LSRTM is important to refine the image quality that is degraded by the inherent limitation of the adjoint operation (RTM) and by seismic acquisition constraints (e.g., aliasing, band-limited recording, etc.) under time and computational resources constraints. My findings on this subject were presented at a SEG annual meeting, and were also published as a peer-reviewed article in **Geophysics**:
  - Rocha, D., Sava, P.C., Guitton, A., 2017, Acoustic 3D least-squares reverse time migration using the energy norm, Proceedings of the 87th Annual International Meeting, Society of Exploration Geophysicists.
  - Rocha, D., Sava, P.C., Guitton, A., 2018, 3D acoustic least-squares reverse time migration using the energy norm, **Geophysics**, May 2018, v. 83, no. 3, pp. S261-S270.

- In Chapter 5, titled "Elastic least-squares reverse time migration with the energy norm", I also exploit the energy norm in least-squares reverse time migration (LSRTM)

but for elastic wavefields and multicomponent data. I propose a new LSRTM scheme that uses anisotropic elastic wavefields and generates a scalar image. I illustrate this method with 2D synthetic and field data examples. I presented this chapter at a SEG annual meeting and I also published it as a peer-reviewed article in **Geophysics**:

  - Rocha, D., Sava, P.C., 2017, Elastic least-squares reverse time migration using the energy norm, Proceedings of the 87th Annual International Meeting, Society of Exploration Geophysicists.
  - Rocha, D., Sava, P.C., 2018, Elastic least-squares reverse time migration using the energy norm, **Geophysics**, May 2018, v. 83, no. 3, pp. S237-S248.

- In Chapter 6, I explore wavefield tomography with the goal of refining the earth model for least-squares energy imaging, which is impractical without such sufficiently accurate models. I implement a wavefield tomography method that imposes petrophysical constraints into inversion while updating separated earth model constituents, i.e., smooth and rough contrasts. Energy least-squares imaging uses an earth model that results from the summation of both smooth and rough model inversions. Similarly to the other chapters, I intend to publish this chapter as an article in a peer-reviewed journal. The following references show expanded abstracts published in conference proceedings:

  - Rocha, D., Sava, P.C., 2018, Elastic reflection waveform inversion with petrophysical model constraints, expanded abstract submitted to the 88th Annual International Meeting, Society of Exploration Geophysicists.
  - Rocha, D., Lim, I., Sava, P.C., 2018, Novel approaches for elastic wavefield imaging and inversion, EAGE Workshop Seismic imaging with rays and waves: Where do we stand? Part II: Imaging, Copenhagen, Denmark.

CHAPTER 2

ANISOTROPIC ELASTIC WAVEFIELD IMAGING USING THE ENERGY NORM

A paper published* in Geophysics

Daniel Rocha**,[1], Nicolay Tanushev[2] and Paul Sava[1]

Based on the energy conservation principle, we derive a scalar imaging condition for anisotropic elastic wavefield migration. Compared to conventional imaging conditions that simply correlate displacement components or potentials from source and receiver wavefields, the proposed imaging condition does not suffer from polarity reversal, which degrades the image quality after stacking over shots. Our imaging condition also accounts for the directionality of the wavefields in space and time, leading to the attenuation of backscattering artifacts, which commonly appear in elastic reverse-time migration images in the presence of strong model contrasts. In addition, our new imaging condition does not require wave-mode decomposition, which demands significant additional cost for elastic wavefields in anisotropic media. To properly image structures, we rely on the anisotropy parameters used in migration, as one would do for any other imaging condition. Our imaging condition is suitable for arbitrary anisotropy. We show the successful application of the anisotropic energy imaging condition by performing numerical experiments on simple and complex geological models. We compare its quality to conventional counterparts by simulating complex geological settings with vertical or tilted transverse isotropy (VTI/TTI).

* Reprinted with permission of *Geophysics*, Vol. 82, No 3 (May-June 2017), pp. S225-S234
** Corresponding author. Direct correspondence to drocha@mines.edu
[1] Center for Wave Phenomena, Colorado School of Mines, 924 16th St., Golden, CO 80401
[2] Z-Terra Inc., 17171 Park Row Dr. #247, Houston, TX 77084

2.1 Introduction

We frame our paper in the context of (1) an elastic earth, supporting the propagation of both compressional and shear waves, and (2) an anisotropic earth, causing wave phenomena such as phase velocity variation with the propagation direction. Although the seismic exploration industry has used the acoustic and isotropic assumptions for a long time, the search for more authentic images and subsurface information, such as fracture distribution, encourages multicomponent elastic wavefield imaging (Chang and McMechan, 1987; Balch and Erdemir, 1994; Denli and Huang, 2008; Yan and Sava, 2011b; Yan and Xie, 2012; Du et al., 2014a; Gong et al., 2016). At the same time, data acquired with larger offsets and the increasing number of acquired azimuths enables one to properly account for the influence of anisotropy in order to image complex geological structures (Mikhailov et al., 2001; Jing et al., 2006; Lu et al., 2010; Zhang and McMechan, 2011; Li et al., 2012; McGarry and Qin, 2013; Hu et al., 2014; Wang et al., 2014).

Wavefield imaging, using either the acoustic or elastic wave equation, is implemented in two steps: (1) wavefield extrapolation in the subsurface, using recorded data and an earth model, and (2) the application of an imaging condition to extract the earth's reflectivity from the extrapolated wavefields (Claerbout, 1971; Etgen, 1988; Yan and Sava, 2009). If a two-way elastic wave equation is used in the wavefield extrapolation step, followed by the zero-lag crosscorrelation of the wavefields as the imaging condition, the procedure is called elastic reverse time migration (ERTM) (Chang and McMechan, 1987; Hokstad et al., 1998). In recent years, many elastic imaging conditions have been proposed by exploiting the multicomponent aspect of the elastic wavefield and, for the isotropic case, by possibly decomposing the displacement fields into P- and S-wave potentials (Dellinger and Etgen, 1990; Zhe and Greenhalg, 1997; Yan and Sava, 2007; Yan and Xie, 2010; Duan and Sava, 2015). For anisotropic media, wave-mode decomposition during wavefield extrapolation is feasible but requires additional computational cost and robust techniques (Yan and Sava, 2009; Zhang and McMechan, 2010; Yan and Sava, 2011a; Cheng and Fomel, 2014). Consid-

ering the high cost of wave-mode decomposition, the straight correlation of the source and receiver displacement fields for each component is a convenient imaging condition for elastic wavefields in anisotropic media (Jiang, 2016; Kim et al., 2016). However, for 3-D imaging, this imaging condition generates nine images (considering all possible correlations among source and receive wavefields components) with a mixture of wave modes, and this large set of images poses serious difficulties for interpretation.

Another problem exhibited by displacement imaging conditions is polarity reversal, which occurs if one correlates displacement components from opposite directions. The main disadvantage of polarity reversal is the degradation of image quality after stacking over experiments. Polarity reversal can be corrected by different techniques (Balch and Erdemir, 1994; Yan and Sava, 2008; Du et al., 2014a; Duan and Sava, 2015), but all such approaches are either approximate (e.g. reversal at zero offset) or costly.

Compared to the acoustic case, elastic imaging involves another issue in addition to polarity reversal. Injection of elastic data into a model (implementing wavefield backpropagation) creates non-physical (or "fake") wave modes during the wavefield extrapolation step, leading to artifacts after the application of an imaging condition (Yan and Sava, 2007; Ravasi and Curtis, 2013; Duan and Sava, 2015). These artifacts degrade image quality, and might be present even after stacking, masking weak reflections in the final image (Duan and Sava, 2014). This type of artifacts is caused by displacement injection into the model and is beyond the scope of this paper.

Analogous to the acoustic case, a second type of artifact appears if the elastic model contains sharp interfaces. These interfaces create backscattered reflections at the wavefield extrapolation step, and conventional correlation of the multicomponent wavefields creates low-wavenumber artifacts in the image at the imaging condition step (Youn and Zhou, 2001; Yoon and Marfurt, 2006; Guitton et al., 2007a; Denli and Huang, 2008; Chen and Huang, 2014; Diaz and Sava, 2015; Rocha et al., 2016b). Ideally, the backscattering artifacts should be attenuated during imaging, without the use of post-imaging artificial filters such as the

Laplacian operator (Zhang and Sun, 2009).

Considering these issues, we seek to facilitate interpretation and provide a concise description of the subsurface structures by defining an imaging condition that yields an attribute of the earth's reflectivity into a single image without wave-mode decomposition, without polarity reversal, and without backscattering artifacts. Our proposed imaging condition is formulated using the energy conservation principle (Yu, 1964; Ben-Menahem and Singh, 1981; Webster, 2000; Rocha et al., 2016a), and extends the previous work on isotropic elastic wavefield imaging (Rocha et al., 2016b).

2.2 Theory

We use energy conservation laws analogous to the acoustic and isotropic elastic cases (Rocha et al., 2016a,b) to derive a function that measures the energy of a wavefield in anisotropic media. This energy function also allows us to form an imaging condition for extrapolated elastic wavefields from sources and receivers.

2.2.1 Elastic wave equation

For an anisotropic medium enclosed by a physical domain $\Omega \subset \mathbb{R}^3$, we can write the equation of motion with no external sources (Aki and Richards, 2002):

$$\rho \ddot{\mathbf{U}} = \nabla \cdot \underline{\mathbf{t}} \; . \tag{2.1}$$

In equation 2.1, the displacement field is a function of space ($\mathbf{x}$), time (t), and the experiment index (e): $\mathbf{U}\left(e, \mathbf{x}, t\right)$ for $\mathbf{x} \in \Omega$ and $t \in [0, T]$, where T is the maximum acquisition time. The experiment index (e) usually represents a shot record, but could also represent a plane wave or other type of shot encoding (Romero et al., 2000; Liu et al., 2006; Godwin and Sava, 2013). The superscript dot indicates time differentiation. The density is a function of space $\rho(\mathbf{x})$. The underlying bar indicates that the stress is a second-order tensor as a function of space, time and experiment index $\underline{\mathbf{t}}\left(e, \mathbf{x}, t\right)$. One needs to use certain relations involving material properties to turn equation 2.1 into a wave equation. Using a general form of linear

Hooke's law

$$\underline{\mathbf{t}} = \underline{\underline{\mathbf{c}}}\underline{\mathbf{e}} \, , \tag{2.2}$$

where $\underline{\mathbf{e}}\,(e, \mathbf{x}, t)$ is the strain tensor, $\underline{\underline{\mathbf{c}}}\,(\mathbf{x})$ is the stiffness tensor, and the underlying double bar indicates that the stiffness is a 4th-order tensor. One can rewrite the equation of motion in (2.1) as a function of the strain tensor

$$\rho\ddot{\mathbf{U}} = \nabla \cdot \left(\underline{\underline{\mathbf{c}}}\underline{\mathbf{e}}\right) \, . \tag{2.3}$$

The strain tensor is a function of the displacement:

$$\underline{\mathbf{e}} = \frac{1}{2}\left(\nabla\mathbf{U} + \nabla\mathbf{U}^{\mathrm{T}}\right) \, . \tag{2.4}$$

Therefore, using the symmetry of the stiffness tensor, we can rewrite equation 2.3 as a wave equation:

$$\rho\ddot{\mathbf{U}} = \nabla \cdot \left[\underline{\underline{\mathbf{c}}}\nabla\mathbf{U}\right] \, . \tag{2.5}$$

Equation 2.5 can be used to extrapolate an elastic wavefield for arbitrary sources, assuming that we know the spatial distribution of the stiffness tensor $\underline{\underline{\mathbf{c}}}\,(\mathbf{x})$.

2.2.2 Elastic wavefield energy

Analogous to the acoustic and isotropic elastic cases disscussed in Rocha et al. (2016a,b), we develop the energy conservation expression for elastic wavefields in anisotropic media by taking a dot product of the time derivative of the displacement wavefield (i.e., particle velocity) with the corresponding wave equation, followed by integration over the entire physical domain Ω:

$$\int_{\Omega} \rho\dot{\mathbf{U}} \cdot \ddot{\mathbf{U}} d\mathbf{x} = \int_{\Omega} \dot{\mathbf{U}} \cdot \left[\nabla \cdot \left(\underline{\underline{\mathbf{c}}}\nabla\mathbf{U}\right)\right] d\mathbf{x} \, . \tag{2.6}$$

Rearranging the term on the left-hand side by the chain rule leads to

$$\frac{1}{2}\frac{\partial}{\partial t}\int_{\Omega} \rho\|\dot{\mathbf{U}}\|^2 d\mathbf{x} = \int_{\Omega} \dot{\mathbf{U}} \cdot \left[\nabla \cdot \left(\underline{\underline{\mathbf{c}}}\nabla\mathbf{U}\right)\right] d\mathbf{x} \, . \tag{2.7}$$

Using the chain rule again on the right-hand side leads to

$$\frac{1}{2}\frac{\partial}{\partial t}\int\limits_{\Omega}\rho|\dot{\mathbf{U}}|^2 d\mathbf{x} = \int\limits_{\Omega}\nabla\cdot\left[\left(\underline{\underline{\mathbf{c}}}\nabla\mathbf{U}\right)\dot{\mathbf{U}}\right]d\mathbf{x} - \int\limits_{\Omega}\nabla\dot{\mathbf{U}} : \left(\underline{\underline{\mathbf{c}}}\nabla\mathbf{U}\right)d\mathbf{x}\,. \tag{2.8}$$

The first term on the right-hand side turns into a surface integral over the boundary using the Divergence Theorem (Boas, 2006). Because we assume homogeneous boundary conditions for the wavefield and its derivatives, this surface integral goes to zero:

$$\frac{1}{2}\frac{\partial}{\partial t}\int\limits_{\Omega}\rho\|\dot{\mathbf{U}}\|^2 d\mathbf{x} = -\int\limits_{\Omega}\nabla\dot{\mathbf{U}} : \left(\underline{\underline{\mathbf{c}}}\nabla\mathbf{U}\right)d\mathbf{x}\,. \tag{2.9}$$

Developing the remaining term on the right-hand side by using the properties of the Frobenius product (Appendix 2.7.1), we obtain

$$\begin{aligned}
\int\limits_{\Omega}\nabla\dot{\mathbf{U}} : \left(\underline{\underline{\mathbf{c}}}\nabla\mathbf{U}\right)d\mathbf{x} &= \int\limits_{\Omega}\mathrm{Tr}\left[\nabla\dot{\mathbf{U}}^{\mathrm{T}}\left(\underline{\underline{\mathbf{c}}}\nabla\mathbf{U}\right)\right]d\mathbf{x}\,, &(2.10)\\
&= \frac{1}{2}\frac{\partial}{\partial t}\int\limits_{\Omega}\mathrm{Tr}\left[\nabla\mathbf{U}^{\mathrm{T}}\left(\underline{\underline{\mathbf{c}}}\nabla\mathbf{U}\right)\right]d\mathbf{x}\,, &(2.11)\\
&= \frac{1}{2}\frac{\partial}{\partial t}\int\limits_{\Omega}\left(\underline{\underline{\mathbf{c}}}\nabla\mathbf{U}\right) : \nabla\mathbf{U}\; d\mathbf{x}\,, &(2.12)
\end{aligned}$$

where $\mathrm{Tr}(\cdot)$ evaluates the trace of a matrix. Substituting equation 2.12 in equation 2.9, we have

$$\frac{1}{2}\frac{\partial}{\partial t}\int\limits_{\Omega}\rho\|\dot{\mathbf{U}}\|^2 + \left(\underline{\underline{\mathbf{c}}}\nabla\mathbf{U}\right) : \nabla\mathbf{U}\; d\mathbf{x} = 0\,. \tag{2.13}$$

Therefore, the function

$$E(t) = \frac{1}{2}\int\limits_{\Omega}\rho\|\dot{\mathbf{U}}\|^2 + \left(\underline{\underline{\mathbf{c}}}\nabla\mathbf{U}\right) : \nabla\mathbf{U}\; d\mathbf{x} \tag{2.14}$$

is conserved in time.

2.2.3 Physical interpretation

The first term in the integrand of equation 2.14 represents the kinetic energy of the wavefield, and the second term is the strain energy (Slawinski, 2003), which represents the potential energy of the wavefield. Therefore, equation 2.13 states the familiar fact that the

total energy $E(t)$ is conserved in time. Substituting the stiffness coefficients for the isotropic case in equation 2.14, we obtain the energy function for the isotropic case shown in Rocha et al. (2016b) (Appendix 2.7.2):

$$E(t) = \frac{1}{2} \int\limits_{\Omega} \rho \|\dot{\mathbf{U}}\|^2 + \lambda \|\nabla \cdot \mathbf{U}\|^2 + \mu \left[\nabla \mathbf{U} : \nabla \mathbf{U} + \nabla \mathbf{U} : \nabla \mathbf{U}^{\mathrm{T}} \right] \, d\mathbf{x} \, . \tag{2.15}$$

The individual terms in equations 2.14 and 2.15 are also related to nonlinear inversion theory as shown by other authors (Hokstad et al., 1998; Zhu et al., 2009).

2.2.4 Imaging condition

Considering two wavefields $\mathbf{U}$ and $\mathbf{V}$, and the elastic energy norm in equation 2.14, we can define the following inner product:

$$< \mathbf{U}, \mathbf{V} >_E = \int\limits_0^T \int\limits_{\Omega} \rho \dot{\mathbf{U}} \cdot \dot{\mathbf{V}} + \left(\underline{\underline{\mathbf{c}}} \nabla \mathbf{U} \right) : \nabla \mathbf{V} \, d\mathbf{x} \, . \tag{2.16}$$

We propose a new elastic imaging condition based on the inner product in equation 2.16 between source and receiver wavefields, followed by summation over time and experiments:

$$I_E = \sum_{e,t} \left[\rho \dot{\mathbf{U}} \cdot \dot{\mathbf{V}} + \left(\underline{\underline{\mathbf{c}}} \nabla \mathbf{U} \right) : \nabla \mathbf{V} \right] . \tag{2.17}$$

Here, $\mathbf{U}\left(e, \mathbf{x}, t\right)$ and $\mathbf{V}\left(e, \mathbf{x}, t\right)$ are the source and receiver vector wavefields, respectively, and $I_E\left(\mathbf{x}\right)$ is a scalar image obtained from the elastic wavefields. We can describe this imaging condition as a dot product between the following vectors:

$$\square \mathbf{U} = \left\{ \rho^{1/2} \dot{\mathbf{U}}, \underline{\underline{\mathbf{c}}}^{1/2} (\nabla \mathbf{U}) \right\} , \tag{2.18}$$

$$\square \mathbf{V} = \left\{ \rho^{1/2} \dot{\mathbf{V}}, \underline{\underline{\mathbf{c}}}^{1/2} (\nabla \mathbf{V}) \right\} . \tag{2.19}$$

The tensor $\underline{\underline{\mathbf{c}}}^{1/2}$ is the square root of $\underline{\underline{\mathbf{c}}}$, which exists and is unique because $\underline{\underline{\mathbf{c}}}$ is positive definite (Shao and Lu, 2009). Equations 2.18 and 2.19 define multidimensional vectors with twelve components (in contrast with three-component vectors in 3-D space). The first three components of the vectors in equations 2.18 and 2.19 are proportional to the wavefield time derivatives, $\dot{\mathbf{U}}$ and $\dot{\mathbf{V}}$, and the other nine components are derived from the displacement

gradients $\nabla\mathbf{U}$ and $\nabla\mathbf{V}$. We can call $\square\mathbf{U}$ and $\square\mathbf{V}$ "energy" vectors since their magnitudes are equal to the energy norm in equation 2.14 for a fixed point in space.

Therefore, we can rewrite equation 2.17 as

$$I_E = \sum_{e,t} \square\mathbf{U} \cdot \square\mathbf{V} \ . \tag{2.20}$$

This expression is analogous to the similar imaging condition developed for acoustic and isotropic elastic wavefields (Rocha et al., 2016a,b), and has similar physical interpretation and application, as discussed in the next section.

2.2.5 Backscattering attenuation

Vectors $\square\mathbf{U}$ and $\square\mathbf{V}$ are related to the polarization and propagation direction of the elastic wavefields $\mathbf{U}$ and $\mathbf{V}$. Consider a plane wavefield $\mathbf{U}$ given by

$$\mathbf{U} = \mathbf{u}_0 \cos\left[\omega\left(\mathbf{p}\cdot\mathbf{x} - t\right)\right] \ , \tag{2.21}$$

where $\mathbf{u}_0$ is the polarization vector, $\mathbf{p}$ is the slowness vector, and ω is the frequency. We assume that ω is large compared to the size of the medium and that the vectors $\mathbf{u}_0$ and $\mathbf{p}$ are slowly varying in space and time, which makes the spatial and temporal derivatives of $\mathbf{u}_0$ and $\mathbf{p}$ small compared to ω. We can rewrite equation 2.21 in index form as

$$U_i = u_i \cos\left[\omega\left(p_m x_m - t\right)\right] \ , \tag{2.22}$$

where indices $i, m = \{1, 2, 3\}$ represent the Cartesian components of wavefield $\mathbf{U}$. We follow the Einstein convention and all repeated indices are summed over. Substituting the plane wave definition in equation 2.22 as a trial solution of the elastic equation in 2.5, and collecting the highest order term in ω, we have

$$\omega^2 \sin\left[\omega\left(p_m x_m - t\right)\right]\left[\rho u_i - u_k c_{ijkl} p_j p_l\right] = 0 \ , \tag{2.23}$$

where $j, k, l = \{1, 2, 3\}$. Since equation 2.23 must hold for any ω, we obtain the Christoffel equation:

$$\rho u_i = u_k c_{ijkl} p_j p_l \ . \tag{2.24}$$

The dot product between equation 2.24 and the polarization vector $\mathbf{u}_0$ yields

$$\rho u_i u_i - u_i u_k c_{ijkl} p_j p_l = 0 \ . \tag{2.25}$$

Using equation 2.22, the term $\dot{\mathbf{U}}$ in index form is

$$\dot{U}_i = \omega u_i \sin\left[\omega\left(p_m x_m - t\right)\right] \ , \tag{2.26}$$

and $\nabla\mathbf{U}$ in index form is

$$U_{i,j} = -\omega u_i p_j \sin\left[\omega\left(p_m x_m - t\right)\right] \ , \tag{2.27}$$

where subscript indices after the comma symbol indicate spatial derivation with respect to one Cartesian component. Therefore, we can rewrite the norm of $\Box\mathbf{U}$, defined in equation 2.18, in index form as

$$\|\Box\mathbf{U}\|^2 = \rho\dot{U}_i\dot{U}_i + c_{ijkl}U_{i,j}U_{k,l} \ . \tag{2.28}$$

Using equations 2.26 and 2.27, the individual terms in equation 2.28 are

$$\begin{aligned} \rho\dot{U}_i\dot{U}_i &= \rho\omega^2 u_i u_i \sin^2\left[\omega\left(p_m x_m - t\right)\right] \ , & (2.29)\\ c_{ijkl}U_{i,j}U_{k,l} &= \omega^2 u_i u_k c_{ijkl} p_j p_l \sin^2\left[\omega\left(p_m x_m - t\right)\right] \ . & (2.30) \end{aligned}$$

Hence, the norm of $\Box\mathbf{U}$ is

$$\|\Box\mathbf{U}\|^2 = \omega^2\Big[\rho u_i u_i + u_i u_k c_{ijkl} p_j p_l\Big] \sin^2\left[\omega\left(p_m x_m - t\right)\right] \ . \tag{2.31}$$

We seek to define an imaging condition that attenuates the correlation between waves from the source and receiver wavefields propagating along the same path and with the same polarization, i.e., elastic backscattering. Therefore, elastic backscattering events are characterized by the same plane waves: $V_i = U_i = u_i \cos\left[\omega\left(p_m x_m - t\right)\right]$. Defining $(\Box\mathbf{V})^\dagger$ as

$$(\Box\mathbf{V})^\dagger = \left\{-\rho^{1/2}\dot{\mathbf{V}}, \underline{\underline{\mathbf{c}}}^{1/2}(\nabla\mathbf{V})\right\} \ , \tag{2.32}$$

we compute the dot product between $\Box\mathbf{U}$ and $(\Box\mathbf{V})^\dagger$ for backscattering events as

$$\Box\mathbf{U}\cdot(\Box\mathbf{V})^\dagger = \omega^2[\rho u_i u_i - u_i u_k c_{ijkl} p_j p_l] \sin^2\left[\omega\left(p_m x_m - t\right)\right] \ . \tag{2.33}$$

Using the relation in equation 2.25, we obtain

$$\Box\mathbf{U}\cdot(\Box\mathbf{V})^{\dagger}=0\ , \tag{2.34}$$

i.e., the dot product is equal to zero everywhere except at the locations where reflectors exist or different wave modes interact, since the vectors $\mathbf{p}$ and $\mathbf{u}_0$ are different for $\mathbf{U}$ and $\mathbf{V}$ at these locations. Therefore, the dot product in equation 2.34 nullifies the events that propagate along the same path and have the same polarization. Such events include reflection backscattering, diving, direct, and head waves from the same wave modes. Therefore, the imaging condition

$$I_E^{\dagger}=\sum_{e,t}\Box\mathbf{U}\cdot(\Box\mathbf{V})^{\dagger} \tag{2.35}$$

attenuates backscattering artifacts in elastic RTM images.

2.3 Examples

Using a simple model with a horizontal reflector at $z = 1.5$ km and a vertical displacement source function (Figure 2.1), we test the proposed imaging condition and compare it with conventional imaging conditions (Figure 2.2). We refer to the zero-lag correlation between displacement field components as conventional imaging conditions (Yan and Sava, 2007). Figure 2.1 also shows the model parameters that we use in this experiment following the convention from Thomsen (1986). The presence of the reflector in the migration velocity leads to a velocity contrast, causing backscattering artifacts in the conventional images (Figures 2.2(a)-2.2(c)). In addition, the polarity reversal at normal incidence occurs when different components of the displacement field are correlated (Figure 2.2(b)). In contrast, the energy imaging condition from equation 2.35 effectively attenuates the backscattering artifacts and shows no polarity reversal at the imaged reflector (Figure 2.2(d)). Figure 2.2(d) only contains artifacts that are caused by the non-physical ("fake") modes generated during the wavefield extrapolation. These artifacts are characterized by the correlation of events with different polarization and/or propagation direction. Based on equation 2.33, the energy

image outputs a non-zero dot product between the energy vectors $\Box\mathbf{U}$ and $(\Box\mathbf{V})^{\dagger}$ for these artifacts. For a multiple-shot experiment, the "fake" modes artifacts are attenuated after stacking over shots, whereas backscattering artifacts and polarity reversal effects are not.

Figures 2.3-2.6 show the Marmousi II (Martin et al., 2002) acquisition geometry, model parameters used to simulate synthetic data, the migration model parameters, and the resulted images. As seen in Figure 2.3, the synthetic data are obtained from a horizontal line of receivers that record the displacement field at every grid point of the water bottom ($z = 0.5$ km), and from 76 pressure sources located near the surface of the water layer ($z = 0.05$ km) with a horizontal spacing of 150 m. This acquisition geometry resembles a multicomponent ocean bottom seismic survey (OBS). The migration model parameters are smoothed versions of the true model parameters (Figures 2.4 and 2.5) and contain sharp interfaces to sufficiently create backscattering reflections during the wavefield extrapolation. Such reflections generate artifacts when using conventional imaging conditions. As expected, all conventional images in Figures 2.6(a)-2.6(c) contain backscattering artifacts, and Figure 2.6(b) also shows the effects of a non-constructive stack due to polarity reversal artifacts. In contrast, we attenuate all of these artifacts in Figure 2.6(d) using the imaging condition from equation 2.35. Similar to the simple experiment in Figure 2.2(d), using our new imaging condition, the individual elastic images for shots have only "fake" mode artifacts, which are attenuated after stacking over shots, thus leading to a good quality image, as seen in Figure 2.6(d).

Figures 2.7 and 2.8 show a 3D elastic experiment with constant model parameters above a horizontal reflector at $z = 0.21$ km. The model consists of a 3D TTI anisotropy symmetry system, and the tilt is determined by a 30° angle with the vertical axis, and an azimuth of 45° with respect to the $x-$axis. We use a vertical dislocation source at the surface in the middle of the model ($x = y = 0.45$ km and $z = 0$ km) to generate the source wavefield. The receiver wavefield is extrapolated from receivers at every grid point from the surface ($z = 0$ km). The correlation between displacement components from the source and receiver wavefields generate images with strong backscattering artifacts and polarity reversal effects

(Figures 2.8(a)-Figures 2.8(c)). Using the energy imaging in equation 2.35, we form an image with attenuated artifacts and no polarity reversal (Figure 2.8(d)).

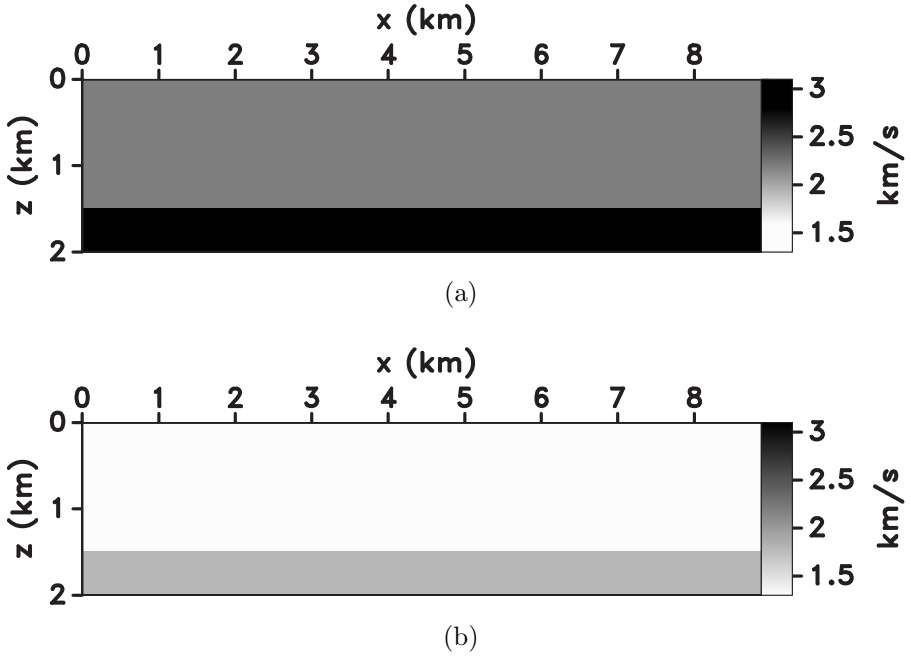

Figure 2.1: Model parameters used for the experiments in Figure 2.2: (a) P and (b) S velocity along the symmetry axis. The anisotropy parameters $\epsilon = 0.4$, $\delta = 0.3$ and $\nu = 26^\circ$ are constant for the entire model.

2.4 Discussion

The main advantage of our method is that we are able to image the subsurface using anisotropic and elastic wavefields without wave-mode decomposition. Substantial improvements have been achieved in recent years through methods based on wave-mode decomposition (Zhang and McMechan, 2010; Yan and Sava, 2011a; Cheng and Fomel, 2014; Sripanich et al., 2015; Wang et al., 2016). Such methods are still computationally intense, as demonstrated by the fact that the vast majority of publications on this subject are limited to decomposing a few wavefield snapshots instead of running complete shot-record migrations. For instance, Cheng and Fomel (2014) use low-rank approximation to implement wave-mode decomposition that has a computational cost of order $O\left(MN_{\mathbf{x}} \log N_{\mathbf{x}}\right)$, where $N_{\mathbf{x}}$ is the spatial dimension of the model and M is the rank, which can vary from 7 to 17 for complex

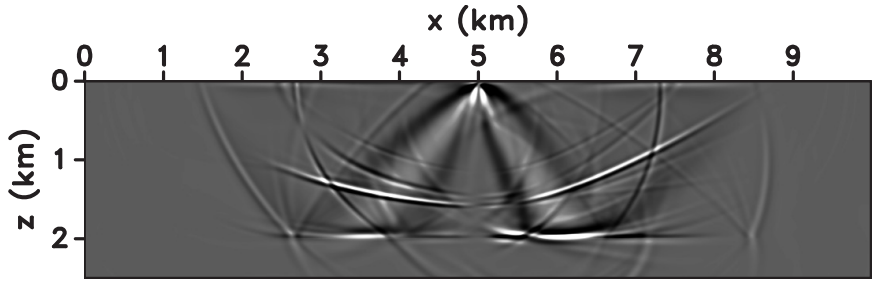

(a)

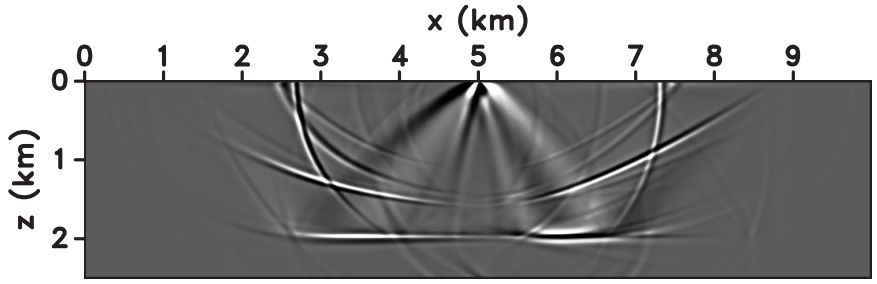

(b)

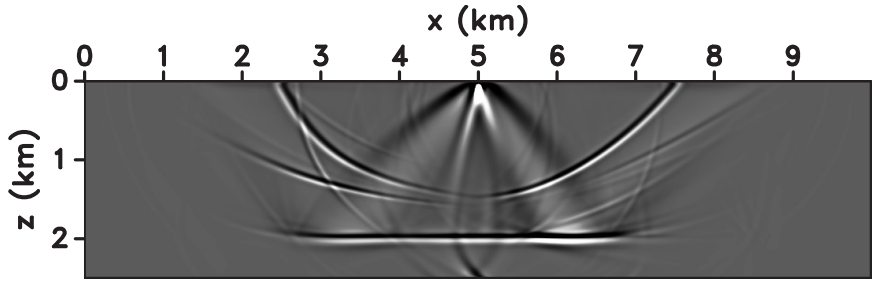

(c)

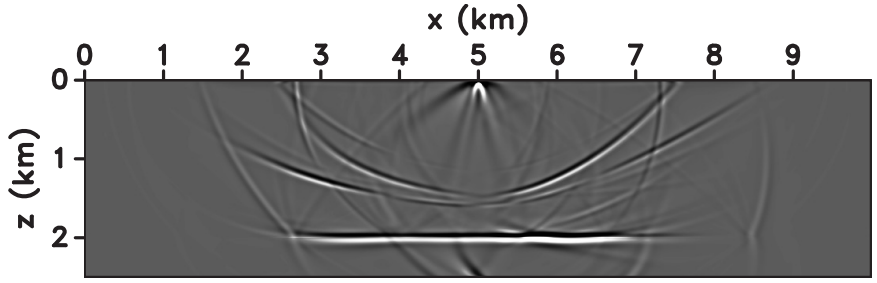

(d)

Figure 2.2: Imaging conditions using displacement components for a horizontal reflector with a vertical displacement source at $x = 5$ km: (a) U_xV_x, (b) U_zV_x, and (c) U_zV_z image, where $\{U_x, U_z\}$ and $\{V_x, V_z\}$ are the horizontal and vertical components of the source and receiver wavefields, respectively. Artifacts present in all images occur due to the "fake" modes (caused by injection of vector fields). Polarity reversal at normal incidence occurs for the image in (b), and backscattering artifacts occur for images in (a)-(c). Comparing to the other images, the energy image in (d) is the only one with attenuated backscattering artifacts and without polarity reversal at normal incidence.

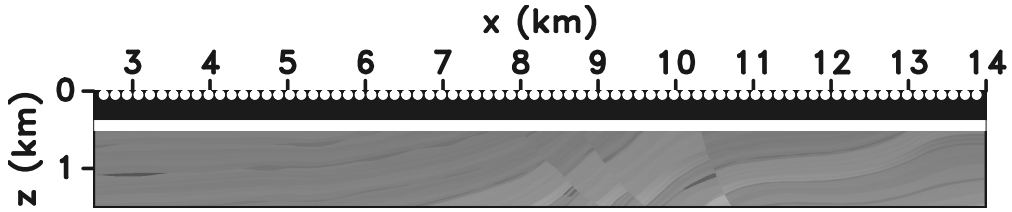

Figure 2.3: Acquisition geometry used in the Marmousi II experiment (Figures 2.4-2.6). The white dots indicate the positions of the seventy-six pressure sources ($z = 0.05$ km), and the white line at the water bottom indicates multicomponent receivers that record the displacement field ($z = 0.5$ km).

models (depending on the desired accuracy). Alternatively, our energy imaging condition requires the same spatial derivatives as those in Helmholtz decomposition, which has a computational cost of order $O\left(N_{\mathbf{x}}\right)$.

However, the absence of wave-mode decomposition in our method limits interpretation by not providing a suitable relationship between compressional and shear wave impedance contrasts, which is systematically studied in reservoir characterization. Our energy imaging condition reflects the balance of energy between the incoming source wavefield and the reflected receiver wavefield. The amplitude information from the energy image and its possible contribution to reservoir characterization are not clear and are subjects for future research.

2.5 Conclusions

The anisotropic energy imaging condition is applicable for arbitrary anisotropy, produces a scalar image without the need for wave-mode decomposition, and does not suffer from polarity reversal, as is the case for displacement images using different components of the source and receiver wavefields. We describe this imaging condition as the scalar product between the energy vectors $\Box\mathbf{U}$ and $\Box\mathbf{V}$, which are built using conventionally extrapolated wavefields $\mathbf{U}$ and $\mathbf{V}$. As inferred from the definition of these vectors, the proposed imaging condition accounts for wavefield directionality, incorporating the wavefield propagation and polarization directions. By exploiting this directionality, we are able to attenuate the backscattering artifacts in the imaging process, and obtain robust, inexpensive and high-

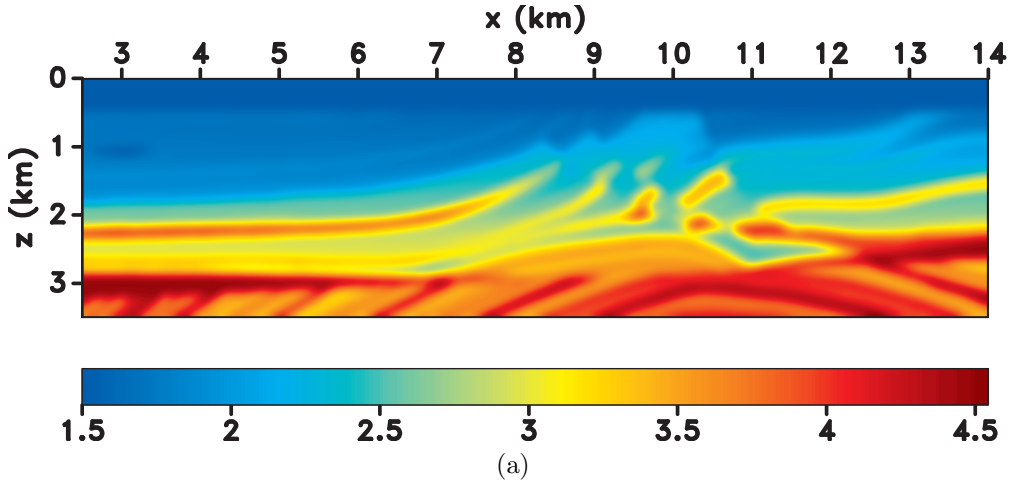

(a)

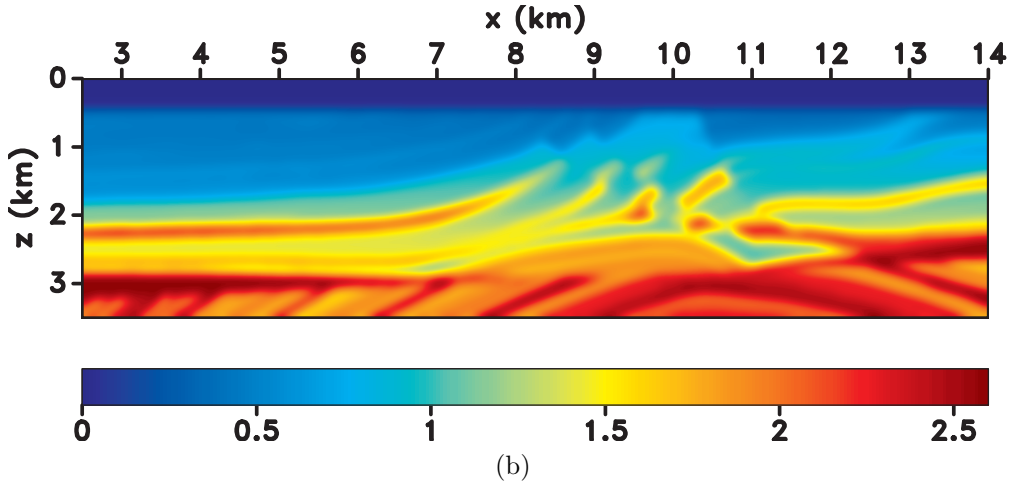

(b)

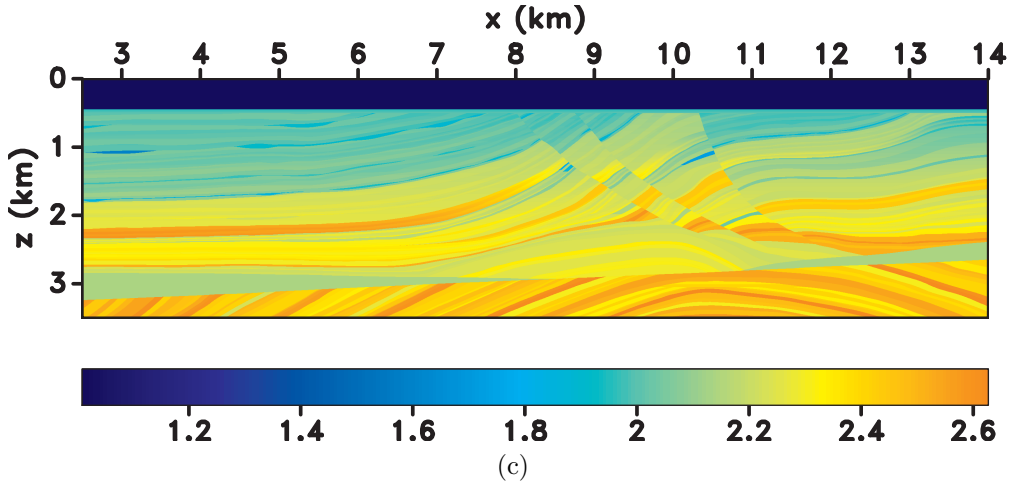

(c)

Figure 2.4: Migration model parameters used for the Marmousi II experiment. (a) P- and (b) S-wave velocity along the local symmetry axis (V_{P0} and V_{S0}, in km/s). (c) Stratigraphic density model used to generate synthetic data (in g/cm^3).

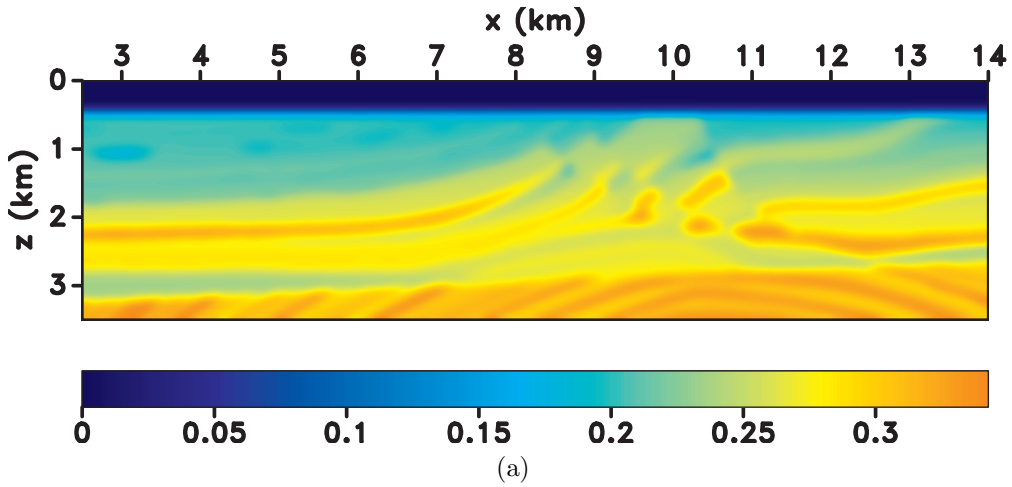

(a)

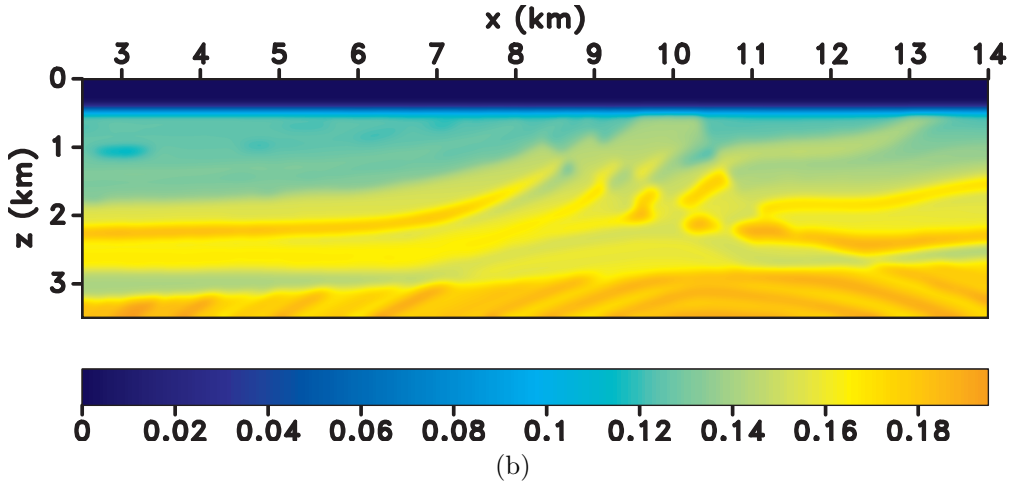

(b)

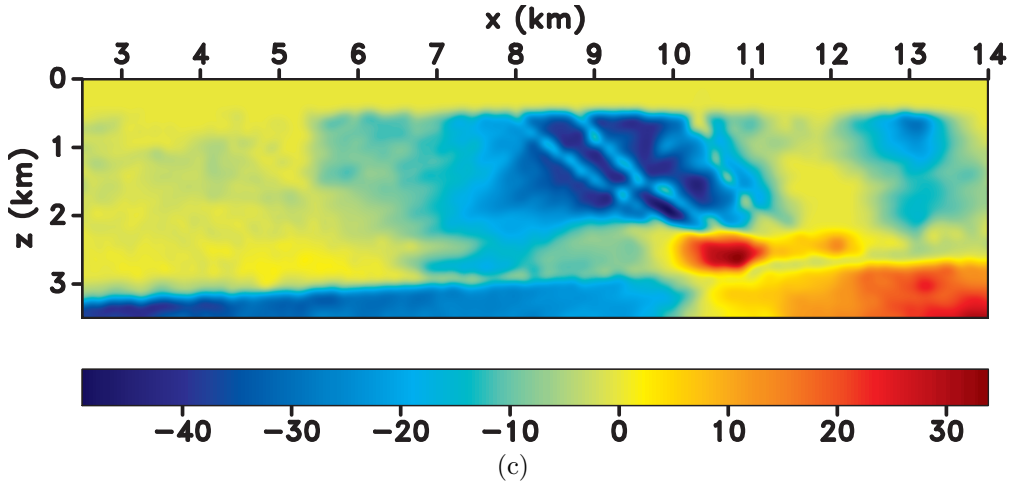

(c)

Figure 2.5: Migration anisotropy parameters used for the Marmousi II experiment. (a) ϵ, (b) δ, and (c) local tilt angle ν (in degrees).

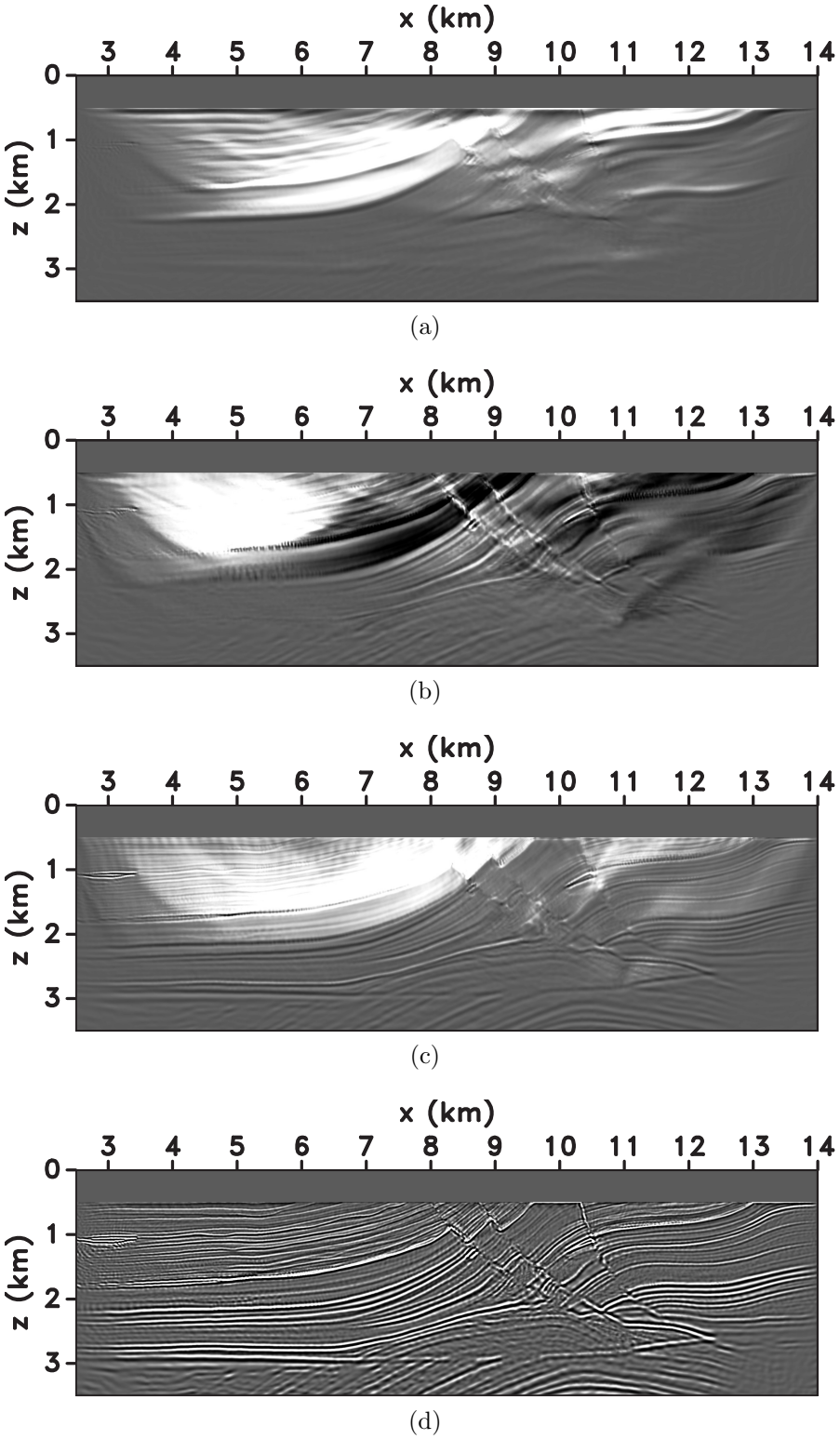

Figure 2.6: Images obtained from the Marmousi II experiment: conventional images using the correlation between displacement components (a) U_xV_x, (b) U_xV_z, and (c) U_zV_z; (d) energy image using the imaging condition in equation 2.35. Polarity reversal effects are visible in (b) by the change in polarity from the low-wavenumber artifacts. The energy image in (d) is the only one without low-wavenumber backscattering artifacts.

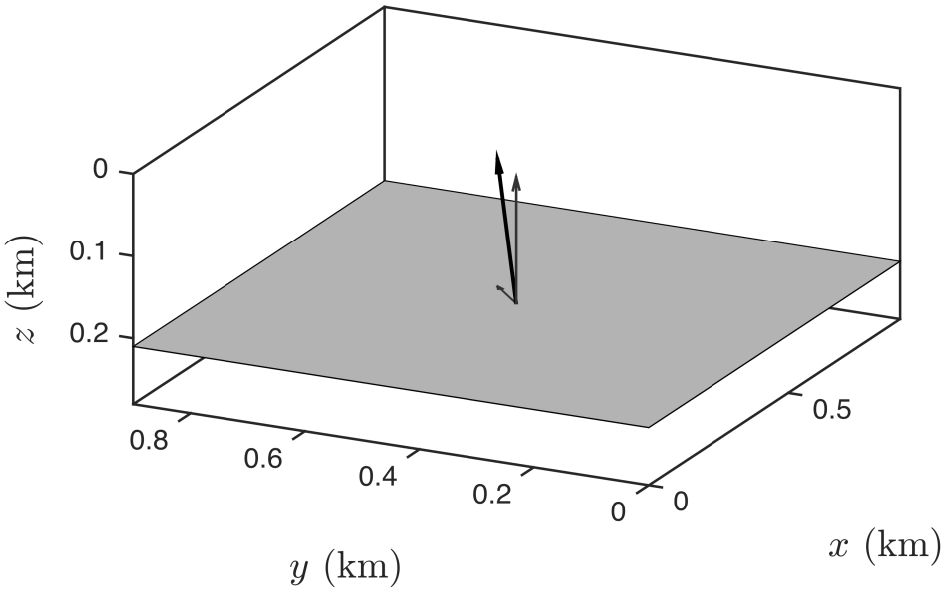

Figure 2.7: Schematic representation of the 3D TTI model used in the experiment of Figure 2.8. The black arrow indicates the tilted symmetry axis. The gray arrows indicate the projections of this vector onto the vertical axis and onto the reflection plane. Model parameters in the original system are $V_{P0} = 2.3$ km/s,$V_{S0} = 1.3$ km/s, $\rho = 2.0$ g/cm^3, $\epsilon = 0.4$, $\delta = 0.1$, and $\gamma = 0.0$.

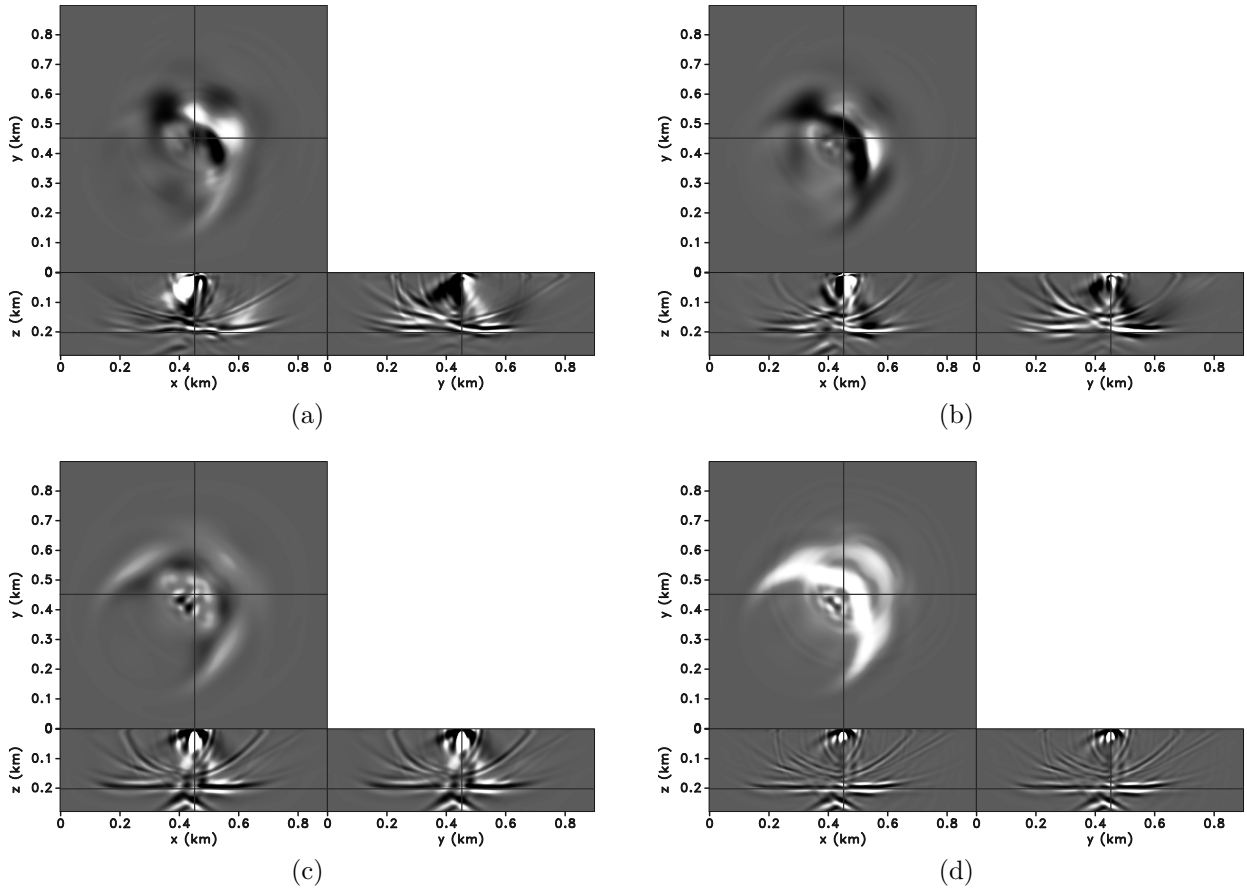

Figure 2.8: Images using the correlation between displacement components: (a) U_xV_y, (b) U_xV_z, and (c) U_zV_z; and an image using the energy imaging condition in (d). Artifacts due to the "fake" modes are present in all images. Backscattering artifacts and polarity reversal occur in the conventional images in (a)-(c) but not in the energy image in (d).

quality elastic images.

2.6 Acknowledgments

We would like to thank sponsor companies of the Center for Wave Phenomena, whose support made this research possible. The reproducible numeric examples in this paper use the Madagascar open-source software package (Fomel et al., 2013) freely available from http://www.ahay.org.

2.7 Appendices

The appendices below elucidate specific points of this current chapter.

2.7.1 Frobenius product and norm

The Frobenius norm in linear algebra generalizes the more conventional vector norm concept. Consider an arbitrary matrix $A_{M\times N}$, this norm is defined as (Golub and Loan, 1996)

$$||A||_F = \sqrt{\sum_{i=1}^{M}\sum_{j=1}^{N}|a_{ij}|^2}\ . \tag{2.36}$$

One can also define a norm of a tensor field using the inner product of associated matrices. Given tensor fields A and B, the Frobenius product is defined as

$$< A, B >_F = A : B = \sum_{i=1}^{M}\sum_{j=1}^{N} a_{ij}b_{ij}\ , \tag{2.37}$$

where M and N are the dimensions of the tensors A and B. This product can also be written in matrix form as

$$< A, B >_F = A : B = \mathrm{Tr}(A^{\mathrm{T}}B) = \mathrm{Tr}(AB^{\mathrm{T}})\ . \tag{2.38}$$

Then, the Frobenius norm of a tensor A is written as

$$||A||_F = \sqrt{\mathrm{Tr}(AA^{\mathrm{T}})}\ . \tag{2.39}$$

2.7.2 Strain-energy function in isotropic media

In a general elastic medium subject to infinitesimal strains, the strain-energy function is (Slawinski, 2003)

$$E(\epsilon) = \frac{1}{2} c_{ijlk} \epsilon_{kl} \epsilon_{ij} \ , \tag{2.40}$$

where c_{ijlk} is an element of the stiffness tensor $\underline{\underline{\mathbf{c}}}$, and ϵ_{ij} is an element of the strain tensor $\underline{\mathbf{e}}$. The repeated indices i, j, k, l imply summation, following the Einstein convention (Robert, 2005). For an isotropic medium, the stiffness coefficients are (Aki and Richards, 2002)

$$c_{ijlk} = \lambda \delta_{ij} \delta_{kl} + \mu \delta_{ik} \delta_{jl} + \mu \delta_{il} \delta_{jk} \ , \tag{2.41}$$

where δ_{ij} is the Kronecker delta function, and λ and μ are the Lamé parameters. Substituting equation 2.41 in equation 2.40, we obtain

$$E(\epsilon) = \frac{1}{2} \left[\lambda \delta_{ij} \delta_{kl} + \mu \delta_{ik} \delta_{jl} + \mu \delta_{il} \delta_{jk} \right] \epsilon_{kl} \epsilon_{ij} \ . \tag{2.42}$$

Considering the Kronecker delta function is equal to unity for equal indices and zero otherwise, we develop each term and obtain

$$E(\epsilon) = \frac{1}{2} \left[\lambda \epsilon_{ii} \epsilon_{kk} + \mu \epsilon_{ij} \epsilon_{ij} + \mu \epsilon_{ji} \epsilon_{ij} \right] . \tag{2.43}$$

These implicit summations can be written in matrix form as

$$E(\mathbf{e}) = \frac{1}{2} \left[\lambda \mathrm{Tr}[\mathbf{e}] \mathrm{Tr}[\mathbf{e}] + \mu \left(\mathbf{e} : \mathbf{e} \right) + \mu \left(\mathbf{e} : \mathbf{e}^{\mathrm{T}} \right) \right] . \tag{2.44}$$

As the strain tensor is symmetric, we obtain

$$E(\mathbf{e}) = \frac{1}{2} \left[\lambda \left(\mathrm{Tr}[\mathbf{e}] \right)^2 + 2\mu \left(\mathbf{e} : \mathbf{e} \right) \right] . \tag{2.45}$$

The strain tensor $\mathbf{e}$ is a function of the wavefield derivatives:

$$\mathbf{e} = \frac{1}{2} \left[\nabla \mathbf{U} + \nabla \mathbf{U}^{\mathrm{T}} \right] \tag{2.46}$$

Substituting equation 2.46 in 2.45, we obtain

$$
\begin{aligned}
E(\mathbf{e}) &= \frac{1}{2}\left[\lambda\|\nabla\cdot\mathbf{U}\|^2 + 2\mu\left(\frac{1}{2}\left(\nabla\mathbf{U}+\nabla\mathbf{U}^{\mathrm{T}}\right):\frac{1}{2}\left(\nabla\mathbf{U}+\nabla\mathbf{U}^{\mathrm{T}}\right)\right)\right] \\
&= \frac{1}{2}\left[\lambda\|\nabla\cdot\mathbf{U}\|^2 + \frac{1}{2}\mu\left(\nabla\mathbf{U}:\nabla\mathbf{U} + 2\nabla\mathbf{U}:\nabla\mathbf{U}^{\mathrm{T}} + \nabla\mathbf{U}^{\mathrm{T}}:\nabla\mathbf{U}^{\mathrm{T}}\right)\right] \\
&= \frac{1}{2}\left[\lambda\|\nabla\cdot\mathbf{U}\|^2 + \mu\left(\nabla\mathbf{U}:\nabla\mathbf{U} + \nabla\mathbf{U}:\nabla\mathbf{U}^{\mathrm{T}}\right)\right] , \qquad (2.47)
\end{aligned}
$$

which corresponds to the potential energy terms of equation 2.15.

2.7.3 Imaging conditions for orthorhombic and vertical transverse isotropic (VTI) media

The most general imaging condition for two anisotropic elastic wavefields $\mathbf{U}(\mathbf{x},t)$ and $\mathbf{V}(\mathbf{x},t)$ is

$$
I_E = \sum_{e,t}\left[\rho\dot{\mathbf{U}}\cdot\dot{\mathbf{V}} + \left(\underline{\underline{\mathbf{c}}}\nabla\mathbf{U}\right):\nabla\mathbf{V}\right] . \qquad (2.48)
$$

In orthorhombic media, equation 2.48 becomes

$$
\begin{aligned}
I_E &= \rho\left[\dot{U}_1\dot{V}_1 + \dot{U}_2\dot{V}_2 + \dot{U}_3\dot{V}_3\right] \\
&+ C_{11}U_{1,1}V_{1,1} + C_{22}U_{2,2}V_{2,2} + C_{33}U_{3,3}V_{3,3} \\
&+ C_{12}\left[U_{1,1}V_{2,2} + U_{2,2}V_{1,1}\right] \\
&+ C_{13}\left[U_{1,1}V_{3,3} + U_{3,3}V_{1,1}\right] \\
&+ C_{23}\left[U_{2,2}V_{3,3} + U_{3,3}V_{2,2}\right] \\
&+ C_{44}\left[U_{2,3}V_{2,3} + U_{2,3}V_{3,2} + U_{3,2}V_{2,3} + U_{3,2}V_{3,2}\right] \\
&+ C_{55}\left[U_{1,3}V_{1,3} + U_{1,3}V_{3,1} + U_{3,1}V_{1,3} + U_{3,1}V_{3,1}\right] \\
&+ C_{66}\left[U_{1,2}V_{1,2} + U_{1,2}V_{2,1} + U_{2,1}V_{1,2} + U_{2,1}V_{2,1}\right] . \qquad (2.49)
\end{aligned}
$$

where C_{ij} for $i,j = \{1,2,3\}$ are the stiffness coefficients in Voigt notation, $U_{i,j}$ or $V_{i,j}$ represents the jth derivative of the ith component from the wavefield $\mathbf{U}$ or $\mathbf{V}$. In wavefield imaging, the density of the medium $\rho(\mathbf{x})$ is often unknown, therefore, we can rewrite equation 2.49 without the density term as

$$
\begin{aligned}
I_E &= \dot{U}_1\dot{V}_1 + \dot{U}_2\dot{V}_2 + \dot{U}_3\dot{V}_3 \\
&+ A_{11}U_{1,1}V_{1,1} + A_{22}U_{2,2}V_{2,2} + A_{33}U_{3,3}V_{3,3} \\
&+ A_{12}\left[U_{1,1}V_{2,2} + U_{2,2}V_{1,1}\right] \\
&+ A_{13}\left[U_{1,1}V_{3,3} + U_{3,3}V_{1,1}\right] \\
&+ A_{23}\left[U_{2,2}V_{3,3} + U_{3,3}V_{2,2}\right] \\
&+ A_{44}\left[U_{2,3}V_{2,3} + U_{2,3}V_{3,2} + U_{3,2}V_{2,3} + U_{3,2}V_{3,2}\right] \\
&+ A_{55}\left[U_{1,3}V_{1,3} + U_{1,3}V_{3,1} + U_{3,1}V_{1,3} + U_{3,1}V_{3,1}\right] \\
&+ A_{66}\left[U_{1,2}V_{1,2} + U_{1,2}V_{2,1} + U_{2,1}V_{1,2} + U_{2,1}V_{2,1}\right] \ . \qquad (2.50)
\end{aligned}
$$

where A_{ij} represents stiffness coefficients normalized by the density (in velocity squared units).

For vertical traverse isotropic (VTI) media, one can reduce the number of stiffness coefficients by using $C_{22} = C_{11}, C_{12} = C_{11} - 2C_{66}, C_{23} = C_{13}$, and $C_{44} = C_{55}$. Therefore:

$$
\begin{aligned}
I_E &= \rho\left[\dot{U}_1\dot{V}_1 + \dot{U}_2\dot{V}_2 + \dot{U}_3\dot{V}_3\right] \\
&+ C_{11}\left[U_{1,1}V_{1,1} + U_{2,2}V_{2,2} + U_{1,1}V_{2,2} + U_{2,2}V_{1,1}\right] \\
&+ C_{33}U_{3,3}V_{3,3} \\
&+ C_{13}\left[U_{1,1}V_{3,3} + U_{3,3}V_{1,1} + U_{2,2}V_{3,3} + U_{3,3}V_{2,2}\right] \\
&+ C_{55}\left[U_{2,3}V_{2,3} + U_{2,3}V_{3,2} + U_{3,2}V_{2,3} + U_{3,2}V_{3,2} + U_{1,3}V_{1,3} + U_{1,3}V_{3,1} + U_{3,1}V_{1,3} + U_{3,1}V_{3,1}\right] \\
&+ C_{66}\left[U_{1,2}V_{1,2} + U_{1,2}V_{2,1} + U_{2,1}V_{1,2} + U_{2,1}V_{2,1} - 2U_{1,1}V_{2,2} - 2U_{2,2}V_{1,1}\right] \ . \qquad (2.51)
\end{aligned}
$$

Using Thomsen parameters (Thomsen, 1986) and the P- and S-wave velocities at the symmetry axis, we can rewrite equation 2.51 as

$$
\begin{aligned}
I_E &= \dot{U}_1\dot{V}_1 + \dot{U}_2\dot{V}_2 + \dot{U}_3\dot{V}_3 \\
&+ (1+2\epsilon)v_{P0}^2\left[U_{1,1}V_{1,1} + U_{2,2}V_{2,2} + U_{1,1}V_{2,2} + U_{2,2}V_{1,1}\right] \\
&+ v_{P0}^2U_{3,3}V_{3,3} + \left[\sqrt{(v_{P0}^2 - v_{S0}^2)(v_{PN}^2 - v_{S0}^2)} - v_{S0}^2\right]\left[U_{1,1}V_{3,3} + U_{3,3}V_{1,1} + U_{2,2}V_{3,3} + U_{3,3}V_{2,2}\right] \\
&+ v_{S0}^2\left[U_{2,3}V_{2,3} + U_{2,3}V_{3,2} + U_{3,2}V_{2,3} + U_{3,2}V_{3,2} + U_{1,3}V_{1,3} + U_{1,3}V_{3,1} + U_{3,1}V_{1,3} + U_{3,1}V_{3,1}\right] \\
&+ (1+2\epsilon)v_{S0}^2\left[U_{1,2}V_{1,2} + U_{1,2}V_{2,1} + U_{2,1}V_{1,2} + U_{2,1}V_{2,1} - 2U_{1,1}V_{2,2} - 2U_{2,2}V_{1,1}\right] \ , \qquad (2.52)
\end{aligned}
$$

where v_{P0} and v_{S0} are the P- and S-wave velocities along the symmetry axis, v_{PN} is the normal moveout P-wave velocity, and ϵ and γ are Thomsen parameters.

CHAPTER 3

3D PASSIVE WAVEFIELD IMAGING USING THE ENERGY NORM

A paper submitted to Geophysics

Daniel Rocha*,[1], Paul Sava[1], Jeffrey Shragge[1,2] & Ben Witten[3]

In passive monitoring of microseismicity, full-wavefield imaging offers a robust approach for estimating source locations and subsurface properties. With multicomponent data back-propagated with the 3D elastic wave equation, the coexistence of P- and S-modes at the source location allows for application of migration-based imaging conditions to identify the source position. Correlation between decomposed P- and S-wavefields is the most common imaging condition used in passive elastic wavefield imaging. However, this operation produces a nodal plane at the source location that can lead to inaccurate source localization, and requires Helmholtz decomposition, which is costly for anisotropic media. We propose an imaging condition for passive wavefield imaging that is based on energy conservation and is related to the Lagrangian operator of the elastic wave equation. Our energy passive imaging condition (EPIC) not only compares the different modes present in the displacement field, but also produces a strong and focused correlation at the source location without requiring wave-mode decomposition at each time step. Numerical experiments on 3D synthetic and field data demonstrate the advantages of the proposed imaging condition (compared to PS correlation with decomposed wave modes), its sensitivity with respect to velocity inaccuracy, and its quality and efficacy in estimating the source location.

* Corresponding author. Direct correspondence to drocha@mines.edu
[1] Center for Wave Phenomena, Colorado School of Mines, 924 16th St., Golden, CO 80401
[2] Formerly University of Western Australia, 35 Stirling Highway, Perth WA 6009, Australia
[3] School of Earth Sciences, University of Western Australia, 35 Stirling Highway, Perth WA 6009, Australia

3.1 Introduction

Passive seismic monitoring uses signals caused by either natural or induced seismicity to infer earthquake locations, source mechanisms and subsurface properties. Its differences with respect to conventional exploration seismology mainly consist of the absence of a controlled source, but also of distinct array geometries, continuous recording times, and low signal-to-noise ratios, among others. Although the source locations for passive seismic scenario are unknown a priori, one can apply imaging and inversion methods adapted from active source seismic scenarios to generate an image, showing the estimated source location, and/or to reconstruct a 3D earth model, with information about subsurface physical properties (Duncan and Eisner, 2010; Maxwell et al., 2010; Xuan and Sava, 2010; Behura et al., 2013; Blias and Grechka, 2013; Douma and Snieder, 2015; Witten and Shragge, 2015; Bazargani and Snieder, 2016; Witten and Shragge, 2017a,b).

In oil and gas exploration, passive seismic monitoring is commonly termed microseismic monitoring (Warpinski et al., 2012; Maxwell, 2014; Grechka and Heigl, 2017), since this type of induced seismicity typically has low orders of moment magnitudes (i.e., $M_w \leq 0$). Microseismic monitoring is a powerful technique for obtaining production attributes from unconventional reservoirs, especially when investigating hydraulic fracturing. Where fluid injection into a reservoir induces microseismicity observable from surface or borehole monitoring arrays, one can use recorded data to estimate microseismic source locations and thereby gain insight as to where hydraulic fracturing is occurring in the subsurface (Maxwell, 2010; Michel and Tsvankin, 2013). Beyond source location estimation, microseismic monitoring (using a catalog of detected events) facilitates other useful applications such as estimating source mechanisms, which potentially provides geomechanical information such as fault and fracture orientation (Jeremic et al., 2014; Zhebel and Eisner, 2015).

One common approach for analyzing microseismic data involves applying a Kirchhoff-based migration algorithm to stack windowed events along traveltime trajectories and over all possible source initiation times, assuming a sufficiently accurate velocity model (Kao

and Shan, 2004; Baker et al., 2005). However, such approach does not stack over the full waveform and implicitly rely on strong assumptions about velocity model accuracy and associated wave propagation effects (e.g., neglecting multipathing) that are not appropriate for realistic scenarios. Alternatively, approaches based on wave-equation migration have gained interest for passive seismic imaging (Artman et al., 2010; Xuan and Sava, 2010; Witten and Shragge, 2015; Nakata and Beroza, 2016) since they use the full waveform of these signals (beyond stacking along traveltime trajectories), accurately handle wave propagation in complex earth models, and offer a range of imaging conditions that effectively stack over the full microseismic waveform.

Full-wavefield imaging adapted to the problem of estimating microseismic source locations is usually implemented in two steps: (1) time-reversed wavefield extrapolation (or more simply, backpropagation) of the recorded wavefield into an earth model; and (2) application of an imaging condition to extract the source location and/or origin time from the extrapolated wavefield (McMechan, 1982; Gajewski and Tessmer, 2005; Xuan and Sava, 2010; Nakata and Beroza, 2016). Generally, the imaging condition involves computing the zero-lag autocorrelation of the 4D wavefield, collapsing it into a 3D image volume. Assuming a correct velocity model and proper treatment of source radiation patterns, the peak amplitude of the image corresponds to the true source location; however, not satisfying these assumptions can often lead to severe mislocation of imaged events. To address velocity model inaccuracy, it is insufficient to rely solely on zero-lag wavefield autocorrelation to provide information for velocity improvement. As explored in active seismic scenarios (Rickett and Sava, 2002; Sava and Fomel, 2006; Sava and Vasconcelos, 2011; Yang and Sava, 2015) and more recently in passive seismic ones (Witten and Shragge, 2015), wavefield correlation beyond zero lag generates so-called extended images (since they represent an extension of zero-lag images), which provide the sufficient and necessary information to improve the migration velocities within the adjoint-state tomography framework (Witten and Shragge, 2017a).

For multicomponent microseismic data, one typically employs wave extrapolation and imaging procedures that exploit distinct elastic wave modes. The colocation of P- and S-wavefields at the source excitation point allows for a PS imaging condition to be implemented in three steps: (1) elastic (or pseudo-elastic) backpropagation of the recorded multicomponent wavefield; (2) wave-mode decomposition of the backpropagated displacement field; and (3) crosscorrelation of the two P- and S-wavefields (Artman et al., 2010; Witten and Artman, 2010). However, especially in 3D applications involving an anisotropic medium, step 2 is computationally expensive and thus impedes a quick and robust imaging implementation as it must be repeated at each extrapolation time step. Another shortcoming of the elastic PS correlation is that it does not properly handle the different polarization directions at the locus of maximum P- and S-phase correlation, producing a nodal plane (i.e., a zero) at the actual source location. Ideally (and especially in the presence of low signal-to-noise ratio), one would expect to encounter the peak amplitude at the source position; to expect otherwise would pose both interpretation as well as inversion challenges.

We aim to address these shortcomings of the multicomponent elastic PS imaging condition that are detrimental to both source location identification and migration velocity analysis of microseismic data. By substituting PS for energy correlation (Rocha et al., 2016b, 2017), we propose an energy passive imaging condition (EPIC) that has five key advantages over conventional PS imaging condition: (1) naturally accounts for source radiation patterns; (2) produces a peak image amplitude at the estimated source location; (3) precludes the need for wave-mode decomposition at each time step; (4) downweights the correlation between identical wave modes away from the source while enhancing the correlation of different wave modes at the source location; and (5) offers a straightforward complement to extended image attributes that are important for microseismic migration velocity analysis based on the temporal separation of P- and S-wave arrivals. For the purpose of improving image quality, we implement wave-mode separation - advantage (3) - only once in the data domain.

In this paper, we review the theory of elastic modeling and associated conventional imaging conditions; introduce the energy imaging condition, originally developed for active-source wavefield imaging - elastic reverse time migration (ERTM); and detail how we adapt it to passive seismic scenarios. Then, we present the extended-domain versions of PS and energy imaging conditions, and show a novel methodology applied in our numerical experiments to mitigate imaging artifacts, albeit with an increase in computational cost. We demonstrate our methodology with 3D synthetic examples of increasing complexity, as well as with field data. The paper concludes with a discussion of the merits and caveats of our method, and with suggestions for further refinement of the method.

3.2 Theory

In this section, we review the elastic wave equations used in full-wavefield imaging, as well as the most commonly employed imaging conditions for multicomponent passive data. Then, we propose an imaging condition based on the energy norm for elastic wavefields. Finally, we introduce the extended version of our proposed imaging condition that is potentially important for velocity estimation applications.

3.2.1 Elastic modeling

The elastic wave equation in the absence of external sources may be written as (Aki and Richards, 2002)

$$\rho\ddot{\mathbf{U}} = \nabla \cdot \left[\underline{\underline{\mathbf{c}}}\nabla\mathbf{U}\right] \ , \tag{3.1}$$

where $\mathbf{U}(\mathbf{x}, t)$ is the displacement field as a function of space ($\mathbf{x}$) and time (t), $\rho(\mathbf{x})$ is the medium density, and $\underline{\underline{\mathbf{c}}}(\mathbf{x})$ is the 4th-rank stiffness tensor. A superscript dot on the displacement field indicates first-order time differentiation. If we assume a slowly varying isotropic medium, equation 3.1 reduces to

$$\rho\ddot{\mathbf{U}} = (\lambda + 2\mu)\nabla(\nabla \cdot \mathbf{U}) - \mu\nabla \times (\nabla \times \mathbf{U}) \ , \tag{3.2}$$

where $\lambda(\mathbf{x})$ and $\mu(\mathbf{x})$ are Lamé parameters. Equation 3.2 can be written as a function of velocities by substituting $V_P^2 = \frac{\lambda+2\mu}{\rho}$ and $V_S^2 = \frac{\mu}{\rho}$:

$$\ddot{\mathbf{U}} = V_P^2 \nabla (\nabla \cdot \mathbf{U}) - V_S^2 \nabla \times (\nabla \times \mathbf{U}) \ , \tag{3.3}$$

where $V_P(\mathbf{x})$ and $V_S(\mathbf{x})$ are the P- and S-wave velocities, respectively. Using multicomponent data recorded at the receivers, a displacement field $\mathbf{U}$ can be extrapolated forward or backward in time throughout a subsurface model using either equations 3.1 or 3.3, depending on the assumptions about anisotropy of the medium. Although more realistic in nature, incorporating anisotropy involves complex phenomena such as shear-wave splitting (Crampin, 1985; Alford, 1986), which introduces two shear wave modes with different polarizations and phase velocities in wavefield extrapolation. Without loss of generality, we assume isotropy in the following numerical experiments so as to analyze only a single shear-wave mode (and for clarity purposes). We discuss the extension of our imaging approach to anisotropic media in the Discussion section.

3.2.2 Passive imaging conditions: autocorrelation

Different imaging conditions acting directly on the wavefield displacement have been proposed for estimating the source locations in passive wavefield imaging (Steiner et al., 2008; Jeremic et al., 2015). For instance, Steiner et al. (2008) propose to use the absolute value of the particle velocity, i.e. the time derivative of the displacement vector field, while Saenger (2011) presents an imaging condition based on the product between stress and strain fields. More commonly, one implements wave-mode decomposition of the extrapolated displacement field into its P- and S-wavefield constituents, typically implemented using Helmholtz decomposition operators (Dellinger and Etgen, 1990; Yan and Sava, 2009):

$$P = \nabla \cdot \mathbf{U} \ , \tag{3.4}$$
$$\mathbf{S} = \nabla \times \mathbf{U} \ , \tag{3.5}$$

where $P(\mathbf{x},t)$ is a scalar wavefield containing the compressional wave mode, and $\mathbf{S}(\mathbf{x},t)$ is a vector wavefield containing the transverse wave mode.

Because a scalar wavefield image is generally preferable to a vector or tensor image, but the S-wavefield from this decomposition remains a 3D vector field, passive imaging conditions can use the energy densities E_P and E_S of the decomposed P- and S-wavefields (Morse and Feshbach, 1953):

$$E_P(\mathbf{x},t) = \|P\|\,, \tag{3.6}$$
$$E_S(\mathbf{x},t) = \|\mathbf{S}\|\,, \tag{3.7}$$

where $\|\cdot\|$ indicates the magnitude of a scalar or vector wavefield. Separated wave modes and their energy densities allow one to implement autocorrelation passive imaging conditions:

$$I_{PP}(\mathbf{x}) = \sum_t P(\mathbf{x},t)\,P(\mathbf{x},t) \equiv \sum_t E_P^2(\mathbf{x},t)\,, \tag{3.8}$$
$$I_{SS}(\mathbf{x}) = \sum_t \mathbf{S}(\mathbf{x},t)\cdot\mathbf{S}(\mathbf{x},t) \equiv \sum_t E_S^2(\mathbf{x},t)\,. \tag{3.9}$$

3.2.3 Passive imaging conditions: cross-correlation

A recurrent problem with the imaging conditions in equations 3.8 and 3.9 is that the correlation of the wavefield with itself produces low-wavenumber content along the propagation path, e.g. between the source in the subsurface and the receivers on the surface or in a borehole. The same problem occurs with imaging conditions that directly use the displacement field in the absence of wave-mode decomposition. This poses significant challenges for microseismic migration and inversion-based analyses that require tightly focused event images.

Alternatively, one can use the different modes of the displacement field to define an imaging condition free of low-wavenumber autocorrelation artifacts. For a non-scattering medium and assuming finite source bandwidth, extrapolated P- and S-waves from a single microseismic event propagate at different speeds and only coexist in space and time at the

vicinity of the source location and at initiation time. Exploiting this fact, one can define a PS imaging condition (PSIC) (Artman et al., 2010):

$$\mathbf{I}_{PS}(\mathbf{x}) = \sum_{t} P(\mathbf{x}, t)\, \mathbf{S}(\mathbf{x}, t) \ , \tag{3.10}$$

where $\mathbf{I}_{PS}(\mathbf{x})$ is a vector image, whose individual components represent the correlation between $P(\mathbf{x}, t)$ and the corresponding components of $\mathbf{S}(\mathbf{x}, t)$. Yan and Sava (2008) also propose a similar PS imaging condition, but in the context of elastic reverse time migration (ERTM). However, one drawback is that, in a 3D experiment, three images are available instead of a scalar one concisely showing the source location. Considering this, one could conveniently compute a scalar PS image using the S-wave energy density in equation 3.7:

$$I_{PS}(\mathbf{x}) = \sum_{t} P(\mathbf{x}, t)\, E_S(\mathbf{x}, t) \ . \tag{3.11}$$

For isotropic media, equation 3.11 is quite straightforward to implement; however, this is not the case in anisotropic media for which wave-mode decomposition is significantly more expensive to compute (Dellinger and Etgen, 1990; Zhang and McMechan, 2010; Yan and Sava, 2011a; Cheng and Fomel, 2014). Also, the PS correlation - either in equation 3.10 or 3.11 - produces a zero amplitude at the source location and an associated nodal plane, whose positive and negative side lobes suggest the source localization at the zero crossing. Although pre-processing techniques exist to address this problem (Eisner et al., 2008; Ay et al., 2012; Witten and Shragge, 2015), they lead to lower-frequency wavefields and loss of spatial resolution.

3.2.4 Energy norm imaging conditions

In contrast, the energy norm (Rocha et al., 2016a,b) allows one to define a pair of imaging conditions for many applications, with no difficulty in its implementation regardless of anisotropy of the medium. In that context, this pair of imaging conditions is defined as (Rocha et al., 2017)

$$I_E^H(\mathbf{x}) = \sum_t \left[\rho\dot{\mathbf{U}}\cdot\dot{\mathbf{V}} + \left(\underline{\underline{\mathbf{c}}}\nabla\mathbf{U}\right) : \nabla\mathbf{V}\right], \tag{3.12}$$

$$I_E^L(\mathbf{x}) = \sum_t \left[\rho\dot{\mathbf{U}}\cdot\dot{\mathbf{V}} - \left(\underline{\underline{\mathbf{c}}}\nabla\mathbf{U}\right) : \nabla\mathbf{V}\right], \tag{3.13}$$

where $\mathbf{U}(\mathbf{x},t)$ and $\mathbf{V}(\mathbf{x},t)$ are two state wavefields, and the symbol : indicates the Frobenius product (Golub and Loan, 1996). The imaging condition in equation 3.12 represents the temporal integration of the total energy product between the two wavefields, while that in equation 3.13 is a differential energy measure that attenuates events within the two wavefields sharing the same polarization and propagation direction. The correlation between such events generates the aforementioned detrimental low-wavenumber artifacts. Rocha et al. (2017) successfully use the imaging condition in equation 3.13 for ERTM (where $\mathbf{U}(\mathbf{x},t)$ and $\mathbf{V}(\mathbf{x},t)$ are the source and receiver wavefields), suppressing these artifacts and concisely imaging subsurface reflectors.

For passive imaging, where we extrapolate a single wavefield containing all wave modes, we can also define a pair of autocorrelation imaging conditions by establishing $\mathbf{U} = \mathbf{V}$ in equations 3.12 and 3.13. With such substitution, the individual terms have a special meaning in reference to the energy of the elastic wavefield: the first and second terms in equations 3.12 and 3.13 represent the kinetic and potential energies of the single wavefield, respectively. Therefore, equation 3.12 is related to the Hamiltonian operator (superscript H stands for Hamiltonian), which measures total wavefield energy, while equation 3.13 is related to the Lagrangian operator (superscript L stands for Lagrangian), defined as the difference between kinetic and potential energy terms (Ben-Menahem and Singh, 1981). We note that Saenger (2011) uses the potential term alone as an imaging condition, but here we extend this approach by combining kinetic and potentials terms to effectively mitigate low-wavenumber content away from the source and to generate the temporal integral of the wavefield Lagrangian at the source location.

Although the passive imaging condition in equation 3.13 involves autocorrelation of the displacement field $\mathbf{U}$, the correlation between the same wave modes is attenuated as shown by Rocha et al. (2016b, 2017). In contrast, at the source, the correlation between P- and S-wave modes is preserved, producing a peak amplitude directly related to the source mechanism (see Appendix 3.8.1) instead of a nodal plane as the PS correlation. Therefore, the energy passive imaging condition (EPIC) correlates different modes using the displacement field directly, without wave-mode decomposition at each extrapolation time step.

3.2.5 Passive imaging conditions: extended domain

The passive imaging conditions presented above are based on zero-lag wavefield correlation; thus, they can be considered as special cases of a more general correlation-based comparison between wavefields. As discussed previously, extending wavefield correlation beyond zero lag is useful since it provides additional information such as velocity accuracy (Sava and Vasconcelos, 2011). The temporal and spatial dependences of the wavefields allow one to compute space-lag image gathers (Rickett and Sava, 2002) and/or time-lag image gathers (Sava and Fomel, 2006). Extended imaging conditions (EICs) are also applicable to passive imaging as shown by Witten and Shragge (2015) for extrapolated scalar wavefields.

For wave-mode decomposed elastic wavefields, we define

$$I_{\alpha_1\alpha_2}\left(\mathbf{x},\boldsymbol{\lambda},\tau\right)=\sum_{t}\alpha_1\left(\mathbf{x}+\boldsymbol{\lambda},t+\tau\right)\alpha_2\left(\mathbf{x}-\boldsymbol{\lambda},t-\tau\right)\ , \tag{3.14}$$

where $\boldsymbol{\lambda}$ and τ are the spatial and temporal lags, respectively. Symbols α_1 and α_2 stand for either $P\left(\mathbf{x},t\right)$ or components of $\mathbf{S}\left(\mathbf{x},t\right)$ from equation 3.10; however, this can generate many possible extended images for elastic potentials when using the S-vector potential components. Exploiting the scalar S-wave energy density leads to a single extended image similar to equation 3.11. For EPIC (equation 3.13), we adapt the approach used in equation 3.14 to write

$$I_E^L(\mathbf{x},\boldsymbol{\lambda},\tau)=\sum_t\Big[\Big(\rho(\mathbf{x}+\boldsymbol{\lambda})\,\dot{\mathbf{U}}(\mathbf{x}+\boldsymbol{\lambda},t+\tau)\Big)\cdot\Big(\dot{\mathbf{U}}(\mathbf{x}-\boldsymbol{\lambda},t-\tau)\Big) - \Big(\underline{\underline{\mathbf{c}}}(\mathbf{x}+\boldsymbol{\lambda})\,\nabla\mathbf{U}(\mathbf{x}+\boldsymbol{\lambda},t+\tau)\Big):\big(\nabla\mathbf{U}(\mathbf{x}-\boldsymbol{\lambda},t-\tau)\big)\Big], \tag{3.15}$$

where we note that ρ and $\underline{\underline{\mathbf{c}}}$ are similarly shifted leaving the resulting image volumes asymmetric. We can also obtain the extended imaging condition for the Hamiltonian form by changing the sign between the two terms inside the brackets in equation 3.15.

In general, one can estimate the velocity inaccuracy on extended image gathers by evaluating focusing quality around zero lag. The more focused the energy is around zero lag, the closer the migration velocity is to the true velocity, as shown in many cases for active source seismic wavefield tomography (Albertin et al., 2005; Yang and Sava, 2011; Diaz et al., 2013; Yang et al., 2013; Yang and Sava, 2015). More recently, Witten and Shragge (2017a,b) use extended images in passive source wavefield tomography and show how calculating a single EIC at each estimated event location can assist with the elastic velocity inversion procedure. In this paper, besides evaluating the quality of the energy image with the correct velocity, we investigate the extended images for both PSIC and EPIC to investigate sensitivity to velocity inaccuracy and thereby infer potential application to the microseismic velocity estimation problem.

3.3 Methodology

Although EPIC exploits the interaction of backpropagated P- and S- direct arrivals, we need to address some caveats that arise during practical implementation of elastic time-reversal wavefield extrapolation: limited aperture and the presence of fake-mode artifacts. In general, acquired seismic data are incomplete and possibly spatially aliased, causing truncation artifacts (especially at the edges of the receiver acquisition patch) during backpropagation. Truncations are characterized with the same wave mode as the original data events, but have different propagation directions that can cause spurious artifacts when applying EPIC. With a straightforward numerical experiment in the Examples section, we illustrate

how the truncations create such artifacts - and demonstrate how they can be mitigated.

A second class of artifact appearing in both PS and energy images arises from the injection of single-mode data events as wavefield displacement into the extrapolation model. This generates both P- and S-wave modes regardless of their single-mode character, which are commonly called "fake modes" since they do not represent true data events (Yan and Sava, 2008; Ravasi and Curtis, 2013; Duan and Sava, 2015).

In order to mitigate both types of artifacts in the PS and energy images and obtain a better source location estimation result, we choose to first separate P- and S-wave arrivals in the data domain and generate two elastic wavefields, one with each individual wave mode arrival. Following this approach leads to PS and energy images with wave-mode separated wavefields. Then, such images may be subtracted from the corresponding PS and energy images that use both P- and S-arrivals as input to generate a final image I free of artifacts

$$I = I^{(P,S)} - I^{(P)} - I^{(S)} \,, \tag{3.16}$$

where $I^{(P)}$ and $I^{(S)}$ are images using P- and S-wave arrivals only as input, respectively, while $I^{(P,S)}$ uses both arrivals. We compute all image terms in equation 3.16 with the same imaging condition, either PS (I_{PS}) or energy (I_E): the superscripts with parentheses only indicate images formed with P- and/or S-data events. By following this novel approach of mitigating extrapolation-related artifacts, we obtain an energy image free of correlated truncation events and with attenuated fake-mode artifacts.

Separating P- and S-wave arrivals in the multicomponent data domain is computationally inexpensive, but does introduce a preprocessing step that requires user input in determining appropriate windowing parameters. Only one additional wavefield extrapolation is necessary, considering that we can generate wavefield $\mathbf{U}$ - from the P-arrival only - and wavefield $\mathbf{V}$ - from the S-arrival only. A third composite wavefield, $\mathbf{W} = \mathbf{U} + \mathbf{V}$, is effectively equal to extrapolation using both P- and S-arrivals by considering linearity of the extrapolators. Witten and Shragge (2017a) also require wave-mode separation in the data domain and two wavefield extrapolations for their acoustic passive imaging and inversion implementations.

It is important to note that this data-domain separation approach would be more difficult for a swarm of microseismic events containing overlapping P- and S-wave arrivals.

3.4 3-D numerical examples

In this section, we present PS and energy images showing the estimated source position for correct constant velocity models. Then, we analyze the imprint of velocity inaccuracy on both conventional and extended images. We examine the benefits of applying EPIC in a more complex 3D synthetic velocity model with realistic acquisition configuration. We conclude by applying the method to a microseismic event from a 3D field dataset.

3.4.1 Experiment 1: focusing with correct velocity

Our first numerical experiment investigates the imaging conditions developed above in an idealized microseismic monitoring experiment where the true velocity model is constant and known ($V_P = 3.0$km/s and $V_S = 1.8$km/s). In this scenario, we expect that a well-devised imaging condition should deliver a strong and focused correlation at the correct event location. Figure 3.1(a) shows the acquisition and model geometry of such an experiment where multicomponent receivers are distributed at the surface with a realistic fixed spacing ($\Delta x = \Delta y = 0.25$km, covering a 16km^2 area). We locate the microseismic event at the center of the 3D model ($x = y = z = 2$km) and assume a stress source mechanism oriented at 45° with respect to the x-axis. For this scenario, the source moment tensor has nonzero components of $\tau_{zz} = 1$ and $\tau_{xx} = -1$. Using a Ricker wavelet with peak frequency of 16Hz and model grid spacing of $\Delta x = \Delta y = \Delta z = 0.01$km, we generate 3D synthetic elastic data, followed by backpropagation and the application of the various imaging conditions.

Figures 3.1(b) and 3.1(c) show the images obtained using the autocorrelation of the P- and S-wavefields (equations 3.8 and 3.9), respectively. In either image, the low-wavenumber content arising due to wavefield autocorrelation contaminates the whole image space (especially its shallow part), and effectively prevents an identifiable focus at the source location. Alternatively, the cross-correlation of P- and S-wave modes (equation 3.11) generates the im-

age in Figure 3.1(d) with minimal low-wavenumber content and a strong amplitude event at the correct source location. The EPIC based on the Hamiltonian operator I_E^H (Figure 3.1(e), using equation 3.12) represents the total energy stacked over time, which results in a strong low-wavenumber pattern similar to those in the autocorrelation images (Figures 3.1(b) and 3.1(c)). In contrast, the EPIC based on the Lagrangian operator I_E^L (Figure 3.1(f), using equation 3.13) shows a result similar to the PS image, with a strong and focused correlation at the source location. In all images, one should consider smearing and truncation artifacts when estimating a source location using wavefield imaging methods for passive seismic, since sparse and band-limited data acquisition prevents extrapolated waves from collapsing into an idealized focus.

To obtain all images in Figure 3.1, we use the procedure explained in the methodology section, i.e. computing three separated energy images such as $I = I^{(P,S)} - I^{(P)} - I^{(S)}$. This is necessary because truncation events correlate with the true events and create a strong artifact at the center of the energy image. Figures 3.2(a) and 3.2(b) show schematic representations of the truncation wavefronts away and close to the source location, respectively. In Figure 3.2(c), we show the vertical component of the back-propagated elastic wavefield at a snapshot prior to events focusing at the source location. Besides the true wave events (P- and S-backpropagated microseismic arrivals), truncations exist and interact with the true events close to the focusing location and time. Note how the S-wave truncations interfere both with themselves and with the incoming P-wave event. In addition, the fake P-wave mode also appears strong in Figure 3.2(c), but generates artifacts mostly in the shallow area (down to 1km in depth). Figure 3.2(d) shows the same energy image as in Figure 3.1(f), but without the subtraction of such imaging artifacts. We note residual low-wavenumber content and the different correlation at the source in Figure 3.2(d) as compared to Figure 3.1(f). This experiment in a constant-velocity medium demonstrates how: (1) low-wavenumber artifacts from wavefield autocorrelation impede a visual interpretation of the source location; (2) truncation events substantially alter the imaged events; and (3) imaging conditions that

exploit different wave modes in the displacement field localize the source by producing a focused correlated event at the true source position, especially for EPIC which produces a focused peak at the source location.

3.4.2 Experiment 2: sensitivity to changes in velocity and extended images

Our second experiment investigates the sensitivity of the different imaging conditions when using the incorrect velocity. We expect that the correlation between P- and S-waves occurs at a different location and time than for the correct model scenarios; however, we would still expect a coherent pattern useful for interpretation and migration velocity analysis. In Figures 3.3 and 3.4, we compute PS and energy images for different velocities using the same experimental setup as in Figure 3.1. We create incorrect constant velocities by globally increasing or decreasing the original velocities by 8%. For improved visualization, we show zoomed slices from the original image volumes. The images exhibit misfocusing due to the incorrect velocities, and show a correlation point either too shallow or too deep with respect to the correct source location. We note that all PS images have a zero crossing at the point of maximum correlation (e.g., at $x = y = z = 2$km in Figure 3.3(e)). Though present in Experiment 1, but more noticeable here, the usage of the absolute value of the S-vector potential creates zero-crossing patterns throughout the images due to the existence of nodal planes. However, for energy images computed with incorrect velocities (Figure 3.4), we observe a more straightforward and interpretable moveout pattern from the unfocused events relative to the PS images because of their fewer side lobes, as well as an absence of visible nodal planes. This misfocusing of event images for incorrect velocities is important in the context of assessing velocity and source location errors.

We also compute extended images with correct and incorrect velocities for both PSIC (Figure 3.5) and EPIC (Figure 3.6). These extended image examples are generated with the same incorrect velocities and displayed similarly to Figures 3.3 and 3.4. For simplicity, we evaluate these extended images at a single spatial point located at the correct source position and with spatial lags only (with axes $\lambda_x, \lambda_y, \lambda_z$), thus generating the 3D volumes

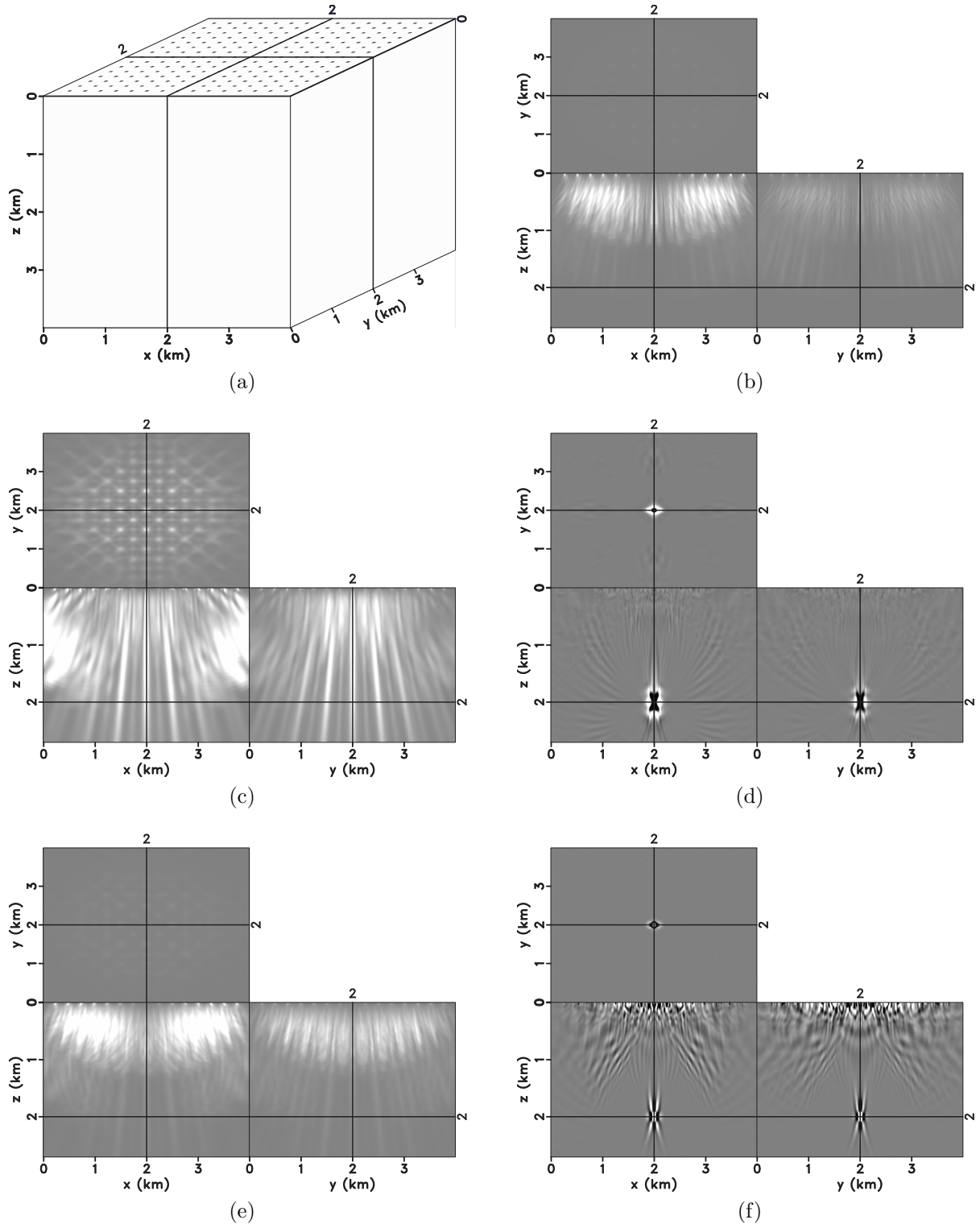

Figure 3.1: Constant-velocity experiment that consists of (a) an earth model with 4×4×4 km^3 and multicomponent receivers (black dots) spaced by 0.25km at the surface. (b) PP, (c) SS, (d) PS and energy images using equation 3.12 (e) and equation 3.13 (f). The PS and energy images have strong and focused peaks at the source location compared to all other images that exhibit strong low-wavenumber artifacts.

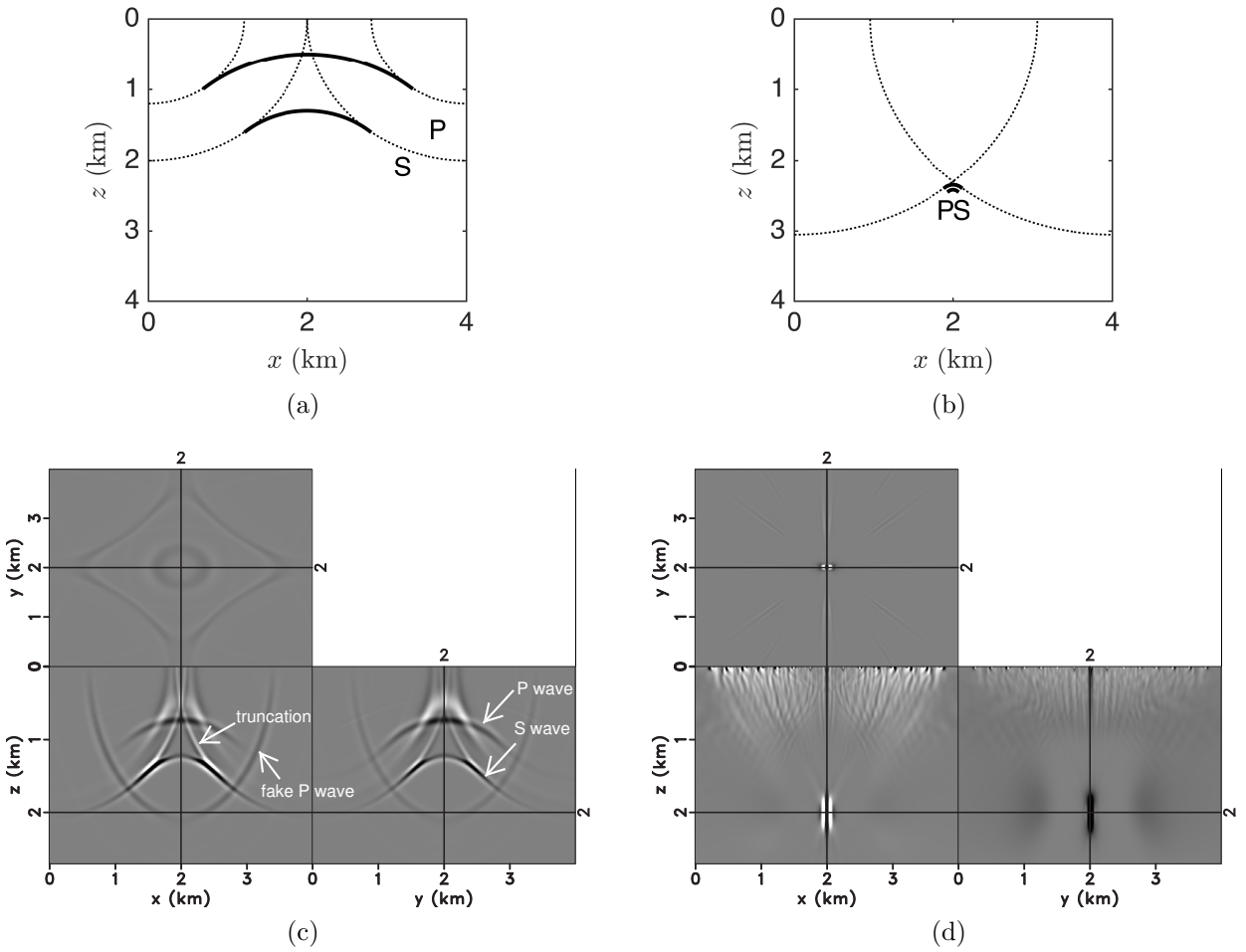

Figure 3.2: Schematic representation of (a) P- and S-waves backpropagated with truncation events (dashed lines). Close to their focus points, (b) P- and S- waves correlate with their respective truncation events, which have the polarity of their original wave but different propagation directions. (c) Snapshot of the vertical component from the back-propagated elastic wavefield. As indicated by the arrows, note the true backpropagated events and the associated artificial extrapolated events. (d) Energy image with the strong artifact caused by the truncation, as opposed to the energy image without such artifact (Figure 3.1(f)).

shown in Figures 3.5 and 3.6. As discussed above, we expect to observe unfocused events in the extended domain when velocities are incorrect, and a focused event at zero lag when both P- and S-wave velocities are correct. Indeed, we note that these misfocusing attributes exist in the extended domain for both imaging conditions, but are expressed differently. Compared to the extended PS image, the energy one shows significantly fewer lobes and no nodal planes, and therefore, exhibits imaged waveforms more straightforward to interpret. However, whereas the extended energy image exhibits symmetric unfocused events with respect to the λ_z axis, the extended PS image shows a single unfocused event either at positive or negative λ_z values. This indicates that, although the events in the extended energy image exhibit more straightforward waveforms, interpreting the direction of the required velocity update (either positive or negative) is more challenging. For instance, by looking at the extended energy images when we perturb only the S-wave velocity by $-\%8$ or $+\%8$ (Figures 3.6(d) and 3.6(f)), we note a similar dislocation from zero lag but different focusing attributes. Therefore, the extend energy image correctly provides the magnitude of the velocity perturbation, but apparently has lower sensitivity with respect to the perturbation sign. Based on such differing sensitivity, we infer that the two extended imaging conditions would provide complementary information for microseismic migration velocity analysis.

3.4.3 Experiment 3: SEG/EAGE 3-D overthrust model

Our third numerical test investigates how PSIC and EPIC compare using a more complex velocity model - SEG/EAGE 3D overthrust (Aminzadeh et al., 1994). We place the source at the center of the model ($x = y = 3.048$km, $z = 1.073$km in Figure 3.7(a)), and use a non-uniform distribution of 192 multicomponent receivers at elevations ranging between $z = -213$m and $z = -423$m (Figure 3.7(c)). These receiver coordinates mimic the acquisition geometry of the following field data example. Because the original 3D overthrust model contains only the P-wave velocity, we arbitrarily create a S-wave velocity model using an oscillatory PS velocity ratio as a function of depth (Figure 3.7(b)). We model and extract synthetic data at the 192 receiver locations, and compare PS and energy images using a

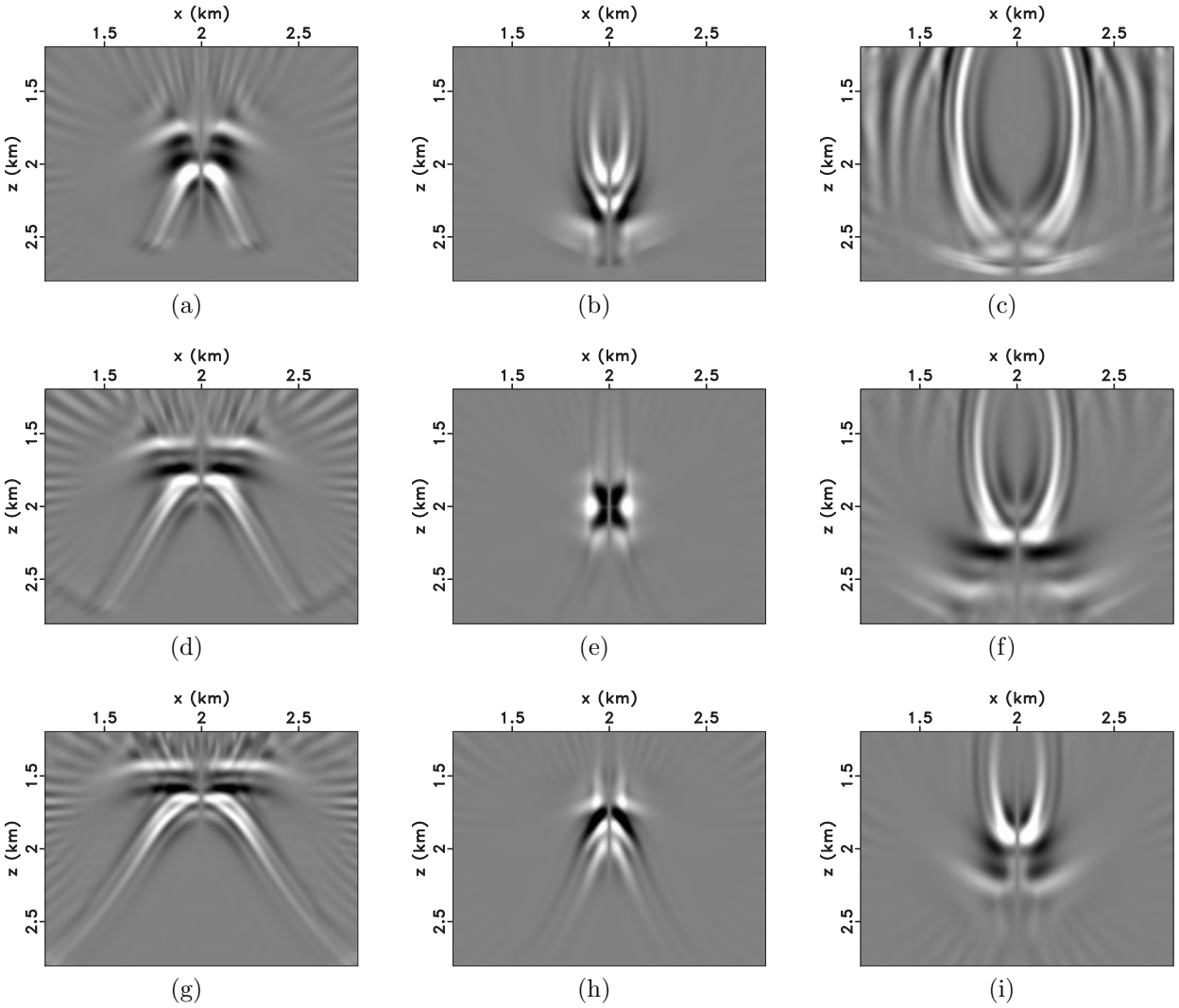

Figure 3.3: PS images with incorrect velocities with respect to a $V_P = 3.0$km/s and $V_S = 1.8$km/s. Top, middle and bottom rows correspond to -8%, 0%, $+8\%$ changes in the P-wave velocity; and left, middle and right columns correspond to -8%, 0%, $+8\%$ changes in the S-wave velocity. Note the unfocused events with respect to the focused correlation in the central image (which uses the correct velocity).

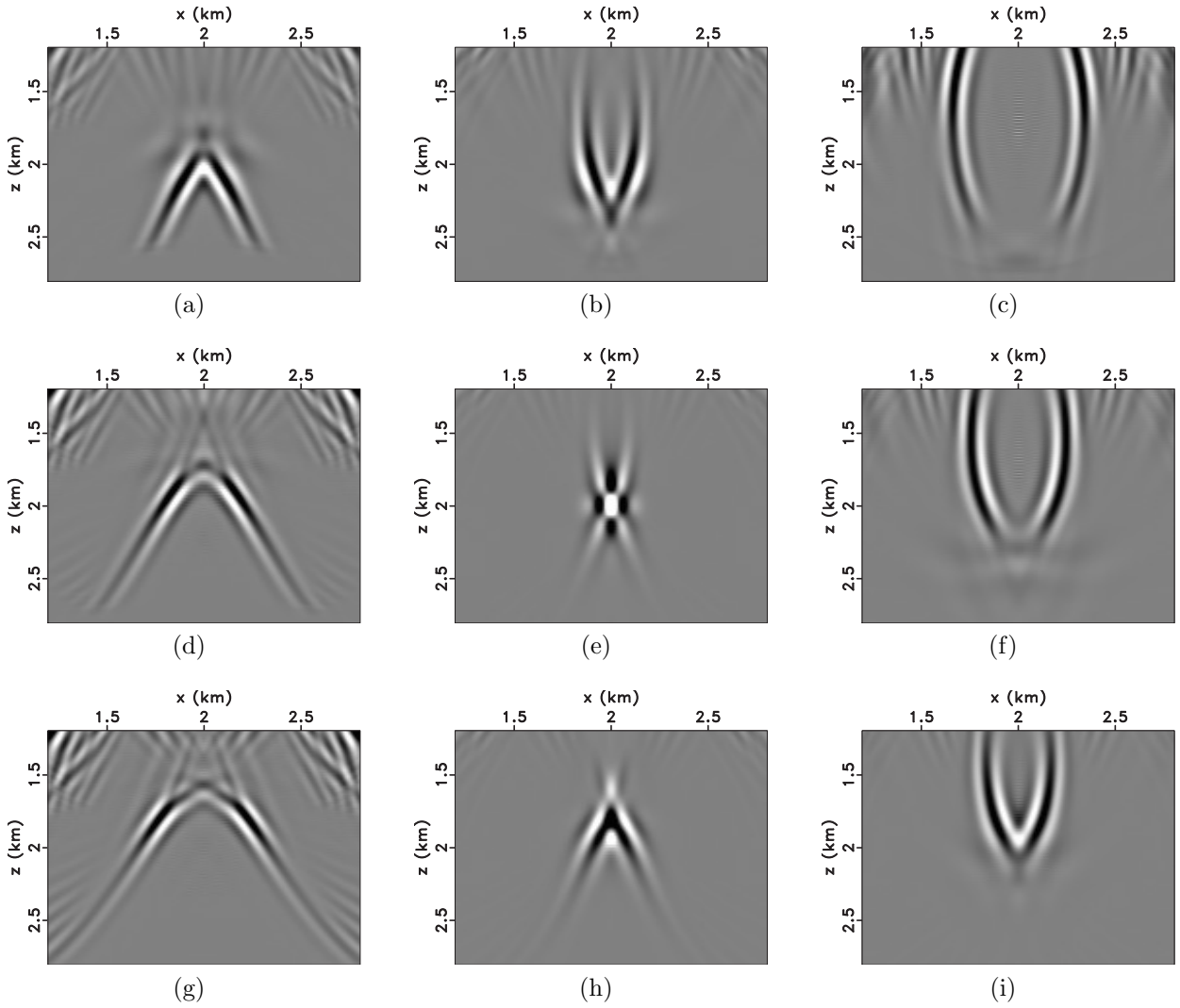

Figure 3.4: Energy images with incorrect velocities, computed and displayed as in Figure 3.3. Compared to the PS images in Figure 3.3, the energy correlation produces unfocused imaged events that are more straightforward to interpret and without zero crossings.

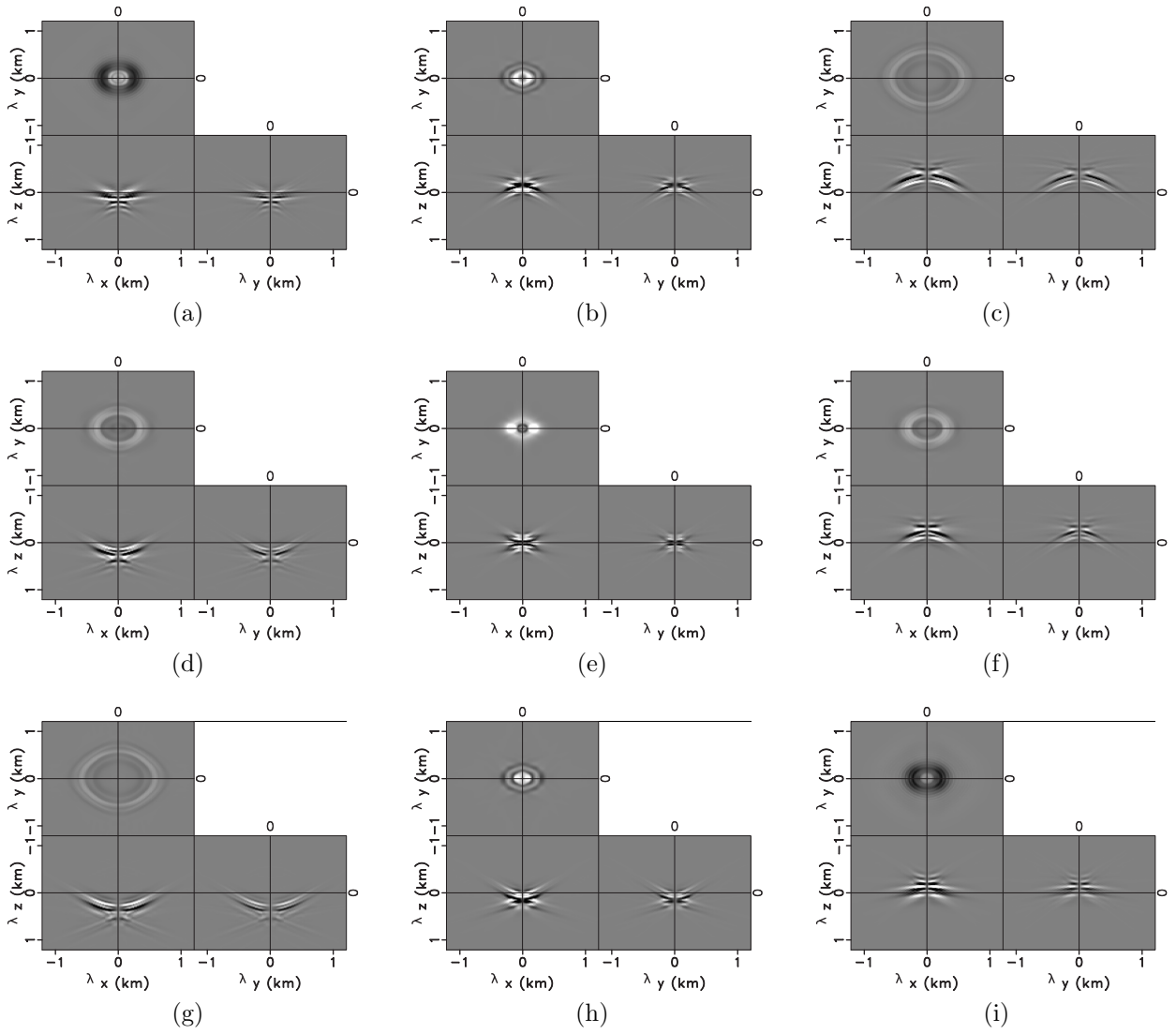

Figure 3.5: Extended PS images with incorrect velocities. Top, middle and bottom rows correspond to -8%, 0%, $+8\%$ changes in the P-wave velocity; and left, middle and right columns correspond to -8%, 0%, $+8\%$ changes in the S-wave velocity. Note the unfocused events with respect to the focused correlation in the central image (which uses the correct velocity).

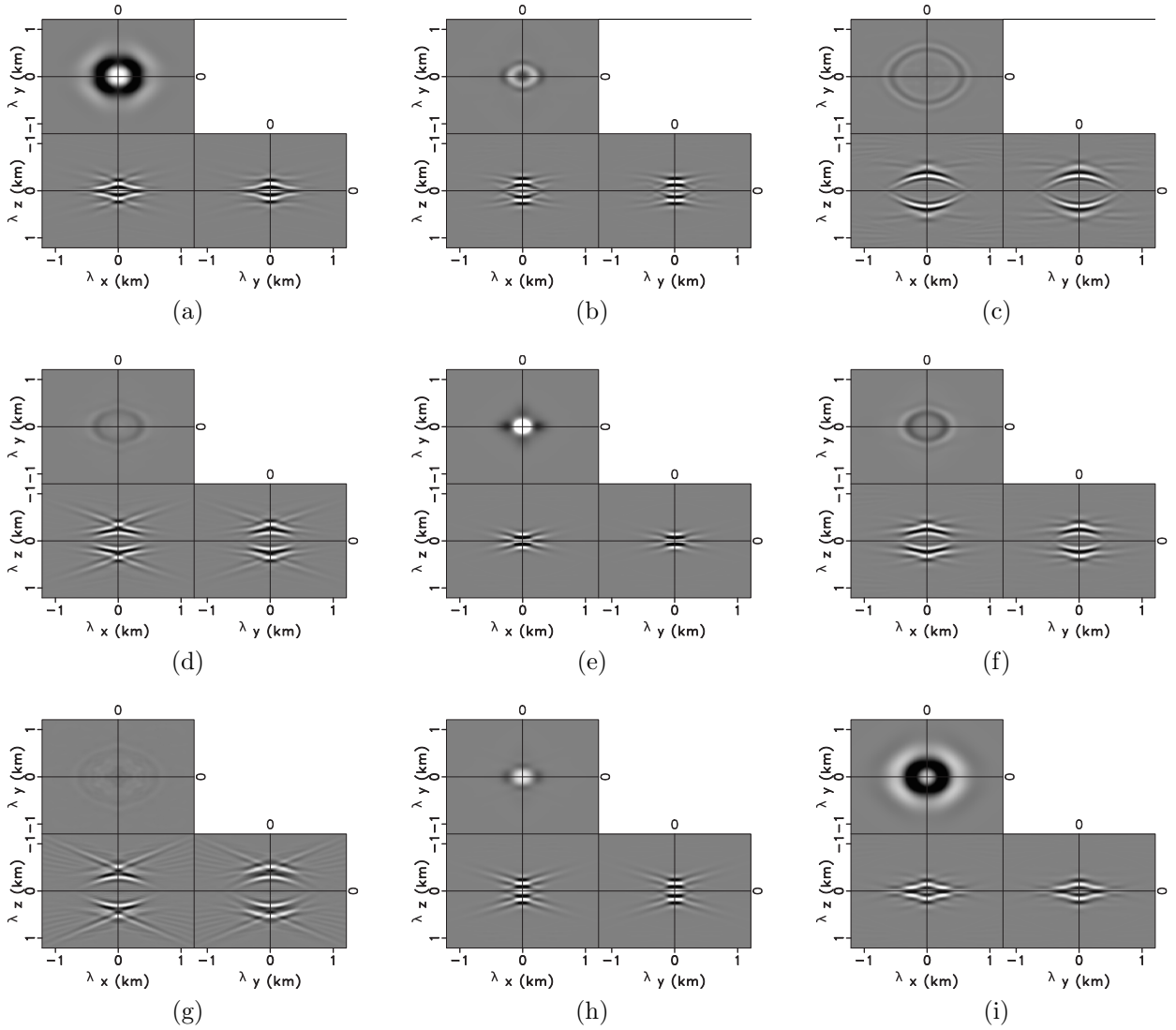

Figure 3.6: Extended energy images with incorrect velocities, organized similarly to Figure 3.5. Compared to the PS images in Figure 3.5, the energy correlation produces unfocused images that are more straightforward to interpret, are symmetric with respect to the λ_z axis, and contain no zero crossings.

source mechanism different from the previous two numerical experiments. The corresponding source moment tensor has nonzero components of $\tau_{zz} = 1$, $\tau_{yy} = -2$, and $\tau_{xx} = 1$.

Figure 3.8 shows the PS and energy images for this numerical experiment. Figures 3.8(a) and 3.8(b) show the entire image volumes, while Figures 3.8(c) and 3.8(d) zoom around the source location. Originally, both PS and energy images have strong artifacts in the shallow subsurface due to the aforementioned caveats (i.e., truncated acquisition, non-existent modes created by displacement injection) from elastic wavefield extrapolation; however, by applying a straightforward exponential gain with depth to both images to mitigate these effects, we obtain the images shown in Figures 3.8(a) and 3.8(b). The image locations colored in red represent clipped colorbar amplitudes, and are generally consistent with the estimated source locations for both images (Figure 3.8(c) and 3.8(d)). The PS image (Figure 3.8(c)) exhibits the clipped amplitudes about 200m away from the source location, mainly due to the zero crossing that occurs at the known source location. Meanwhile, the energy image (Figure 3.8(d)) has the clipped amplitudes within one grid cell of the true source location. Therefore, by comparing the zoomed images in Figures 3.8(c) and 3.8(d), we observe more consistent focusing of the energy image relative to the PS image, and the misplacement of the clipped peak amplitude for the PS image. As discussed in the theory section, data preprocessing could handle polarization issues with the PS correlation, but potentially at the cost of a lower resolution image.

To observe focusing in the extended domain, we generate extended images for both imaging conditions using the correct velocity only (Figures 3.8(e) and 3.8(f)). As previously, the extended PS image has a nodal plane at zero lag and exhibits substantial defocusing away from zero lag even though the velocities are exact. The extended energy image shows a more focused event at zero lag without nodal planes. The $\lambda_x - \lambda_y$ plane of the energy image in Figure 3.8(f) might suggest that the source has its primary stress component in the $y-$axis due to the elongation direction of the imaged event. However, validating a direct extraction of the source mechanism warrants further research beyond the scope of this paper.

The SEG/EAGE 3D overthrust experiment demonstrates that the direct correlation between Helmholtz decomposed P- and S- wavefields produces strong imaging artifacts with amplitudes surpassing the correlation at the true source position. EPIC involves an indirect correlation of P- and S- waves that produces a stronger correlation at the source location compared to the imaging artifacts, both in the conventional and extended domains. The difference between PSIC and EPIC becomes more evident with increasing model complexity.

3.4.4 Experiment 4: field data example

The final experiment uses microseismic field data recorded by a passive seismic acquisition campaign during a hydraulic stimulation program in eastern Ohio, USA. Witten and Shragge (2017b) present a thorough description of the experiment, dataset and subsequent pre-processing. The receiver array consists of 192 multicomponent (3C) geophones whose geometry is shown in Figure 3.7(c). We use P- and S-wave velocity models (Figure 3.9) obtained by the image-domain velocity inversion described in Witten and Shragge (2017b). From a data catalog of 28 high-S/N microseismic events, we select one microseismic event (single P- and S-arrivals) of magnitude $M_w = 0.24$. The processing applied prior to back-propagation and imaging involves different steps compared to the acoustic implementation from Witten and Shragge (2017b): (1) rotating the northing and easting components to x, y components consistent with the velocity model geometry (by an angle of 41°); (2) applying a bandpass filter from 4 to 30Hz (with no trace normalization, nor application of envelope filter); and (3) implementing stronger weighting of early P- and S-wave arrivals. Figure 3.10 shows the multicomponent dataset processed using such approach.

We inject the microseismic event shown in Figure 3.10 into the velocity model (Figure 3.9), and apply both PSIC and EPIC. We use the same image subtraction procedure ($I = I^{(P,S)} - I^{(P)} - I^{(S)}$) and exponential gain with depth as in Experiment 3. Figure 3.11 presents the final results of the imaging procedure. Because in this field dataset example we do not know the true source location, we elect to present image slices corresponding to the point of maximum amplitude for each imaging condition clipped using the same percentile

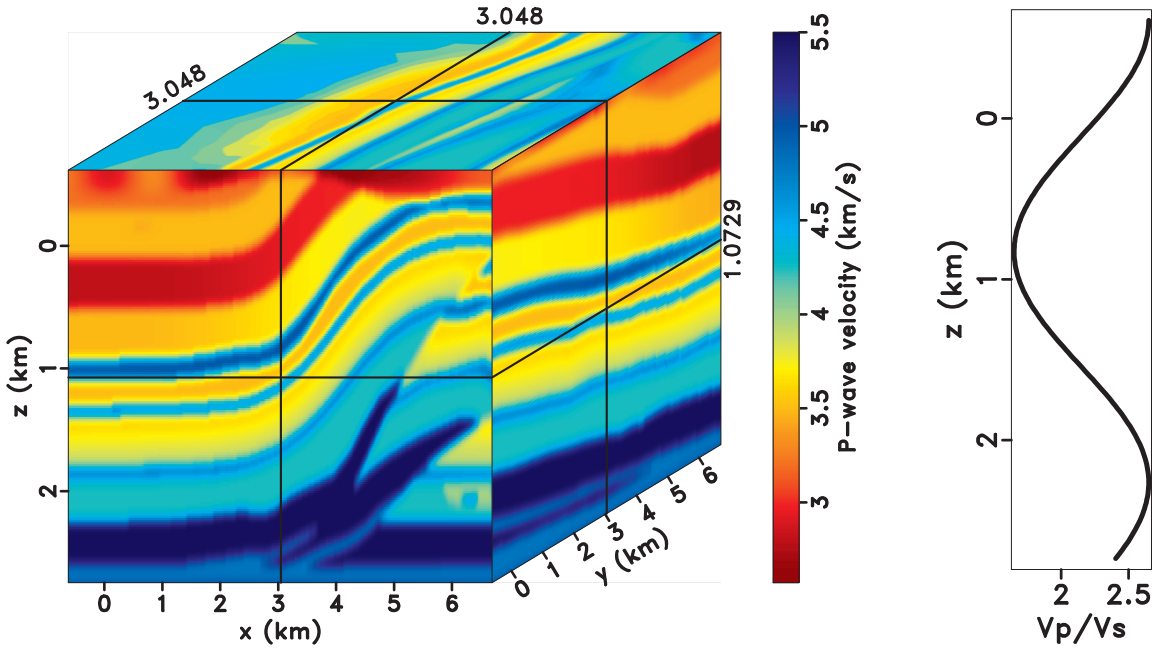

(a) (b)

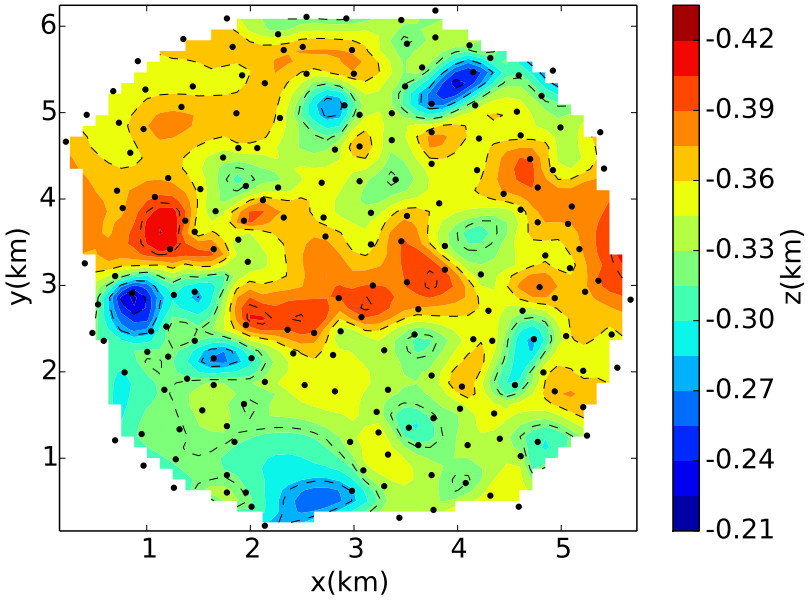

(c)

Figure 3.7: SEG/EAGE overthrust experiment: (a) P-wave velocity from the 3D overthrust model and (b) PS velocity ratio. (c) Receiver coordinates used for the overthrust and field acquisition experiments shown in Figures 3.9 and 3.11.

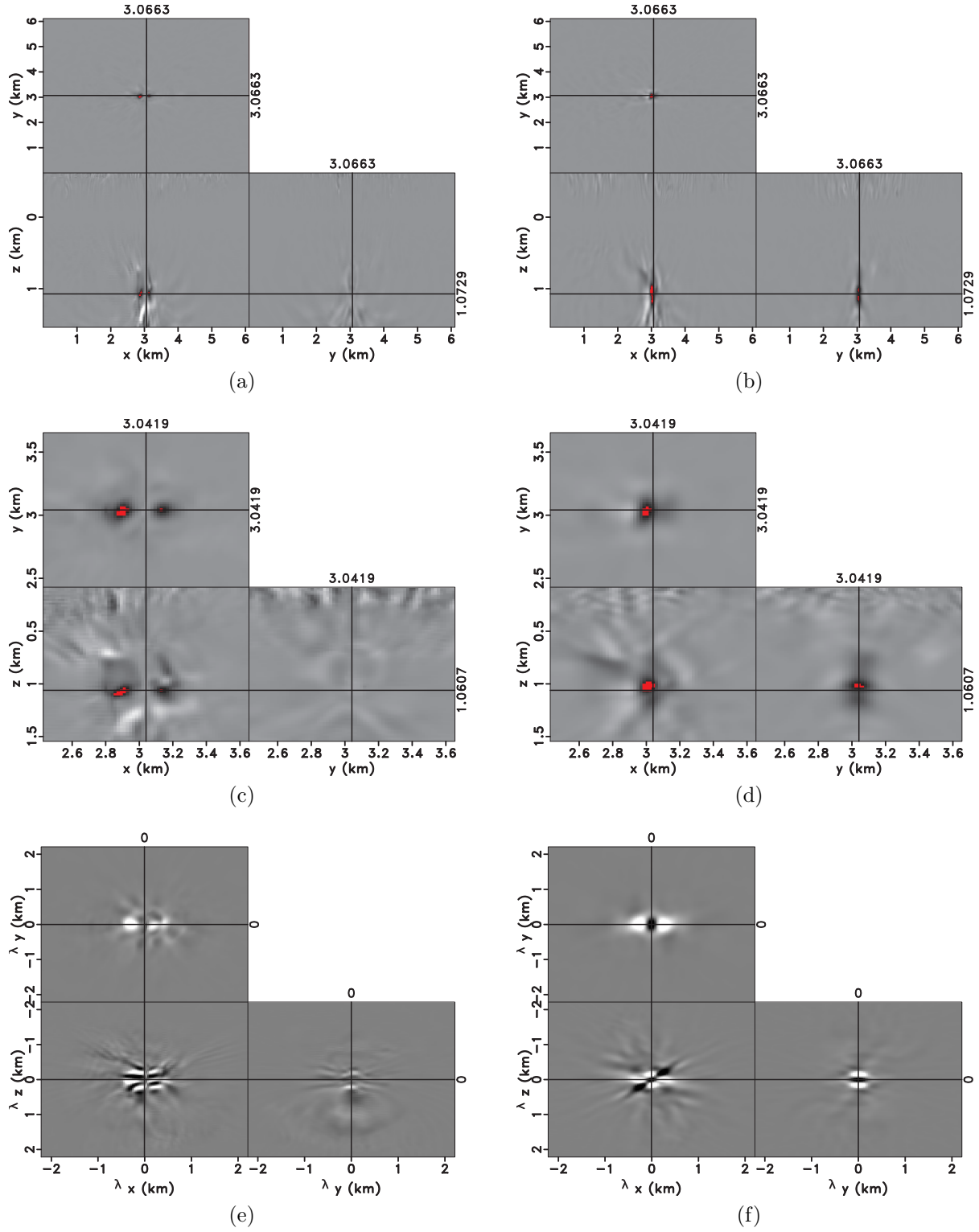

Figure 3.8: SEG/EAGE overthrust experiment: (a) PS and (b) energy images for a stress source with $\tau_{xx} = -2, \tau_{yy} = 1, \tau_{zz} = 1$. Zoomed (c) PS and (d) energy images, as well as extended (e) PS and (f) energy images. The energy correlation exhibits peak amplitudes (in red) that are closer to the source location in (d) when compared to (c), and are more focused in the extended domain in (f) when compared to (e).

(Figure 3.11(a) and 3.11(b)). As observed in the image slices, the discrepancy between the estimated PS and energy source locations is $[\Delta x, \Delta y, \Delta z] = [366, 146, 91]$m. The PS image in Figure 3.11(a) exhibits more artifacts away from its presumed source location (especially on the $x - y$ plane) when compared to the energy image in Figure 3.11(b). Looking at the zoomed images (Figures 3.11(c) and 3.11(d)), we note a further advantage of the energy image relative to the PS image: most of the correlated energy is positive. Finally, the extended energy image (Figure 3.11(f)) exhibits a more centralized focus around zero lag when compared to the extended PS image (Figure 3.11(e)). Although there is residual energy beyond zero lag, both extended images indicate that the provided velocities obtained by image-domain tomographic inversion are sufficiently consistent and, therefore, accurate by the self-consistency principle (Witten and Shragge, 2017a). Overall, the field data example demonstrates that EPIC behaves well in the presence of noise, realistic acquisition geometry, as well as possible residual errors in the velocity models. This experiment also illustrates that elastic wavefield imaging methods are more effective for real surface passive seismic with relatively dense receiver geometry, after the complementary image provided by the energy correlation.

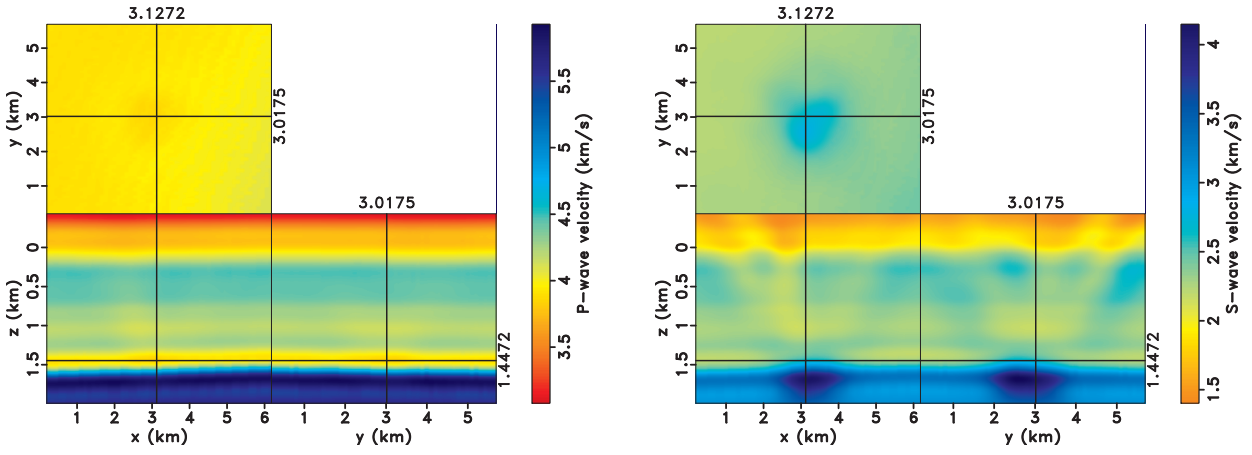

(a) (b)

Figure 3.9: Field data experiment: (a) P- and (b) S-wave velocity models.

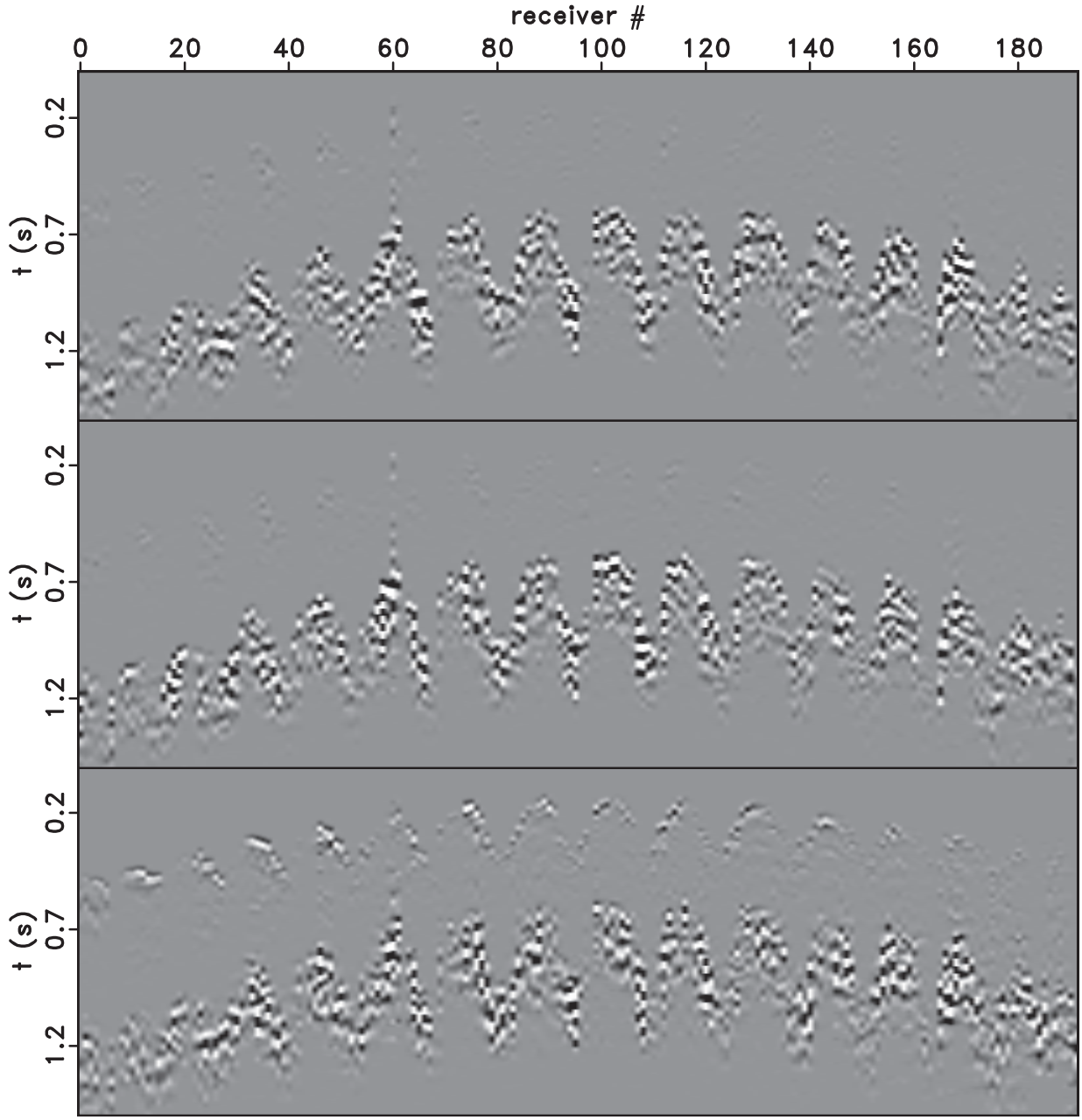

Figure 3.10: Field data experiment: x (top), y (middle) and z (bottom) components from the processed dataset containing a single microseismic event. Note the P- (from $t = 0$s to $t = 0.6$s) and S- (from $t = 0.6$ to $t = 1.5$s) arrivals, and how the P-wave arrival is stronger in the vertical (z) component.

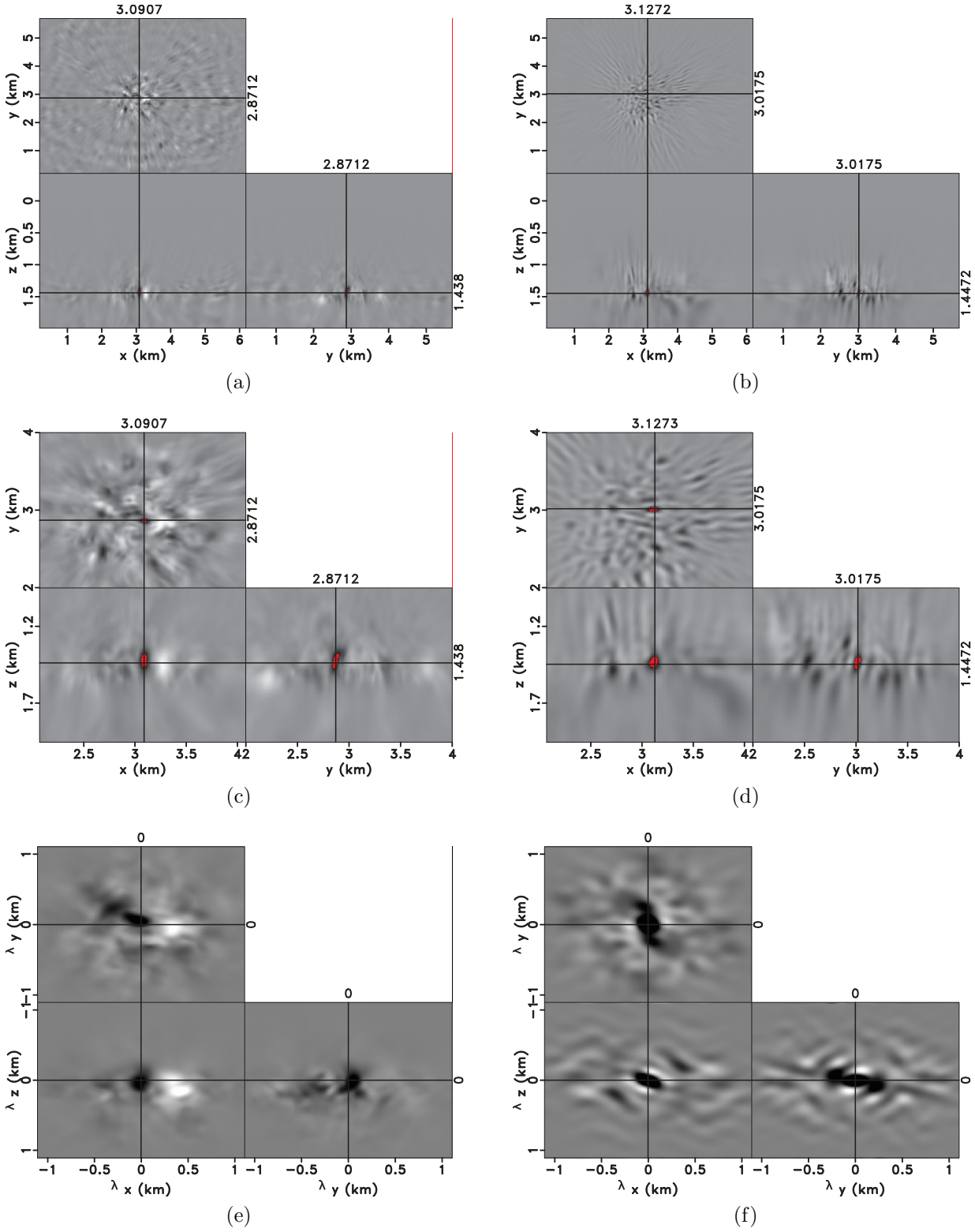

Figure 3.11: Field data experiment: (a) PS and (b) energy images for the field dataset. Zoomed (c) PS and (d) energy images, as well as extended (e) PS and (f) energy images. The energy correlation has peak amplitudes (in red) that are closer to the source location in (d) when compared to (c), and are more centralized in the extended domain in (f) when compared to (e).

3.5 Discussion

Based on the numerical examples presented in this paper, EPIC not only serves as an alternative procedure for obtaining source location estimates and examining velocity accuracy, but offers some improvements relative to the conventional PSIC. The more directly interpretable images obtained by the proposed imaging condition not only reduces uncertainty of the event location, but also helps velocity estimation based on migration velocity analysis methodology (i.e., semblance principle). This interpretational simplicity is due to the absence of nodal planes and associated polarity changes, which are ubiquitous in PS correlation. The penalty function commonly used in image-domain wavefield tomography (Symes and Carazzone, 1991; Mulder and ten Kroode, 2002; Yang and Sava, 2015; Witten and Shragge, 2017a) requires extended-domain images with fewer artifacts and better delineated events. In the context of passive imaging and inversion, our examples show that such characteristics are enhanced by the energy correlation. However, computing tomographic velocity updates requires reliable gradient magnitude and direction information, and the latter appears to not be sufficiently distinguishable by the energy correlation alone. In addition, for both imaging conditions, differentiating between P- and S-wave velocity inaccuracies is only possible with complementary information from autocorrelation P- and S-wave imaging conditions, as shown previously in Witten and Shragge (2017a). Thus, we view these various extended imaging conditions could play a complementary - but important - role in applications of microseismic migration velocity analysis.

The fact that the energy correlation formalism introduced above is able to handle anisotropy is not demonstrated here; however, the pathway for incorporating anisotropy should be clear based on the theory presented in this paper. Current wave-mode decomposition methods during wavefield extrapolation for anisotropic media remain computationally intensive (Zhang and McMechan, 2010; Yan and Sava, 2011a; Cheng and Fomel, 2014; Sripanich et al., 2015; Wang et al., 2016; Rocha et al., 2017). Until they become more efficient, the energy correlation serves as a formal and cost-effective method for correlating different wave modes

for anisotropic elastic passive imaging. Our imaging condition does not add a significant computational burden since it requires the same spatial derivatives as those in Helmholtz decomposition and straightforward temporal derivatives (identical to those computed at each elastic extrapolation time step). Moreover, the extended energy image is sufficiently computed at a single common image point (CIP) for migration velocity analysis (Witten and Shragge, 2017a).

We also advocate the usage of elastic wavefield extrapolation as opposed to acoustic extrapolation, which is applied to the same field dataset in a related paper (Witten and Shragge, 2017b). Acoustic time-reversal involves normalization of each individual trace and computing the complex envelope of the seismic signals, thereby altering the amplitude and phase of the acquired signals. While essential for acoustic velocity analysis, such procedure undermines any possible cotemporal radiation pattern analysis (i.e., through joint microseismic velocity analysis and moment-tensor inversion). Acoustic extrapolation assumes single-component data and, therefore, does not exploit the polarization of seismic waves. Elastic extrapolation does not involve these issues and offers finer imaging sampling considering the same frequency band from data. However, it remains substantially more expensive than its acoustic counterpart especially for 3D models, though it is achievable at the scale of a small cluster or even a high-end workstation when using GPU-based 3-D elastic propagators (Weiss and Shragge, 2013).

3.6 Conclusions

For passive wavefield imaging with surface-recorded multicomponent data, EPIC offers an elegant solution for locating seismic sources within an arbitrary earth model. Based on energy conservation for extrapolated wavefields, our imaging condition represents the temporal integral of the Lagrangian operator (which is the difference between kinetic and potential wavefield energy terms) and produces an image that is theoretically related to the source mechanism. For simple models, we demonstrate that the energy image exhibits better attributes than PS images in terms of image quality and velocity sensitivity. For more

realistic synthetic and field data examples, the improved results from applying EPIC are similarly illustrated despite the introduction of field data noise, sparser and non-uniform receiver geometry, and more complex earth models. The preclusion of wave-mode decomposition during extrapolation in our method permits its implementation to anisotropic earth models without substantial additional cost or complication, as opposed to the conventional PSIC that generally relies on Helmholtz decomposition.

In summary, we have validated the five advantages stated in the Introduction: (1) handling radiation patterns without the generation of nodal planes; (2) producing a peak amplitude at the source location; (3) precluding wave-mode decomposition at each time step; (4) downweighting identical wave modes and enhancing distinct ones during correlation; and (5) offering complementary extended image attributes for migration velocity analysis. Future work involves exploring the further benefits of EPIC for anisotropic media, potential inferences on focal mechanism and its inversion, and the development of a microseismic migration velocity inversion framework using the unfocused energy on extended image gathers.

3.7 Acknowledgments

We thank the sponsors of the Center for Wave Phenomena, whose support made this research possible. We thank an anonymous company and ESG/Spectraseis for delivering the field dataset. We acknowledge Ivan Lim Chen Ning, Paul Fowler and Roel Snieder for helpful discussions, and Yuting Duan for sharing her wavefield modeling codes. The reproducible numeric examples in this paper use the Madagascar open-source software package (Fomel et al., 2013) freely available from http://www.ahay.org.

3.8 Appendix

The appendix below elucidates specific points of this current chapter.

3.8.1 Hamilton's Principle

Considering a displacement field $\mathbf{U}(\mathbf{x},t)$, the Lagrangian density function is (Ben-Menahem and Singh, 1981)

$$\mathcal{L}(\mathbf{U},\mathbf{x},t) = \frac{1}{2}\rho\|\dot{\mathbf{U}}\|^2 - \frac{1}{2}\left(\underline{\underline{\mathbf{c}}}\nabla\mathbf{U}\right) : \nabla\mathbf{U} \; . \tag{3.17}$$

The first and second terms in the Lagrangian function represent the kinetic and potential energies of the wavefield, respectively. In a medium with no external forces, the action is defined as the Lagrangian density function integrated over time

$$A(\mathbf{U}) = \int_0^T \mathcal{L}(\mathbf{U},t)\,\mathrm{d}t \; . \tag{3.18}$$

Hamilton's variational principle states that the action is stationary under small displacements, and can be expressed as (Slawinski, 2003):

$$\delta A(\mathbf{U},\mathbf{x}) = \delta \int_0^T \mathcal{L}(\mathbf{U},t)\,\mathrm{d}t = 0 \; , \tag{3.19}$$

where δ indicates the variation of a function. The variation is permutable with a definite integral and can be defined with respect to the displacement variable (Lanczos, 1970). Hence,

$$\begin{aligned} \delta A(\mathbf{U},\mathbf{x}) &= \int_0^T \delta\mathcal{L}(\mathbf{U},t)\,\mathrm{d}t \\ &= \int_0^T \left[\mathcal{L}(\mathbf{U}+\delta\mathbf{U},t) - \mathcal{L}(\mathbf{U},t)\right]\mathrm{d}t = 0 \; . \end{aligned} \tag{3.20}$$

where $\delta\mathbf{U}(\mathbf{x},t)$ is a small displacement satisfying $\delta\mathbf{U}(\mathbf{x},t=0) = \delta\mathbf{U}(\mathbf{x},t=T) = 0$.

We can characterize the Lagrangian, $\mathcal{L}(\mathbf{U},t)$, for a particle at rest from $t=0$ to $t=T$, i.e., $\mathbf{U}=0$, for $0 \le t \le T$. We can consider the displacement field acting on this particular point as a small perturbance to the particle at the rest. Therefore,

$$\delta A(\mathbf{U},\mathbf{x}) = \int_0^T \mathcal{L}(\delta\mathbf{U},t)\,\mathrm{d}t = 0 \; . \tag{3.21}$$

This implies that, in the absence of external work from sources and in the presence of small displacements, the energy imaging condition defined as the integral of the Lagrangian density

function is zero.

In a volume V that contains sources, the action is defined as (Yu, 1964):

$$A\left(\mathbf{U},\mathbf{x}\right)=\int_{0}^{T}\int_{V}\left[\mathcal{L}\left(\mathbf{U},t\right)\mathrm{d}V+W\right]\mathrm{d}t\ , \tag{3.22}$$

where the external work W is

$$W=\int_{V}\rho\mathbf{F}\cdot\mathbf{U}\mathrm{d}V+\int_{S}\left(\underline{\mathbf{t}}\cdot\mathbf{U}\right)\cdot\mathbf{n}\mathrm{d}S\ , \tag{3.23}$$

where $\mathbf{F}\left(\mathbf{x},t\right)$ represents a body force field and $\underline{\mathbf{t}}\left(\mathbf{x},t\right)$ an external stress field acting on the surface of the considered volume. Applying the variation operator on equation 3.23 and using the divergence theorem, we obtain

$$\delta W=\int_{V}\left[\rho\mathbf{F}\cdot\delta\mathbf{U}+\nabla\cdot\left(\underline{\mathbf{t}}\cdot\delta\mathbf{U}\right)\right]\mathrm{d}V\ . \tag{3.24}$$

Applying the variation operator on equation 3.22 and using equation 3.24 leads to

$$\delta A\left(\mathbf{U},\mathbf{x}\right)=\int_{0}^{T}\int_{V}\left[\mathcal{L}\left(\delta\mathbf{U},t\right)+\rho\mathbf{F}\cdot\delta\mathbf{U}+\nabla\cdot\left(\underline{\mathbf{t}}\cdot\delta\mathbf{U}\right)\right]\mathrm{d}V\mathrm{d}t=0\ . \tag{3.25}$$

Consider a sufficient small volume such that it contains only one discrete point. In a point where either a displacement or a stress source exists, Equation 3.25 suggests that the energy imaging condition (defined as the integral of the Lagrangian density function) is equivalent to the action of existing sources

$$I_{EN}\left(\mathbf{x}\right)=\int_{0}^{T}\mathcal{L}\left(\delta\mathbf{U},t\right)\mathrm{d}t=-\int_{0}^{T}\rho\mathbf{F}\cdot\delta\mathbf{U}+\nabla\cdot\left(\underline{\mathbf{t}}\cdot\delta\mathbf{U}\right)\mathrm{d}t\ . \tag{3.26}$$

The energy imaging, for waves generated by a displacement point force, becomes

$$I_{EN}\left(\mathbf{x}\right)=\int_{0}^{T}\mathcal{L}\left(\delta\mathbf{U},t\right)\mathrm{d}t=-\int_{0}^{T}\rho\mathbf{F}\cdot\delta\mathbf{U}\mathrm{d}t\ , \tag{3.27}$$

and by a stress source, generally described as a double couple system of forces, becomes

$$I_{EN}\left(\mathbf{x}\right)=\int_{0}^{T}\mathcal{L}\left(\delta\mathbf{U},t\right)\mathrm{d}t=-\int_{0}^{T}\nabla\cdot\left(\underline{\mathbf{t}}\cdot\delta\mathbf{U}\right)\mathrm{d}t\ . \tag{3.28}$$

CHAPTER 4

3D ACOUSTIC LEAST-SQUARES REVERSE TIME MIGRATION USING THE ENERGY NORM

A paper published* in Geophysics

Daniel Rocha**,[1], Paul Sava[1] and Antoine Guitton[2,1]

We propose a least-squares reverse-time migration (LSRTM) method that uses an energy-based imaging condition to obtain faster convergence rates when compared with similar methods based on conventional imaging conditions. To achieve our goal, we also define a linearized modeling operator that is the proper adjoint of the energy migration operator. The proposed modeling and migration operators use spatial and temporal derivatives that attenuate imaging artifacts and deliver a better representation of the reflectivity and of the scattered wavefields. We apply the method to two Gulf of Mexico field datasets: a 2D towed-streamer benchmark dataset and a 3D ocean-bottom node dataset. We show the LSRTM resolution improvement relative to RTM images, as well as the superior convergence rate obtained by the linearized modeling and migration operators based on the energy norm, coupled with inversion preconditioning using image-domain non-stationary matching filters.

4.1 Introduction

Wavefield migration delivers an image of the subsurface structures using wavefield extrapolation methods (Sun et al., 2003; Biondi, 2012). For complex geological settings, the two-way wave equation is generally used for extrapolation and the migration procedure is known as reverse-time migration (RTM) (Baysal et al., 1983; McMechan, 1983; Lailly, 1983;

* Reprinted with permission of *Geophysics*, Vol. 83, No 3 (May-June 2018), pp. S261-S270
** Corresponding author. Direct correspondence to drocha@mines.edu
[1] Center for Wave Phenomena, Colorado School of Mines, 924 16th St., Golden, CO 80401
[2] DownUnder GeoSolutions (America) LLC, 16200 Park Row Dr. #100, Houston, TX 77084

Levin, 1984; Zhang and Sun, 2009). In practice, however, data recording are always incomplete and possibly aliased and irregular, causing wavefield migration to degrade image quality and resolution especially for greater depths (Zhang et al., 2015). In addition, the obtained image does not fully explain data at receiver locations because migration represents the adjoint operator of single-scattering modeling, and therefore it is not a good approximation of the inverse operator that correctly reverses propagation of seismic data (Claerbout, 1992).

Considering these imaging quality issues, least-squares migration (LSM) is proposed to deliver images with more accurate amplitudes, illumination compensation, and reduced footprint of the acquisition geometry (Chavent and Plessix, 1999; Nemeth et al., 1999; Kuehl and Sacchi, 2003; Aoki and Schuster, 2009). If the RTM engine is used for migration, the method is called least-squares reverse-time migration (LSRTM) (Dai et al., 2010; Yao and Jakubowicz, 2012; Dai and Schuster, 2012; Dong et al., 2012). Least-squares migration involves a forward operator (single-scattering modeling), an adjoint operator (migration), and an objective function which work together to achieve an image that best explains in a least-square sense the reflection data acquired at receivers. The objective function has the role of comparing modeled data with observed data using the image as reflectivity. In order to achieve the least-squares solution, we employ efficient gradient methods that decrease the objective function iteratively (Hestenes and Stiefel, 1952; Scales, 1987).

Because of the high computational cost of LSRTM, which is at least an order of magnitude higher than RTM, techniques that expedite LSRTM convergence towards the true reflectivity model lead to reduction in computational cost while also achieving a satisfying solution in fewer iterations. For instance, a common procedure to obtain faster rates of convergence is to use an approximate of the Hessian operator (Aoki and Schuster, 2009; Tang, 2009; Dai et al., 2010; Kazemi and Sacchi, 2014, 2015; Huang et al., 2016b; Hou and Symes, 2016). Here, we demonstrate that modeling and migration operators based on an imaging condition that delivers more accurate amplitudes and attenuates artifacts, such as the one derived

from the energy norm (Douma et al., 2010; Whitmore and Crawley, 2012; Brandsberg-Dahl et al., 2013; Pestana et al., 2013; Rocha et al., 2016a) also expedites convergence. This migration operator attenuates low-wavenumber artifacts, delivering a better representation of subsurface reflectivity. The corresponding modeling operator uses spatial and temporal derivatives based on the wave equation itself to generate scattered wavefields from the energy image. We also incorporate preconditioning with an approximation of the Hessian operator in our inversion, which expedites LSRTM convergence even more. This approximation of the Hessian is achieved by a non-stationary multidimensional filter that corrects the blurring effect in the image caused by the wavefield modeling and migration operators (Guitton, 2004; Aoki and Schuster, 2009; Fletcher et al., 2016).

4.2 Theory

We can define acoustic wavefield migration as an operator such that

$$\mathbf{m}_0 = \mathbf{L}^{\mathrm{T}} \mathbf{d}_r^{\mathrm{obs}} \ , \tag{4.1}$$

where $\mathbf{L}^{\mathrm{T}}$ is the migration operator based on some imaging condition, $\mathbf{d}_r^{\mathrm{obs}}$ is single-scattered data observed at receiver locations, and $\mathbf{m}_0$ is an image (an estimate of the earth reflectivity). The operator $\mathbf{L}^{\mathrm{T}}$ involves back-propagation of $\mathbf{d}_r^{\mathrm{obs}}$ through an earth model, thus generating a receiver wavefield $\mathbf{u}_r$, and the application of an imaging condition comparing $\mathbf{u}_r$ with the source wavefield $\mathbf{u}_s$. The migration operator is the adjoint operator of single-scattering modeling (or commonly known as linearized modeling). Therefore, $\mathbf{L}$ is a linear operator such that

$$\mathbf{d}_r = \mathbf{L}\mathbf{m} \ , \tag{4.2}$$

and simulates single-scattered data $\mathbf{d}_r$ at receiver locations using an image containing reflectors that act as sources under the action of the source wavefield $\mathbf{u}_s$.

Therefore, we define $\mathbf{m}$ as reflectivity that depends on a certain imaging condition and is not necessarily defined in terms of contrasts in the earth model. The same principle applies to the linearized modeling operator $\mathbf{L}$, which we define as an adjoint operator to a certain

imaging condition, and this operator is not directly related to the physics of single scattering.

4.2.1 Conventional imaging condition and linearized modeling

The conventional imaging condition is defined as the zero-lag cross-correlation between source and receiver wavefields $\mathbf{u}_s$ and $\mathbf{u}_r$:

$$\mathbf{m}_0 = \mathbf{u}_s^{\mathrm{T}} \mathbf{u}_r \ . \tag{4.3}$$

Since we know both wavefields are generated by extrapolation using an earth model and observed data at receivers, we can rewrite equation 4.3 as

$$\mathbf{m}_0 = \left(\mathbf{E}_+ \mathbf{K}_s \mathbf{d}_s\right)^{\mathrm{T}} \mathbf{E}_- \mathbf{K}_r \mathbf{d}_r^{\mathrm{obs}} \ , \tag{4.4}$$

where $\mathbf{E}_+$ and $\mathbf{E}_-$ are forward and backward extrapolator operators, $\mathbf{K_s}$ and $\mathbf{K_r}$ are source and receiver injection operators (see Appendix 4.7.1), respectively, and $\mathbf{d}_s$ is the source function. The subscripts in the extrapolator operators indicate extrapolation direction for either positive $(+)$ or negative $(-)$ times. Note two important relations between the extrapolator operators: $\mathbf{E}_+ = \mathbf{E}_-^{\mathrm{T}}$ and $\mathbf{E}_- = \mathbf{E}_+^{\mathrm{T}}$. Then, one can write equation 4.4 similarly to equation 4.1:

$$\mathbf{m}_0 = \mathbf{L}^{\mathrm{T}} \mathbf{d}_r^{\mathrm{obs}} \ , \tag{4.5}$$

where

$$\mathbf{L}^{\mathrm{T}} = \left(\mathbf{E}_+ \mathbf{K}_s \mathbf{d}_s\right)^{\mathrm{T}} \mathbf{E}_- \mathbf{K}_r \ . \tag{4.6}$$

We can obtain the operator $\mathbf{L}$ (adjoint of $\mathbf{L}^{\mathrm{T}}$) if we apply the adjoint for each individual operator and reverse the order of operators. Therefore, conventional linearized modeling is defined as

$$\mathbf{d}_r = \mathbf{L}\mathbf{m} \ , \tag{4.7}$$

where

$$\mathbf{L} = \mathbf{K}_r^{\mathrm{T}} \mathbf{E}_+ \left(\mathbf{E}_+ \mathbf{K}_s \mathbf{d}_s\right) = \mathbf{K}_r^{\mathrm{T}} \mathbf{E}_+ \mathbf{u}_s \ . \tag{4.8}$$

In other words, single-scattered data $\mathbf{d}_r$ are obtained by extraction at the receiver locations ($\mathbf{K}_r^{\mathrm{T}}$), and wavefield extrapolation ($\mathbf{E}_+$) using $\mathbf{u}_s\mathbf{m}$ as the source term.

4.2.2 Energy imaging condition and linearized modeling

For an extrapolated wavefield that satisfies the acoustic wave equation, we can compute its energy norm in discretized space and time as (Rocha et al., 2016a)

$$\|\mathbf{u}\|_E^2 = \sum_{\mathbf{x},t} \left[\frac{\dot{\mathbf{u}}^2}{v^2(\mathbf{x})} + |\nabla \mathbf{u}|^2 \right] , \tag{4.9}$$

where $v(\mathbf{x})$ is the migration velocity, superscript dot indicates time differentiation, and ∇ is the spatial gradient. On the right-hand side of equation 4.9, the first term inside the brackets corresponds to the kinetic energy of the wavefield, and the second term corresponds to its potential energy. Based on this norm, we can define an imaging condition that ignores wave events between source and receiver wavefields that share the same propagation direction, thus suppressing low-wavenumber artifacts in reverse-time migration that do not characterize subsurface reflectivity:

$$\mathbf{m}_0(\mathbf{x}) = \sum_t \left[\frac{\dot{\mathbf{u}}_s \dot{\mathbf{u}}_r}{v^2} - \nabla \mathbf{u}_s \cdot \nabla \mathbf{u}_r \right] . \tag{4.10}$$

A more compact form of equation 4.10 utilizes the energy operator

$$\square = \left\{ \nabla, \frac{1}{v(\mathbf{x})} \frac{\partial}{\partial t} \right\} , \tag{4.11}$$

which computes a four-dimensional vector field from the scalar wavefield. A negative time derivative is implied for the back-propagated receiver wavefield $\mathbf{u}_r$. If we compute the dot product between such vector fields obtained from source and receiver wavefields at each spatial location (implying summation over time), we can rewrite equation 4.10 as

$$\mathbf{m}_0 = (\square \mathbf{u}_s)^{\mathrm{T}} \square \mathbf{u}_r . \tag{4.12}$$

Using the operators introduced in equation 4.4, equation 4.12 becomes

$$\mathbf{m}_0 = (\square \mathbf{E}_+ \mathbf{K}_s \mathbf{d}_s)^{\mathrm{T}} \square \mathbf{E}_- \mathbf{K}_r \mathbf{d}_r^{\mathrm{obs}} . \tag{4.13}$$

Since equation 4.13 is a function of $\mathbf{d}_r$, we can write the corresponding migration operation as

$$\mathbf{m}_0 = \mathbf{L}^{\mathrm{T}} \mathbf{d}_r^{\mathrm{obs}} \ , \tag{4.14}$$

where

$$\mathbf{L}^{\mathrm{T}} = \left(\square \mathbf{E}_+ \mathbf{K}_s \mathbf{d}_s\right)^{\mathrm{T}} \square \mathbf{E}_- \mathbf{K}_r \ . \tag{4.15}$$

Therefore, the linearized modeling operation based on the energy norm is defined as

$$\mathbf{d}_r = \mathbf{L}\mathbf{m} \ , \tag{4.16}$$

where

$$\mathbf{L} = \mathbf{K}_r^{\mathrm{T}} \mathbf{E}_+ \square^{\mathrm{T}} \square \left(\mathbf{E}_+ \mathbf{K}_s \mathbf{d}_s\right) = \mathbf{K}_r^{\mathrm{T}} \mathbf{E}_+ \square^{\mathrm{T}} \square \mathbf{u}_s \ . \tag{4.17}$$

In other words, single-scattered data $\mathbf{d}_r$ are obtained by extraction at the receiver locations ($\mathbf{K}_r^{\mathrm{T}}$), and wavefield extrapolation ($\mathbf{E}_+$) with $\square^{\mathrm{T}} \square \mathbf{u}_s \mathbf{m}$ as the source term, which for a point in space and time can explicitly be written as

$$\left[\square^{\mathrm{T}} \square \mathbf{u}_s \mathbf{m}\right](\mathbf{x}, t) = \frac{\mathbf{m}(\mathbf{x})}{v^2(\mathbf{x})} \ddot{\mathbf{u}}_s(\mathbf{x}, t) - \nabla \cdot \left[\mathbf{m}(\mathbf{x}) \nabla \mathbf{u}_s(\mathbf{x}, t)\right] \ , \tag{4.18}$$

The same procedure to find a proper adjoint operator is applicable to other imaging conditions. For instance, applying a Laplacian operator on a conventional image is theoretically equivalent to the application of the energy imaging condition but in the far field (Douma et al., 2010). Knowing that the Laplacian operator is self-adjoint, the imaging condition with Laplacian filtering can be written as

$$\mathbf{m}_0 = \nabla^2 \mathbf{u}_s^{\mathrm{T}} \mathbf{u}_r \ . \tag{4.19}$$

The corresponding linearized modeling is written as

$$\mathbf{d}_r = \mathbf{L}\mathbf{m} \ , \tag{4.20}$$

where

$$\mathbf{L} = \mathbf{K}_r^{\mathrm{T}} \mathbf{E}_+ \left(\mathbf{E}_+ \mathbf{K}_s \mathbf{d}_s\right) \nabla^2 = \mathbf{K}_r^{\mathrm{T}} \mathbf{E}_+ \mathbf{u}_s \nabla^2 \ . \tag{4.21}$$

The source term for this case is $\mathbf{u}_s\nabla^2\mathbf{m}$ and can explicitly be written for each point in space and time as

$$\left[\mathbf{u}_s\nabla^2\mathbf{m}\right](\mathbf{x},t) = \mathbf{u}_s(\mathbf{x},t)\,\nabla^2\mathbf{m}\ . \tag{4.22}$$

4.2.3 Least-squares migration and preconditioning with an approximation of the Hessian

A pair of linearized modeling and migration operators enables us to compute an image that minimizes the L_2 norm of the difference between observed and modeled data:

$$E(\mathbf{m}) = \frac{1}{2}\|\mathbf{L}\mathbf{m} - \mathbf{d}_r^{\text{obs}}\|^2\ , \tag{4.23}$$

and such image is mathematically described by

$$\mathbf{m}^{\text{LS}} = \left(\mathbf{L}^{\text{T}}\mathbf{L}\right)^{-1}\mathbf{L}^{\text{T}}\mathbf{d}_r^{\text{obs}}\ . \tag{4.24}$$

To find $\mathbf{m}^{\text{LS}}$, one generally employs iterative procedures that exploit the direction of the gradient of the objective function in equation 4.23 at a given iteration i:

$$\mathbf{g}_i = \frac{\partial E(\mathbf{m}_i)}{\partial \mathbf{m}_i} = \mathbf{L}^{\text{T}}\left(\mathbf{L}\mathbf{m}_i - \mathbf{d}_r^{\text{obs}}\right)\ , \tag{4.25}$$

and the model update at each iteration in steepest descent and conjugate gradient methods is a scaled version of the gradient

$$\mathbf{m}_{i+1} = \mathbf{m}_i - \alpha\mathbf{g}_i\ , \tag{4.26}$$

In equation 4.24, the term $\mathbf{L}^{\text{T}}\mathbf{L}$ is known as the Hessian operator of $E(\mathbf{m})$. If the inverse of the Hessian is applied to the RTM image $\mathbf{L}^{\text{T}}\mathbf{d}_r^{\text{obs}}$, the least-squares solution is achieved. However, in practice, the Hessian operator cannot explicitly be computed for least-squares migration problems. As suggested by Guitton (2004), we can obtain an approximation of the Hessian operator if we compute an image

$$\mathbf{m}_1 = \mathbf{L}^{\text{T}}\mathbf{L}\mathbf{m}_0\ , \tag{4.27}$$

where $\mathbf{m}_0 = \mathbf{L}^{\text{T}}\mathbf{d}_r^{\text{obs}}$ is the standard RTM image. The operator $\mathbf{B}$ that minimizes

$$E(\mathbf{B}) = \|\mathbf{m}_0 - \mathbf{B}\mathbf{m}_1\|^2\ , \tag{4.28}$$

is a good approximation of the inverse of the Hessian $\left(\mathbf{L}^{\mathrm{T}}\mathbf{L}\right)^{-1}$ according to equation 4.27. Here, we define the operator $\mathbf{B}$ as a multidimensional convolutional operator along all spatial axes (Rickett et al., 2001).

Once we obtain the approximation of the inverse of the Hessian, we can expedite convergence in least-squares inversion by preconditioning the gradient with the operator $\mathbf{B}$ before updating the model at each iteration. Incorporating the preconditioning, equation 4.26 becomes

$$\mathbf{m}_{i+1} = \mathbf{m}_i - \alpha \mathbf{B} \mathbf{g}_i \ , \tag{4.29}$$

4.3 Examples

In order to show how LSRTM with proper imaging operators can get faster convergence rates relative to conventional methods, we perform a LSRTM experiment using a 2D Gulf of Mexico (GOM) dataset, used by many authors in the past as a benchmark dataset (Dragoset, 1999; Guitton and Cambois, 1999; Hadidi et al., 1999; Lamont et al., 1999; Lokshtanov, 1999; Verschuur and Prein, 1999), and described by Guitton et al. (2012). Such 2D dataset is useful to test the capability of the energy imaging operators in attenuating low-wavenumber artifacts caused by strong velocity contrasts (such as a salt body), and to benchmark our inversion procedure before application to a larger 3D dataset. Standard pre-processing is applied to the dataset prior to LSRTM, such as surface-related multiple suppression. We use 71 of the original 1001 shot records, with the first source location at $x = 4000$m and the last at $x = 22670$m, resulting in a source spacing of approximately 267m. The shot decimation decreases the computational cost of the entire experiment but also introduces truncation artifacts, which are useful to test the effectiveness of the proposed LSRTM in attenuating acquisition artifacts. Each shot record contains 180 traces with receiver spacing of 26.67m and a maximum offset of 4874m. For migration, we use a maximum frequency of 40Hz and a spatial sampling of 6.67m. A standard RTM migration (Figure 4.1(a)) exhibits

low-wavenumber artifacts and poor illumination in the subsalt area. We test two alternative LSRTMs, one using modeling and migration with the Laplacian operator (equations 4.19 and 4.21), and the other based on the energy norm (equations 4.15 and 4.17). For this experiment, the final images from the Laplacian and energy LSRTMs are similar in quality and resolution, and we show the final energy LSRTM image in Figure 4.1(b), which contains suppressed low-wavenumber artifacts above the salt body as compared to the conventional image in Figure 4.1(a). Also, the objective functions (Figure 4.1(c)) of both alternative LSRTMs decrease faster than the one from conventional LSRTM, with the one based on the energy norm decreasing slightly faster when compared to its Laplacian counterpart. Although the two alternative LSRTM implementations are theoretically equivalent far from the source and receiver locations, one computes the imaging condition in the image domain and the other in the wavefield domain, leading to slightly different numerical implementations and, therefore, convergence performances. The energy migration and modeling operators applied either in the wavefield domain (equation 4.18) or in the image domain as a Laplacian operator provide faster convergence rates towards the final reflectivity model.

We apply our method to a 3D ocean-bottom node (OBN) dataset from the Gulf of Mexico. We process the dataset to obtain only the down-going pressure component and perform mirror imaging (Godfrey et al., 1998; Ronen et al., 2005; Wong et al., 2010, 2015) of shallow geological structures with a fine spatial sampling of 12.5m. We use 37 node gathers with sources densely distributed at the water surface (Figure 4.2(a)), and the velocity model used is shown in Figure 4.2(b). In total, as seen in Figure 4.2(c), we perform four LSRTM experiments: conventional LSRTM, Laplacian-based LSRTM, energy-norm based LSRTM with and without preconditioning. Similarly to the preceding example, conventional LSRTM has a worse performance in terms of objective function decrease, and the energy LSRTM has a slightly smaller objective function value over iterations compared to its Laplacian counterpart. We compute the matching filter for the preconditioning using the energy RTM image ($\mathbf{m}_0 = \mathbf{L}^{\mathrm{T}}\mathbf{d}_r^{obs}$) and an image generated by $\mathbf{m}_1 = \mathbf{L}^{\mathrm{T}}\mathbf{L}\mathbf{m}_0$, where the modeling ($\mathbf{L}$)

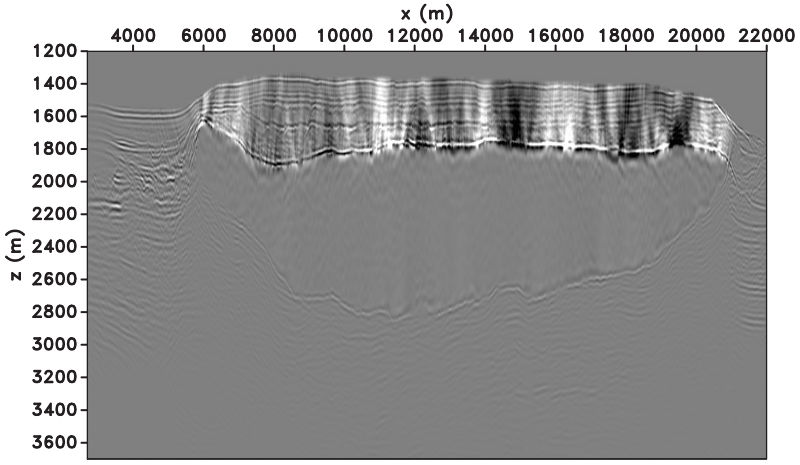

(a)

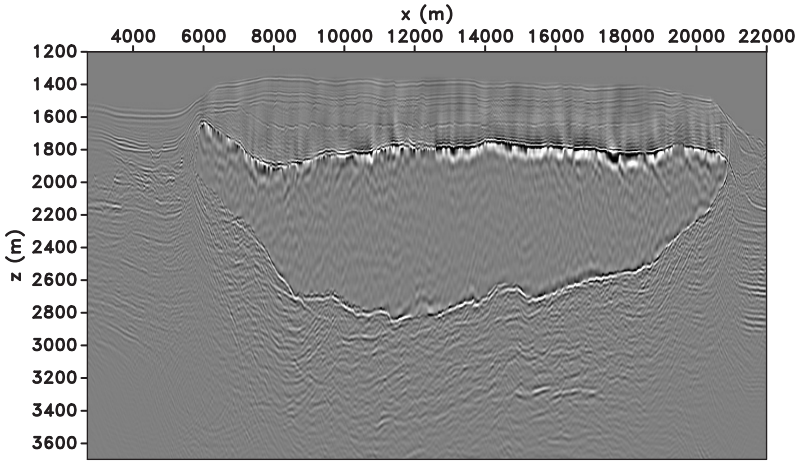

(b)

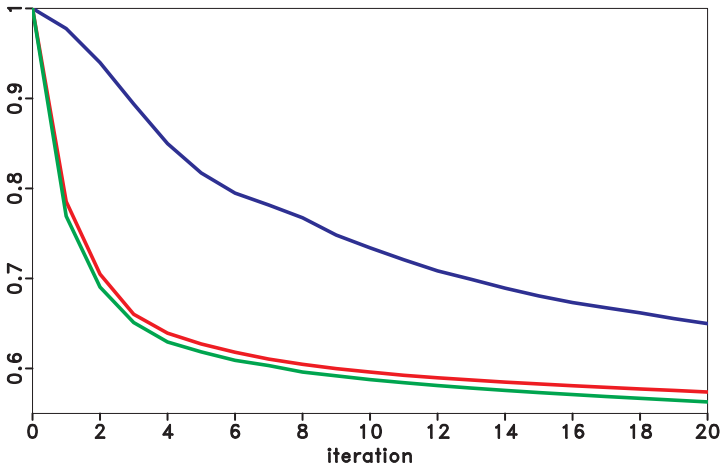

(c)

Figure 4.1: GOM 2D dataset: (a) conventional RTM image and (b) LSRTM image with the energy modeling and migration operators. (c) Normalized objective functions for conventional LSRTM (blue), LSRTM with Laplacian (red) and based on the energy norm (green). Note suppression of low-wavenumber artifacts above the salt and the convergence speed-up obtained by the alternative LSRTMs.

and migration ($\mathbf{L}^{\mathrm{T}}$) operators are based on the energy norm. We use the preconditioning at the two first iterations and switch it off at the second iteration (solid black and green lines in Figure 4.2(c)), because the computed matching filter is related to the images at the first and second iterations ($\mathbf{m}_0$ and $\mathbf{m}_1$). The matching filter is biased toward the strong amplitude changes between such images at first iterations, and keeping preconditioning on does not give substantial benefit to the inversion at later iterations, thus only increasing computational cost. Although we apply the preconditioning only at the first iterations, we obtain a significant speed-up in the convergence rate over all subsequent iterations.

For two different areas of the migration volume, the depth slices in Figure 4.3 compare RTM, conventional LSRTM, and the proposed LSRTM that utilizes energy imaging operators and preconditioning. Although conventional LSRTM fits less data and has the worst convergence rate based on Figure 4.2(c), it delivers images closer in quality to the proposed LSRTM images (Figures 4.3(e) and 4.3(f)). In these depth slices, some imaged events that seem to disappear or become blurry after LSRTM might indicate that they do not correctly predict reflection events in the data domain, considering our imaging operator is isotropic and acoustic. Figure 4.4 compares RTM and the proposed LSRTM cross-section images side-by-side, and shows the visual benefit due to the increase in illumination and frequency content (especially towards low frequencies) in the LSRTM image. To confirm the increase in bandwidth for the depth slices, we transform the images from Figure 4.3 to the wavenumber domain and obtain the spectral images in Figure 4.5. Note how LSRTM recovers high resolution content by spreading the amplitudes towards the edges of the wavenumber domain. However, one needs to consider that some recovered high-wavenumber content might emerge from noise existent in the data.

As discussed in the theory section, one of the benefits in LSRTM is to suppress acquisition footprint. In some shallow areas of the migration volume, very close to the edges of the model and to the water bottom, imaging artifacts exist in the RTM image due to the large decimation of nodes for this experiment (from 924 to 37 nodes, causing nodes to be

quite sparse as seen in Figure 4.2(a)) and the irregularity of source and receiver locations with respect to the regular extrapolation grid. Figure 4.6 shows an example: LSRTM (Figure 4.6(b)) attenuates some of these acquisition footprint artifacts at the water bottom from the RTM image (Figure 4.6(a)). Figure 4.7 compares observed and predicted data at the last iteration, and the difference (residual) between the two for a gather of traces sorted by increasing offset at a particular node location ($x = 214.5$km, $y = 44.9$km). Note that the main reflections at near- and mid-offsets are correctly predicted, but the far-offset amplitudes are not matched mainly because of elasticity and anisotropy, which are not counted for by our acoustic imaging operators. As expected, the residual in 4.7(c) still exhibits noise, such as a large dipping event that goes from $t = 2.2$s at trace 0 to $t = 3.0$s at trace 10000. In summary, with a number of iterations corresponding to an order of magnitude of the standard RTM computational cost, we obtain LSRTM images that exhibit more focused diffractions and delineated structures, as shown by the depth slices in Figure 4.3.

4.4 Discussion

The main advantage of our method when compared to conventional LSRTM is accelerated convergence to an optimal solution, as seen in Figures 4.1(c) and 4.2(c). The energy imaging better recovers the reflector amplitudes and scattered wavefields, resulting in a closer match between observed and simulated data. Second-order factors accountable for the decrease of the objective function include the mitigation of imaging artifacts and sharper focusing of events, and both of these improvements are similar between energy (Figures 4.3(e) and 4.3(f)) and conventional (Figures 4.3(c) and 4.3(d)) LSRTM images.

In terms of computational cost, the energy LSRTM does not add significant burden. During extrapolation of source and receiver wavefields, the same finite-difference differential operators applied at each time step of wave extrapolation can also be applied to compute the terms required for the image (equation 4.10) or for the linearized source term (equation 4.18). In case these operators cannot be efficiently applied to the wavefields (e.g., insufficient memory storage for additional wavefield variables), the Laplacian-based imaging

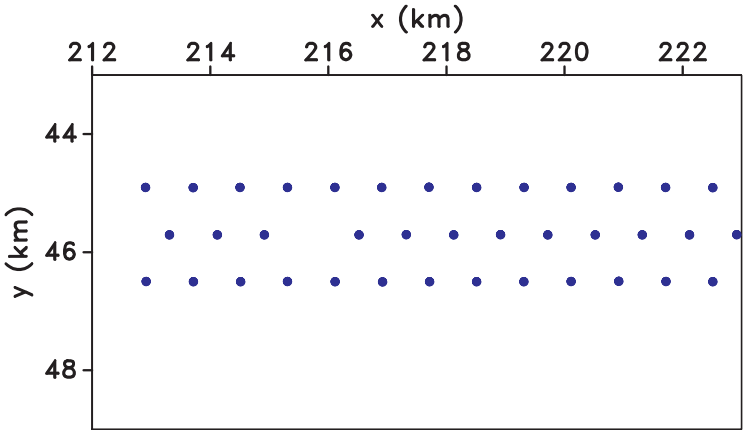

(a)

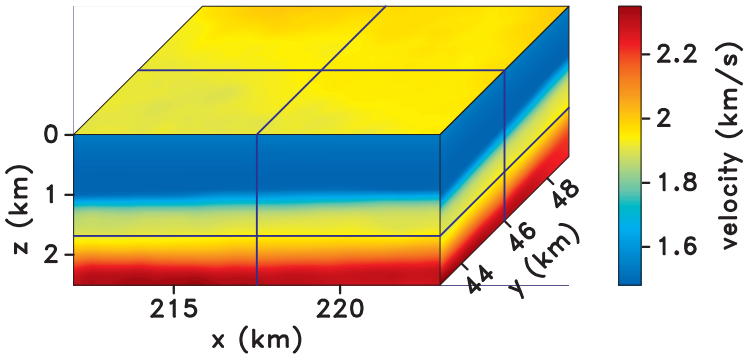

(b)

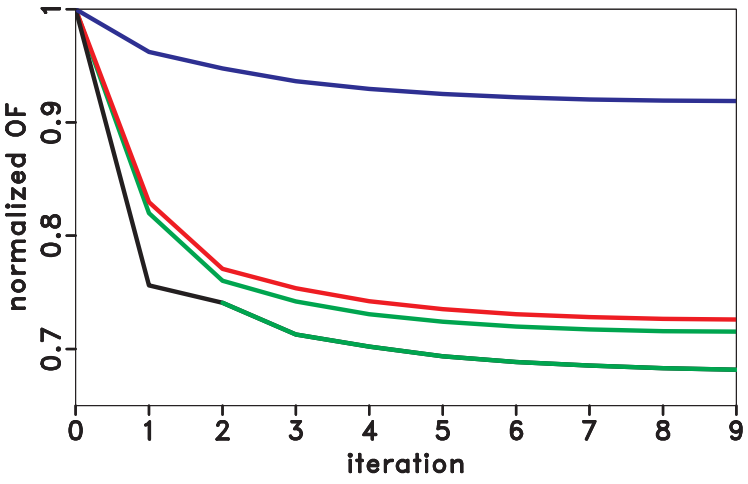

(c)

Figure 4.2: GOM 3D dataset: (a) 37 nodes spaced by approximately 800m, and sources densely distributed at the surface of the model. (b) Velocity model. (c) Normalized objective functions for conventional (blue), Laplacian-based (red), energy-based (green), and preconditioned energy-based (black and then green at iteration 2) LSRTMs. The energy LSRTM has best performance if we apply preconditioning at the first two iterations.

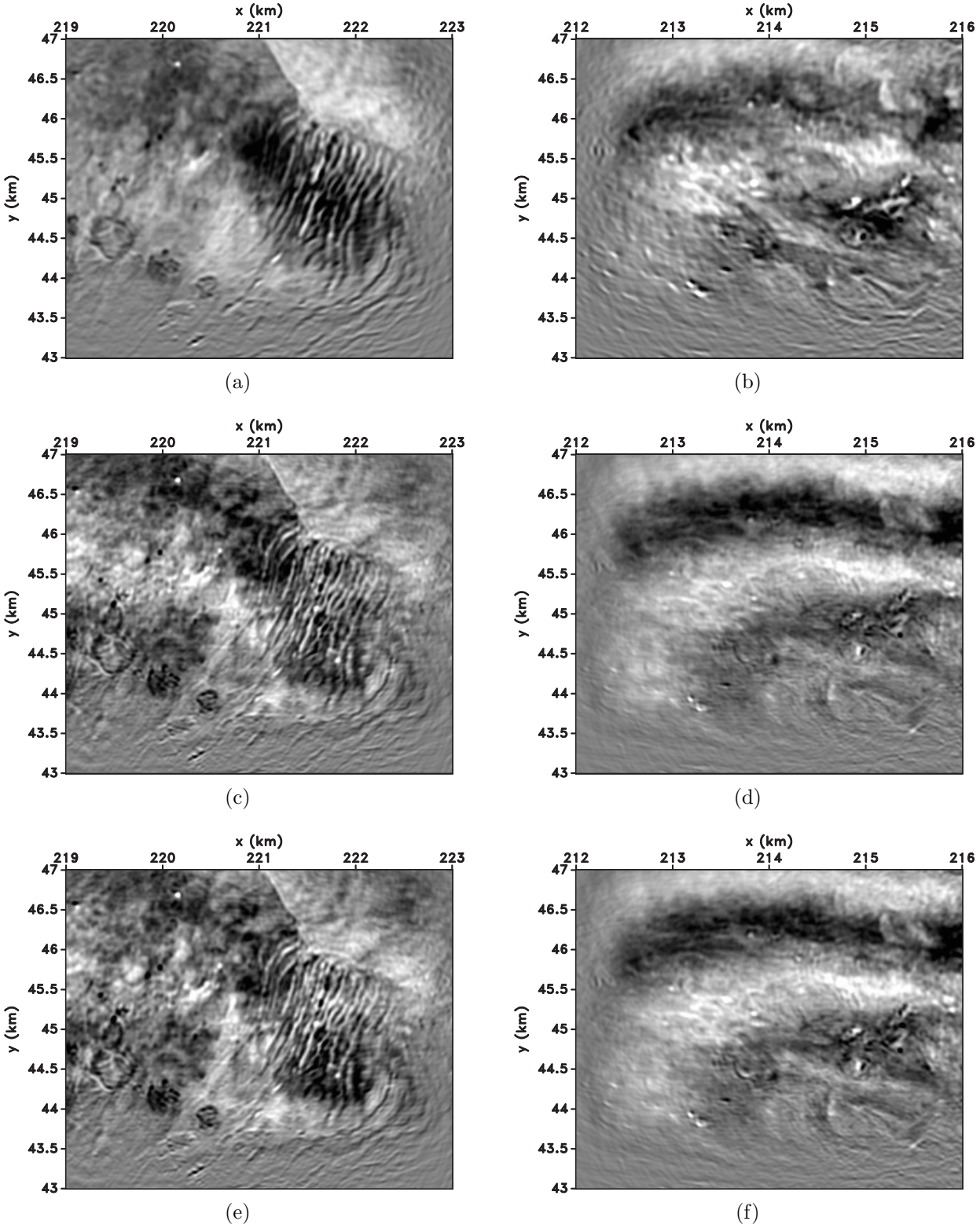

Figure 4.3: GOM 3D dataset: depth slices at $z = 1.55$km and $z = 1.77$km, respectively, for (a)/(b) RTM, (c)/(d) conventional LSRTM, and (e)/(f) energy LSRTM with preconditioning. In the LSRTM images, note the improvement in focusing of the diffractors and in delineation of the reflectors.

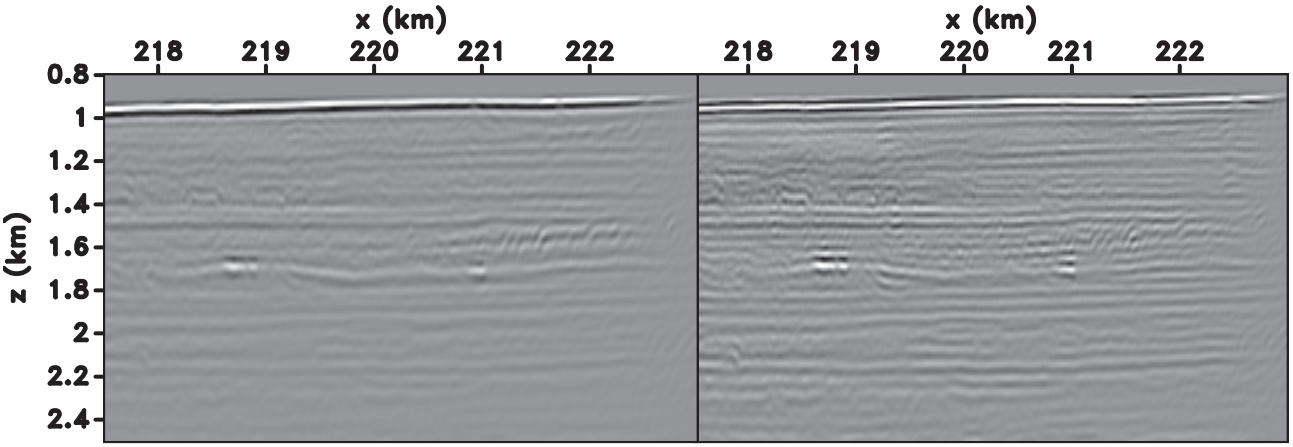

Figure 4.4: GOM 3D dataset: inline sections for energy RTM (left) and LSRTM with preconditioning (right) at $y = 44.9$km. Note the increase in frequency content and illumination for the LSRTM image compared to RTM.

operators, although only adequate for image regions away from source and receiver locations, serve as good substitutes as seen by the convergence plots in Figures 4.1(c) and 4.2(c).

We empirically observe that the preconditioning based on the matching filters benefit the first two iterations only (Figure 4.2(c)). This effect can be explained analytically by the fact that the least-squares solution of the filter estimation problem is

$$\hat{\mathbf{B}} = \left(\mathbf{M}_1^{\mathrm{T}}\mathbf{M}_1\right)^{-1}\mathbf{M}_1^{\mathrm{T}}\mathbf{M}_0 \;, \tag{4.30}$$

where

$$\mathbf{M}_1 = \mathbf{L}^{\mathrm{T}}\mathbf{L}\mathbf{M}_0 \tag{4.31}$$

is the non-stationary convolutional operator using the entries of $\mathbf{m}_1$. Similarly, $\mathbf{M}_0$ is the corresponding convolutional operator for $\mathbf{m}_0$. Substituting equation 4.31 into equation 4.30 yields

$$\hat{\mathbf{B}} = \left(\mathbf{M}_0^{\mathrm{T}}\mathbf{L}^{\mathrm{T}}\mathbf{L}\mathbf{L}^{\mathrm{T}}\mathbf{L}\mathbf{M}_0\right)^{-1}\mathbf{M}_0^{\mathrm{T}}\mathbf{L}^{\mathrm{T}}\mathbf{L}\mathbf{M}_0 \;, \tag{4.32}$$

which shows that the filters can be seen as a least-squares estimate of the inverse Hessian operator $\left(\mathbf{L}^{\mathrm{T}}\mathbf{L}\right)^{-1}$, left- and right-multiplied by the convolutional operator $\mathbf{M}_0$. There is, therefore, an influence of the starting image $\mathbf{m}_0$ to the approximate inverse Hessian. In

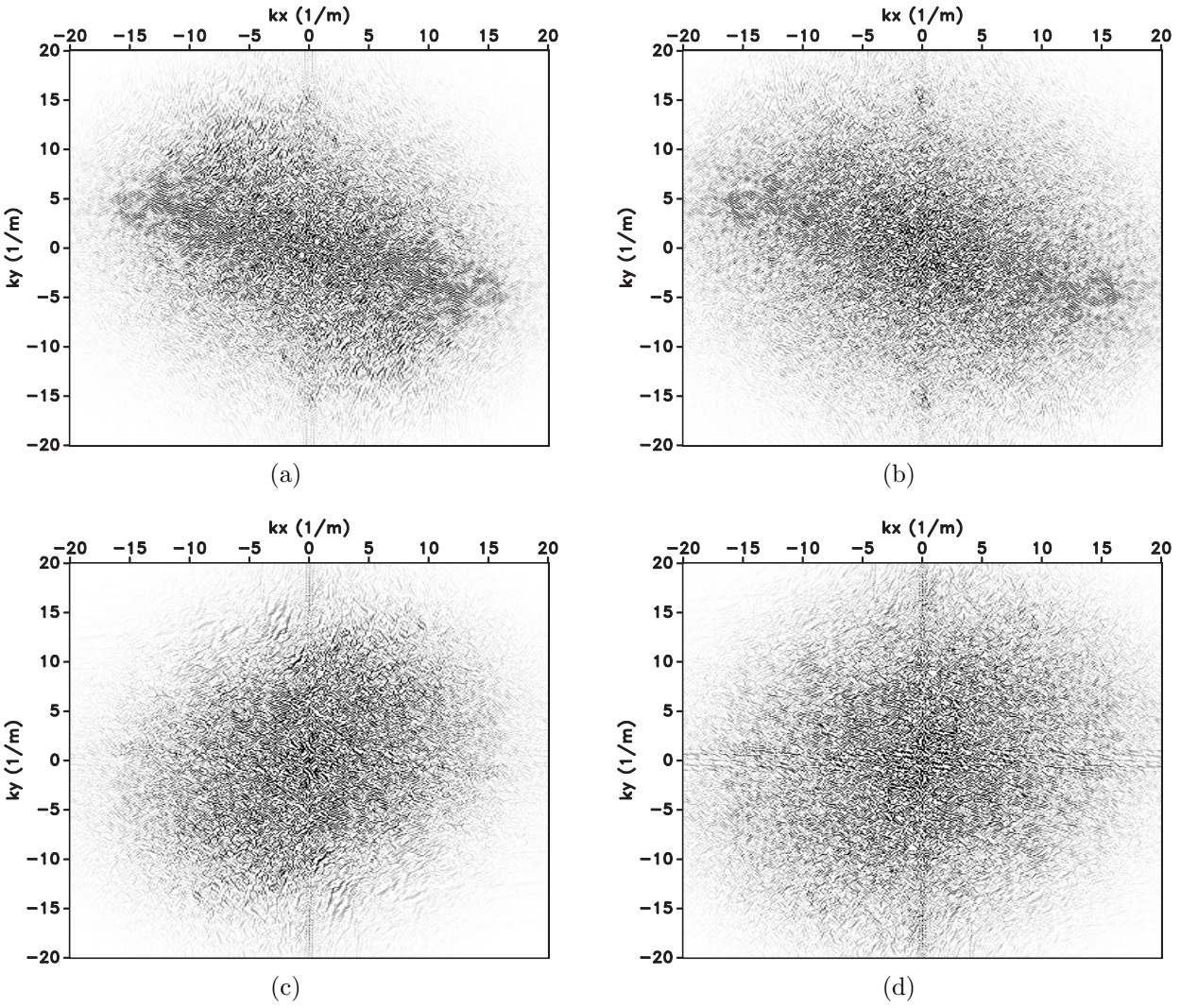

Figure 4.5: GOM 3D dataset: wavenumber-domain RTM (a)/(c) and energy LSRTM (b)/(d) images from Figure 4.3 (at $z = 1.55$km and $z = 1.77$km, respectively). Note the stronger amplitudes recovered by LSRTM at the high wavenumbers (near the corners of the plot).

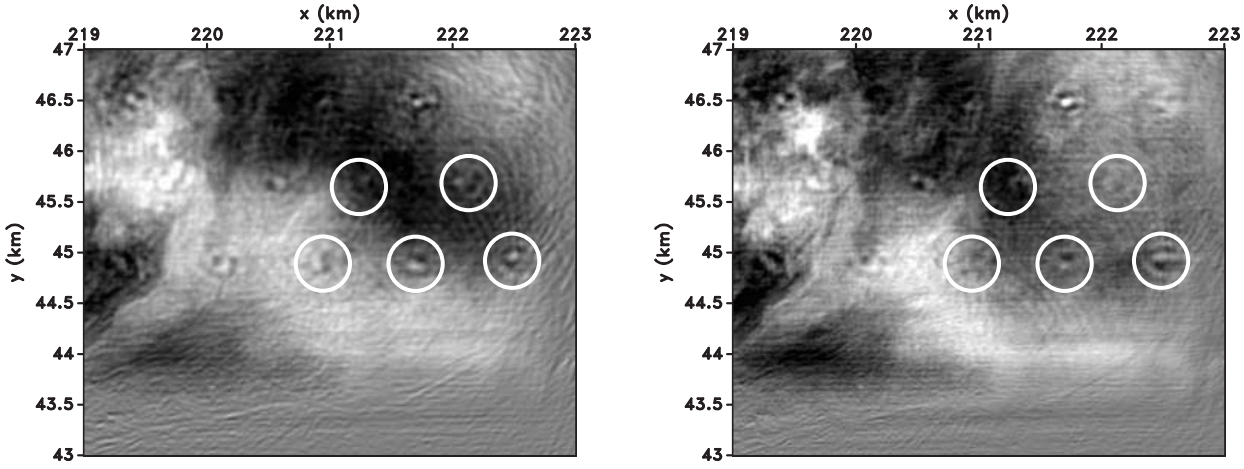

(a) (b)

Figure 4.6: GOM 3D dataset: depth slices for RTM (left) and LSRTM (right) at the water bottom ($z = 1.20$km). Note the artifact suppression in some locations indicated by the white circles.

effect, the matching filters are a very good approximation of the operator taking us between the vectors $\mathbf{m}_0$ and $\mathbf{m}_1$ of the Krylov subspace generated by $\mathbf{L}^{\mathrm{T}}\mathbf{L}$ only (and used in the first two iterations of the conjugate gradient method). Beyond these two iterations, the matching filters do not provide any benefit anymore and switching to a non-preconditioned inversion proves the most effective strategy (as illustrated in Figure 4.2(c)). Guitton (2017) also exemplifies this point on 3D synthetic and field data cases. As possible improvements, but not tested here, one could re-estimate the matching filters as the iterations go on, or find different reference images $\mathbf{m}_0$ and $\mathbf{m}_1$ for the filter estimation step.

Alternatively, our LSRTM preconditioning with matching filters can be implemented using point-spread functions (PSFs) (Fletcher et al., 2016). In our case, this approach involves creating a reference image $\mathbf{m}_0$ with spikes regularly spaced, and then computing $\mathbf{m}_1$ after linearized modeling and migration of the reference image with spikes ($\mathbf{m}_0$). However, spike spacing parameterization involves an inherent trade-off between fine and coarse sampling. Too much fine sampling causes an overlap of the blurred events, thus undermining our ability to accurately extract the PSFs, and too much coarse does not capture enough the subsurface

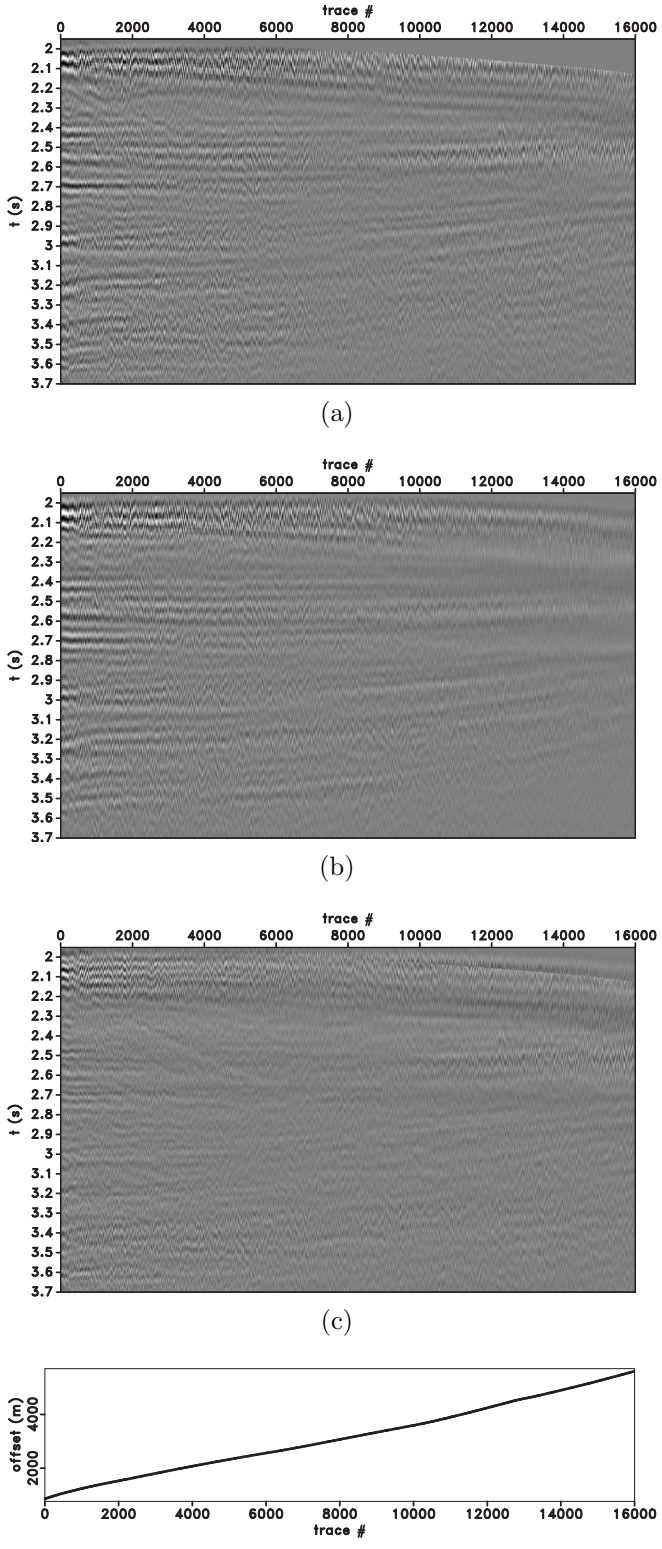

Figure 4.7: GOM 3D dataset: Node gather at $x = 214.5$km and $y = 44.9$km sorted by increasing offset: (a) observed, final (b) predicted and (c) residual data. (d) Offset values for each trace. Note that the main reflection events are predicted and eliminated in the data residual, especially for events at near- and mid-offsets. Linear moveout is applied on these plots for display purposes.

structure details. In addition, this approach requires a robust interpolation of the matching filter for image samples away from the spikes. Therefore, we do not use this alternative approach for the computation of the matching filters.

4.5 Conclusions

We demonstrate that using proper linearized modeling and migration operators expedites LSRTM, which otherwise suffers from high computational cost. We test modeling and migration operators based on the energy norm, and we obtain faster convergence rates for LSRTM inversion, since the energy operators attenuate artifacts that do not properly characterize subsurface reflectivity. In addition, a preconditioning operator that utilizes a multidimensional non-stationary matching filter decreases the objective function substantially at the first iterations, allowing a significant speed-up for the following iterations. Our field data examples show significant image quality improvement within less than 10 inversion iterations by using an accelerated LSRTM compared to regular RTM.

4.6 Acknowledgments

We thank the sponsors of the Center for Wave Phenomena, whose support made this research possible. We are grateful to Shell Exploration and Production Company for sharing the 3D Gulf of Mexico dataset with Colorado School of Mines, and their permission to publish the results using this dataset. The authors appreciate the constructive comments from the anonymous reviewers of this paper. The reproducible numeric examples in this paper use the Madagascar open-source software package (Fomel et al., 2013) available at http://www.ahay.org.

4.7 Appendices

The appendices below elucidate specific points of this current chapter.

4.7.1 Conventional migration and modeling operators

For source and receiver wavefields $\mathbf{u}_s(\mathbf{x},t)$ and $\mathbf{u}_r(\mathbf{x},t)$, an image $\mathbf{m}_0(\mathbf{x})$ is conventionally obtained by

$$\mathbf{m}_0 = \mathbf{u}_s^{\mathrm{T}}\mathbf{u}_r \ . \tag{4.33}$$

We can represent equation 4.33 and the following equations pictorially using matrices, which indicate the relative dimensions of operators and variables:

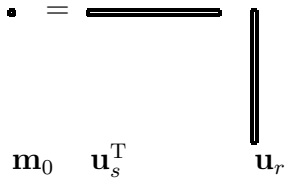

By using forward and backward extrapolator operators $\mathbf{E}_+(\mathbf{x},t)$ and $\mathbf{E}_-(\mathbf{x},t)$, and source and receiver injection operators $\mathbf{K_s}(\mathbf{x},\mathbf{x}_s,t)$ and $\mathbf{K_r}(\mathbf{x},\mathbf{x}_r,t)$, we have

$$\mathbf{m}_0 = \left(\mathbf{E}_+\mathbf{K}_s\mathbf{d}_s\right)^{\mathrm{T}}\mathbf{E}_-\mathbf{K}_r\mathbf{d}_r^{\mathrm{obs}} \ , \tag{4.34}$$

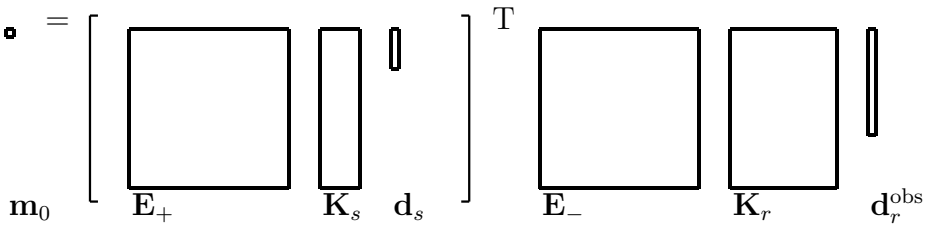

where $\mathbf{d}_s(\mathbf{x}_s,t)$ and $\mathbf{d}_r^{\mathrm{obs}}(\mathbf{x}_r,t)$ are the source and receiver data, respectively. In compact form, we can rewrite equation 4.34 as

$$\mathbf{m}_0 = \mathbf{L}^{\mathrm{T}}\mathbf{d}_r^{\mathrm{obs}} \ . \tag{4.35}$$

Linearized modeling is defined as

$$\mathbf{d}_r = \mathbf{L}\mathbf{m} \tag{4.36}$$

Based on equations 4.34 and 4.35, we can rewrite equation 4.36 as

$$\mathbf{d}_r = \mathbf{K}_r^{\mathrm{T}}\mathbf{E}_-^{\mathrm{T}}\mathbf{u}_s\mathbf{m} \ , \tag{4.37}$$

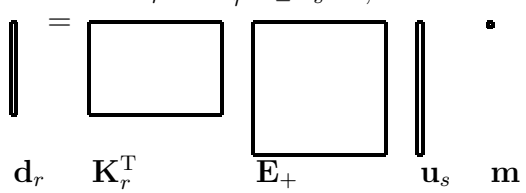

or

$$\mathbf{d}_r = \mathbf{K}_r^{\mathrm{T}} \mathbf{E}_+ \left(\mathbf{E}_+ \mathbf{K}_s \mathbf{d}_s \right) \mathbf{m} \; , \tag{4.38}$$

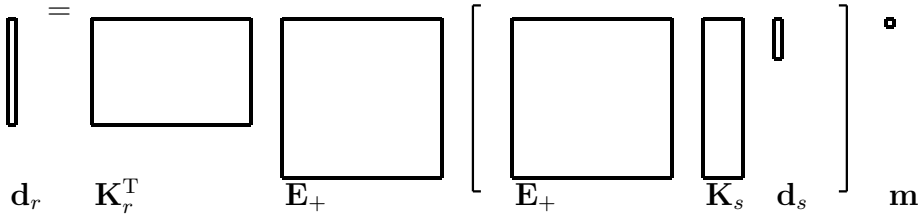

where $\mathbf{E}_-^{\mathrm{T}} = \mathbf{E}_+$, and $\mathbf{K}_r^{\mathrm{T}}$ represents the extraction at the receiver locations (adjoint operator of the injection operator).

4.7.2 Energy migration and modeling operators

The energy image $\mathbf{m}_0 \left(\mathbf{x} \right)$ is obtained by

$$\mathbf{m}_0 = \left(\square \mathbf{u}_s \right)^{\mathrm{T}} \square \mathbf{u}_r \; . \tag{4.39}$$

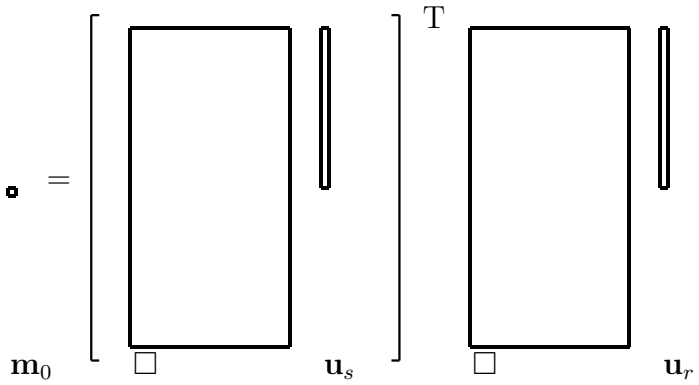

The operator $\square$ turns an acoustic wavefield into a vector field whose components are spatial and temporal. We represent this increase in dimensions pictorially by making the matrix of $\square$ considerably larger than the wavefields matrices. Using extrapolator and injection operators, we have

$$\mathbf{m}_0 = \left(\square \mathbf{E}_+ \mathbf{K}_s \mathbf{d}_s \right)^{\mathrm{T}} \square \mathbf{E}_- \mathbf{K}_r \mathbf{d}_r^{\mathrm{obs}} \; , \tag{4.40}$$

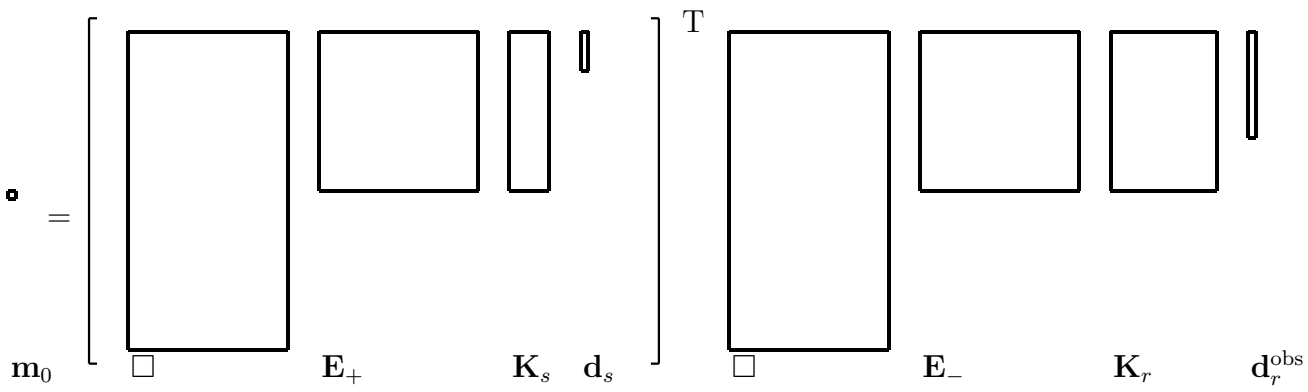

In compact form, we can rewrite equation 4.40 as

$$\mathbf{m}_0 = \mathbf{L}^{\mathrm{T}}\mathbf{d}_r^{\text{obs}} \,, \tag{4.41}$$

Linearized modeling is defined as

$$\mathbf{d}_r = \mathbf{L}\mathbf{m} \tag{4.42}$$

Based on equations 4.40 and 4.41, we can rewrite equation 4.42 as

$$\mathbf{d}_r = \mathbf{K}_r^{\mathrm{T}}\mathbf{E}_-^{\mathrm{T}}\square^{\mathrm{T}}\square\mathbf{u}_s\mathbf{m} \,, \tag{4.43}$$

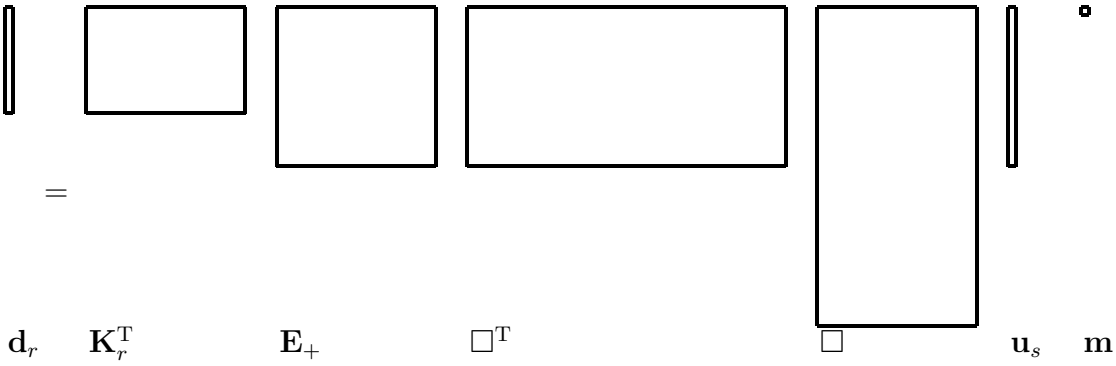

or

$$\mathbf{d}_r = \mathbf{K}_r^{\mathrm{T}}\mathbf{E}_+\square^{\mathrm{T}}\square\left(\mathbf{E}_+\mathbf{K}_s\mathbf{d}_s\right)\mathbf{m} \,. \tag{4.44}$$

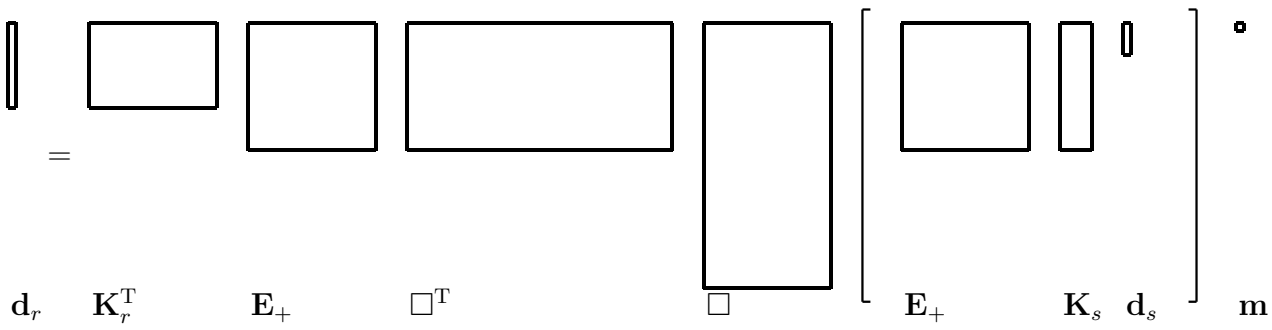

CHAPTER 5

ELASTIC LEAST-SQUARES REVERSE TIME MIGRATION USING THE ENERGY NORM

A paper published* in Geophysics

Daniel Rocha**,[1] and Paul Sava[1]

Incorporating anisotropy and elasticity into least-squares migration (LSM) is an important step towards recovering accurate amplitudes in seismic imaging. An efficient way to extract reflectivity information from anisotropic elastic wavefields exploits properties of the energy norm. We derive linearized modeling and migration operators based on the energy norm in order to perform anisotropic least-squares reverse time migration (LSRTM) describing subsurface reflectivity and correctly predicting observed data without costly decomposition of wave modes. Imaging operators based on the energy norm have no polarity reversal at normal incidence and remove backscattering artifacts caused by sharp interfaces in the earth model, thus accelerating convergence and generating images of higher quality when compared to images produced by conventional methods. With synthetic and field data experiments, we show that our elastic LSRTM method generates high-quality images that predict the data for arbitrary anisotropy, without the complexity of wave-mode decomposition and with high convergence rate.

5.1 Introduction

The search for more reliable seismic images and additional subsurface information, such as fracture distribution, drives advances in seismic acquisition, such as larger offsets, wider

* Reprinted with permission of *Geophysics*, Vol. 83, No 3 (May-June 2018), pp. S237-S248
** Corresponding author. Direct correspondence to drocha@mines.edu
[1] Center for Wave Phenomena, Colorado School of Mines, 924 16th St., Golden, CO 80401

azimuths and multicomponent recording. All of these advances facilitate incorporating anisotropy and elasticity into wavefield extrapolation and reverse time migration (RTM), which is the state-of-art wavefield imaging algorithm suitable for complex geological structures (Baysal et al., 1983; McMechan, 1983; Lailly, 1983; Levin, 1984; Chang and McMechan, 1987; Hokstad et al., 1998; Zhang and Sun, 2009; Farmer et al., 2009). Although seismic acquisition improves with such advances, it always involves practical limitations, such as finite and irregular data sampling, that negatively impact wavefield imaging methods. Even if anisotropy and elasticity are assumed in wavefield migration, such limitations still exist. Consequently, this type of migration often leads to images with poor resolution and unbalanced illumination due to such practical acquisition constraints, even though image amplitudes are more reliable when compared to acoustic and/or isotropic imaging (Lu et al., 2009; Phadke and Dhubia, 2012; Hobro et al., 2014; Du et al., 2014b).

A common solution to these limitations is the implementation of least-squares migration (LSM), which iteratively attenuates artifacts caused by truncated acquisition and provides high-quality images that best predict observed data at receiver locations in a least-squares sense (Chavent and Plessix, 1999; Nemeth et al., 1999; Kuehl and Sacchi, 2003; Aoki and Schuster, 2009; Yao and Jakubowicz, 2012; Dong et al., 2012). In particular, if the two-way wave equation is used for extrapolation, the method is called least-squares reverse-time migration (LSRTM) (Dai et al., 2010; Yao and Jakubowicz, 2012; Dai and Schuster, 2012; Dong et al., 2012). However, to overcome these issues from acquisition and to exploit the advantages of more realistic wave extrapolation, some authors propose LSRTM that accounts for multiparameter earth models, which can either incorporate solely anisotropy (Huang et al., 2016a), elastic (Duan et al., 2017; Feng and Schuster, 2017; Xu et al., 2016; Alves and Biondi, 2016; Ren et al., 2017), or viscosity effects (Dutta and Schuster, 2014; Sun et al., 2015). For instance, the visco-acoustic and pseudo-acoustic implementations define earth reflectivity in terms of contrast from a single model parameter (Dutta and Schuster, 2014; Huang et al., 2016a) or in terms of a scalar image based on conventional cross-correlation

between wavefields (Sun et al., 2015). Alternatively, elastic LSRTM implementations in isotropic media provide multiple images that are defined in terms of cross-correlation between decomposed wave modes (Duan et al., 2017; Feng and Schuster, 2017; Xu et al., 2016; Alves and Biondi, 2016). However, wave-mode decomposition in anisotropic media is costly and not as straightforward as in isotropic media; and therefore, anisotropic wave-mode decomposition remains a subject of ongoing research (Yan and Sava, 2009; Zhang and McMechan, 2010; Yan and Sava, 2011a; Cheng and Fomel, 2014; Sripanich et al., 2015; Wang et al., 2016).

Incorporating both elasticity and anisotropy into LSRTM is possible with elastic wavefield imaging using the energy norm (Rocha et al., 2017). This type of imaging exploits realistic vector displacement field extrapolation within a multiparameter anisotropic and elastic earth model, and generates scalar images of the subsurface without costly decomposition of wave modes. As opposed to more conventional imaging conditions, the elastic imaging condition based on the energy norm exhibits no polarity reversal at normal incidence, and computes an appropriate correlation between wavefields that attenuates low-wavenumber artifacts caused by waves that do not correctly characterize subsurface reflectivity (e.g. wave backscattering from salt interfaces). Such artifacts are harmful to the LSRTM inversion and retard convergence because they do not accurately characterize reflections in the subsurface. One outstanding issue with energy imaging is the physical interpretation of the scalar image; we interpret the resulting amplitudes as a measure of the collective perturbation in all earth model parameters, in contrast with more conventional images that represent either individual earth model perturbations or amplitude conversion (e.g. P into S) for different incident and reflected wave modes. As for any other wavefield migration method, its quality suffers from the acquisition limitations discussed earlier. Therefore, we define a linearized modeling operator that generates anisotropic elastic scattered wavefields, and we propose a LSRTM method that uses the energy image as a proxy for the reflectivity model. This LSRTM method is ideal to generate high-resolution images that correctly predict observed multicomponent data, without the shortcomings of different wave modes and full-wavefield

phenomena present in anisotropic elastic wavefields. We demonstrate all the benefits of the method with synthetic and field data experiments.

5.2 Theory

We can express elastic wavefield migration with mathematical operators such that

$$\mathbf{m} = \mathbf{L}^{\mathrm{T}}\mathbf{d}_r \ , \tag{5.1}$$

where $\mathbf{L}^{\mathrm{T}}$ is the migration operator, $\mathbf{d}_r$ is single-scattered multicomponent data recorded at receiver locations, and $\mathbf{m}$ is an image or a set of images associated with the earth reflectivity. The operator $\mathbf{L}^{\mathrm{T}}$ involves backpropagation of $\mathbf{d}_r$ through an earth model generating a receiver wavefield $\mathbf{u}_r$, and the application of an imaging condition comparing $\mathbf{u}_r$ with the source wavefield $\mathbf{u}_s$ (extrapolated from a source function and location). For instance, an elastic imaging condition can involve decomposition of the wavefields $\mathbf{u}_s$ and $\mathbf{u}_r$ into separated wave modes and the application of crosscorrelation between wave modes (Yan and Sava, 2007). One generally considers wavefield migration as the adjoint operator of linearized modeling (also known as single-scattering modeling) (Claerbout, 1992). Therefore, $\mathbf{L}$ is the linearized modeling operator such that

$$\mathbf{d}_r = \mathbf{L}\mathbf{m} \ , \tag{5.2}$$

and generates single-scattered data $\mathbf{d}_r$ at receiver locations using an image containing reflectors that act as sources under the action of the background (or source) wavefield $\mathbf{u}_s$ (embedded in the operator $\mathbf{L}$).

5.2.1 Energy-norm linearized modeling and migration operators

For two anisotropic elastic source and receiver wavefields, which are functions of space $\mathbf{x}$ and time t, $\mathbf{u}_s\left(\mathbf{x},t\right)$ and $\mathbf{u}_r\left(\mathbf{x},t\right)$, we can form an image using the energy imaging condition (Rocha et al., 2017):

$$I_E\left(\mathbf{x}\right) = \sum_t \left[\rho\dot{\mathbf{u}}_s \cdot \dot{\mathbf{u}}_r - \left(\underline{\underline{\mathbf{c}}}\nabla\mathbf{u}_s\right) : \nabla\mathbf{u}_r\right] \ , \tag{5.3}$$

where $\rho(\mathbf{x})$ is the density of the medium and $\underline{\underline{\mathbf{c}}}\,(\mathbf{x})$ is the second-order stiffness tensor. The superscript dot applied on the wavefields indicates time differentiation and ∇ is the spatial gradient. The symbol : indicates Frobenius product between two matrices resulting in a scalar quantity (Golub and Loan, 1996). A more compact form of equation 5.3 utilizes the so-called energy vectors, which are defined as

$$\square\mathbf{u}_s = \left\{\rho^{1/2}\dot{\mathbf{u}}_s, \quad \underline{\underline{\mathbf{c}}}^{1/2}(\nabla\mathbf{u}_s)\right\} \ , \tag{5.4}$$

$$\square\mathbf{u}_r = \left\{\rho^{1/2}\dot{\mathbf{u}}_r, -\underline{\underline{\mathbf{c}}}^{1/2}(\nabla\mathbf{u}_r)\right\} \ . \tag{5.5}$$

Analyzing the terms in equations 5.4 and 5.5, one can note that the energy vectors contain twelve components, three from the terms $\rho^{1/2}\dot{\mathbf{u}}_{s,r}$ and nine from $\underline{\underline{\mathbf{c}}}^{1/2}(\nabla\mathbf{u}_{s,r})$. We can also define $\square$ as the energy operator containing derivatives and medium parameters applicable to a multicomponent wavefield. Using the definition of energy vectors, the imaging condition in equation 5.3 becomes

$$I_E = \sum_t \square\mathbf{u}_s \cdot \square\mathbf{u}_r \ . \tag{5.6}$$

In order to obtain the adjoint operator associated with the imaging condition in equation 5.6, we rewrite the expression in operator form:

$$\mathbf{m} = \left(\square\mathbf{u}_s\right)^{\mathrm{T}} \square\mathbf{u}_r \ . \tag{5.7}$$

We can write the elastic wavefields $\mathbf{u}_s$ and $\mathbf{u}_r$ in terms of a sequence of operators applied to the source function $\mathbf{d}_s$ and to the receiver data $\mathbf{d}_r$, respectively. First, we implement injection of the multicomponent source function and receiver data into the earth model by operators $\mathbf{K}_s$ and $\mathbf{K}_r$, respectively. Second, we apply forward and backward elastic wavefield extrapolation operators $\mathbf{E}_+$ and $\mathbf{E}_-$. Hence, we express the wavefields by $\mathbf{u}_s = \mathbf{E}_+\mathbf{K}_s\mathbf{d}_s$ and $\mathbf{u}_r = \mathbf{E}_-\mathbf{K}_r\mathbf{d}_r$, and we can rewrite equation 5.7 as

$$\mathbf{m} = \left(\square\mathbf{E}_+\mathbf{K}_s\mathbf{d}_s\right)^{\mathrm{T}} \square\mathbf{E}_-\mathbf{K}_r\mathbf{d}_r \ . \tag{5.8}$$

Equation 5.8 is in the form $\mathbf{m} = \mathbf{L}^{\mathrm{T}}\mathbf{d}_r$, where

$$\mathbf{L}^{\mathrm{T}} = (\square\mathbf{E}_{+}\mathbf{K}_s\mathbf{d}_s)^{\mathrm{T}}\,\square\mathbf{E}_{-}\mathbf{K}_r = (\square\mathbf{u}_s)^{\mathrm{T}}\,\square\mathbf{E}_{-}\mathbf{K}_r\ . \tag{5.9}$$

Therefore, this chain of operators $\mathbf{L}^{\mathrm{T}}$ represents the migration based on the energy norm. We can obtain the operator $\mathbf{L}$ (adjoint of $\mathbf{L}^{\mathrm{T}}$) if we apply the adjoint for each individual operator and reverse the order of operators:

$$\mathbf{L} = \mathbf{K}_r^{\mathrm{T}}\mathbf{E}_{+}\square^{\mathrm{T}}\,(\square\mathbf{E}_{+}\mathbf{K}_s\mathbf{d}_s) = \mathbf{K}_r^{\mathrm{T}}\mathbf{E}_{+}\square^{\mathrm{T}}\square\mathbf{u}_s\ , \tag{5.10}$$

where $\mathbf{E}_{-}^{\mathrm{T}} = \mathbf{E}_{+}$. This chain of operators $\mathbf{L}$ represents the linearized modeling based on the energy norm, involving extraction of multicomponent single-scattered data at the receiver locations ($\mathbf{K}_r^{\mathrm{T}}$), and elastic wavefield extrapolation ($\mathbf{E}_{+}$) from virtual multicomponent sources computed by $\square^{\mathrm{T}}\square\mathbf{u}_s\mathbf{m}$.

To elucidate the linearized modeling based on the energy norm, here are the steps involved in computing the scattered data at receivers ($\mathbf{d}_r$):

1. Inject the source wavelet $\mathbf{d}_s$ by utilizing $\mathbf{K}_s$.
2. Extrapolate ($\mathbf{E}_{+}$) the injected source $\mathbf{K}_s\mathbf{d}_s$, generating the background wavefield $\mathbf{u}_s$;
3. Compute $\square\mathbf{u}_s$, a twelve-component vector field shown in equation 5.4;
4. Multiply each component of $\square\mathbf{u}_s$ by the scalar reflectivity model $\mathbf{m}$;
5. Compute $\square^{\mathrm{T}}\square\mathbf{u}_s\mathbf{m}$, a three-component virtual source field;
6. Extrapolate ($\mathbf{E}_{+}$) the virtual source $\square^{\mathrm{T}}\square\mathbf{u}_s\mathbf{m}$, generating the scattered wavefield $\mathbf{u}_r$;
7. Extract data at receiver locations $\mathbf{d}_r$ by applying $\mathbf{K}_r^{\mathrm{T}}$ to the scattered wavefield.

In Appendix 5.6.1, we represent all individual operators involved in $\mathbf{L}$ and $\mathbf{L}^{\mathrm{T}}$ pictorially in order to illustrate the series of increases and reductions in dimensionality throughout our linearized modeling and migration. Also, in Appendix 5.6.2, we show all the components of the virtual source term $\square^{\mathrm{T}}\square\mathbf{u}_s\mathbf{m}$ explicitly for a 2D vertical transversely isotropic (VTI) medium.

5.2.2 Physical interpretation of energy imaging operators

For arbitrary anisotropy, we can write the energy linearized source term explicitly as

$$\mathbf{f}(\mathbf{x},t) = \left[\rho\ddot{\mathbf{u}}_s - \nabla\cdot\left(\underline{\underline{\mathbf{c}}}\nabla\mathbf{u}_s\right)\right]\frac{\delta m}{m}\ , \tag{5.11}$$

where $\mathbf{f}(\mathbf{x},t)$ is a displacement field and $\frac{\delta m}{m}(\mathbf{x})$ is the medium perturbation capturing contributions for all earth model parameters. Notice that the terms $\rho\ddot{\mathbf{u}}_s$ and $\nabla\cdot\left(\underline{\underline{\mathbf{c}}}\nabla\mathbf{u}_s\right)$ have the units of force per volume:

$$\rho\ddot{\mathbf{u}}_s \quad \text{(mass} \times \text{acceleration / volume)}\ , \tag{5.12}$$

$$\nabla\cdot\left(\underline{\underline{\mathbf{c}}}\nabla\mathbf{u}_s\right) \quad \text{(pressure/distance)}\ , \tag{5.13}$$

and $\frac{\delta m}{m}$ is dimensionless. Therefore, the linearized source is proportional to the force generated by the energy terms from the background wavefield, and to the distribution of the collective perturbation of the earth model. The imaging condition in equation 5.3, which is the adjoint operation of the proposed linearized modeling, delivers an image representing the relative contribution of all earth model perturbations ($\delta m/m$). Linearized modeling can also be implemented in terms of individual perturbations from each earth model parameter, and in this case, the linearized source is written as

$$\mathbf{f}(\mathbf{x},t) = \ddot{\mathbf{u}}_s\delta\rho - \nabla\cdot\left(\delta\underline{\underline{\mathbf{c}}}\nabla\mathbf{u}_s\right)\ . \tag{5.14}$$

By defining linearized modeling in terms of individual earth model perturbations, equation 5.14 is analogous to the Born source defined in adjoint-state methods for wavefield tomography (Tarantola, 1988; Tromp et al., 2005; Zhu et al., 2009).

If we assume a fixed perturbation $\delta m/m$ in all model parameters, we can obtain equation 5.11 as in Born approximation, i.e. small perturbation in the earth model parameters generating a single-scattered wavefield. The elastic wave equation for an anisotropic medium is

$$\rho_0\ddot{\mathbf{u}}_s = \nabla\cdot\left(\underline{\underline{\mathbf{c}}}_0\nabla\mathbf{u}_s\right)\ . \tag{5.15}$$

Without loss of generality, for the following discussion, we simplify it to the isotropic elastic wave equation

$$\rho_0 \ddot{\mathbf{u}}_s = \lambda_0 \left[\nabla \left(\nabla \cdot \mathbf{u}_s\right)\right] + \mu_0 \left[\nabla \cdot \left(\nabla \mathbf{u}_s + \nabla \mathbf{u}_s^{\mathrm{T}}\right)\right] \ , \tag{5.16}$$

where $\lambda_0(\mathbf{x})$ and $\mu_0(\mathbf{x})$ are background Lamé model parameters (Aki and Richards, 2002), and $\rho_0(\mathbf{x})$ is the background density. The Born approximation involves the addition of a weak-scattered wavefield $\delta\mathbf{u}_s(\mathbf{x}, t)$ generated by small perturbations in the background earth model parameters. Writing such perturbations as fixed relative increments in all parameters, we have

$$\rho = \rho_0 \left(1 + \delta m/m\right) \ , \tag{5.17}$$
$$\lambda = \lambda_0 \left(1 + \delta m/m\right) \ , \tag{5.18}$$
$$\mu = \mu_0 \left(1 + \delta m/m\right) \ . \tag{5.19}$$

To simplify notation, we can omit the denominator in $\delta m/m$ for the following equations. We express the wave equation with the total wavefield (background plus scattered) as

$$\begin{aligned} (1+\delta m)\,\rho_0 \left(\ddot{\mathbf{u}}_s + \ddot{\delta\mathbf{u}}_s\right) &= (1+\delta m)\,\lambda_0 \left[\nabla\left(\nabla\cdot\mathbf{u}_s\right) + \nabla\left(\nabla\cdot\delta\mathbf{u}_s\right)\right] \\ &+ (1+\delta m)\,\mu_0 \left[\nabla\cdot\left(\nabla\mathbf{u}_s + \nabla\mathbf{u}_s^{\mathrm{T}}\right) + \nabla\cdot\left(\nabla\delta\mathbf{u}_s + \nabla\delta\mathbf{u}_s^{\mathrm{T}}\right)\right] \ . \end{aligned} \tag{5.20}$$

Subtracting equation 5.16 from equation 5.20, and ignoring higher-order terms involving the product of δm with $\delta\mathbf{u}_s$, we obtain

$$\begin{aligned} \rho_0 \ddot{\delta\mathbf{u}}_s - \lambda_0 \left[\nabla\left(\nabla\cdot\delta\mathbf{u}_s\right)\right] - \mu_0 \left[\nabla\cdot\left(\nabla\delta\mathbf{u}_s + \nabla\delta\mathbf{u}_s^{\mathrm{T}}\right)\right] &= \\ -\delta m \Big\{ \rho_0 \ddot{\mathbf{u}}_s - \lambda_0 \left[\nabla\left(\nabla\cdot\mathbf{u}_s\right)\right] - \mu_0 \left[\nabla\cdot\left(\nabla\mathbf{u}_s + \nabla\mathbf{u}_s^{\mathrm{T}}\right)\right] \Big\} \quad , \end{aligned} \tag{5.21}$$

which means that the perturbed wavefield $\delta\mathbf{u}_s$ is generated using the right-hand side of equation 5.21 as the source term $\mathbf{f}(\mathbf{x}, t)$. The energy linearized modeling (equation 5.21) and the energy imaging condition that delivers δm can be written in operator form. We write these operators a function of the individual model parameters for a 2-D isotropic medium in Appendix 5.6.3.

5.2.3 Energy-norm elastic least-squares migration

The linearized modeling operator $\mathbf{L}$ and its adjoint enables us to compute an image that minimizes the objective function

$$E\left(\mathbf{m}\right) = \frac{1}{2}\|\mathbf{L}\mathbf{m} - \mathbf{d}_r\|^2 \ . \tag{5.22}$$

The reflectivity that minimizes equation 5.22 is mathematically described as

$$\mathbf{m}^{LS} = \left(\mathbf{L}^{\mathrm{T}}\mathbf{L}\right)^{-1}\mathbf{L}^{\mathrm{T}}\mathbf{d}_r \ . \tag{5.23}$$

However, to find $\mathbf{m}^{LS}$, one generally utilizes iterative methods that exploit the gradient of the objective function in equation 5.22. For a linear problem, such as LSRTM, the conjugate gradient algorithm is generally used (Hestenes and Stiefel, 1952; Scales, 1987). The gradient of the objective function in equation 5.22 with respect to a model at a given iteration i is

$$\mathbf{g}_i = \frac{\partial E\left(\mathbf{d}, \mathbf{m}_i\right)}{\partial \mathbf{m}_i} = \mathbf{L}^{\mathrm{T}}\left(\mathbf{L}\mathbf{m}_i - \mathbf{d}_r\right) \ . \tag{5.24}$$

The model update at each iteration can be a scaled version of the gradient, or ideally can incorporate an approximation of the Hessian operator $\mathbf{H} = \left(\mathbf{L}^{\mathrm{T}}\mathbf{L}\right)$ (Aoki and Schuster, 2009; Tang, 2009; Dai et al., 2010):

$$\mathbf{m}_{i+1} = \mathbf{m}_i - \mathbf{H}^{-1}\mathbf{g}_i \ , \tag{5.25}$$

For all numerical experiments shown in this paper, we set the initial model to be zero and apply an illumination compensation on the gradient at every iteration. This illumination compensation computed from the wavefields is considered to be an approximation of the Hessian operator and act as a preconditioner for each iteration of the conjugate-gradient algorithm (Rickett, 2003; Plessix and Mulder, 2004; Du et al., 2012). We use the energy norm of the source wavefield at every spatial location as our illumination compensation factor:

$$\mathbf{h}\left(\mathbf{x}\right) = \|\mathbf{u}_s\|_E^2 = \Box\mathbf{u}_s \cdot \Box\mathbf{u}_s \ , \tag{5.26}$$

5.3 Examples

The following numerical examples demonstrate how the linearized modeling and migration operators based on the energy norm behave during LSRTM. First, we perform an experiment with a single flat reflector to convey some intuition about how the method works; second, we show an experiment using a realistic synthetic earth model containing many reflectors and structures to test the method in more complex geological settings with sharp interfaces that create backscattering artifacts in conventional imaging methods; finally, we validate the method by applying it to a North Sea field dataset.

5.3.1 Single-reflector linearized modeling

We use a constant background earth model and a simple reflectivity model (containing one flat reflector) to show an example of a scattered wavefield obtained by the energy linearized modeling, and to compare the quality of the energy imaging condition with its conventional counterparts, which are based on wave-mode decomposition and generate PP, PS, SP and SS images (Yan and Sava, 2008). The parameters of the background earth model are $\rho = 2.5$ g/cm^3, $V_{P0} = 2.2$km/s (P-wave velocity along the symmetry axis), $V_{S0} = 1.3$km/s (S-wave velocity along the symmetry axis), and Thomsen parameters $\epsilon = 0.4$ and $\delta = 0.3$ (Thomsen, 1986). The source is located at $x = 1.5$ km at the surface and consists of a vertical displacement force that generates both P and S waves, as seen in Figure 5.1(a). The source (or background) wavefield interacts with the reflectivity model at $z = 0.55$km and generates the scattered wavefield shown in Figure 5.1(b), in which we can observe PP (first event, top to bottom), PS (second) and SP (third) reflections. At a later time, the linearized modeling also generates a SS reflection. As these Figures indicate, the proposed linearized modeling procedure generates a multicomponent scattered wavefield that contains only primary reflection events. Non-reflection events such as head waves are not generated as would be with full-wavefield modeling.

With the extrapolated wavefields, we generate energy and conventional images (Figure 5.1(c)-5.1(g)). Although the scattered wavefield is not generated from the receiver locations, we use it in place of the receiver wavefield in all imaging conditions. We make this choice such that the computed images do not contain artifacts caused by acquisition geometry and by fake events generated with backpropagation of injected displacement at receiver locations. Also, because the background earth model is constant, no backscattering artifacts exist in this experiment. The remaining artifacts are considered crosstalk artifacts caused not by reflections, but instead by the interaction between different wave modes. For both background and scattered wavefields extrapolated for all times, we compute Helmholtz decomposition and obtain PP, PS, SP and SS images. Since the earth model is vertical transversely isotropic (VTI), Helmholtz decomposition does not fully separate wave modes and causes crosstalk artifacts for all images due to some residual in the decomposed modes. Although the energy image (Figure 5.1(g)) does not involve wave-mode decomposition, it exhibits cross-talk artifacts that are similar in amplitude from the ones in the conventional images. As stated elsewhere (Rocha et al., 2017), the energy imaging condition only attenuates events from source and receiver wavefields that share the same propagation and polarization directions, which is not the case for crosstalk between different wave modes from source and receiver wavefields. The space-time diagram in Figure 5.1(h) shows all the wave events related to this experiment, and indicates two crosstalk correlations that are independent of wave-mode decomposition. Such correlations are caused by the slower incident S wave that interacts with the faster PP and PS reflections, generating artifacts in SP and SS images, respectively.

5.3.2 Single-reflector LSRTM

We demonstrate energy-based LSRTM using the same earth model from the previous simple experiment but with a contrast at the reflector location. The reflector consists of the following contrasts: $\Delta\rho = 0.7$ g/cm^3, $\Delta V_{P0} = 0.6$km/s, and $\Delta V_{S0} = 0.5$km/s. Figure 5.2(a) shows the density model and the acquisition geometry that consists of 10 sources

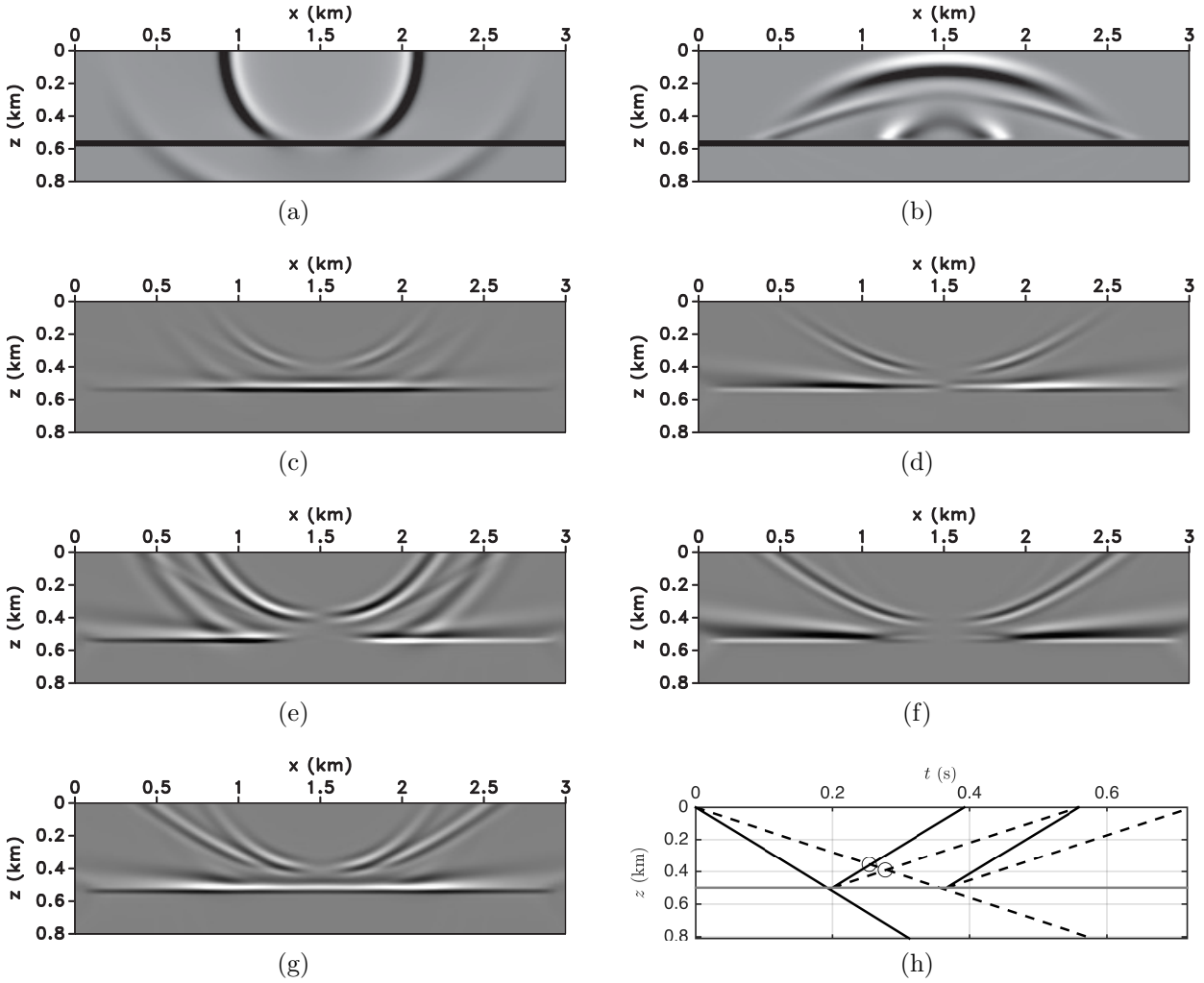

Figure 5.1: Snapshots of the vertical components of (a) background and (b) scattered wavefields at $t = 0.52$s. The black line at $z = 0.55$km indicates the position of the reflector. Using the scattered wavefield in place of the receiver wavefield, we obtain (c) PP, (d) PS, (e) SP, (f) SS, and (g) energy images. The incomplete wave-mode decomposition creates artifacts in PP, PS, SP and SS images, and crosstalk correlation creates artifacts in all images. The space-time diagram in (h) shows all wave events associated with this experiment: solid and dashed lines indicate P and S waves, respectively, and the horizontal gray line indicates the reflector. With this diagram, we can note that (e) SP and (f) SS images contain additional crosstalk artifacts due to the correlation of the incident S wave with the the decomposed PP and PS reflections, respectively, as seen by the intersections between these events indicated by the unfilled circles in the diagram.

and a line of receivers at the surface. We create a scalar reflectivity based on the contrast of the earth model (Figure 5.2(b)). We generate shot records by two different methods: (a) full-wavefield modeling, which uses the earth model with contrasts as conventionally implemented to generate synthetic elastic data; (b) linearized modeling based on the energy norm, which applies the operator in equation 5.10 to the reflectivity from Figure 5.2(b) using the background earth model (without contrast). We migrate both synthetic datasets using the energy imaging condition. Figures 5.2(c) and 5.2(d) show the stacked energy RTM images that use the full-modeled data and linearized-modeled data, respectively. We also compute 10 iterations of energy LSRTM for both datasets: Figures 5.2(e) and 5.2(e) show the final stacked LSRTM images that use the full-modeled data and linearized-modeled data, respectively. By comparing the LSRTM images with their RTM counterparts, one can observe the better quality of LSRTM images: the artifacts caused by the truncated acquisition are attenuated and the amplitudes are closer to the true reflectivity.

One can note that the RTM and LSRTM images using the linearized-modeled data have less artifacts than the ones using the full-modeled data. To explain why, we show both synthetic datasets in Figures 5.3(a) and 5.3(b). From early to late arrival times, the three visible events in each dataset correspond to (1) P-P (apex around $t = 0.6$s), (2) P-S/S-P (apex around $t = 0.8$s), and (3) S-S reflections (apex around $t = 0.9$s). For the near offsets, we notice that events in both datasets match in phase and polarity because only specular reflections exist at these near offsets. However, since the linearized modeling is a simplification of full-wavefield modeling, it can only predict single-scattering events and cannot predict wave phenomena that are beyond the critical angle, such as head waves, and these phenomena influence the amplitude of the three events at the far offsets of Figure 5.3(a). One can also notice such behavior on the data residuals at iteration 10 (Figures 5.3(c) and 5.3(d)). The linearized modeling embedded in the engine of both LSRTM results can only predict amplitude from reflections events, and cannot match the far-offset amplitudes from the full-modeled data (Figure 5.3(c)). Alternatively, by using the same linearized modeling

operator to generate synthetic data, the data residual (Figure 5.3(d)) and its related objective function (Figure 5.3(e)) decrease substantially more and are close to zero at the last iteration, as our operators are proper adjoints of each other, and can perfectly match the dataset containing only reflections after several iterations.

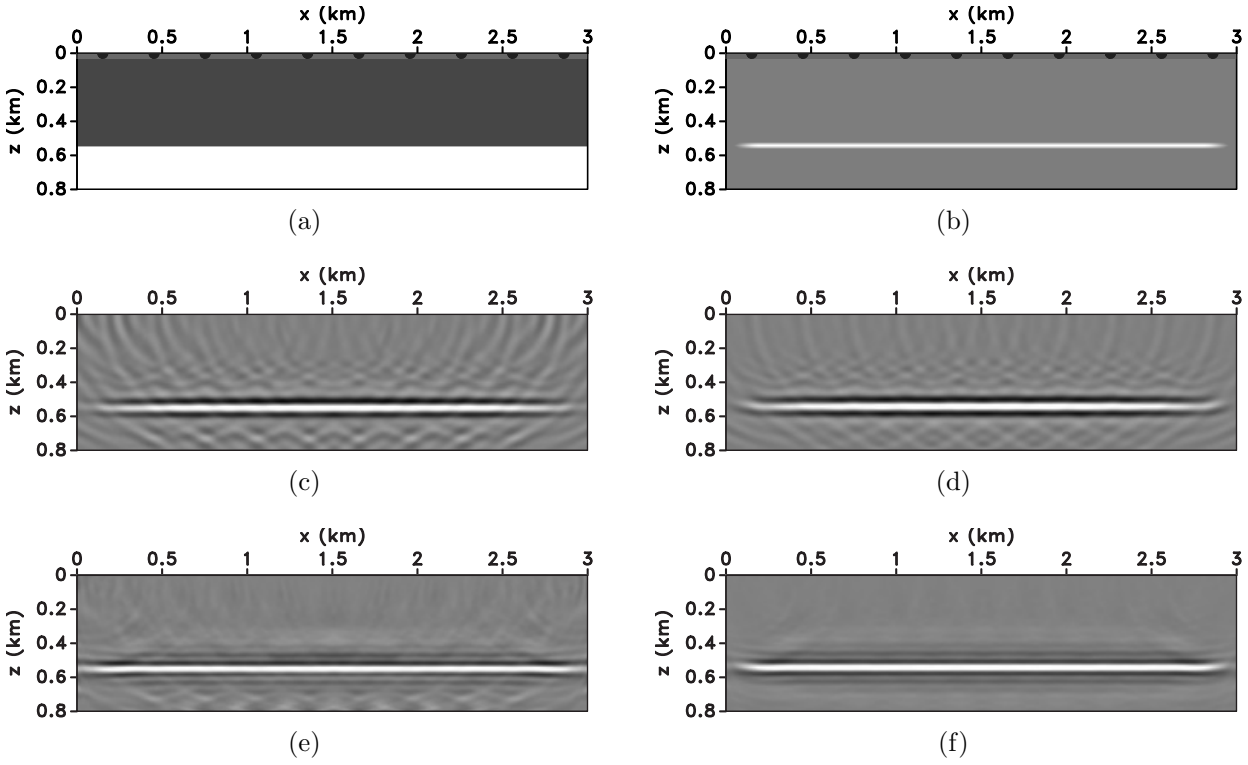

Figure 5.2: (a) Density model used in full-wavefield modeling, and (b) reflectivity model used in linearized modeling. The acquisition geometry consists of 10 sources and a line of receivers (black dots and gray line at the top). Elastic energy RTM image with (c) full-modeled data and with (d) linearized-modeled data. Elastic energy LSRTM image with (e) full-modeled data and with (f) linearized-modeled data. Note how LSRTM attenuates artifacts caused by sparse acquisition.

5.3.3 2007 BP TTI anisotropic benchmark model

We use a portion of the 2007 BP tilted transversely isotropic (TTI) benchmark model to test the method in a more complicated synthetic model. The original model consists of V_{P0}, ϵ, δ, and the tilt of the symmetry axis at every point (ν); we create V_{S0} and ρ from V_{P0} (Figure 5.4). The experiment geometry consists of 55 pressure sources equally spaced in the

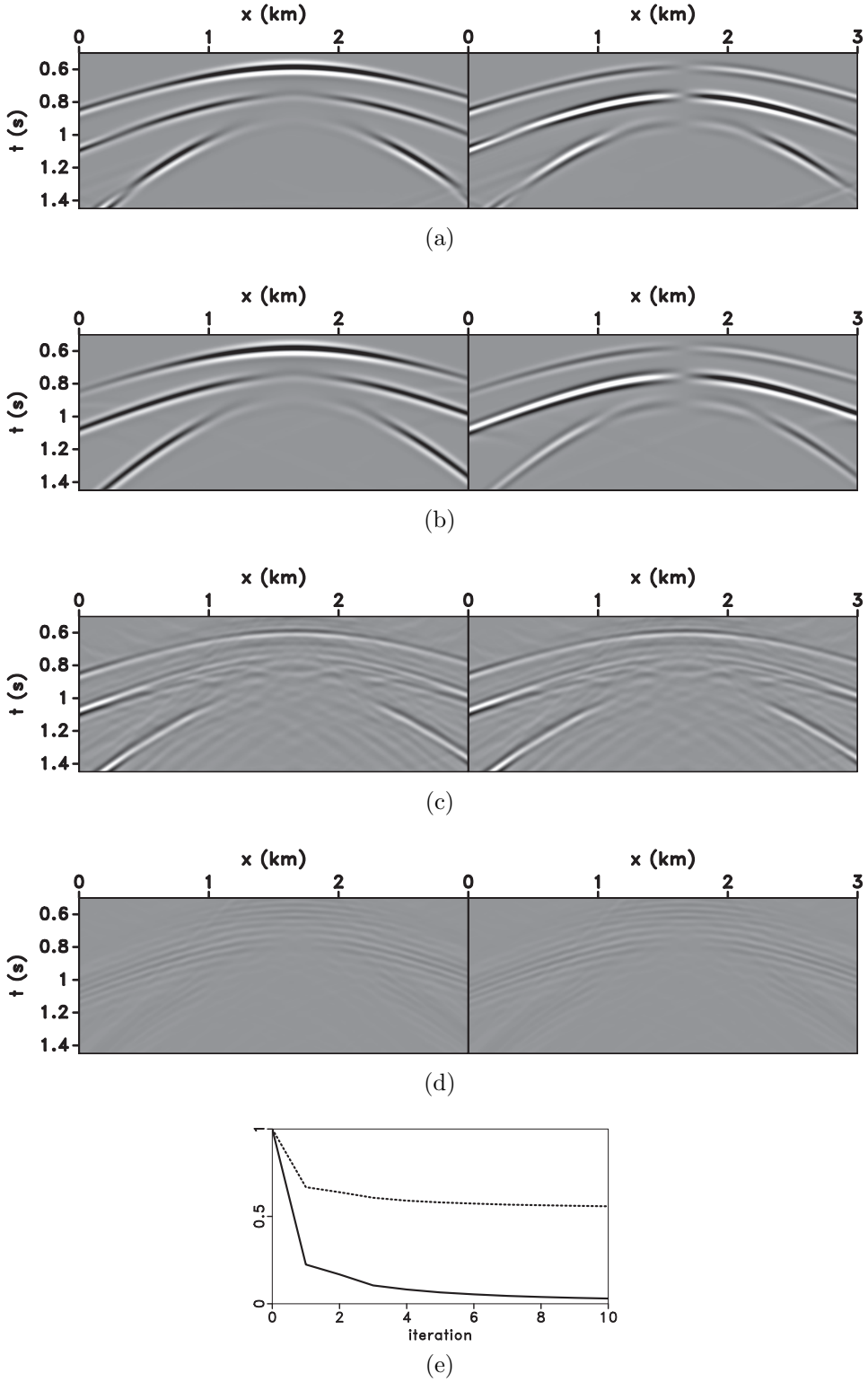

Figure 5.3: Vertical- (left) and horizontal- (right) component data from (a) full modeling and from (b) linearized modeling. Data residuals from the LSRTM images using (c) full modeling and from (d) linearized modeling. (e) Normalized objective functions for inversion using full-modeled data (dashed) and linearized data (solid). The far-offset amplitudes from full-modeled data are not correctly predicted by the linearized modeling operator.

water at the surface ($z = 0.092$km), and a line of multicomponent receivers at every grid point at the water bottom, which varies between the depths of $z = 1.0$km and $z = 1.4$km. Similarly to the preceding example, we generate two different datasets by (a) full-wavefield modeling, using the density model with contrasts (Figure 5.4(f)), and (b) linearized modeling, using a constant density model and the reflectivity model in Figure 5.5(e) to generate reflections. All other earth model parameters are kept the same between the two experiments.

We obtain energy RTM and LSRTM images using linearized-modeled data (Figures 5.5(a) and 5.5(c)) and full-modeled data (Figures 5.5(b) and 5.5(d)). We apply a power gain with depth on the RTM images for a fair comparison with LSRTM images, since RTM images commonly have weaker amplitudes for greater depths and these amplitudes can easily be compensated by such gain. Notice that artifacts in the shallow part (mainly caused by the limited acquisition) are attenuated, and the deep reflectors as well as the salt flanks are better illuminated in the LSRTM images compared to their RTM counterparts. Both LSRTM images contain sharper reflectors and are closer to the assumed true reflectivity models shown in Figures 5.5(e) and 5.5(f). For the LSRTM images, one can observe low-wavenumber artifacts inside the salt because most of the waves in this region do not scatter towards the receivers due to this particular experiment, which images only one side of the salt body. These events create artifacts that accumulate over iterations, and they are part of the null space for the inversion, i.e., they do not predict any reflections in the observed data. Although such artifacts do not represent actual reflectors, they are not harmful to the inversion process since they reside in the null space of the reflectivity model and do not mask any reflectors inside the salt body.

In Figures 5.6(a) and 5.6(b), we show the observed data at a particular shot location ($x = 41.4$km) containing offsets up to 8km for linearized and full-wavefield modeling, respectively. The corresponding data residuals after 20 iterations are shown in Figures 5.6(c) and 5.6(d), which are diminished when compared to the original datasets. The objective functions for both experiments are shown in Figure 5.6(e). As expected, the objective function for the

inversion using the dataset generated with the linearized modeling operator itself converges to zero, as our migration and modeling operators are proper adjoints of each other. The objective function for the experiment with full-modeled data decreases substantially and can potentially decrease more if more iterations are allowed, since the objective function at iteration 20 retains a significant slope, as seen in Figure 5.6(e). However, we expect the rate of convergence to be smaller over iterations until the objective function reaches a plateau, because our modeling operator cannot predict events beyond single-scattering in full-modeled data. In addition, differently from the single-reflector preceding example, several reflectors in this earth model cause multiple scattering events during full-wavefield modeling that are also not predicted by our linearized modeling operator. All events that exist in the data and are not predicted by our operator might form artifacts in the image, as for any other migration methods applied on data that contains multiple reflections, turning waves, etc.

5.3.4 Volve OBC real dataset

We apply the method to a field dataset acquired by an ocean-bottom cable (OBC) in the Volve field, located in the North Sea (Szydlik et al., 2007). Although the original dataset is 3D, we use a 2D section near the central crossline to reduce computational cost. The earth model is elastic VTI and the corresponding parameters are shown in Figure 5.7. The prominent layer around $z = 3$ km is a chalk layer that corresponds to the hydrocarbon reservoir (Szydlik et al., 2007). The dataset provided was pre-processed to retain only the down-going pressure component, and a particular common shot gather for a source at $x = 6.3$km is shown in Figure 5.8(a). We obtain energy RTM and LSRTM images after 15 iterations, shown in Figures 5.9(a) and Figure 5.9(b), and the corresponding objective function in Figure 5.8(d). The LSRTM image exhibits more detailed reflectors compared to the RTM image, and enhances the amplitudes at the edges of the model. With a smooth muting of far-offset events, the objective function decreases substantially reaching 40% of its initial value at the last iteration. By comparing the modeled data and residual at the last iteration (Figures 5.8(c) and 5.8(b)), and the observed data (Figure 5.8(a)), one can note

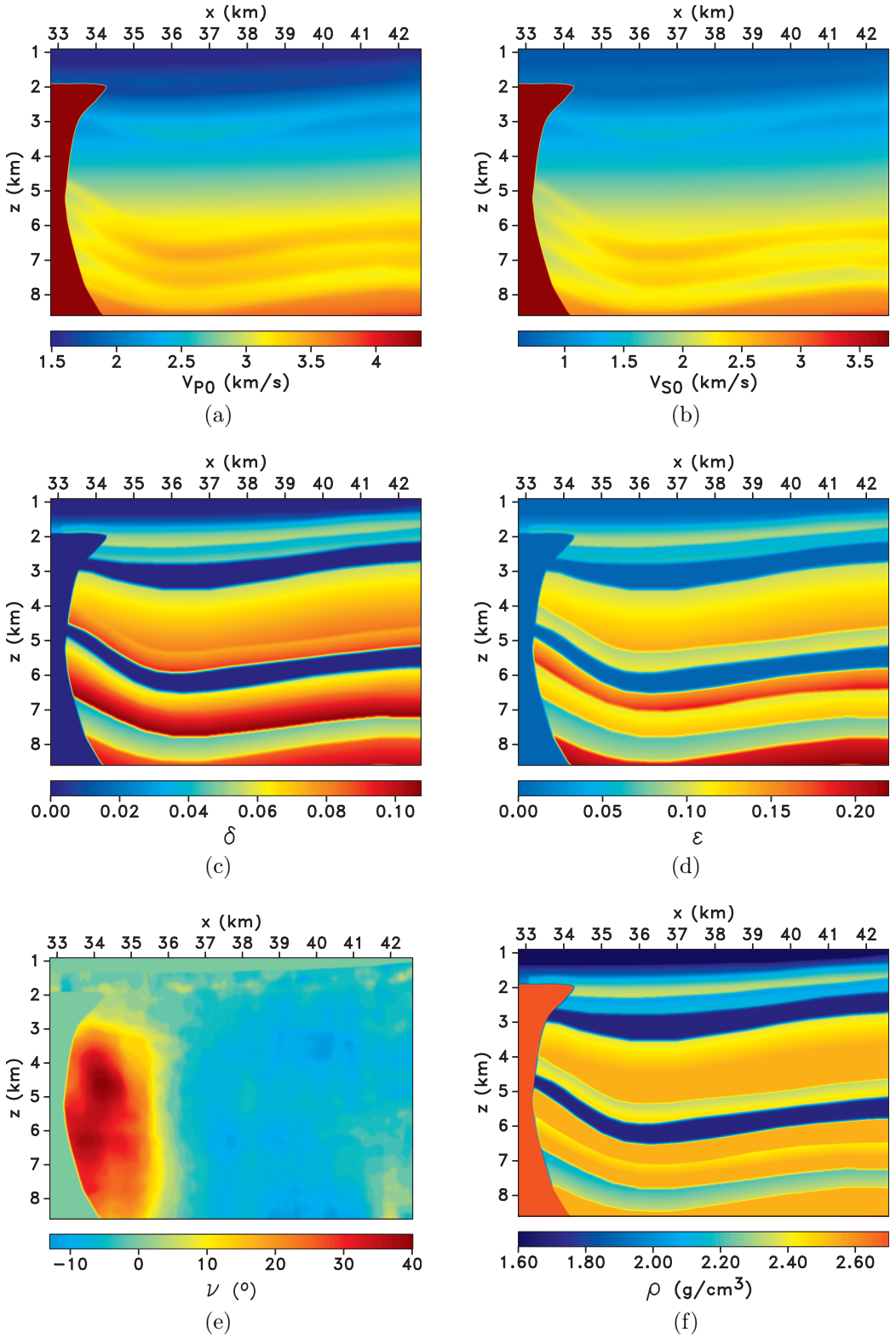

Figure 5.4: BP TTI model parameters: (a) P-wave and (b) S-wave velocities along the symmetry axis; Thomsen parameters (c) δ and (d) ϵ along the symmetry axis; (e) tilt of the symmetry axis (ν); (f) density with contrasts for full-wavefield modeling experiment.

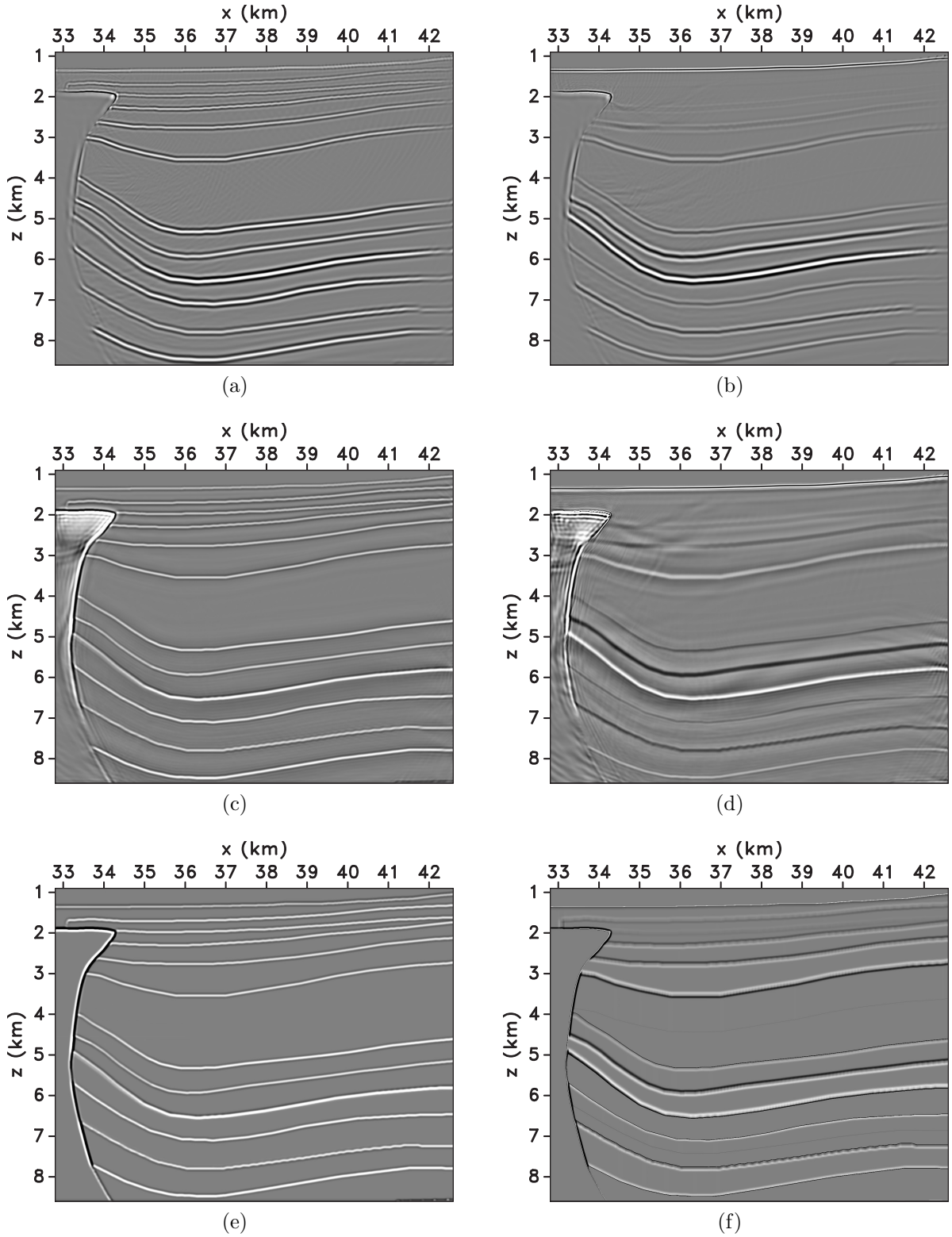

Figure 5.5: RTM images using (a) linearized-modeled data and (b) full-modeled data. LSRTM images after 20 iterations using (c) linearized-modeled data and (d) full-modeled data. (e) True reflectivity model for linearized-modeled data and (f) Laplacian operator applied on the density model in Figure 5.4(f) in order to show contrasts that create reflections in the full-wavefield modeling.

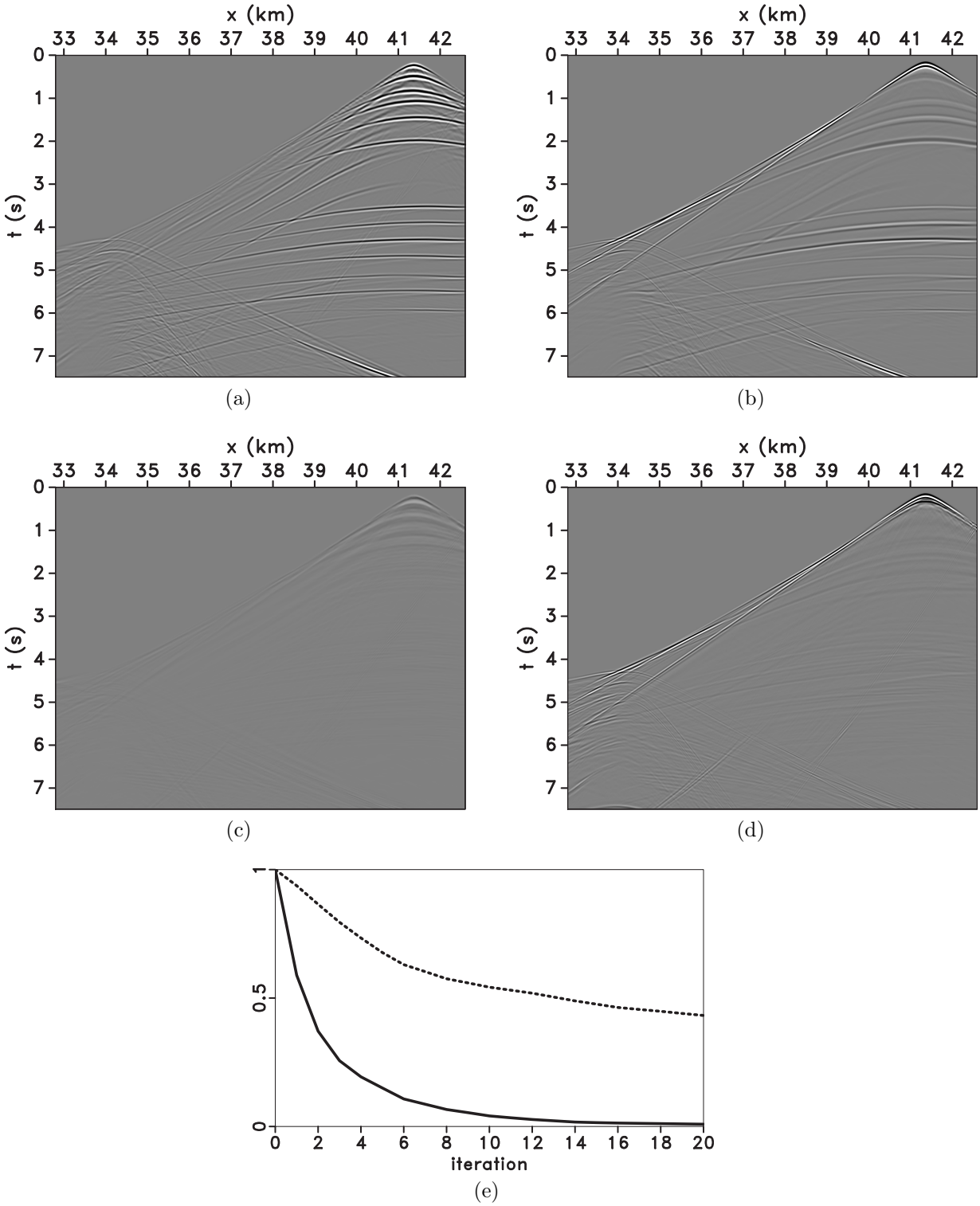

Figure 5.6: Vertical component of observed data at a $x_s = 41.4$km obtained by (a) linearized modeling using the reflectivity model in Figure 5.5(e), and (b) full-wavefield modeling using density model in Figure 5.4(f). Vertical component data residuals after 20 iterations for (c) linearized and (d) full-wavefield modeling experiments. (e) Normalized objective function for experiments using (dashed) full-modeled and (solid) linearized data.

that our linearized modeling operator and the image at the last iteration predict the main reflections and do not predict events such as noise, direct arrival, far-offset amplitudes, etc.

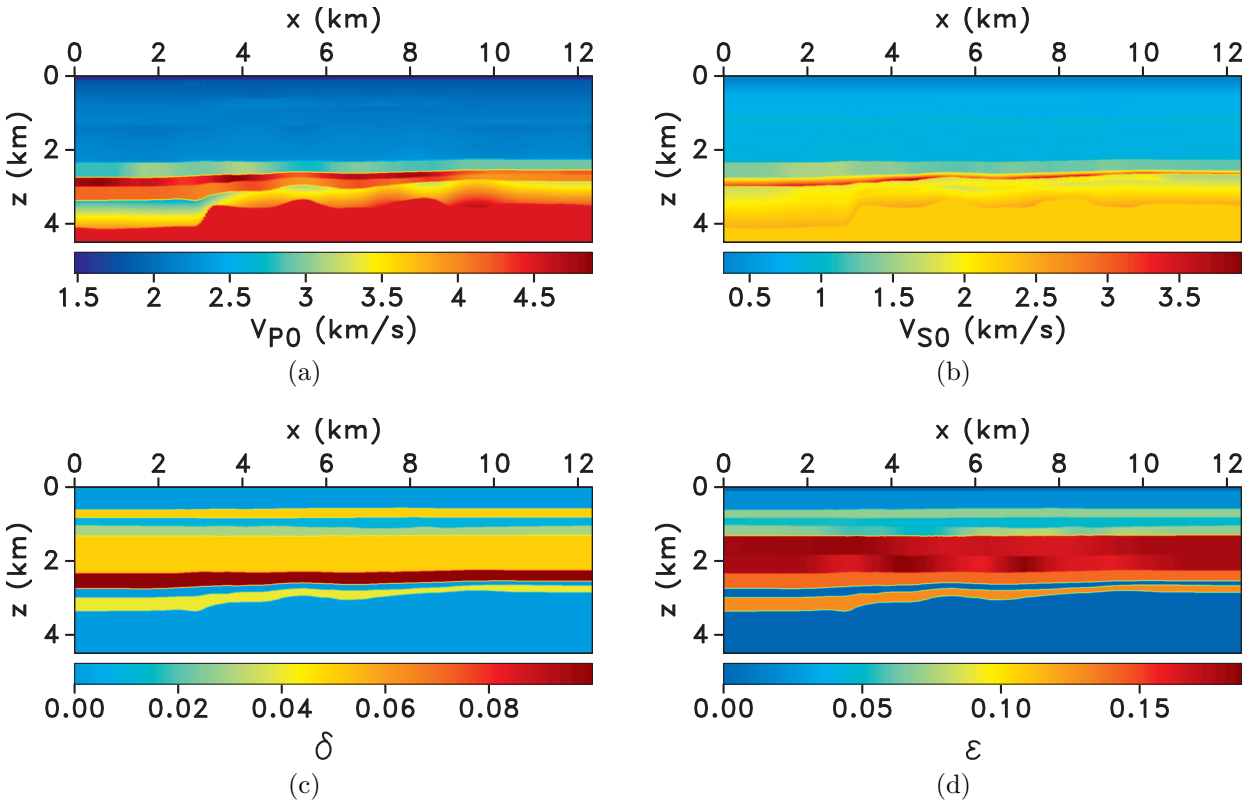

Figure 5.7: Volve 2D model parameters: (a) P-wave and (b) S-wave velocities along the vertical symmetry axis; Thomsen parameters (c) δ and (d) ϵ.

5.4 Conclusions

We propose an elastic LSRTM method that uses imaging operators based on the energy norm and delivers a scalar image that contains attenuated artifacts and explains data at receiver locations. The absence of strong backscattering artifacts in our results shows the advantage of our migration operator compared to its conventional counterparts. The obtained scalar image represents the collective contribution of all perturbations in earth model parameters. Using displacement fields directly and without costly wave-mode decomposition, our linearized modeling operator generates multicomponent datasets with a scalar reflectivity that correctly predicts the amplitude and phase of the reflections in observed

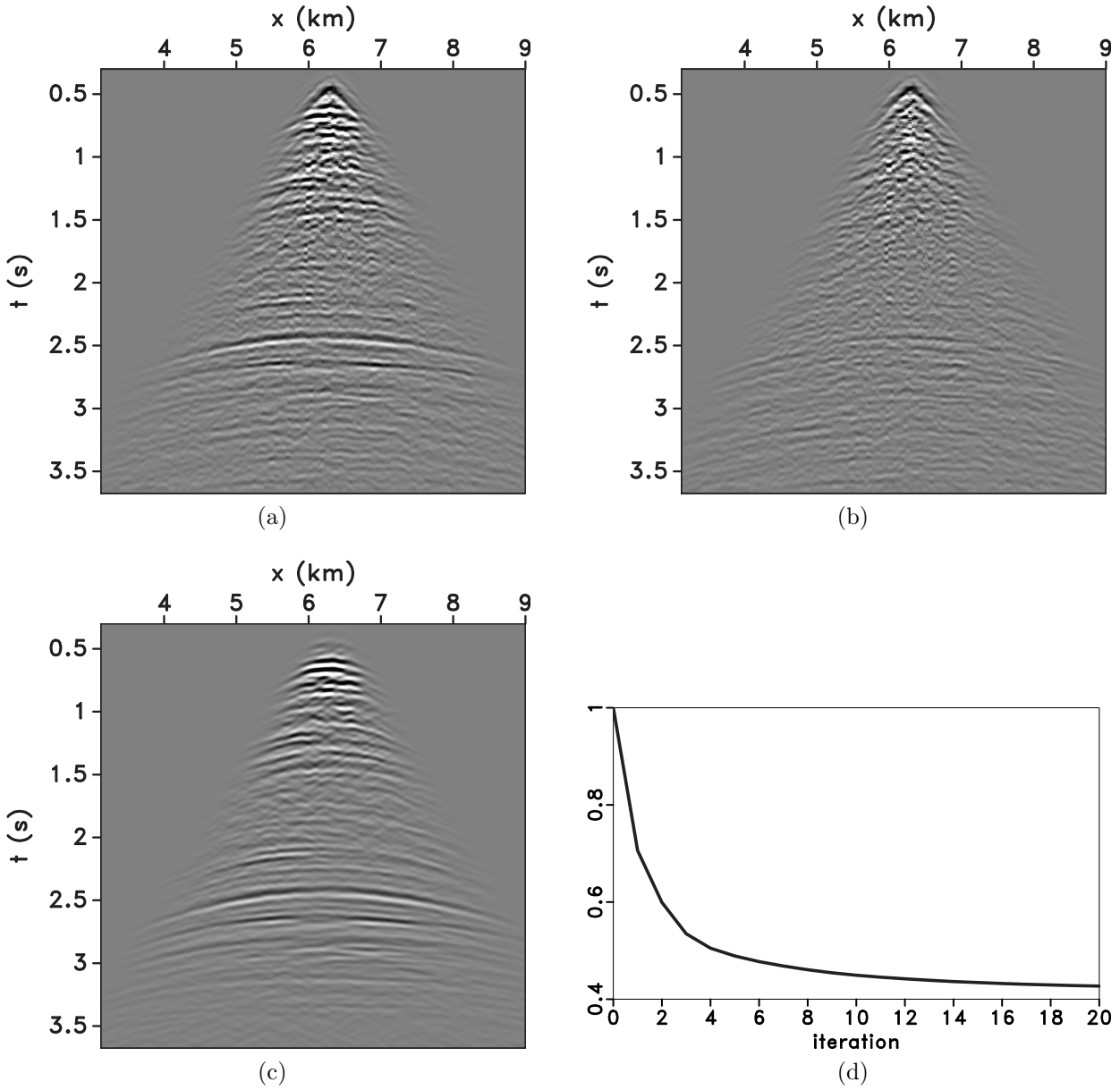

Figure 5.8: Volve experiment: (a) observed, (b) residual and (c) modeled (after 15 iterations) pressure shot gathers for a source at $x = 6.4$km. The main reflections are correctly predicted by our modeling operator. (c) Normalized objective function for LSRTM.

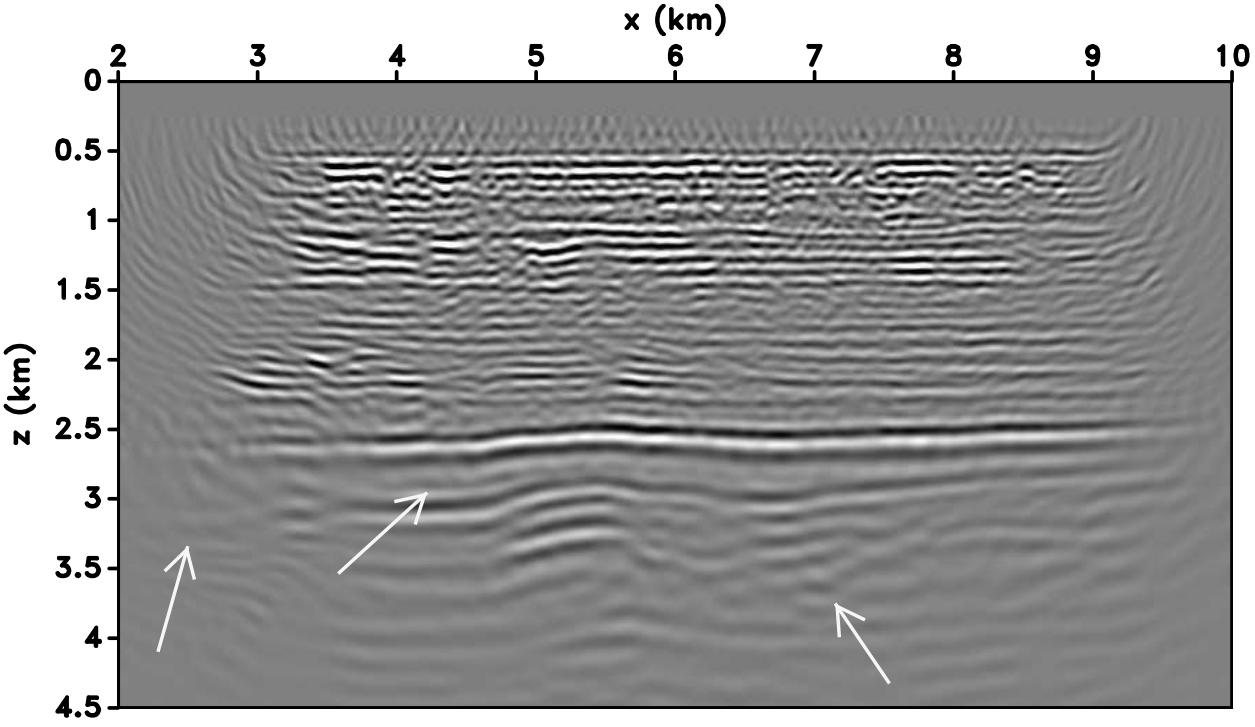

(a)

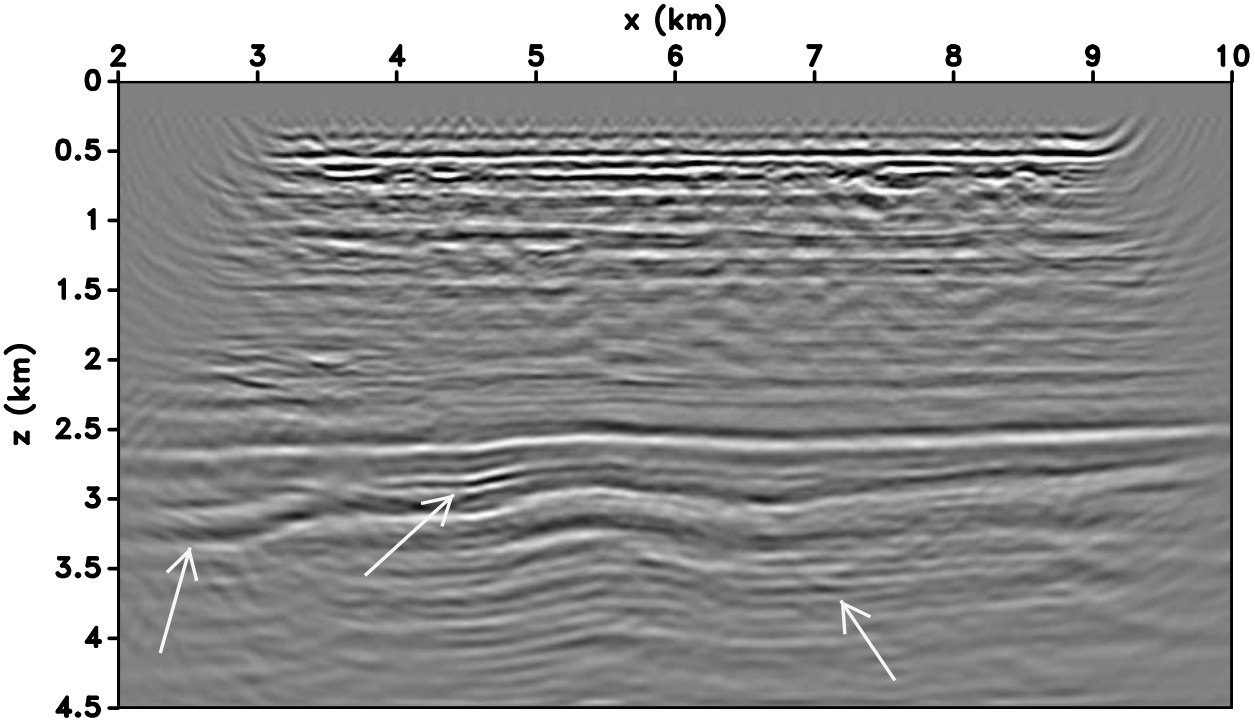

(b)

Figure 5.9: Volve experiment: energy (a) RTM and (b) LSRTM images. Reflectors around $z = 3.0$km become sharper, especially at the edges of the image. The arrows indicate reflectors that become more visible in the LSRTM image relative to RTM.

data, as illustrated by the final modeled data and objective functions from our numerical examples. As for any other linearized modeling procedure, events that are not reflections are inaccurately predicted by our linearized operator, and these events show in the image as artifacts. Future work involves application of our method to another multicomponent field dataset that contains both vertical and horizontal displacement components, and to 3D earth models.

5.5 Acknowledgments

We thank the sponsors of the Center for Wave Phenomena, whose support made this research possible. We acknowledge Hemang Shah and BP Exploration Operation Company Limited for creating the TTI model. We are grateful to Statoil ASA and the Volve license partners ExxonMobil E&P Norway AS and Bayerngas Norge AS for the release of the Volve data. We would like to thank Marianne Houbiers at Statoil for helping us with the Volve dataset. The authors appreciate the constructive comments from the anonymous reviewers of this paper. We acknowledge Antoine Guitton for helpful discussions. The synthetic examples in this paper use the Madagascar open-source software package (Fomel et al., 2013) freely available from http://www.ahay.org.

5.6 Appendices

The appendices below elucidate specific points of this current chapter.

5.6.1 Energy-based modeling and migration operators

The energy image $\mathbf{m}(\mathbf{x})$ is obtained by the expression

$$\mathbf{m} = (\Box \mathbf{u}_s)^{\mathrm{T}} \Box \mathbf{u}_r \ , \tag{5.27}$$

which can be represented schematically as

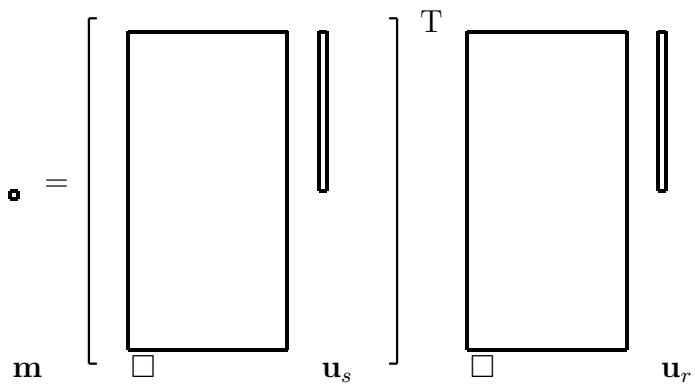

The operator $\square$ turns a three-component displacement field into a twelve-component vector field that contains spatial and temporal derivatives. Equation 5.27 also implies summation over time. We represent this increase in dimensions pictorially by making the matrix of $\square$ considerably larger than the wavefield vectors $\mathbf{u}_s$ and $\mathbf{u}_r$. Using extrapolator and injection operators, as explained in the body of the paper, we have

$$\mathbf{m} = \left(\square\mathbf{E}_+\mathbf{K}_s\mathbf{d}_s\right)^{\mathrm{T}} \square\mathbf{E}_-\mathbf{K}_r\mathbf{d}_r \ . \tag{5.28}$$

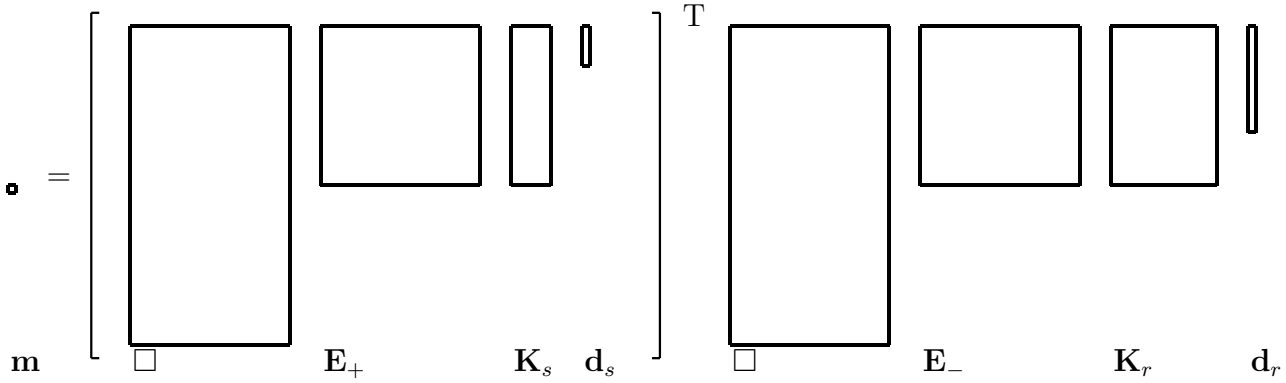

In compact form, we can rewrite equation 5.28 as

$$\mathbf{m} = \mathbf{L}^{\mathrm{T}}\mathbf{d}_r \ . \tag{5.29}$$

Linearized modeling is defined as

$$\mathbf{d}_r = \mathbf{L}\mathbf{m} \ . \tag{5.30}$$

Based on equation 5.28, we can rewrite equation 5.30 as

$$\mathbf{d}_r = \mathbf{K}_r^{\mathrm{T}}\mathbf{E}_-^{\mathrm{T}}\square^{\mathrm{T}}\square\mathbf{u}_s\mathbf{m} \ , \tag{5.31}$$

which is represented schematically as

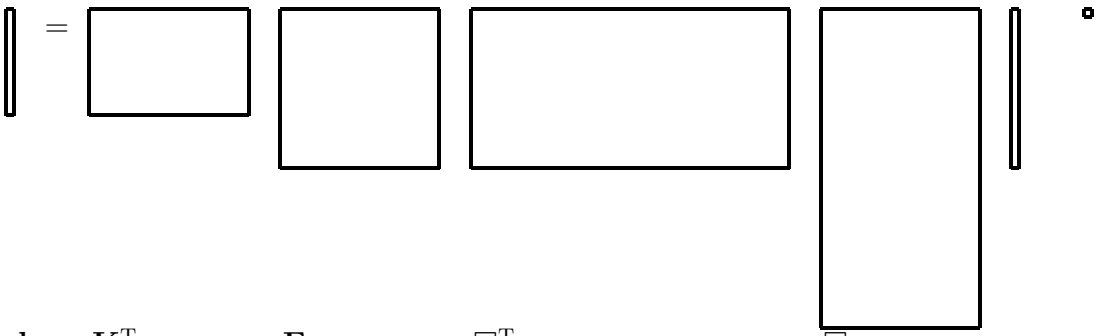

or

$$\mathbf{d}_r = \mathbf{K}_r^{\mathrm{T}} \mathbf{E}_+ \square^{\mathrm{T}} \square \left(\mathbf{E}_+ \mathbf{K}_s \mathbf{d}_s \right) \mathbf{m} \, . \tag{5.32}$$

represented as

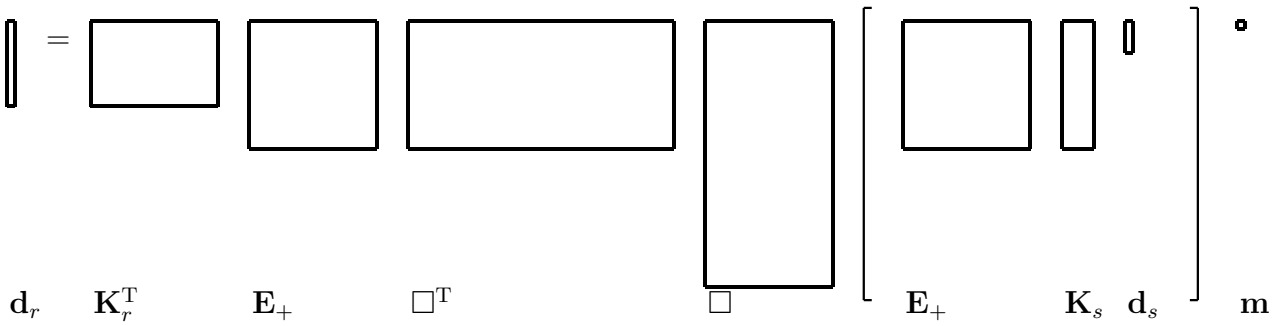

The virtual multicomponent source computed for the generation of the scattered wavefield is represented by the chain of operators $\square^{\mathrm{T}} \square \left(\mathbf{E}_+ \mathbf{K}_s \mathbf{d}_s \right) \mathbf{m} = \square^{\mathrm{T}} \square \mathbf{u}_s \mathbf{m}$.

5.6.2 Multicomponent virtual source for 2D VTI linearized modeling

We can write the energy imaging condition (equation 5.3) for a two-dimensional vertical transversely isotropic medium in matrix notation as

$$I_E \left(\mathbf{x} \right) = \rho \begin{bmatrix} \dot{U}_1^s & \dot{U}_3^s \end{bmatrix} \begin{bmatrix} \dot{U}_1^r \\ \dot{U}_3^r \end{bmatrix} - \begin{bmatrix} C_{11} U_{1,1}^s + C_{13} U_{3,3}^s & C_{55} \left(U_{1,3}^s + U_{3,1}^s \right) \\ C_{55} \left(U_{1,3}^s + U_{3,1}^s \right) & C_{33} U_{3,3}^s + C_{13} U_{1,1}^s \end{bmatrix} : \begin{bmatrix} U_{1,1}^r & U_{3,1}^r \\ U_{1,3}^r & U_{3,3}^r \end{bmatrix} \, , \tag{5.33}$$

where $U_{i,j}^{s,r}$ is the j-th derivative of the ith-component of wavefield $\mathbf{u}_s$ or $\mathbf{u}_r$, and C_{ij} are the stiffness coefficients in Voigt notation (Helbig, 1994). The symbol : represents Frobenius product between two matrices: an element-wise product between matrices with the corresponding sum of the products resulting in a scalar. Indices $i, j = \{1, 2, 3\}$ refer to $\{x, y, z\}$.

The superscript dot on $U_i^{s,r}$ indicates time differentiation. Rewriting all derivatives applied to U^r as operators, we obtain

$$I_E = \rho \begin{bmatrix} \dot{U}_1^s & \dot{U}_3^s \end{bmatrix} \begin{bmatrix} D_t & 0 \\ 0 & D_t \end{bmatrix} \begin{bmatrix} U_1^r \\ U_3^r \end{bmatrix} - \begin{bmatrix} C_{11}U_{1,1}^s + C_{13}U_{3,3}^s & C_{55}\left(U_{1,3}^s + U_{3,1}^s\right) \\ C_{55}\left(U_{1,3}^s + U_{3,1}^s\right) & C_{33}U_{3,3}^s + C_{13}U_{1,1}^s \end{bmatrix} : \begin{bmatrix} D_1 & 0 \\ 0 & D_3 \end{bmatrix} \begin{bmatrix} U_1^r & U_3^r \\ U_1^r & U_3^r \end{bmatrix}, \tag{5.34}$$

where D_t, D_1, and D_3 indicate derivative operators in time, x, and z, respectively. Therefore, the application of the energy imaging condition can be considered as an operator acting on the receiver wavefield $[U_1^r \; U_3^r]$. Its adjoint operator (linearized modeling) acts on the image (or reflectivity) I_E:

$$[f_1 \; f_3] = \left[\begin{bmatrix} D_t^{\mathrm{T}} & 0 \\ 0 & D_t^{\mathrm{T}} \end{bmatrix} \begin{bmatrix} \dot{U}_1^s \\ \dot{U}_3^s \end{bmatrix} \rho I_E \right]^{\mathrm{T}} - \begin{bmatrix} D_1^{\mathrm{T}} & D_3^{\mathrm{T}} \end{bmatrix} \begin{bmatrix} C_{11}U_{1,1}^s + C_{13}U_{3,3}^s & C_{55}\left(U_{1,3}^s + U_{3,1}^s\right) \\ C_{55}\left(U_{1,3}^s + U_{3,1}^s\right) & C_{33}U_{3,3}^s + C_{13}U_{1,1}^s \end{bmatrix} I_E, \tag{5.35}$$

where $[f_1 \;\; f_3]$ is a two-component virtual source that generates the scattered wavefield $[U_1^r \; U_3^r]$. We can rewrite the expression for each component individually for such virtual source:

$$\begin{aligned} f_1(\mathbf{x},t) = \;& D_t^{\mathrm{T}} \; \rho D_t U_1^s I_E - \\ & D_1^{\mathrm{T}} \; \left[C_{11}D_1U_1^s + C_{13}D_3U_3^s\right] I_E - \\ & D_3^{\mathrm{T}} \; \left[C_{55}\left(D_3U_1^s + D_1U_3^s\right)\right] I_E \; , \end{aligned} \tag{5.36}$$

$$\begin{aligned} f_3(\mathbf{x},t) = \;& D_t^{\mathrm{T}} \; \rho D_t U_3^s I_E - \\ & D_1^{\mathrm{T}} \; \left[C_{55}\left(D_3U_1^s + D_1U_3^s\right)\right] I_E - \\ & D_3^{\mathrm{T}} \; \left[C_{33}D_3U_3^s + C_{13}D_1U_1^s\right] I_E \; . \end{aligned} \tag{5.37}$$

Therefore, we can consider the generation of the energy scattered wavefield in an elastic 2D VTI medium as the extrapolation of a virtual multicomponent source defined by equations 5.36 and 5.37.

5.6.3 Perturbation of model parameters in energy migration and linearized modeling

For a two-dimensional isotropic medium, images representing perturbations for each earth model parameter can be written as

$$\begin{bmatrix}\delta\rho\\ \delta\lambda\\ \delta\mu\end{bmatrix} = \mathbf{M}\begin{bmatrix}U_1^r\\ U_3^r\end{bmatrix}\ , \tag{5.38}$$

where

$$\mathbf{M} = \begin{bmatrix}\rho\dot{U}_1^s D_t & \rho\dot{U}_3^s D_t\\ -\lambda\left(U_{1,1}^s + U_{3,3}^s\right) D_1 & -\lambda\left(U_{1,1}^s + U_{3,3}^s\right) D_3\\ -\mu\left[2U_{1,1}^s D_1 + \left(U_{1,3}^s + U_{3,1}^s\right) D_3\right] & -\mu\left[2U_{3,3}^s D_3 + \left(U_{1,3}^s + U_{3,1}^s\right) D_1\right]\end{bmatrix}\ . \tag{5.39}$$

Here, we use the same notation for the operators from Appendix 5.6.2. This type of images based on model perturbations are used in other LSRTM implementations (Alves and Biondi, 2016; Feng and Schuster, 2017; Xu et al., 2016; Duan et al., 2017; Ren et al., 2017), and conform with adjoint-state tomography (Tarantola, 1988; Tromp et al., 2005; Zhu et al., 2009). We can invoke the summation of the model perturbations utilizing a stacking operator $[1 \quad 1 \quad 1]$ such that

$$\delta m = [1 \quad 1 \quad 1]\begin{bmatrix}\delta\rho\\ \delta\lambda\\ \delta\mu\end{bmatrix} = [1 \quad 1 \quad 1]\,\mathbf{M}\begin{bmatrix}U_1^r\\ U_3^r\end{bmatrix}\ . \tag{5.40}$$

Applying the stacking operator to both left- and right-hand sides of equation 5.40 yields

$$\delta m = \delta\rho + \delta\lambda + \delta\mu = \begin{bmatrix}\rho\dot{U}_1^s D_t - \lambda\left(U_{1,1}^s + U_{3,3}^s\right) D_1 - \mu\left[2U_{1,1}^s D_1 + \left(U_{1,3}^s + U_{3,1}^s\right) D_3\right]\\ \rho\dot{U}_3^s D_t - \lambda\left(U_{1,1}^s + U_{3,3}^s\right) D_3 - \mu\left[2U_{3,3}^s D_3 + \left(U_{1,3}^s + U_{3,1}^s\right) D_1\right]\end{bmatrix}^{\mathrm{T}}\begin{bmatrix}U_1^r\\ U_1^r\end{bmatrix} \tag{5.41}$$

Equation 5.41 represents the summation of the perturbation images and is equivalent to the the energy imaging condition for a 2-D isotropic medium. Its adjoint, energy linearized modeling, is expressed as

$$\begin{bmatrix}f_1\\ f_3\end{bmatrix} = \begin{bmatrix}D_t^{\mathrm{T}}\dot{U}_1^s\rho - D_1^{\mathrm{T}}\left(U_{1,1}^s + U_{3,3}^s\right)\lambda - \left[2D_1^{\mathrm{T}}U_{1,1}^s + D_3^{\mathrm{T}}\left(U_{1,3}^s + U_{3,1}^s\right)\right]\mu\\ D_t^{\mathrm{T}}\dot{U}_3^s\rho - D_3^{\mathrm{T}}\left(U_{1,1}^s + U_{3,3}^s\right)\lambda - \left[2D_3^{\mathrm{T}}U_{3,3}^s + D_1^{\mathrm{T}}\left(U_{1,3}^s + U_{3,1}^s\right)\right]\mu\end{bmatrix}\delta m\ , \tag{5.42}$$

which can be rewritten in terms of individual model parameters and the stacking operator:

$$\begin{bmatrix} f_1 \\ f_3 \end{bmatrix} = \begin{bmatrix} D_t^{\mathrm{T}} \dot{U}_1^s \rho - D_1^{\mathrm{T}} \left(U_{1,1}^s + U_{3,3}^s \right) \lambda - \left[2 D_1^{\mathrm{T}} U_{1,1}^s + D_3^{\mathrm{T}} \left(U_{1,3}^s + U_{3,1}^s \right) \right] \mu \\ D_t^{\mathrm{T}} \dot{U}_3^s \rho - D_3^{\mathrm{T}} \left(U_{1,1}^s + U_{3,3}^s \right) \lambda - \left[2 D_3^{\mathrm{T}} U_{3,3}^s + D_1^{\mathrm{T}} \left(U_{1,3}^s + U_{3,1}^s \right) \right] \mu \end{bmatrix} \begin{bmatrix} 1 & 1 & 1 \end{bmatrix} \begin{bmatrix} \delta\rho \\ \delta\lambda \\ \delta\mu \end{bmatrix} \tag{5.43}$$

or in terms of a spraying operator (adjoint of stacking) and the adjoint of $\mathbf{M}$:

$$\begin{bmatrix} f_1 \\ f_3 \end{bmatrix} = \mathbf{M}^{\mathrm{T}} \begin{bmatrix} 1 \\ 1 \\ 1 \end{bmatrix} \delta m \ , \tag{5.44}$$

CHAPTER 6

ELASTIC REFLECTION WAVEFORM INVERSION WITH PETROPHYSICAL MODEL CONSTRAINTS

A paper to be submitted to a peer-reviewed journal

Daniel Rocha[*,1] and Paul Sava[1]

Elastic wavefield tomography faces challenging pitfalls due to its multiparameter and multicomponent characters, which are absent in the acoustic case. Inter-parameter crosstalk and the absence of petrophysical constraints may cause elastic inversion to fail, delivering unphysical and artifact-contaminated models. In addition, one of the goals of wavefield tomography is to deliver an earth model that generates accurate and high-quality images; however, this might not be the case for conventional data-domain tomography methods that exclude image optimization during inversion. Therefore, we propose to use the elastic reflection waveform inversion (ERWI) methodology, which inverts both for the background velocity model and for the reflectivity image, coupled with a petrophysical constraint term in the objective function. We demonstrate that constraining ERWI is successful in delivering more plausible models with fewer artifacts and that satisfy the imposed constraints. We alternate between smooth model and reflectivity updates, keeping both data fitting, image focusing and petrophysical constraints consistently satisfied in a common objective function. Compared to unconstrained inversion, our numerical examples show less-contaminated models and higher-quality images, as well as improved convergence and accuracy.

[*] Corresponding author. Direct correspondence to drocha@mines.edu
[1] Center for Wave Phenomena, Colorado School of Mines, 924 16th St., Golden, CO 80401

6.1 Introduction

As the state-of-the-art technology for imaging subsurface structures in complex geological settings, wavefield tomography involves numerical extrapolation of recorded seismic waves to constrain physical properties (e.g., seismic velocity) as solutions to inverse problems. As opposed to ray-based methods (Bishop et al., 1985; Bording et al., 1987; Lines, 1991; Cerveny, 2005), wavefield tomography is preferred as the main method for high-resolution velocity estimation since it exploits the full waveform and bandwidth of seismic signals in the velocity update, and handles accurate wave propagation in complex media subject to multipathing. Its implementations are generally classified as either data-domain (Lailly, 1983; Tarantola, 1984; Gauthier et al., 1986) and/or as image-domain (Symes and Carazzone, 1991; Sava and Biondi, 2004a; Albertin et al., 2005; Symes, 2008; Yang and Sava, 2011; Diaz et al., 2013; Yang and Sava, 2015).

Full waveform inversion (FWI) (Sirgue et al., 2004; Vigh and Starr, 2008; Virieux and Operto, 2009; Plessix et al., 2013) is the most common data-domain wavefield tomography method, using wavefield extrapolation to obtain a physical model update. Such update is driven by an objective function whose gradient is obtained by crosscorrelation between the state and the adjoint wavefields (Tarantola, 1984; Hindlet and Kolb, 1988; Plessix, 2006). This crosscorrelation between extrapolated wavefields is analogous to imaging conditions in reverse time migration (RTM) (Baysal et al., 1983; McMechan, 1983; Whitmore, 1983). The adjoint wavefield is extrapolated from a data residual, often defined as the difference between observed and modeled data, although the residual could also utilize other discrepancy metric between datasets (Shin and Ha, 2008; Brossier et al., 2010; Ma and Hale, 2013; Chi et al., 2014; Gao et al., 2014; Yang et al., 2018). For image-domain methods, wave-equation migration velocity analysis (WEMVA) (Sava and Biondi, 2004a,b; Shen et al., 2005; Hou and Symes, 2018) stands as the main method that relies on the semblance principle, i.e., the imaged events must be focused if extrapolated with the correct velocity (Symes and Carazzone, 1991; Mulder and ten Kroode, 2002; Shen and Symes, 2008). In this case, the

objective function and the associated residual are constructed with extended image gathers; which can be functions of offset, reflection angle or wavefield correlation spatial/temporal lags (Rickett and Sava, 2002; Sava and Biondi, 2004a; Sava and Vasconcelos, 2011; Yang and Sava, 2011).

Each domain of inversion investigation offers its own benefits and disadvantages. For an initial earth model far from the true one, FWI suffers from cycle skipping, i.e., when the modeled waveforms differ from the observed ones by more than a half cycle. Although FWI is more suitable for diving and direct waves, reflections usually dominate the surface-recorded data and represent the main constituent of migrated images. Conventional FWI does not explicitly constrain the migrated images, possibly delivering models that do not substantially improve image quality. Alternatively, WEMVA seeks the model that delivers the most focused image; however, the obtained model exhibits low resolution and might not directly match observed data, since this optimization is implemented in the image domain.

Reflection waveform inversion (RWI) has recently gained interest as a technology using both reflections in data-domain wavefield tomography and also jointly inverting for the migrated image; (Hicks and Pratt, 2001; Xu et al., 2012; Wang et al., 2013; Guo and Alkhalifah, 2017). This technique exploits an objective function and its residual in the data domain, and separately updates the smooth and rough (i.e., image) parts of the earth model. Least-squares migration robustly computes the rough model (Alves and Biondi, 2016; Feng and Schuster, 2017; Duan et al., 2017; Ren et al., 2017), while optimization via adjoint-state method provides the smooth updates (Tarantola, 1988; Sava, 2014). Therefore, we can classify RWI as a mixed-domain (both data- and image-domain) wavefield tomography method. RWI provides low-wavenumber updates for the smooth earth model, and therefore, avoids high-wavenumber content that harms the inversion at initial iterations.

For any of the aforementioned wavefield tomography methods, one can pursue a multiparameter earth model through elastic wavefield extrapolation (Chang and McMechan, 1987; Yan and Sava, 2011b; Ravasi and Curtis, 2013; Duan and Sava, 2015). Elastic extrapolation

is feasible with multicomponent data recordings, and delivers more realistic reflectivity and valuable subsurface information, such as fracture distribution (Schoenberg, 1983; Grechka and Kachanov, 2006; Zhang et al., 2017). However, multiparameter inversion is subject to leakage (i.e., crosstalk) among inverted parameters (Operto et al., 2013; Pan and Innanen, 2016). Coupling between the multiple elastic wave modes (which become three in the presence of anisotropy) and their different illumination responses are responsible for such crosstalk, and leads to contamination of the inverted earth model. Considering the multitude of elastic modeling parameters and the reasons for choosing a certain parameterization, radiation pattern analysis is important to understand the ambiguity among physical properties with respect to the reflection angle and model parameterizations (Burridge et al., 1998; Köhn et al., 2012; Kamath and Tsvankin, 2016; Oh and Alkhalifah, 2016). This analysis also shows that the amplitude responses overlap for different earth model contrasts, thus expressing the difficulty to isolate sensitivity kernels for different parameters. In addition, limited acquisition coverage and subsurface complexity contributes to highly irregular illumination, thus reducing the effectiveness of radiation pattern analysis.

To mitigate the crosstalk between inverted elastic model parameters and, therefore, obtain a more geological-plausible earth model, various authors propose to use known physical relationships between parameters to constrain the elastic inversion. Baumstein (2013) imposes box constraints (i.e., allowed maximum and minimum values for a certain model parameter) using projection onto convex sets, while Peters et al. (2015) apply a similar method with additional smoothness constraints. Instead of simply imposing box constraints, Duan and Sava (2016) perform data-domain wavefield tomography using logarithmic barrier constraints based on known linear petrophysical relationships between P- and S-wave velocities. Such barrier constraints are incorporated in the inversion by an additional term in the objection function, as opposed to constraints imposed at the line search step with convex sets formulation. This methodology delivers more realistic earth models since crosstalk and artifacts do not obey petrophysical properties and are attenuated during inversion with

imposition of such constraints.

Inter-parameter crosstalk represents one of the main challenges facing elastic wavefield tomography, as we seek an earth model that matches the data and also generates high-quality images. Our choice is to impose physical constraints on the earth model and implement a scheme that simultaneously optimizes the model and the migrated image. Therefore, we impose logarithmic barrier constraints similarly to the method by Duan and Sava (2016), but applied in the context of mixed-domain elastic wavefield tomography, i.e., elastic RWI. Therefore, our method avoids the combined harmful effect of inter-parameter crosstalk (by physical constraints) and high-wavenumber updates (by low-wavenumber RWI gradients) into the inversion. The total model is constructed by adding the smooth background and the sharp perturbation models. However, such sharp contrasts cause backscattering during wavefield extrapolation, thus producing low-wavenumber artifacts when implementing conventional imaging conditions, including the ones based on model perturbations. We address this problem by applying the energy imaging condition in a least-squares sense (Rocha et al., 2016b, 2017; Rocha and Sava, 2018) for imaging with the total earth model.

6.2 Theory

Reflection waveform inversion involves decomposition of the extrapolated wavefields into their background and scattered constituents, as well as separation of the earth model into smooth and rough components. We obtain the rough models through least-squares migration based on the separated background and scattered wavefields. For updating the smooth earth model, we use wavefield tomography also based on this single-scattering wavefield decomposition. We incorporate a physical constraint term in the objective function of wavefield tomography, thus leading the inversion toward plausible models that satisfy known petrophysical relationships.

6.2.1 Single-scattering and migration operators based on earth model perturbations

We consider the second-order elastic wave equation for isotropic media

$$\rho\ddot{\mathbf{u}} - \nabla\left[\lambda\left(\nabla\cdot\mathbf{u}\right)\right] - \nabla\cdot\left[\mu\left(\nabla\mathbf{u} + \nabla\mathbf{u}^{\mathrm{T}}\right)\right] = \mathbf{f}\ , \tag{6.1}$$

where $\mathbf{u}\left(\mathbf{x},t\right)$ is the wavefield, $\mathbf{f}\left(\mathbf{x},t\right)$ is the source term, $\lambda\left(\mathbf{x}\right)$ and $\mu\left(\mathbf{x}\right)$ are Lamé parameters, $\rho\left(\mathbf{x}\right)$ is the density of the medium, ∇ represents spatial derivative operators, and the superscript dot indicates time differentiation. Under the single-scattering assumption, one can consider each one of the medium parameters as composed of a background and a small perturbation. Similarly, the associated wavefield is also decomposed into background and weak-scattering parts. Therefore, we can write

$$\rho = \rho_0 + \delta\rho\ , \tag{6.2}$$
$$\lambda = \lambda_0 + \delta\lambda\ , \tag{6.3}$$
$$\mu = \mu_0 + \delta\mu\ , \tag{6.4}$$
$$\mathbf{u} = \mathbf{u}_0 + \delta\mathbf{u}\ , \tag{6.5}$$

where δ indicates small perturbations, and the subscript $_0$ indicates background quantities. Substituting equations 6.2-6.5 in equation 6.1, and ignoring higher-order terms involving the product of the small earth model perturbations with $\delta\mathbf{u}$, we obtain

$$\begin{aligned}\rho_0\delta\ddot{\mathbf{u}} - \nabla\left[\lambda_0\left(\nabla\cdot\delta\mathbf{u}\right)\right] - \nabla\cdot\left[\mu_0\left(\nabla\delta\mathbf{u} + \nabla\delta\mathbf{u}^{\mathrm{T}}\right)\right] = \\ -\delta\rho\ddot{\mathbf{u}}_0 + \nabla\left[\delta\lambda\left(\nabla\cdot\mathbf{u}_0\right)\right] + \nabla\cdot\left[\delta\mu\left(\nabla\mathbf{u}_0 + \nabla\mathbf{u}_0^{\mathrm{T}}\right)\right] + \mathbf{f}\ .\end{aligned} \tag{6.6}$$

We write equation 6.6 to indicate the interaction between model perturbations $(\delta\rho, \delta\lambda, \delta\mu)$ and the background wavefield $\mathbf{u}_0$ is in the source term for the scattered wavefield $\delta\mathbf{u}$, which captured at receiver locations $\mathbf{x}_r$ leads to the scattered data $\delta\mathbf{d}\left(\mathbf{x}_r,t\right) = \mathbf{K}_r\delta\mathbf{u}$ ($\mathbf{K}_r$ is an operator that extracts $\delta\mathbf{u}$ at $\mathbf{x}_r$ forming $\delta\mathbf{d}$). Therefore, we can write the model perturbations generating recorded scattered data as

$$\delta\mathbf{d} = \mathbf{K}_r\delta\mathbf{u} = \mathbf{L}\delta\mathbf{m}\ , \tag{6.7}$$

where $\delta\mathbf{m} = [\delta\rho \;\; \delta\lambda \;\; \delta\mu]^{\mathrm{T}}$, and $\mathbf{L}$ is the single-scattering operator (see Appendix 6.6.1). Its adjoint is the migration operator

$$\delta\mathbf{m}_{mig} = \mathbf{L}^{\mathrm{T}}\delta\mathbf{d} \; . \tag{6.8}$$

For more than one experiment (e.g., shot gather), $\delta\mathbf{d}$ also depends on the experiment index e. In this case, $\mathbf{L}^{\mathrm{T}}$ involves summation over migrated images from different experiments, and $\mathbf{L}$ sprays $\delta\mathbf{m}$ for different modelings.

Least-squares migration leads to a more robust perturbation image by minimizing the following objective function

$$\mathcal{J}_{LSM} = \frac{1}{2}\|\mathbf{L}\delta\mathbf{m} - \delta\mathbf{d}\|^2 \; , \tag{6.9}$$

where the subscript LSM stands for least-squares migration. Using equations 6.7 and 6.8, the image that minimizes equation 6.9 in a least-squares sense corresponds to

$$\delta\mathbf{m}_{LS} = \left(\mathbf{L}^{\mathrm{T}}\mathbf{L}\right)^{-1}\mathbf{L}^{\mathrm{T}}\delta\mathbf{d} \; . \tag{6.10}$$

Equation 6.10 describes a procedure that only inverts for the model perturbation $\delta\mathbf{m}$, while keeping the background model $\mathbf{m}_0 = [\rho_0 \;\; \lambda_0 \;\; \mu_0]^{\mathrm{T}}$ unchanged. In order to update the background model, we need to perform non-linear inversion with updates computed by the adjoint-state method. Instead of simply applying the migration operator, inverting for $\delta\mathbf{m}$ helps the subsequent inversion for $\mathbf{m}_0$ by providing a higher-quality image with fewer artifacts for more accurate single-scattering modeling.

6.2.2 Waveform inversion with background and scattered wavefields

Equation 6.1 can also be formulated as

$$\mathbf{A}(\mathbf{m})\mathbf{u} = \mathbf{f} \; , \tag{6.11}$$

where $\mathbf{A}(\mathbf{m})$ is the elastic wave-equation operator, which is non-linear and depends on the total model vector $\mathbf{m} = [\rho \;\; \lambda \;\; \mu]^{\mathrm{T}}$. The total wavefield computed by equation 6.11 is captured at receiver locations (again, by the extraction operator $\mathbf{K}_r$) and forms the modeled data $\mathbf{d}\left(\mathbf{x}_r, t\right)$, which is then compared with observed data in waveform inversion by the following

objective function

$$\mathcal{J}_D = \sum_e \frac{1}{2}\|\mathbf{d} - \mathbf{d}_{obs}\|^2 = \sum_e \frac{1}{2}\|\mathbf{K}_r\mathbf{u} - \mathbf{d}_{obs}\|^2 \ , \tag{6.12}$$

where the summation over experiments (e.g., shot gathers) is indicated by the index e, and the subscript D indicates that the objective function involves only data comparison. In order to construct the model update in waveform inversion, one needs to compute the gradient of the objective function in equation 6.12 with respect to the model parameters. Based on adjoint-state theory (Tarantola, 1988; Plessix, 2006; Sava, 2014), such gradient is represented by

$$\frac{\partial \mathcal{J}_D}{\partial \mathbf{m}} = \sum_e \frac{\partial \mathbf{A}}{\partial \mathbf{m}}\mathbf{u} \star \mathbf{a} \ . \tag{6.13}$$

The derivative of the wave-equation operator with respect to model parameters ($\frac{\partial \mathbf{A}}{\partial \mathbf{m}}$) is detailed in Appendix 6.6.2. The symbol $\star$ in equation 6.13 represents zero-lag crosscorrelation between the state ($\mathbf{u}$) and adjoint ($\mathbf{a}$) wavefields. The adjoint wavefield uses the adjoint wave-equation operator and the objective function derivative with respect to the state wavefield as its source term:

$$\mathbf{A}^{\mathrm{T}}(\mathbf{m})\mathbf{a} = \frac{\partial \mathcal{J}_D}{\partial \mathbf{u}} = \mathbf{K}_r^{\mathrm{T}}\left(\mathbf{d} - \mathbf{d}_{obs}\right) \ . \tag{6.14}$$

Conventional full-waveform inversion uses the gradient expression in equation 6.13. However, for reflection-waveform inversion, both state and adjoint wavefields are decomposed into background and scattered parts based on equation 6.5. Such wavefield decomposition uses the single-scattering modeling expressed in equation 6.6, and thus the model perturbation vector $\delta\mathbf{m}$. We rewrite equation 6.13 as

$$\frac{\partial \mathcal{J}_D}{\partial \mathbf{m}} = \sum_e \frac{\partial \mathbf{A}}{\partial \mathbf{m}}\left(\mathbf{u}_0 + \delta\mathbf{u}\right) \star \left(\mathbf{a}_0 + \delta\mathbf{a}\right) \ . \tag{6.15}$$

Distributing the zero-lag cross correlation in equation 6.15, we obtain four terms for the total gradient:

$$\frac{\partial \mathcal{J}_D}{\partial \mathbf{m}} = \sum_e \frac{\partial \mathbf{A}}{\partial \mathbf{m}} \mathbf{u}_0 \star \delta \mathbf{a} + \sum_e \frac{\partial \mathbf{A}}{\partial \mathbf{m}} \delta \mathbf{u} \star \mathbf{a}_0 + \sum_e \frac{\partial \mathbf{A}}{\partial \mathbf{m}} \mathbf{u}_0 \star \mathbf{a}_0 + \sum_e \frac{\partial \mathbf{A}}{\partial \mathbf{m}} \delta \mathbf{u} \star \delta \mathbf{a} \, . \tag{6.16}$$

The separation between background and scattered wavefields is useful to obtain the low-wavenumber content of the waveform inversion gradient. The first summation in equation 6.16 involves crosscorrelation of waves propagating from the source to the image point, while the second summation correlates waves propagating from the receivers to the image point. Hence, such events coincide in space and time along their similar propagation paths, resulting in low-wavenumber content. The other two terms involve crosscorrelation of waves that only coincide at the image point, producing reflectivity that is characterized by high wavenumbers. In that sense, the low-wavenumber gradient corresponds to the background model ($\mathbf{m}_0$) update. Therefore, the RWI gradient is

$$\frac{\partial \mathcal{J}_D}{\partial \mathbf{m}_0} = \sum_e \left[\frac{\partial \mathbf{A}}{\partial \mathbf{m}} \mathbf{u}_0 \star \delta \mathbf{a} + \frac{\partial \mathbf{A}}{\partial \mathbf{m}} \delta \mathbf{u} \star \mathbf{a}_0 \right] \, . \tag{6.17}$$

6.2.3 Physical constraints

Auxiliary terms in the objective function that act in the model space are useful to prevent inversion results with unphysical models, which commonly emerge with data-misfit objection functions. The most familiar model objective function term penalizes inverted models far from a known reference model:

$$\mathcal{J}_M = \frac{1}{2} \mathbf{W}_m \|\mathbf{m} - \mathbf{m}_{\text{ref}}\|^2 \, , \tag{6.18}$$

where $\mathbf{W}_m$ is called model weighting matrix, and subscript "ref" stands for reference model. Such matrix can be a shaping operator, or more simply, a diagonal operator imposing larger weights on certain parts of the model space. For instance, considering updates in λ and μ while keeping density ρ constant, the gradient of equation 6.18 with respect to model parameters is

$$\frac{\partial \mathcal{J}_M}{\partial \lambda} = \mathbf{W}_\lambda^{\mathrm{T}} \mathbf{W}_\lambda \left(\lambda - \lambda_{\mathrm{ref}}\right) \quad , \tag{6.19}$$

$$\frac{\partial \mathcal{J}_M}{\partial \mu} = \mathbf{W}_\mu^{\mathrm{T}} \mathbf{W}_\mu \left(\mu - \mu_{\mathrm{ref}}\right) \quad . \tag{6.20}$$

An additional model objective function term exploits known physical relationships between two sets of model parameters, for example, implemented by a logarithmic penalty function (Peng et al., 2002; Gasso et al., 2009; Duan and Sava, 2016):

$$\mathcal{J}_C = -\eta \sum_{\mathbf{x}} \left[\log(h_u) + \log(h_l)\right] \ , \tag{6.21}$$

where η is a weighting scalar parameter relative to the other objective function terms, while h_u and h_l define linear functions in the dual-model space determining its upper and lower bounds. Note that equation 6.21 involves summation over all model samples. If we want to constrain the model parameters λ and μ, we write the upper and lower bounds as

$$h_u = -\lambda + c_u \mu + b_u = 0 \ , \tag{6.22}$$

$$h_l = \quad \lambda - c_l \mu - b_l = 0 \ , \tag{6.23}$$

where $c_{u,l}$ and $b_{u,l}$ are the slopes and intercepts of the lines. For model pairs that fall inside the region bounded by h_u and h_l, the distance to the barrier lines determines the value of the physical constraint. On one hand, the further and more equidistant to h_u and h_l a certain model sample is, the larger is the argument of the logarithm, and therefore, smaller is $\mathcal{J}_C$. On the other hand, model samples that are close to one of the barrier lines during inversion lead to large $\mathcal{J}_C$, and are thus forced to move away from that barrier.

The gradient of equation 6.21 with respect to either λ or μ is

$$\frac{\partial \mathcal{J}_C}{\partial \lambda} = \frac{-\eta}{\lambda - c_u \mu - bu} \ - \ \frac{\eta}{\lambda - c_l \mu - bl} \ , \tag{6.24}$$

$$\frac{\partial \mathcal{J}_C}{\partial \mu} = \frac{\eta c_u}{\lambda - c_u \mu - bu} \ + \ \frac{\eta c_l}{\lambda - c_l \mu - bl} \ . \tag{6.25}$$

Equations 6.24 and 6.25 show that the gradient tends to ∞ if any of its denominators tends to zero. This happens for model samples that get close to one of the barriers. Therefore, the physical constraint term ensures that the inverted models are between these bounds by imposing large corrective updates to anomalous model samples relative to the desired petrophysical trend.

Finally, we can write the total objective function involving data-misfit term, model-misfit tern with respect to a reference model, and petrophysical constraint term:

$$\mathcal{J} = \mathcal{J}_D + \mathcal{J}_M + \mathcal{J}_C \ . \tag{6.26}$$

6.3 Examples

The following numerical examples demonstrate how imposing model regularization and petrophysical constraints delivers more geological-plausible ERWI models. We also obtain improved convergence rates and image quality when compared to unconstrained inversion. We apply the method on a simple experiment with a single reflector and a Gaussian anomaly. We also illustrate the method with a more complex and realistic synthetic model. In all cases, we assume that petrophysical information is available to constrain the model parameters.

6.3.1 Single-reflector with a Gaussian anomaly

We illustrate our ERWI method with the synthetic elastic model shown in Figure 6.1, where the top of Figures 6.1(a) and 6.1(b) show the acquisition geometry, the reflector location and the Gaussian anomalies for the true λ and μ models, respectively. We start inversion from a constant background; and after 38 inversion iterations, alternating between smooth and rough model updates, we obtain the unconstrained (middle of Figure 6.1) and constrained (bottom of Figure 6.1) models. Note how the constrained ERWI mitigates the spurious artifacts (around the anomaly) existent in the unconstrained inverted model, which are caused by a combination of sparse geometry, limited bandwidth and crosstalk between

model parameters.

The constraint term uses two barrier lines defined by $h_l = \lambda - 1.5\mu - 1.98$ and $h_u = -\lambda + \mu + 5.43$ according to equations 6.22 and 6.23. The background of Figure 6.2 shows a map of $\mathcal{J}_C$ with two visible convergent barrier lines, and all model samples from unconstrained and constrained inversions. The unconstrained model samples are more broadly spread into the model space, while the constrained samples are confined within the barriers and closer to the line of true model samples. The point at $[\mu, \lambda] = [5.194, 10.388]$ GPa represents the background model value, from where both constrained and unconstrained inversions start. Both unconstrained and constrained ERWIs alternate between image (rough model) and background (smooth model) inversions as shown in the objective function plot in Figure 6.3. The unconstrained inversion has a smaller objective function for the first 20 iterations. However, for the remaining iterations, the constrained ERWI has better performance, finalizing with smaller residuals for both smooth and rough model inversions relatively to the unconstrained ERWI.

To show how ERWI with physical constraints delivers a model that effectively increases image quality, we show the model perturbation $\delta\lambda$ and $\delta\mu$ images in Figures 6.4(a) and 6.4(b), respectively. The top reverse time migration (RTM) images show the cross-cutting artifacts due to sparse acquisition and a false subsidence of the flat reflector due to imaging with the wrong velocity (which is the initial velocity with the constant background value). Least-squares migration (LSRTM) on the same wrong model improves the image (middle of Figure 6.4) by mitigating the cross-cutting artifacts and sharpening the imaged reflector, but still exhibits the imprint of the wrong velocity at the center of the reflector for $\delta\lambda$, and at $[x, z] = [1, 0.8]$ km and $[x, z] = [2, 0.8]$ km for $\delta\mu$. Finally, using the constrained ERWI model, LSRTM delivers the bottom images in Figure 6.4, which show a horizontal reflector closer to the true one.

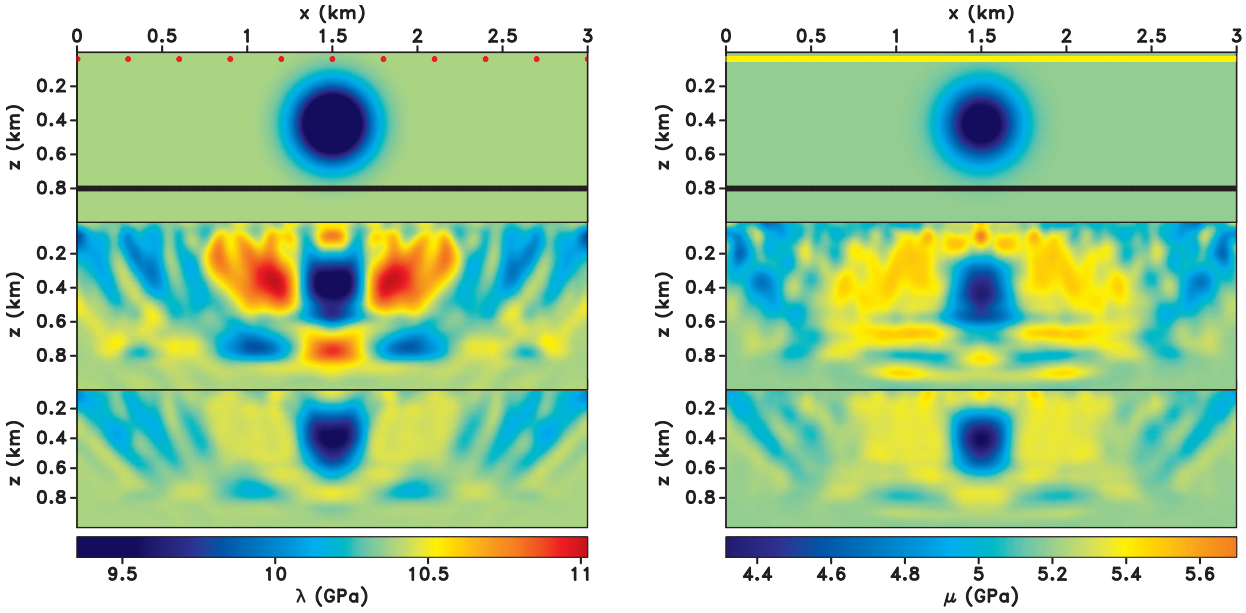

(a) (b)

Figure 6.1: True (top), unconstrained (middle), and constrained (bottom) inverted models for (a) λ and (b) μ. The top panels also show the 11 sources (red) and the line of multi-component receivers (yellow), and the reflector (black). Adding the physical constraint term into the inversion mitigates the spurious artifacts from inter-parameter crosstalk and sparse acquisition, delivering a more plausible earth model.

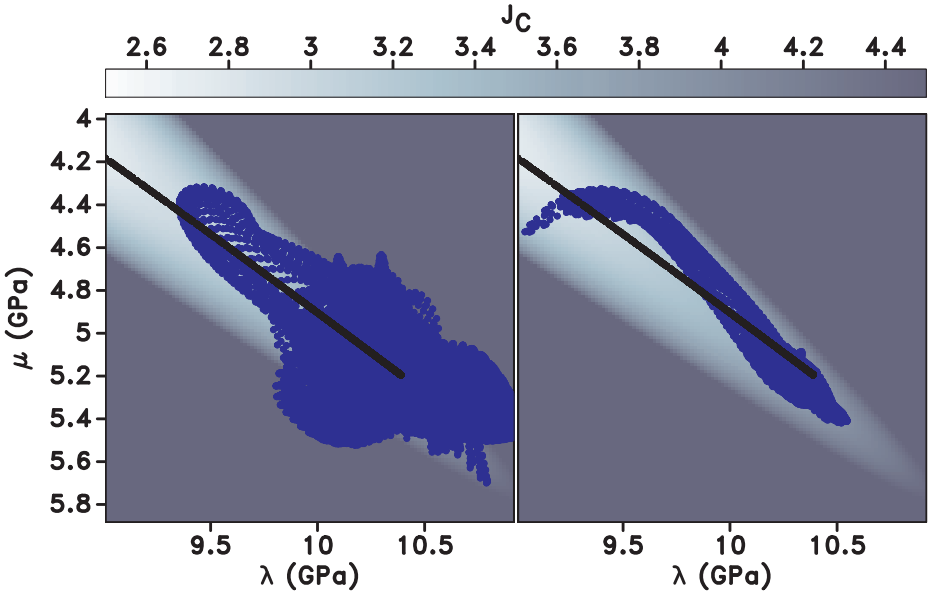

Figure 6.2: Crossplot in λ-μ space of inverted models: unconstrained (left) and constrained (right). The black line corresponds to the true model. The logarithmic barrier function used in the constrained inversion is plotted in the background. The unconstrained inverted model is spread throughout the model space without following a trend, while the constrained model is restricted to the region delimited by the barriers.

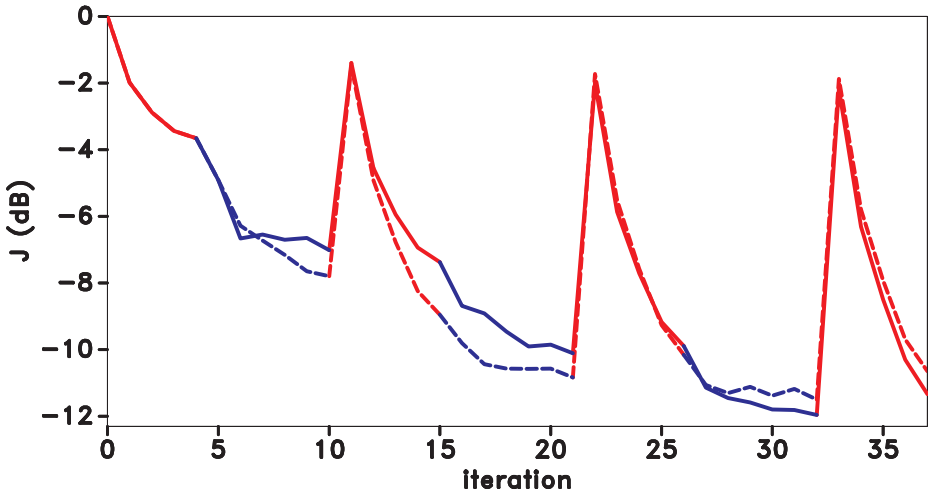

Figure 6.3: Objective functions in decibel scale for unconstrained (dashed) and constrained (solid) ERWIs, which alternate between least-squares migration of model perturbations (red) and waveform inversion of background model (blue). Note how constrained ERWI performs better at the final iterations for both smooth model (at iteration 32) and image (final) inversions.

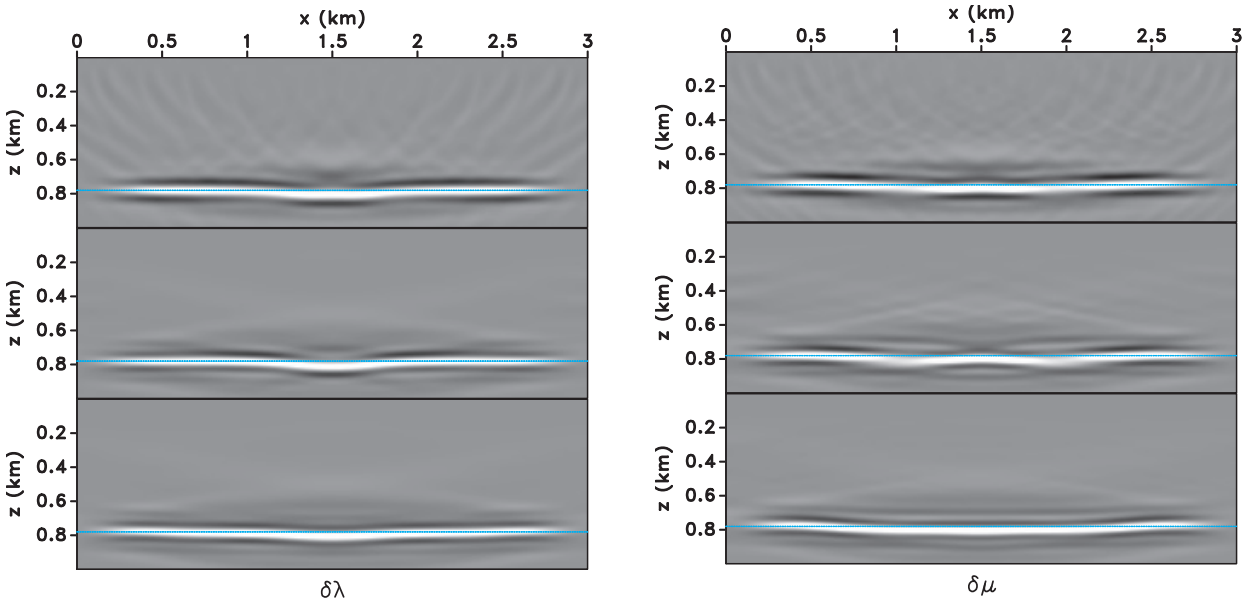

(a) (b)

Figure 6.4: RTM (top) and LSRTM (middle) images obtained with the initial velocity, and LSRTM (bottom) images obtained with constrained inverted velocities for (a) $\delta\lambda$ and (b) $\delta\mu$. The faint dashed cyan line corresponds to the true reflector. Note the sparse acquisition artifacts in RTM, the irregularity of the imaged flat reflector for RTM and LSRTM as imprint of wrong velocity, and the improved reflector flatness and focusing for LSRTM with the constrained inverted velocity.

6.3.2 Marmousi II

We test our method on a portion of the Marmousi II model (Martin et al., 2002) with independent P- and S-wave velocities. The model parameters, acquisition geometry and well locations used in our experiment are shown in Figure 6.5. Figure 6.5(a) shows the λ model, the horizontal line of receivers that record the displacement field at every grid point of the water bottom ($z = 0.17$ km), the 17 pressure sources located near the surface of the water layer ($z = 0.05$ km) spaced by 0.250 km. This acquisition geometry resembles a multicomponent ocean bottom seismic survey (OBS). Figure 6.5(b) shows the μ model and the three well locations at $x = [0.5, 2.1, 3.7]$ km, from where we have an estimate of the true model parameters, as shown in Figure 6.6. In the following ERWI experiments, we use a 7.5 Hz peak Ricker wavelet for the source signature.

Figure 6.7 shows the initial model (top), the reference model (middle) used in the definition of $\mathcal{J}_M$ (equation 6.18), and a low-pass version of the true model (bottom) that corresponds to the maximum resolution possible with the source wavelet of 7.5 Hz. We apply image-guided interpolation (Hale, 2009, 2010) to construct the reference model using as input the LSRTM energy image (Rocha et al., 2016b, 2017; Rocha and Sava, 2018) computed with the initial velocity (second image from top to bottom in Figure 6.11(b)), and the three velocity profiles from the well locations (Figure 6.6).

Figure 6.8 shows the inverted models for data-misfit minimization only ($\mathcal{J}_D$, top), data-misfit term plus reference model term ($\mathcal{J}_D + \mathcal{J}_M$, middle), and all three objection function terms including the petrophysical constraint ($\mathcal{J}_D + \mathcal{J}_M + \mathcal{J}_C$, bottom). Note the spurious artifacts that contaminate the model in the $\mathcal{J}_D$ inversion, and how they are attenuated with the introduction of the $\mathcal{J}_M$ and $\mathcal{J}_C$ terms. Comparing middle and bottom models in Figure 6.8, we note that adding only $\mathcal{J}_M$ is not sufficient for attenuating most of these artifacts, and therefore, the ERWI involving all three terms leads to the best inverted model.

To show how petrophysical constraints force the inverted model to follow the estimated geological trend from the wells, we show $\lambda - \mu$ plots in Figure 6.9. We only apply the petro-

physical constraints to the shallow model part (with values ranging from $[\lambda, \mu] = [5.75, 0]$ GPa to $[\lambda, \mu] = [7.5, 1.1]$ GPa) since it delivers the greatest impact in image quality. In addition, deeper model formations obey different $\lambda - \mu$ ratios, requiring the implementation of multiple constraint terms, which we avoid in these experiments for simplicity. The background of each individual plot in Figure 6.9 maps $\mathcal{J}_C$ for the selected model space. Figure 6.9(a) shows the model points from the three well locations, which serve as the basis for the constraint barriers $h_l = \lambda - 3.1\mu - 4.0$ and $h_u = -\lambda + 3.1\mu + 6.0$. Figure 6.9(b) shows the model pairs for the unconstrained inversion (J_D only) and how they spread beyond the barrier lines. Figure 6.9(c) shows the model samples for the constrained inversion ($\mathcal{J}_D + \mathcal{J}_M + \mathcal{J}_C$), which follow the imposed trend. The constrained model samples are mostly concentrated in the midpoint between the two barriers, but some samples comply more with data, as indicated by the points concentrated in the bottom-left corner ($\mu > 0.5$ GPa and $\lambda > 7.3$ GPa). Also, by observing the true model crossplot in Figure 6.9(d), we note that the constrained model in Figure 6.9(c) is closer to the true one relative to the unconstrained model in Figure 6.9(b).

Figure 6.10 shows the objective function evolution over iterations for both unconstrained (J_D) and constrained ($\mathcal{J}_D + \mathcal{J}_M + \mathcal{J}_C$) ERWIs. As explained previously, ERWI alternates between rough (red graph) and (blue) smooth model updates. Similarly to the simple reflector experiment, the unconstrained inversion exhibits better performance in the first iterations, up to iteration 17. For the remaining iterations, the constrained ERWI outperforms the unconstrained ERWI, with smaller magnitude and less variation of its objective function.

To show the impact on image quality from wavefield tomography with petrophysical constraints, least-squares migration and energy imaging condition, we show a series of images in Figure 6.11. For higher resolution, we use a 15.0 Hz peak Ricker wavelet for all shown images as opposed to the source signature used to obtain the ERWI models. From top to bottom, Figures 6.11(a) (for $\delta\lambda$) and 6.11(b) (for energy imaging condition) show (1) RTM images with the initial velocity, (2) LSRTM images with the initial velocity, (3) LSRTM with the

unconstrained ERWI model, (4) LSRTM with the constrained ERWI model, and (5) LSRTM with the true model. The energy images do not have backscattering artifacts characterized by low-wavenumber content, which otherwise occur for the perturbation images. Note the amplitude balance improvement, the mitigation of sparse-acquisition artifacts, and increase in reflectivity resolution from RTM (1) to LSRTM (2) even if imaging with incorrect velocity. Using the inverted velocities in (3) and (4) further improves LSRTM when compared to (2), with more obvious improvements in the $\delta\lambda$ images around $[x, z] = [1.5, 0.4]$ km. The LSRTM images that use the constrained model (4) show slight improvements when compared to its unconstrained counterpart (3): the most obvious feature is the mitigation of four diffraction-like artifacts around $[x, z] = [1.0, 0.3]$ km in the energy images. For a complete comparison among all images, we show LSRTM images with the true velocity (5) which represent the optimal result.

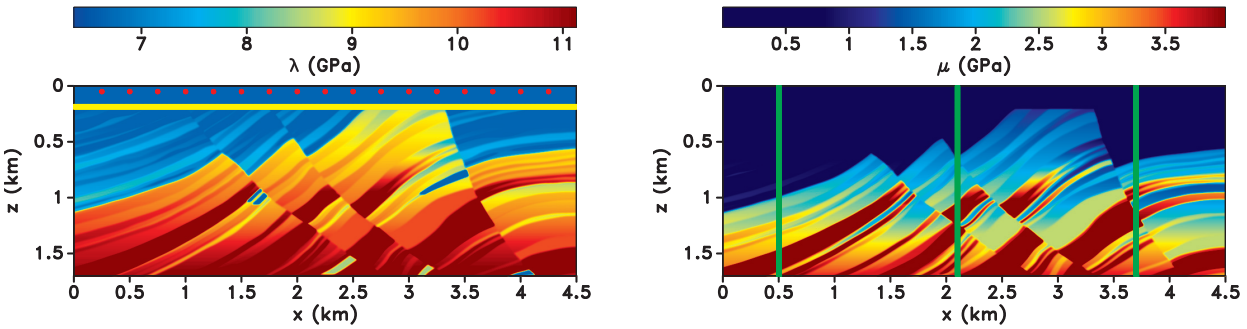

(a) (b)

Figure 6.5: Lamé parameters λ (a) and μ (b) from the Marmousi II model. The acquisition geometry, which consists of 17 pressure sources (red) near the water surface and a line (yellow) of multicomponent receivers, is also shown in (a). The locations for the three wells used as prior information are indicated by green lines in (b).

6.4 Conclusions

We use the mixed-domain elastic reflection waveform inversion framework, coupled with petrophysical constraints, to achieve both high-quality images and plausible earth models. Smooth updates are possible for the background model by separating the wavefields into their

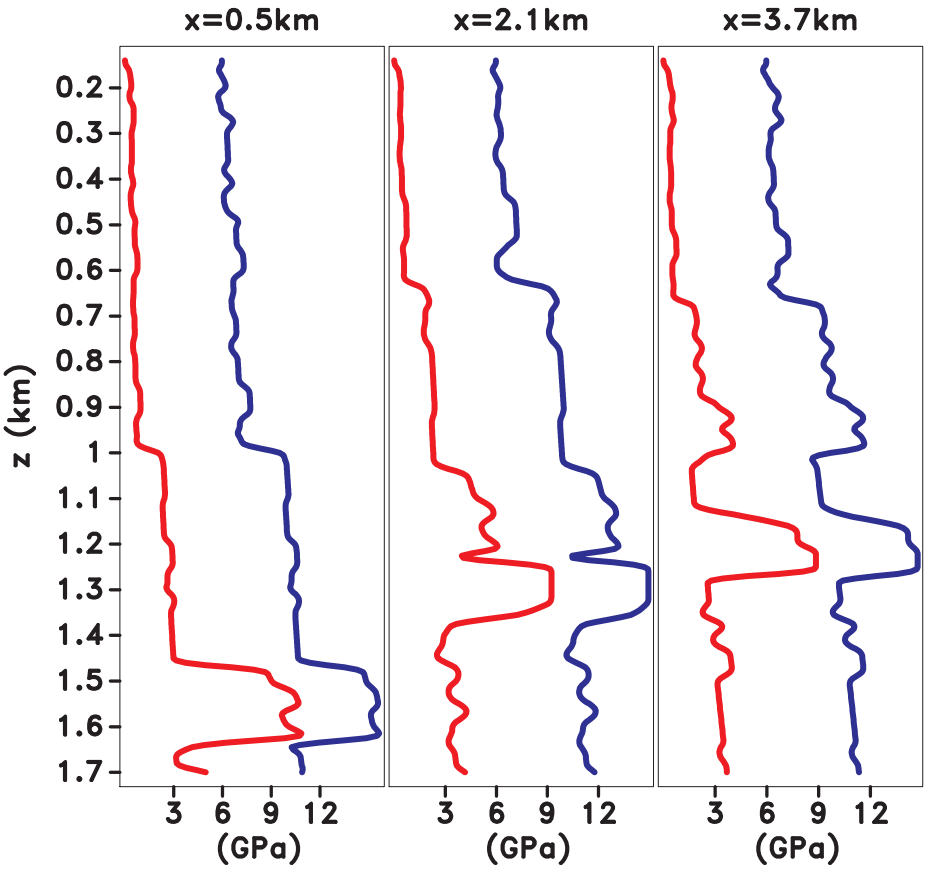

Figure 6.6: Lamé parameters λ (blue) and μ (red) well-log profiles at the three locations shown in Figure 6.5. This information is used for the reference model ($\mathcal{J}_M$) and to define the petrophysical constraints ($\mathcal{J}_C$) implemented in the ERWI experiments.

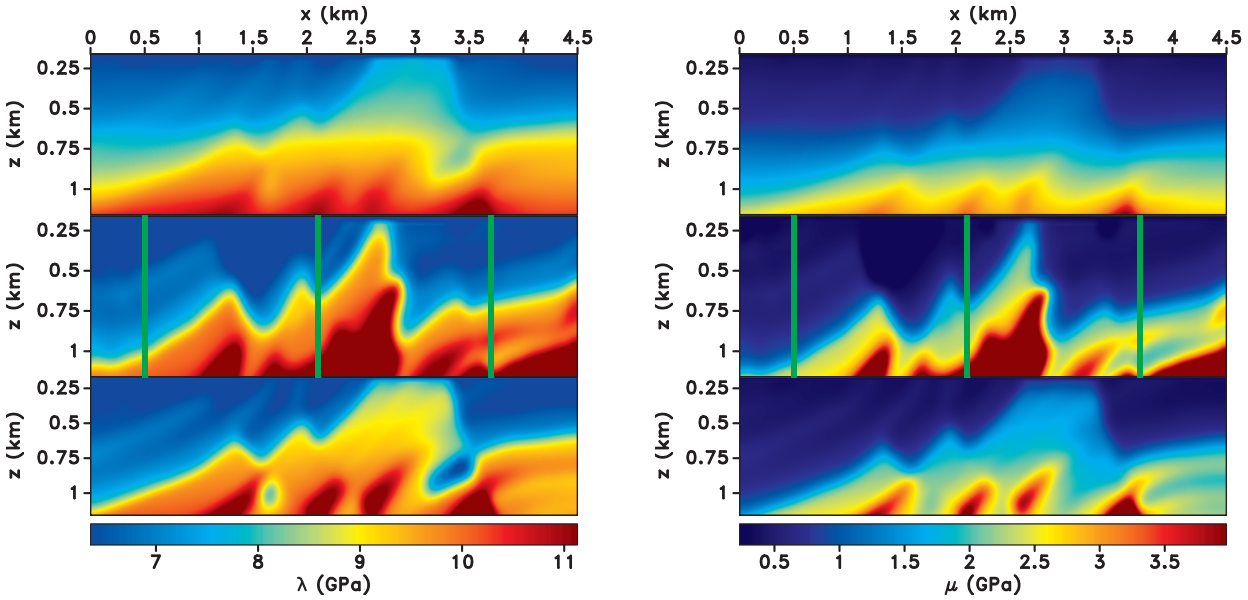

(a) (b)

Figure 6.7: Initial (top), reference (middle) and low-pass true (bottom) models. The green lines indicate the three well locations used as input for the image-guided interpolation among wells to create the reference model.

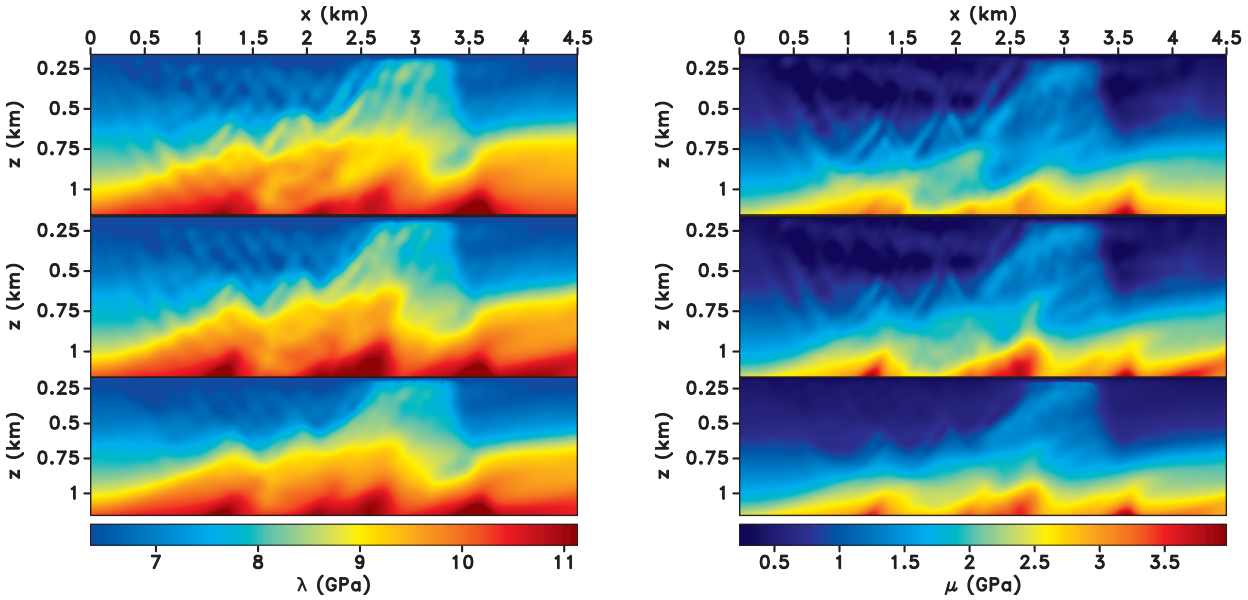

(a) (b)

Figure 6.8: Inverted models using the objective functions $\mathcal{J}_D$ (top), $\mathcal{J}_D + \mathcal{J}_M$ (middle), and $\mathcal{J}_D + \mathcal{J}_M + \mathcal{J}_C$. Note the attenuation of spurious artifacts with addition of reference model term (middle), and further improvement with petrophysical constraint term (bottom).

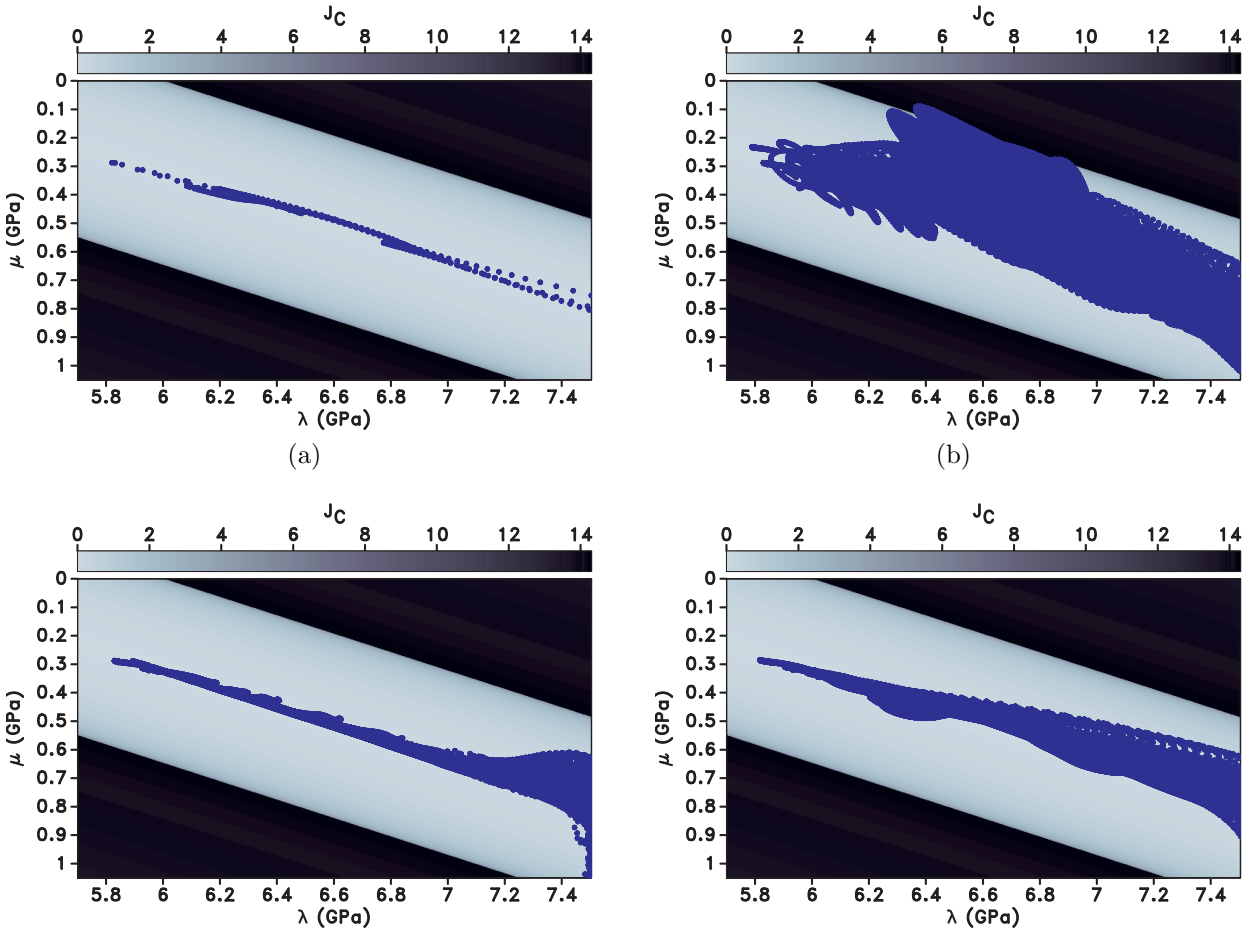

Figure 6.9: Crossplots in $\lambda - \mu$ space of (a) well-log samples, whose apparent slope is used to construct the barriers; (b) unconstrained inverted model; (c) constrained inverted model; and (d) true model. As opposed to the model points in (b), which do not follow a trend, the model pairs in (c) obey the imposed constrained constructed from (a) and conforms with the true model in (d).

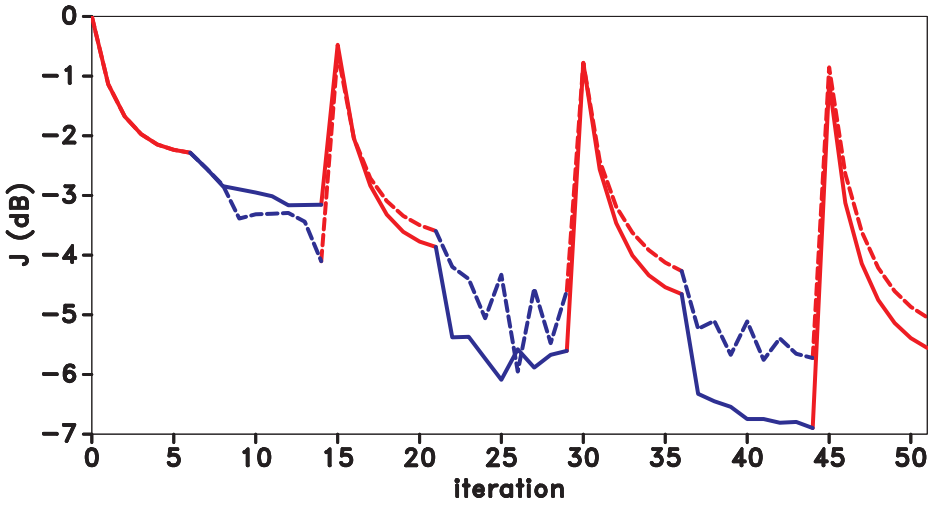

Figure 6.10: Objective functions in decibel scale for unconstrained (dashed) and constrained (solid) ERWIs, which alternate between least-squares migration of model perturbations (red) and waveform inversion of background model (blue). Note how constrained ERWI performs better at the final iterations for both the smooth model (at iteration 44) and the image (final) inversions. Also, the constrained ERWI objective function for waveform inversion (solid blue) exhibits less variation when compared to its unconstrained counterpart (dashed blue).

background and scattered constituents, whose proper correlation provides low-wavenumber gradients. Our model constraints are based on a linear trend derived from petrophysical input, which deters the inversion from delivering unphysical models with crosstalk artifacts. Although our constrained ERWI method has an additional constraint term in the objective function, we achieve improved convergence compared to conventional data-misfit minimization. We advocate for direct incorporation of prior geological information into wavefield tomography, which thus leads to robust model estimates and high-quality images, even with sparse acquisition and poor subsurface illumination.

6.5 Acknowledgments

We thank the sponsors of the Center for Wave Phenomena (CWP), whose support made this research possible. We acknowledge Antoine Guitton and CWP iTeam members for helpful discussions. We are grateful to Vladimir Li for suggestions on the image-guided

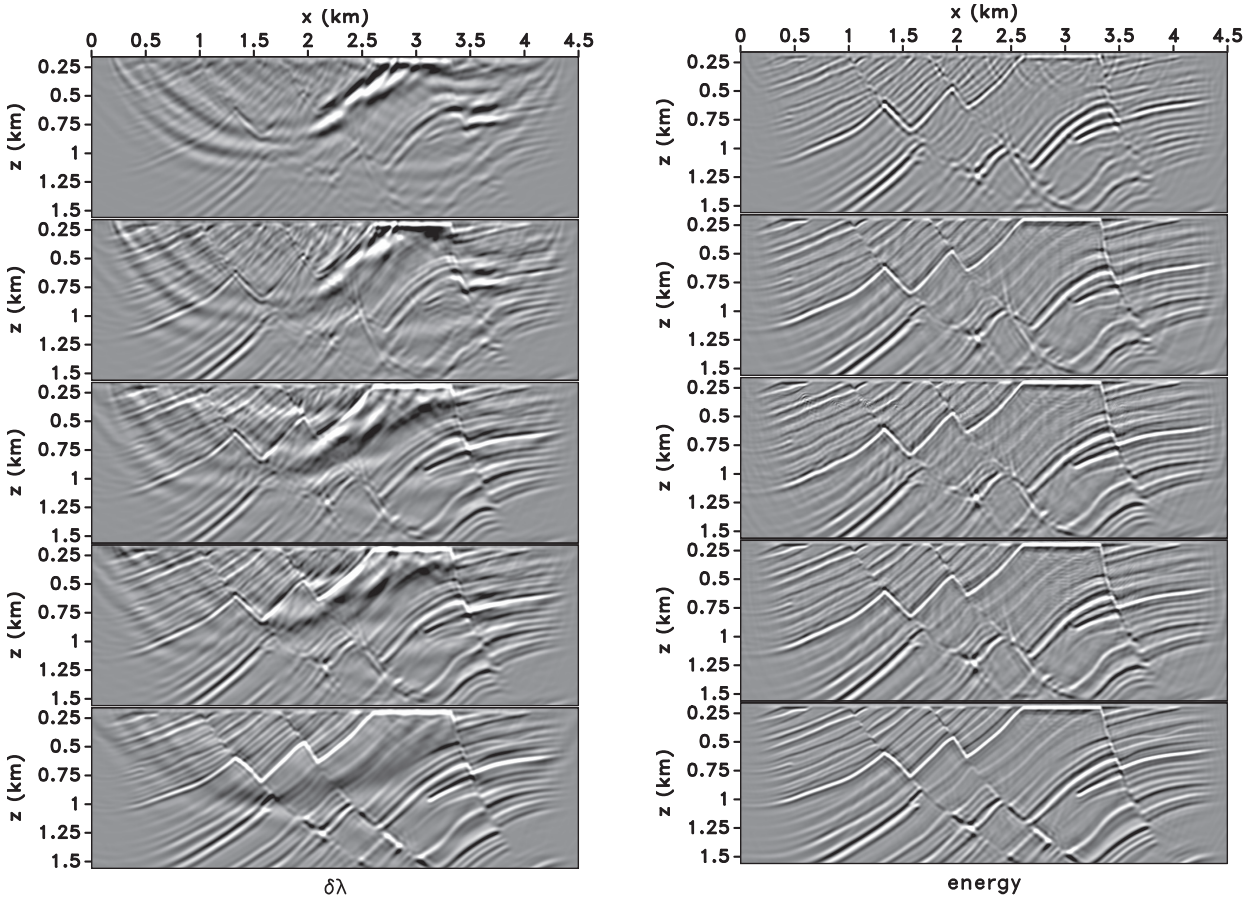

(a) (b)

Figure 6.11: From top to bottom: (1) RTM images with the initial velocity, LSRTM images with (2) initial velocity, (3) unconstrained, (4) constrained and (5) true models, for $\delta\lambda$ (a) and energy (b) imaging conditions. Note how the energy images are higher-quality and do not show low-wavenumber artifacts. Also note how improving the velocity model leads to better focused reflectors, and how least-squares migration is superior to conventional migration.

smoothing. The synthetic examples in this paper use the Madagascar open-source software package (Fomel et al., 2013) freely available from http://www.ahay.org.

6.6 Appendices

The appendices below elucidate specific points of this current chapter.

6.6.1 Single-scattering and migration operators based on model perturbations

We can write single-scattering modeling as

$$\delta\mathbf{d} = \mathbf{L}\delta\mathbf{m} = \left(\mathbf{K}_r\mathbf{A}\mathbf{S}\right)\delta\mathbf{m}\ , \tag{6.27}$$

where

$$\mathbf{S} = \begin{bmatrix} -D_t\dot{u}^0_1 & D_1\left(u^0_{1,1}+u^0_{3,3}\right) & 2D_1u^0_{1,1}+D_3\left(u^0_{1,3}+u^0_{3,1}\right) \\ -D_t\dot{u}^0_3 & D_3\left(u^0_{1,1}+u^0_{3,3}\right) & 2D_3u^0_{3,3}+D_1\left(u^0_{1,3}+u^0_{3,1}\right) \end{bmatrix}\ , \tag{6.28}$$

$$\delta\mathbf{m} = \begin{bmatrix} \delta\rho \\ \delta\lambda \\ \delta\mu \end{bmatrix}\ , \tag{6.29}$$

and $\mathbf{A}$ is the elastic wave-equation extrapolator. Indices $i,j = \{1,3\}$ refer to $\{x,z\}$. $u^0_{i,j}$ is the j-th derivative of the ith-component of the background vector wavefield $\mathbf{u}^0$. The superscript dot on u^0_i indicates time differentiation. D_t, D_1, and D_3 indicate derivative operators in time, x, and z, respectively, which are applied to the scattered wavefield instead of the background wavefield in the adjoint of single-scattering modeling: migration,

$$\delta\mathbf{m} = \mathbf{L}^{\mathrm{T}}\delta\mathbf{d} = \left(\mathbf{S}^{\mathrm{T}}\mathbf{A}^{\mathrm{T}}\mathbf{K}_r^{\mathrm{T}}\right)\delta\mathbf{d}\ , \tag{6.30}$$

where

$$\mathbf{S}^{\mathrm{T}} = \begin{bmatrix} -\dot{u}^0_1D_t & -\dot{u}^0_3D_t \\ \left(u^0_{1,1}+u^0_{3,3}\right)D_1 & \left(u^0_{1,1}+u^0_{3,3}\right)D_3 \\ 2u^0_{1,1}D_1+\left(u^0_{1,3}+u^0_{3,1}\right)D_3 & 2u^0_{3,3}D_3+\left(u^0_{1,3}+u^0_{3,1}\right)D_1 \end{bmatrix}\ . \tag{6.31}$$

Most elastic LSRTM implementations use images based on model perturbations (Alves and Biondi, 2016; Feng and Schuster, 2017; Xu et al., 2016; Duan et al., 2017; Ren et al., 2017).

6.6.2 Waveform inversion gradients in isotropic elastic media based on adjoint-state method

The expression for the waveform inversion gradient in equation 6.13 requires the computation of $\frac{\partial \mathbf{A}}{\partial \mathbf{m}}$, the derivative of the wave-equation operator with respect to model parameters (Tarantola, 1988; Tromp et al., 2005; Zhu et al., 2009). For each one of the model parameters, we have

$$\begin{bmatrix} \frac{\partial \mathbf{A}}{\partial \rho} \\ \frac{\partial \mathbf{A}}{\partial \lambda} \\ \frac{\partial \mathbf{A}}{\partial \mu} \end{bmatrix} \mathbf{u} = \begin{bmatrix} \frac{\partial}{\partial \rho} \\ \frac{\partial}{\partial \lambda} \\ \frac{\partial}{\partial \mu} \end{bmatrix} \left\{ \rho \ddot{\mathbf{u}} - \nabla \left[\lambda \left(\nabla \cdot \mathbf{u} \right) \right] - \nabla \cdot \left[\mu \left(\nabla \mathbf{u} + \nabla \mathbf{u}^{\mathrm{T}} \right) \right] - \mathbf{f} \right\}, \tag{6.32}$$

which leads to (using chain rule)

$$\begin{bmatrix} \frac{\partial \mathbf{A}}{\partial \rho} \\ \frac{\partial \mathbf{A}}{\partial \lambda} \\ \frac{\partial \mathbf{A}}{\partial \mu} \end{bmatrix} \mathbf{u} = \begin{bmatrix} \ddot{\mathbf{u}} \\ -\nabla \left(\nabla \cdot \mathbf{u} \right) \\ -\nabla \cdot \left(\nabla \mathbf{u} + \nabla \mathbf{u}^{\mathrm{T}} \right) \end{bmatrix}. \tag{6.33}$$

Therefore, we rewrite Equation 6.13 as

$$\frac{\partial \mathcal{J}_D}{\partial \mathbf{m}} = \begin{bmatrix} \frac{\partial \mathcal{J}_D}{\partial \rho} \\ \frac{\partial \mathcal{J}_D}{\partial \lambda} \\ \frac{\partial \mathcal{J}_D}{\partial \mu} \end{bmatrix} = \begin{bmatrix} \frac{\partial \mathbf{A}}{\partial \rho} \\ \frac{\partial \mathbf{A}}{\partial \lambda} \\ \frac{\partial \mathbf{A}}{\partial \mu} \end{bmatrix} \mathbf{u} \star \mathbf{a} = \begin{bmatrix} \ddot{\mathbf{u}} \star \mathbf{a} \\ -\nabla \left(\nabla \cdot \mathbf{u} \right) \star \mathbf{a} \\ -\nabla \cdot \left(\nabla \mathbf{u} + \nabla \mathbf{u}^{\mathrm{T}} \right) \star \mathbf{a} \end{bmatrix}. \tag{6.34}$$

Equation 6.34 shows that the gradient expression for waveform inversion uses similar derivative operators involved in wavefield extrapolation.

CHAPTER 7

CONCLUSION

In this thesis, I present various applications relevant to seismic imaging that exploit the concept of energy norm. One application utilizes an imaging condition for elastic wavefields in arbitrarily anisotropic media that mitigates spurious artifacts, such as low-wavenumber content caused by violating the single-scattering assumption in models with sharp contrasts in elastic properties. I implement this imaging condition in reverse time migration (RTM) for active-source seismic scenarios (Chapter 2). Similarly, I implement an analogous imaging condition for the passive-source case (Chapter 3), which involves a single wavefield extrapolated from the receivers towards the unknown passive source in the subsurface. Therefore, the energy norm formulation enables two straightforward imaging applications for different areas of seismology. Both techniques improve imaging without significant implementation obstacles, which exist in conventional methods that rely on wave-mode decomposition for anisotropic media.

The imaging technology based on wavefield extrapolation illustrated in Chapters 2 and 3 can be incorporated into the inversion framework. This improves the estimation of subsurface reflectivity by seeking the generalized inverse solution of the imaging problem, instead of the simpler application of the adjoint operator of single-scattering modeling. In Chapters 4 and 5, I explore both acoustic and elastic least-squares reverse time migration (LSRTM) methods that employ imaging operators based on the energy norm, in order to achieve a more accurate representation of subsurface reflectivity compared to standard RTM. For instance, acoustic LSRTM achieves expedited convergence rates with the energy imaging operators. For the passive-source scenario, I infer that improved estimates of source location and mechanism are possible with a similar least-squares inversion approach. The adjoint operator, which corresponds to the backpropagation of the recorded passive wavefield followed by the

application of the energy imaging condition, is defined and illustrated in Chapter 3; however, the forward modeling operator in this context requires a proper formulation that I will leave out for future work.

All of the aforementioned imaging methods, including the ones driven by least-squares inversion, require a sufficiently accurate earth model to avoid unfocused and mispositioned imaged structures. The earth model optimization through wavefield tomography requires a proper conditioning of the inverse problem. In Chapter 5, I demonstrate that conditioning wavefield tomography with petrophysical constraints may deliver geologically plausible models. The proposed mixed-domain tomography method separates the smooth and rough parts of the model, mitigating undesired high model wavenumbers during inversion, which otherwise impede accurate convergence. As demonstrated in all chapters, an accurate model from tomography enables the energy imaging technology to deliver high-quality images.

The methodology explored here is applicable to other fields of study, since one can formulate the energy imaging operators for other types of wavefields and wave equations. For instance, imaging methods using electromagnetic wavefields, such as ground-penetrating radar, include problems similar to those found in seismic imaging, and the energy norm can potentially be applied with effectiveness similar to that of seismic imaging. Additionally, as shown by He et al. (2017), RTM and LSRTM technologies are not restricted to seismic and are applicable to damage monitoring in composite metallic plates, which are utilized in aerospace engineering. Incorporating the energy imaging operators into LSRTM, but in the context of damage imaging in metallic plates, could potentially improve and expedite damage detection.

As demonstrated in this thesis, the wavefield imaging methods presented are successful with complex synthetic models and also with field datasets. Furthermore, because the underlying physics is quite general and applicable to other situations, the technology developed in this thesis has immense potential not only in seismology, but in other scientific areas including non-destructive monitoring.

REFERENCES CITED

Aki, K., and P. G. Richards, 2002, Quantitative Seismology, 2nd ed.: University Science Books.

Albertin, U., P. Sava, J. Etgen, and M. Maharramov, 2005, Adjoint wave-equation velocity analysis: 76th Annual International Meeting, SEG, Expanded Abstracts, 3345–3349.

Alford, R. M., 1986, Shear data in the presence of azimuthal anisotropy: 56th Annual International Meeting, SEG, Expanded Abstracts, 476–479.

Alves, G., and B. Biondi, 2016, Imaging condition for elastic reverse time migration: 86th Annual International Meeting, SEG, Expanded Abstracts, 3959–3965.

Aminzadeh, F., N. Burkhard, L. Nicoletis, F. Rocca, and K. Wyatt, 1994, SEG/EAEG 3-D modeling project: 2nd update: The Leading Edge, **13**, 949–952.

Aoki, N., and G. T. Schuster, 2009, Fast least-squares migration with a deblurring filter: Geophysics, **74**, no. 6, WCA83–WCA93.

Artman, B., I. Podladtchikov, and B. Witten, 2010, Source location using time-reverse imaging: Geophysical Prospecting, **58**, no. 1, 861–873.

Asnaashari, A., R. Brossier, S. Garambois, F. Audebert, P. Thore, and J. Virieux, 2013, Regularized seismic full waveform inversion with prior model information: Geophysics, **78**, no. 2, R25–R36.

Ay, E., H. S. Kuleli, F. Song, and M. N. Toksoz, 2012, Detection and enhancement of microseismic signals with correlation operators: cross product and master event methods: International Geophysical Conference and Oil & Gas Exhibition.

Baker, T., R. Granat, and R. W. Clayton, 2005, Real-time earthquake location using Kirchhoff reconstruction: Bulletin of the Seismological Society of America, **95**, 699–707.

Balch, A. H., and C. Erdemir, 1994, Sign-change correction for prestack migration of P-S converted wave reflections: Geophysical Prospecting, **42**, 637–663.

Baumstein, A., 2013, POCS-based geophysical constraints in multiparameter full wavefield inversion: 75th European Association of Geoscientists and Engineers Conference and Exhibition.

Baysal, E., D. D. Kosloff, and J. W. C. Sherwood, 1983, Reverse time migration: Geophysics, **48**, 1514–1524.

Bazargani, F., and R. Snieder, 2016, Optimal source imaging in elastic media: Geophysical Journal International, **204**, no. 1, 1134–1147.

Behura, J., F. Forghani, and F. Bazargani, 2013, Improving microseismic imaging: role of acquisition, velocity model, and imaging condition: 83rd Annual International Meeting, SEG, Expanded Abstracts, 2119–2123.

Ben-Menahem, A., and S. J. Singh, 1981, Seismic waves and sources: Springer-Verlag.

Biondi, B., 2012, 3D Seismic Imaging: Society of Exploration Geophysicists.

Bishop, T., K. Bube, R. Cutler, R. Langan, P. Love, J. Resnick, R. Shuey, D. Spindler, and H. Wyld, 1985, Tomographic determination of velocity and depth in laterally varying media: Geophysics, **50**, 903–923.

Blias, E., and V. Grechka, 2013, Analytic solutions to the joint estimation of microseismic event locations and effective velocity model: Geophysics, **78**, no. 3, KS51–KS61.

Boas, M. L., 2006, Mathematical Methods in the Physical Sciences, 3rd ed.: John Wiley & Sons.

Bording, R. P., A. Gersztenkorn, L. R. Lines, J. A. Scales, and S. Treitel, 1987, Applications of seismic traveltime tomography: Geophysical Journal of the Royal Astronomincal Society, **90**, 285–303.

Brandsberg-Dahl, S., N. Chemingui, D. Whitmore, S. Crawley, E. Klochikhina, and A. Valenciano, 2013, 3D RTM angle gathers using an inverse scattering imaging condition: 83rd Annual International Meeting, SEG, Expanded Abstracts, 3958–3962.

Brossier, R., S. Operto, and J. Virieux, 2010, Which data residual norm for robust elastic frequency-domain full waveform inversion?: Geophysics, **75**, no. 3, R37–R46.

Burridge, R., M. V. de Hoop, D. Miller, and C. Spencer, 1998, Multiparameter inversion in anisotropic elastic media: Geophysical Journal International, **134**, 757–777.

Cerveny, V., 2005, Seismic ray theory: Cambridge University Press.

Chang, W.-F., and G. A. McMechan, 1987, Elastic reverse-time migration: Geophysics, **52**, 1365–1375.

Chavent, G., and R.-E. Plessix, 1999, An optimal true–amplitude least–squares prestack depth–migration operator: Geophysics, **64**, 508–515.

Chen, T., and L. Huang, 2014, Elastic reverse-time migration with an excitation amplitude imaging condition: 84th Annual International Meeting, SEG, Expanded Abstracts, 1868–1872.

Cheng, J., and S. Fomel, 2014, Fast algorithms for elastic-wave-mode separation and vector decomposition using low-rank approximation for anisotropic media: Geophysics, **79**, no. 4, C97–C110.

Chi, B., L. Dong, and Y. Liu, 2014, Full waveform inversion method using envelope objective function without low frequency data: Journal of Applied Geophysics, **109**, 36–46.

Claerbout, J. F., 1971, Toward a unified theory of reflector mapping: Geophysics, **36**, 467–481.

———, 1992, Earth soundings analysis: Processing versus inversion: Blackwell Scientific Publications.

Crampin, S., 1985, Evaluation of anisotropy by shear-wave splitting: Geophysics, **50**, 142–152.

Dai, W., C. Boonyasiriwat, and G. Schuster, 2010, 3D multisource least-squares reverse-time migration: 80th Annual International Meeting, SEG, Expanded Abstracts, 3120–3124.

Dai, W., and G. T. Schuster, 2012, Plane-wave Least-squares Reverse Time Migration: 82rd Annual International Meeting, SEG, Expanded Abstracts.

Dellinger, J., and J. Etgen, 1990, Wave-field separation in two-dimensional anisotropic media: Geophysics, **55**, 914–919.

Denli, H., and L. Huang, 2008, Elastic-wave reverse-time migration with a wavefield-separation imaging condition: 78th Annual International Meeting, SEG, Expanded Abstracts,, 2346–2350.

Diaz, E., and P. Sava, 2015, Wavefield tomography using reverse time migration backscattering: Geophysics, **80**, no. 1, R57–R69.

Diaz, E., P. Sava, and T. Yang, 2013, Data-domain and image-domain wavefield tomography: The Leading Edge, **32**, no. 1, 1064–1072.

Dong, S., J. Cai, M. Guo, S. Suh, Z. Zhang, B. Wang, and Z. Li, 2012, Least-squares reverse time migration: towards true amplitude imaging and improving the resolution: 82rd Annual International Meeting, SEG, Expanded Abstracts.

Douma, H., D. Yingst, I. Vasconcelos, and J. Tromp, 2010, On the connection between artifact filtering in reverse-time migration and adjoint tomography: Geophysics, **75**, no. 6, S219–S223.

Douma, J., and R. Snieder, 2015, Focusing of elastic waves for microseismic imaging: Geophysical Journal International, **200**, no. 1, 390–401.

Dragoset, B., 1999, A practical approach to surface multiple attenuation: The Leading Edge, **18**, 104–108.

Du, Q., X. Gong, M. Zhang, Y. Zhu, and G. Fang, 2014a, 3D PS-wave imaging with elastic reverse-time migration: Geophysics, **79**, no. 5, S173–S184.

Du, Q., M. Zhang, G. Fang, X. Gong, and C. Guo, 2014b, Relatively amplitude-preserved ADCIGs based on elastic RTM by modifying the initial condition as the boundary condition: 84th Annual International Meeting, SEG, Expanded Abstracts, 1888–1893.

Du, X., R. Fletcher, E. Mobley, and E. Yarman, 2012, Source and Receiver Illumination Compensation for Reverse-time Migration: 74th European Association of Geoscientists and Engineers Conference and Exhibition.

Duan, Y., and P. Sava, 2014, Elastic reverse-time migration with OBS multiples: 84th Annual International Meeting, SEG, Expanded Abstracts, 4071–4076.

———, 2015, Scalar imaging condition for elastic reverse time migration: Geophysics, **80**, no. 4, S127–S136.

———, 2016, Elastic wavefield tomography with physical model constraints: Geophysics, **81**, no. 6, R447–R456.

Duan, Y., P. Sava, and A. Guitton, 2017, Elastic least-squares reverse time migration: Geophysics, **82**, no. 4, S315–S325.

Duncan, P., and L. Eisner, 2010, Reservoir characterization using surface microseismic monitoring: Geophysics, **75**, no. 5, A139–A146.

Dussaud, E., W. W. Symes, P. Williamson, L. Lemaistre, P. Singer, B. Denel, and A. Cherrett, 2008, Computational strategies for reverse–time migration: 78th Annual International Meeting, SEG, Expanded Abstracts, 2267–2271.

Dutta, G., and G. T. Schuster, 2014, Attenuation compensation for least-squares reverse time migration using the viscoacoustic-wave equation: Geophysics, **79**, no. 6, S251–S262.

Eisner, L., D. Abbott, W. Barker, J. Lakings, and M. Thornton, 2008, Noise suppression for detection and location of microseismic events using a matched filter: 78th Annual International Meeting, SEG, Expanded Abstracts, 1431–1435.

Etgen, J. T., 1988, Prestacked migration of P- and SV-waves: 58th Annual International Meeting, SEG, Expanded Abstracts, 972–975.

Farmer, P., Z. Z. Zhou, and D. Jones, 2009, The role of reverse time migration in imaging and model estimation: The Leading Edge, **28**, no. 4, 436–441.

Feng, Z., and G. T. Schuster, 2017, Elastic least-squares reverse time migration: Geophysics, **82**, no. 2, S143–S157.

Fletcher, R. P., D. Nichols, R. Bloor, and R. T. Coates, 2016, Least-squares migration : Data domain versus image domain using point spread functions: The Leading Edge, **35**, no. 2, 157–162.

Fomel, S., P. Sava, I. Vlad, Y. Liu, and V. Bashkardin, 2013, Madagascar: open-source software project for multidimensional data analysis and reproducible computational experiments: Journal of Open Research Software, 8th ed., DOI: http://dx.doi.org/10.5334/jors.ag.

Gajewski, D., and E. Tessmer, 2005, Reverse modelling for seismic event characterization: Geophysical Journal International, **163**, no. 1, 276–284.

Gao, F., P. Williamson, and R. G. Pratt, 2014, A new objective function for full waveform inversion : differential semblance in the data domain: 84th Annual International Meeting, SEG, Expanded Abstracts, 1178–1183.

Gasso, G., A. Rakotomamonjy, and S. Canu, 2009, Recovering sparse signals with a certain family of non-convex penalties and DC programming: IEEE Transactions on Signal Processing, **57**, 4686–4698.

Gauthier, O., J. Virieux, and A. Tarantola, 1986, Two-dimensional nonlinear inversion of seismic waveforms: Numerical results: Geophysics, **51**, 1387–1403.

Godfrey, R., P. Kristiansen, B. Armstrong, M. Copper, and E. Thorogood, 1998, Imaging the Foinaven ghost: 68th Annual International Meeting, SEG, Expanded Abstracts, 1333–1335.

Godwin, J., and P. Sava, 2013, A comparison of shot-encoding schemes for wave-equation migration: Geophysical Prospecting, **61**, no. 1, 391–408.

Golub, G. H., and C. F. V. Loan, 1996, Matrix computations, 3rd ed.: John Hopkins University Press.

Gong, T., B. D. Nguyen, and G. A. McMechan, 2016, Polarized wavefield magnitudes with optical flow for elastic angle-domain common-image gathers: Geophysics, **81**, no. 4, S239–S251.

Grechka, V., and W. Heigl, 2017, Microseismic monitoring: Society of Exploration Geophysicists.

Grechka, V., and M. Kachanov, 2006, Effective elasticity of fractured rocks: A snapshot of the work in progress: Geophysics, **71**, no. 6, W45–W58.

Guitton, A., 2004, Amplitude and kinematic corrections of migrated images for nonunitary imaging operators: Geophysics, **69**, 1017–1024.

———, 2017, Fast 3D Least-Squares RTM by Preconditioning with Non-Stationary Matching Filters: 87th Annual International Meeting, SEG, Expanded Abstracts.

Guitton, A., G. Ayeni, and E. Daz, 2012, Constrained full–waveform inversion by model reparameterization: Geophysics, **77**, no. 2, R117–R127.

Guitton, A., and G. Cambois, 1999, Multiple elimination using a pattern–recognition technique: The Leading Edge, **18**, 92–98.

Guitton, A., B. Kaelin, and B. Biondi, 2007a, Least-squares attenuation of reverse-time-migration artifacts: Geophysics, **72**, no. 1, S19–S23.

Guitton, A., B. Kaelin, and F. Ortigosa, 2007b, 3D migration of a simulated wide-azimuth towed streamer survey: 77th Annual International Meeting, SEG, Expanded Abstracts, 2049–2052.

Guo, Q., and T. Alkhalifah, 2017, Elastic reflection-based waveform inversion with a nonlinear approach: Geophysics, **82**, no. 6, R309–R321.

Hadidi, M. T., M. Sabih, D. E. Johnston, and C. Calderon-Macias, 1999, Mobil's results for the 1997 workshop on multiple attenuation: The Leading Edge, **18**, 100–103.

Hale, D., 2009, Imageguided blended neighbor interpolation of scattered data: 79th Annual International Meeting, SEG, Expanded Abstracts, 1127–1131.

———, 2010, Imageguided 3D interpolation of borehole data: 80th Annual International Meeting, SEG, Expanded Abstracts, 1266–1270.

He, J., D. Rocha, P. Leser, P. Sava, and W. Leser, 2017, Least-squares reverse time migration (LSRTM) for damage imaging using Lamb waves: 44th Annual Review of Progress in Quantitative Nondestructive Evaluation.

Helbig, K., 1994, Foundations of anisotropy for exploration seismics: Elsevier Science Serials.

Hestenes, M. R., and E. Stiefel, 1952, Methods of Conjugate Gradients for Solving Linear Systems: Journal of Research of the National Bureau of Standards, **49**, no. 6, 409–436.

Hicks, G. J., and R. G. Pratt, 2001, Reflection waveform inversion using local descent methods: estimating attenuation and velocity over a gas–sand deposit: Geophysics, **66**, no. 2, 598–612.

Hindlet, F., and P. Kolb, 1988, Inversion of prestack field data: An application to 1-D acoustic media: 58th Annual International Meeting, SEG, Expanded Abstracts, 1073–1076.

Hobro, J. W. D., C. H. Chapman, and J. O. A. Robertsson, 2014, A method for correcting acoustic finite-difference amplitudes for elastic effects: Geophysics, **79**, no. 4, T243–T255.

Hokstad, K., R. Mittet, and M. Landrø, 1998, Elastic reverse time migration of marine walkaway vertical seismic profiling data: Geophysics, **63**, 1685–1695.

Hou, J., and W. W. Symes, 2016, Accelerating extended least-squares migration with weighted conjugate gradient iteration: Geophysics, **81**, no. 4, S165–S179.

———, 2018, Inversion velocity analysis in the subsurface-offset domain: Geophysics, **83**, R189–R200.

Hu, C., U. Albertin, and T. Johnsen, 2014, Optical flow equation based imaging condition for elastic reverse time migration: 84th Annual International Meeting, SEG, Expanded Abstracts, 3877–3881.

Huang, J., D. Si, Z. Li, and J. Huang, 2016a, Plane-wave least-squares reverse time migration in complex VTI media: 86th Annual International Meeting, SEG, Expanded Abstracts, 441–446.

Huang, W., P. Deng, and H.-W. Zhou, 2016b, Least-squares reverse-time migration with hessian preconditioning: 86th Annual International Meeting, SEG, Expanded Abstracts, 1043-1046.

Huang, Y., R. Nammour, and W. Symes, 2016c, Flexibly preconditioned extended least-squares migration in shot-record domain: Geophysics, **81**, no. 5, S299–S315.

Jeremic, A., J. Kurpan, M. Thornton, and P. Duncan, 2015, Passive seismic multicomponent imaging using geometrical optics theory: 85th Annual International Meeting, SEG, Expanded Abstracts, 2610–2614.

Jeremic, A., J. Kurpan, M. Thornton, and M. Mueller, 2014, Extending passive seismic imaging to account for source mechanism effects: 84th Annual International Meeting, SEG, Expanded Abstracts, 3868–3871.

Jiang, Z., 2016, Reverse-time depth migration in elastic media: CSEG Recorder, **39**, no. 10, 42–47.

Jiang, Z., and G. T. Schuster, 2005, Target–oriented least squares migration: 73rd Annual International Meeting, SEG, Expanded Abstracts, 4193–4197.

Jing, C., T. A. Dickens, and G. A. Winbow, 2006, Vector imaging of converted wave data in laterally uniform media with VTI anisotropy: Geophysics, **71**, no. 4, S141–S145.

Kamath, N., and I. Tsvankin, 2016, Elastic full-waveform inversion for VTI media: methodology and sensitivity analysis: Geophysics, **81**, no. 2, C53–C68.

Kao, H., and S. Shan, 2004, The source-scanning algorithm: Mapping the distribution of seismic sources in time and space: Geophysical Journal International, **157**, 589–594.

Kazemi, N., and M. Sacchi, 2014, Filter-based least squares wave equation shot profile migration: 76th EAGE Conference and Exhibition, EAGE, Expanded Abstracts.

Kazemi, N., and M. D. Sacchi, 2015, Block row recursive least-squares migration: Geophysics, **80**, no. 5, A95–A101.

Kim, B. Y., S. J. Seol, H.-Y. Lee, and J. Byun, 2016, Prestack elastic generalized screen migration for multicomponent data: Journal of Applied Geophysics, **126**, no. 2, 116–127.

Kiyashchenko, D., R.-E. Plessix, and B. Kashtan, 2007, Modified imaging principle: An alternative to preserved-amplitude least-squares wave-equation migration: Geophysics, **72**, no. 6, S221–S230.

Köhn, D., D. D. Nil, A. Kurzmann, A. Przebindowska, and T. Bohlen, 2012, On the influence of model parameterization in elastic full waveform tomography: Geophysical Journal International, **191**, 325–345.

Kuehl, H., and M. D. Sacchi, 2003, Least-squares wave-equation migration for AVO/AVA inversion: Geophysics, **68**, 262–273.

Lailly, P., 1983, The seismic inverse problem as a sequence of before stack migrations: Conference on Inverse Scattering, Theory and Application: Society of Industrial and Applied Mathematics, Expanded Abstracts, 206–220.

Lamont, M. G., B. M. Hartley, and N. F. Uren, 1999, Multiple attenuation using the MMO and ISR preconditioning transforms: The Leading Edge, **18**, 110–114.

Lanczos, C., 1970, The variational principles of mechanics, 4th ed.: Dover Publications.

Levin, S. A., 1984, Principle of reverse-time migration: Geophysics, **49**, 581–583.

Li, Y., P. Shen, and C. Perkins, 2012, VTI migration velocity analysis using RTM: 82nd Annual International Meeting, SEG, Expanded Abstracts, 1–6.

Lines, L. R., 1991, Applications of tomography to borehole and reflection seismology: The Leading Edge, **10**, no. 7, 11–17.

Liu, F., D. W. Hanson, N. D. Whitmore, R. S. Day, and R. H. Stolt, 2006, Toward a unified analysis for source plane-wave migration: Geophysics, **71**, no. 4, S129–S139.

Liu, Q., and Y. J. Gu, 2012, Seismic imaging: From classical to adjoint tomography: Tectonophysics, **566**, 31–66.

Liu, Y., J. Teng, T. Xu, Z. Bai, H. Lan, and J. Badal, 2016, An efficient step-length formula for correlative least-squares reverse time migration: Geophysics, **81**, no. 4, S221–S238.

Lokshtanov, D., 1999, Multiple suppression by data–consistent deconvolution: The Leading Edge, **18**, 115–119.

Lu, R., P. Traynin, and J. E. Anderson, 2009, Comparison of elastic and acoustic reverse–time migration on the synthetic elastic Marmousi–II OBC dataset: 79th Annual International Meeting, SEG, Expanded Abstracts, 2799–2803.

Lu, R., P. Traynin, T. Dickens, and J. Anderson, 2010, Impact of TTI Anisotropy on Elastic Reverse Time Migration: 72nd EAGE Annual Meeting.

Luo, S., and D. Hale, 2014, Least-squares migration in the presence of velocity errors: Geophysics, **79**, no. 4, S153–S161.

Ma, Y., and D. Hale, 2013, Wave-equation reflection traveltime inversion with dynamic warping and full-waveform inversion: Geophysics, **78**, no. 6, R223–R233.

Manduca, A., T. Oliphant, M. Dresner, J. Mahowald, S. Kruse, E. Amromin, J. Felmlee, J. Greenleaf, and R. Ehman, 2001, Magnetic resonance elastography: non-invasive mapping of tissue elasticity: Medical Image Analysis, **5**, 237–254.

Martin, G., K. Marfurt, and S. Larsen, 2002, Marmousi-2, an updated model for the investigation of avo in structurally complex areas: 72nd Annual International Meeting, SEG, Expanded Abstracts, 1979–1982.

Maxwell, S., 2010, Microseismic: Growth born from success: The Leading Edge, **29**, 338–343.

———, 2014, Microseismic Imaging of Hydraulic Fracturing: Improved Engineering of Unconventional Shale Reservoirs: Society of Exploration Geophysicists - Distinguished Instructor Series.

Maxwell, S., J. Rutledge, R. Jones, and M. Fehler, 2010, Petroleum reservoir characterization using downhole microseismic monitoring: Geophysics, **75**, no. 5, A129–A137.

McGarry, R., and Y. Qin, 2013, Direction-vector-based angle gathers from anisotropic elastic RTM: 83rd Annual International Meeting, SEG, Expanded Abstracts, 3820–3824.

McMechan, G. A., 1982, Determination of source parameters by wavefield extrapolation: Geophysical Journal International, **71**, no. 3, 613–628.

———, 1983, Migration by extrapolation of time dependent boundary values: Geophysical Prospecting, **31**, 413–420.

Michel, O. J., and I. Tsvankin, 2013, Gradient computation for full-waveform inversion of microseismic data in VTI media: 83rd Annual International Meeting, SEG, Expanded Abstracts, 2238–2242.

Mikhailov, O., J. Johnson, E. Shoshitaishvili, and C. Frasier, 2001, Practical approach to joint imaging of multicomponent data: The Leading Edge, **20**, 1016–1021.

Morse, P., and H. Feshbach, 1953, Methods of Theoretical Physics, 1st vol: McGraw-Hill.

Mulder, W., and A. ten Kroode, 2002, Automatic velocity analysis by differential semblance optimization: Geophysics, **67**, 1184–1191.

Nakata, N., and G. C. Beroza, 2016, Reverse time migration for microseismic sources using the geometric mean as an imaging condition: Geophysics, **81**, no. 2, KS51–KS60.

Nemeth, T., C. Wu, and G. T. Schuster, 1999, Least–squares migration of incomplete reflection data: Geophysics, **64**, 208–221.

Oh, J.-W., and T. Alkhalifah, 2016, Elastic orthorhombic anisotropic parameter inversion: an analysis of parameterization: Geophysics, **81**, no. 6, C279–293.

Operto, S., Y. Gholami, V. Prieux, A. Ribodetti, R. Brossier, L. Metivier, and J. Virieux, 2013, A guided tour of multiparameter full-waveform inversion with multicomponent data: from theory to practice: The Leading Edge, **32**, no. 9, 1040–1054.

Pan, W., and K. A. Innanen, 2016, A summary of several challenges facing multi-parameter elastic full waveform inversion: CSEG recorder, **41**, no. 8, 36–39.

Peng, J., C. Roos, and T. Terlaky, 2002, Self-regular functions and new search directions for linear and semidefinite optimization: Mathematical Programming, **93**, 129–171.

Pestana, R., A. W. G. dos Santos, and E. S. Araujo, 2013, RTM imaging condition using impedance sensitivity kernel combined with Poynting vector: 13th International Congress of The Brazilian Geophysical Society.

Peters, B., Z. Fang, B. R. Smithyman, and F. J. Herrmann, 2015, Regularizing waveform inversion by projections onto convex sets - application to the 2D Chevron 2014 synthetic blind-test dataset: University of British Columbia - Seismic Laboratory for Imaging and Modeling - Research Report.

Phadke, S., and S. Dhubia, 2012, Reverse time migration of marine models with elastic wave equation and amplitude preservation: 82nd Annual International Meeting, SEG, Expanded Abstracts.

Plessix, R., and W. Mulder, 2004, Frequency-domain finite-difference amplitude-preserving migration: Geophysical Journal International, **157**, 975–987.

Plessix, R. E., 2006, A review of the adjoint-state method for computing the gradient of a functional with geophysical applications: Geophysical Journal International, **167**, no. 2, 495–503.

Plessix, R. E., P. Milcik, H. Rynja, A. Stopin, K. Matson, and S. Abri, 2013, Multiparameter full-waveform inversion: Marine and land examples: The Leading Edge, **32**, no. 9, 1030–1038.

Ravasi, M., and A. Curtis, 2013, Elastic imaging with exact wavefield extrapolation for application to ocean-bottom 4C seismic data: Geophysics, **78**, no. 6, S265–S284.

Ren, Z., Y. Liu, and M. K. Sen, 2017, Least-squares reverse time migration in elastic media: Geophysical Journal International, **208**, no. 2, 1103–1125.

Rickett, J., A. Guitton, and D. Gratwick, 2001, Adaptive multiple subtraction with non-stationary helical shaping filters: 63rd Annual Meeting, European Association of Geoscientists and Engineers, Expanded Abstracts, P167.

Rickett, J., and P. Sava, 2002, Offset and angle-domain common image-point gathers for shot-profile migration: Geophysics, **67**, 883–889.

Rickett, J. E., 2003, Illumination-based normalization for wave-equation depth migration: Geophysics, **68**, 1371–1379.

Robert, A., 2005, Linear algebra: Examples and applications: World Scientific, **1**.

Rocha, D., and P. Sava, 2018, Elastic least-squares reverse-time migration using the energy norm: Geophysics, **83**, no. 3, 000–000.

Rocha, D., N. Tanushev, and P. Sava, 2016a, Acoustic wavefield imaging using the energy norm: Geophysics, **81**, no. 4, S151–S163.

———, 2016b, Isotropic elastic wavefield imaging using the energy norm: Geophysics, **81**, no. 4, S207–S219.

———, 2017, Anisotropic elastic wavefield imaging using the energy norm: Geophysics, **82**, no. 3, S225–S234.

Romero, L. A., D. C. Ghiglia, C. C. Ober, and S. A. Morton, 2000, Phase enconding of shot records in prestack migration: Geophysics, **65**, 426–436.

Ronen, S., L. Comeaux, and X.-G. Miao, 2005, Imaging downgoing waves from ocean bottom stations: 75th Annual International Meeting, SEG, Expanded Abstracts, 963–967.

Saenger, E. H., 2011, Time reverse characterization of sources in heterogeneous media: NDT & E International, **44**, 751–759.

Sava, P., 2014, A comparative review of wavefield tomography methods: Center for Wave Phenomena (CWP) Report # 802.

Sava, P., and E. Asphaug, 2018, 3D radar wavefield tomography of comet interiors: Advances in Space Research.

Sava, P., and B. Biondi, 2004a, Wave-equation migration velocity analysis - I: Theory: Geophysical Prospecting, **52**, 593–606.

———, 2004b, Wave-equation migration velocity analysis - II: Subsalt imaging example: Geophysical Prospecting, **52**, 607–623.

Sava, P., and S. Fomel, 2006, Time-shift imaging condition in seismic migration: Geophysics, **71**, no. 6, S209–S217.

Sava, P., and I. Vasconcelos, 2011, Extended imaging condition for wave-equation migration: Geophysical Prospecting, **59**, 35–55.

Scales, J., 1987, Tomographic inversion via the conjugate gradient method: Geophysics, **52**, 179–185.

Schoenberg, M., 1983, Reflection of elastic waves from periodically stratified media with interfacial slip: Geophysical Prospecting, **31**, 265–292.

Shao, Y., and C. Lu, 2009, A direct proof of uniqueness of square-root of a positive semi-definite tensor: Applied Mathematics and Mechanics, **30**, 713–716.

Shen, P., and W. W. Symes, 2008, Automatic velocity analysis by shot profile migration: Geophysics, **73**, VE49–VE59.

Shen, P., W. W. Symes, and C. C. Stolk, 2005, *in* Differential semblance velocity analysis by waveequation migration.

Shin, C., and W. Ha, 2008, A comparison between the behavior of objective functions for waveform inversion in the frequency and Laplace domains: Geophysics, **73**, no. 5, VE119–VE133.

Sirgue, L., , and R. Pratt, 2004, Efficient waveform inversion and imaging: a strategy for selecting temporal frequencies: Geophysics, **69**, 231–248.

Slawinski, M. A., 2003, Seismic waves and rays in elastic media: Elsevier Science, **34**.

Sripanich, Y., S. Fomel, J. Sun, and J. Cheng, 2015, Elastic wave-vector decomposition in orthorhombic media: 85th Annual International Meeting, SEG, Expanded Abstracts, 498–503.

Steiner, B., E. H. Saenger, and S. M. Schmalholz, 2008, Time reverse modeling of low-frequency microtremors: Application to hydrocarbon reservoir localization: Geophysical Research Letters, **35**, no. 3, L03–L07.

Sun, J., S. Fomel, and T. Zhu, 2015, Preconditioning least-squares RTM in viscoacoustic media by Q-compensated RTM: 85th Annual International Meeting, SEG, Expanded Abstracts, 3959–3965.

Sun, J., Y. Zhang, S. Gray, C. Notfors, and J. Young, 2003, 3-D prestack depth migration by wavefield extrapolation methods: ASEG Extended Abstracts 2003, pp 1-4.

Symes, W., and J. Carazzone, 1991, Velocity inversion by differential semblance optimization: Geophysics, **56**, 654–663.

Symes, W. W., 2008, Migration velocity analysis and waveform inversion: Geophysical Prospecting, **56**, 765–790.

Szydlik, T., P. Smith, S. Way, L. Aamodt, and C. Friedrich, 2007, 3D PP/PS prestack depth migration on the Volve field: First Break, **25**, no. 4, 43–47.

Tang, Y., 2009, Target-oriented wave-equation least-squares migration/inversion with phase–encoded hessian: Geophysics, **74**, no. 6, WCA95–WCA107.

Tarantola, A., 1984, Inversion of seismic reflection data in the acoustic approximation: Geophysics, **49**, 1259–1266.

———, 1988, Theoretical background for the inversion of seismic waveforms including elasticity and attenuation: Pure and Applied Geophysics, **128**, 365–399.

———, 2005, Inverse Problem Theory and Methods for Model Parameter Estimation: Society for Industrial and Applied Mathematics.

Thomsen, L., 1986, Weak elastic anisotropy: Geophysics, **51**, 1954–1966.

Tromp, J., C. Tape, and Q. Liu, 2005, Seismic tomography, adjoint methods, time reversal and banana-doughnut kernels: Geophysical Journal International, **160**, 195–216.

Verschuur, D. J., and R. J. Prein, 1999, Multiple removal results from Delft University: The Leading Edge, **18**, 86–91.

Vigh, D., and W. Starr, 2008, 3D prestack plane-wave, full-waveform inversion: Geophysics, **73**, no. 5, VE135–VE144.

Virieux, J., and S. Operto, 2009, An overview of full-waveform inversion in exploration geophysics: Geophysics, **74**, no. 6, WCC1–WCC26.

Wang, C., J. Cheng, and T. Wang, 2014, Local angle domain elastic reverse time migration in anisotropic media: CPS/SEG Beijing 2014 International Geophysical Conference.

Wang, S., F. Chen, H. Zhang, and Y. Shen, 2013, Reflection-based full-waveform inversion (RFWI) in the frequency domain: 83rd Annual International Meeting, SEG, Expanded Abstracts, 877–881.

Wang, W., G. A. McMechan, C. Tang, and F. Xie, 2016, Up/down and P/S decompositions of elastic wavefields using complex seismic traces with applications to calculating Poynting vectors and angle-domain common-image gathers from reverse time migrations: Geophysics, **81**, no. 4, S181–S194.

Warpinski, N., J. Du, and U. Zimmer, 2012, Measurements of hydraulic-fracture-induced seismicity in gas shales: SPE Hydraulic Fracturing Technology Conference,.

Webster, J., 2000, Chapter 8.1 - The Wave Equation, *in* Mechanical variables measurement: solid, fluid and thermal: CRC Press.

Weiss, R. M., and J. Shragge, 2013, Solving 3D anisotropic elastic wave equations on parallel GPU devices: Geophysics, **78**, no. 2, F7–F15.

Whitmore, N. D., 1983, Iterative depth migration by backward time propagation: 53rd Annual International Meeting, SEG, Expanded Abstracts, 382–385.

Whitmore, N. D., and S. Crawley, 2012, Application of RTM inverse scattering imaging conditions: 82nd Annual International Meeting, SEG, Expanded Abstracts, 1–6.

Witten, B., and B. Artman, 2010, Signal-to-noise estimates of time-reverse images: 80th Annual International Meeting, SEG, Expanded Abstracts, 2176–2180.

Witten, B., and J. Shragge, 2015, Extended wave-equation imaging conditions for passive seismic data: Geophysics, **80**, no. 6, WC61–WC72.

———, 2017a, Image-domain velocity inversion and event location for microseismic monitoring: Geophysics, **82**, no. 5, KS71–KS83.

———, 2017b, Microseismic image-domain velocity inversion: Marcellus Shale case study: Geophysics, **82**, no. 6, KS99–KS112.

Wong, M., B. L. Biondi, and S. Ronen, 2010, Joint least-squares inversion of up- and downgoing signal for ocean bottom data sets: 80th Annual International Meeting, SEG, Expanded Abstracts, 2752–2756.

———, 2015, Imaging with primaries and free-surface multiples by joint least-squares reverse time migration: Geophysics, **80**, no. 6, S223–S235.

Xu, L., A. Stanton, and M. D. Sacchi, 2016, Elastic least squares reverse time migration: 86th Annual International Meeting, SEG, Expanded Abstracts, 3959–3965.

Xu, S., D. Wang, F. Chen, and Y. Zhang, 2012, Full waveform inversion for reflected seismic data: 74th European Association of Geoscientists and Engineers Conference and Exhibition.

Xuan, R., and P. Sava, 2010, Probabilistic microearthquake location for reservoir monitoring: Geophysics, **75**, no. 3, MA9–MA26.

Yan, J., and P. Sava, 2007, Elastic wavefield imaging with scalar and vector potentials: 77th Annual International Meeting, SEG, Expanded Abstracts, 2150–2154.

———, 2008, Isotropic angle-domain elastic reverse-time migration: Geophysics, **73**, no. 6, S229–S239.

———, 2009, Elastic wave-mode separation for VTI media: Geophysics, **74**, no. 5, WB19–WB32.

———, 2011a, Elastic wave-mode separation for tilted transverse isotropy media: Geophysical Prospecting, **60**, 29–48.

———, 2011b, Improving the efficiency of elastic wave-mode separation for heterogeneous tti media: Geophysics, **76**, no. 4, T65–T78.

Yan, R., and X.-B. Xie, 2010, The new angle-domain imaging condition for elastic RTM: 80th Annual International Meeting, SEG, Expanded Abstracts, 3181–3186.

———, 2012, An angle-domain imaging condition for elastic reverse time migration and its application to angle gather extraction: Geophysics, **77**, no. 5, S105–S115.

Yang, T., and P. Sava, 2011, Wave-equation migration velocity analysis with time-lag imaging: Geophysical Prospecting, **59**, 635–650.

———, 2015, Image-domain wavefield tomography with extended common-image-point gathers: Geophysical Prospecting, **63**, no. 1, 1086–1096.

Yang, T., J. Shragge, and P. Sava, 2013, Illumination compensation for image-domain wavefield tomography: Geophysics, **78**, no. 5, U65–U76.

Yang, Y., B. Engquist, J. Sun, and B. F. Hamfeldt, 2018, Application of optimal transport and the quadratic Wasserstein metric to full-waveform inversion: Geophysics, **83**, no. 1, R43–R62.

Yao, G., and H. Jakubowicz, 2012, Least-Squares Reverse-Time Migration: 82rd Annual International Meeting, SEG, Expanded Abstracts.

Yoon, K., and K. J. Marfurt, 2006, Reverse-time migration using the Poynting vector: Exploration Geophysics, **37**, 102–107.

Yoon, K., C. Shin, S. Suh, L. Lines, and S. Hong, 2003, 3D reverse-time migration using acoustic wave equation: An experience with the SEG/EAGE data set: The Leading Edge, **22**, 38–41.

Youn, O., and H. W. Zhou, 2001, Depth imaging with multiples: Geophysics, **66**, 246–255.

Yu, Y.-Y., 1964, Generalized Hamilton's Principle and Variational Equation of Motion in Nonlinear Elasticity Theory, with Application to Plate Theory: The Journal of the Acoustic Society of America, **36**, 111–120.

Zhang, Q., and G. A. McMechan, 2010, 2D and 3D elastic wavefield vector decomposition in the wavenumber domain for VTI media: Geophysics, **75**, no. 3, D13–D26.

———, 2011, Common-image gathers in the incident phase-angle domain from reverse time migration in 2D elastic VTI media: Geophysics, **76**, no. 6, S197–S206.

Zhang, Y., L. Duan, and Y. Xie, 2015, A stable and practical implementation of least-squares reverse time migration: Geophysics, **80**, no. 1, V23–V31.

Zhang, Y., and J. Sun, 2009, Practical issues in reverse time migration: true amplitude gathers, noise removal and harmonic source enconding: First Break, **27**, 53–59.

Zhang, Z., T. Alkhalifah, J.-W. Oh, and I. Tsvankin, 2017, Estimation of fracture parameters using elastic full-waveform inversion: 87th Annual International Meeting, SEG, Expanded Abstracts, 3272–3276.

Zhe, J., and S. A. Greenhalg, 1997, Prestack multicomponent migration: Geophysics, **62**, 598–613.

Zhebel, O., and L. Eisner, 2015, Simultaneous microseismic event localization and source mechanism determination: Geophysics, **80**, no. 1, KS1–KS9.

Zhu, H., Y. Luo, T. Nissen-Meyer, C. Morency, and J. Tromp, 2009, Elastic imaging and time-lapse migration based on adjoint methods: Geophysics, **74**, WCA167–WCA177.

APPENDIX - PERMISSIONS FOR CHAPTERS

A.1 Permission from journal

The website URL below shows details of copyright permissions for published papers from **Geophysics**:

- https://seg.org/Publications/Policies-and-Permissions/Open-Access-Policy

The screenshot below shows the paragraph granting permission to use published papers in a dissertation by the main author (highlighted in yellow):

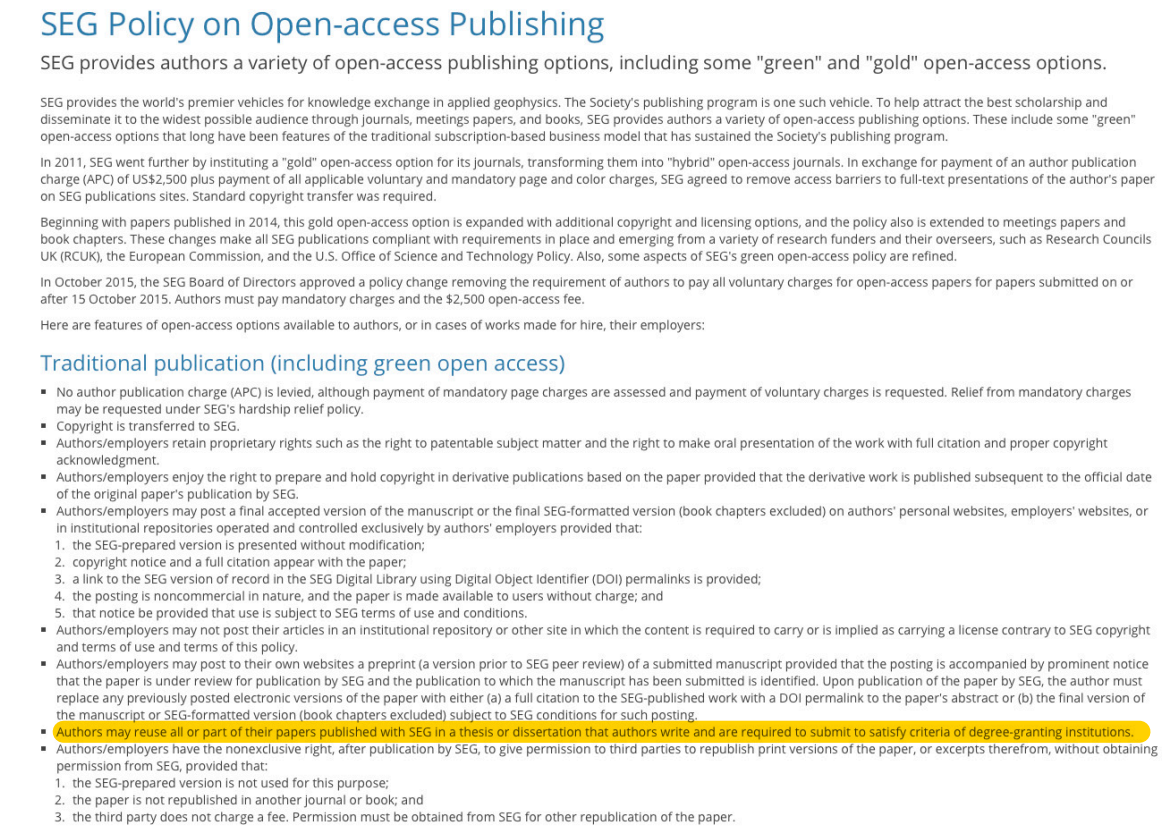

SEG Policy on Open-access Publishing

SEG provides authors a variety of open-access publishing options, including some "green" and "gold" open-access options.

SEG provides the world's premier vehicles for knowledge exchange in applied geophysics. The Society's publishing program is one such vehicle. To help attract the best scholarship and disseminate it to the widest possible audience through journals, meetings papers, and books, SEG provides authors a variety of open-access publishing options. These include some "green" open-access options that long have been features of the traditional subscription-based business model that has sustained the Society's publishing program.

In 2011, SEG went further by instituting a "gold" open-access option for its journals, transforming them into "hybrid" open-access journals. In exchange for payment of an author publication charge (APC) of US$2,500 plus payment of all applicable voluntary and mandatory page and color charges, SEG agreed to remove access barriers to full-text presentations of the author's paper on SEG publications sites. Standard copyright transfer was required.

Beginning with papers published in 2014, this gold open-access option is expanded with additional copyright and licensing options, and the policy also is extended to meetings papers and book chapters. These changes make all SEG publications compliant with requirements in place and emerging from a variety of research funders and their overseers, such as Research Councils UK (RCUK), the European Commission, and the U.S. Office of Science and Technology Policy. Also, some aspects of SEG's green open-access policy are refined.

In October 2015, the SEG Board of Directors approved a policy change removing the requirement of authors to pay all voluntary charges for open-access papers for papers submitted on or after 15 October 2015. Authors must pay mandatory charges and the $2,500 open-access fee.

Here are features of open-access options available to authors, or in cases of works made for hire, their employers:

Traditional publication (including green open access)

- No author publication charge (APC) is levied, although payment of mandatory page charges are assessed and payment of voluntary charges is requested. Relief from mandatory charges may be requested under SEG's hardship relief policy.
- Copyright is transferred to SEG.
- Authors/employers retain proprietary rights such as the right to patentable subject matter and the right to make oral presentation of the work with full citation and proper copyright acknowledgment.
- Authors/employers enjoy the right to prepare and hold copyright in derivative publications based on the paper provided that the derivative work is published subsequent to the official date of the original paper's publication by SEG.
- Authors/employers may post a final accepted version of the manuscript or the final SEG-formatted version (book chapters excluded) on authors' personal websites, employers' websites, or in institutional repositories operated and controlled exclusively by authors' employers provided that:
  1. the SEG-prepared version is presented without modification;
  2. copyright notice and a full citation appear with the paper;
  3. a link to the SEG version of record in the SEG Digital Library using Digital Object Identifier (DOI) permalinks is provided;
  4. the posting is noncommercial in nature, and the paper is made available to users without charge; and
  5. that notice be provided that use is subject to SEG terms of use and conditions.
- Authors/employers may not post their articles in an institutional repository or other site in which the content is required to carry or is implied as carrying a license contrary to SEG copyright and terms of use and terms of this policy.
- Authors/employers may post to their own websites a preprint (a version prior to SEG peer review) of a submitted manuscript provided that the posting is accompanied by prominent notice that the paper is under review for publication by SEG and the publication to which the manuscript has been submitted is identified. Upon publication of the paper by SEG, the author must replace any previously posted electronic versions of the paper with either (a) a full citation to the SEG-published work with a DOI permalink to the paper's abstract or (b) the final version of the manuscript or SEG-formatted version (book chapters excluded) subject to SEG conditions for such posting.
- Authors may reuse all or part of their papers published with SEG in a thesis or dissertation that authors write and are required to submit to satisfy criteria of degree-granting institutions.
- Authors/employers have the nonexclusive right, after publication by SEG, to give permission to third parties to republish print versions of the paper, or excerpts therefrom, without obtaining permission from SEG, provided that:
  1. the SEG-prepared version is not used for this purpose;
  2. the paper is not republished in another journal or book; and
  3. the third party does not charge a fee. Permission must be obtained from SEG for other republication of the paper.

Figure A.1: Permission from **Geophysics**

A.2 Permission for field datasets

I include copies of the emails exchanged with company representatives, who granted permission to include the field dataset examples in the dissertation.

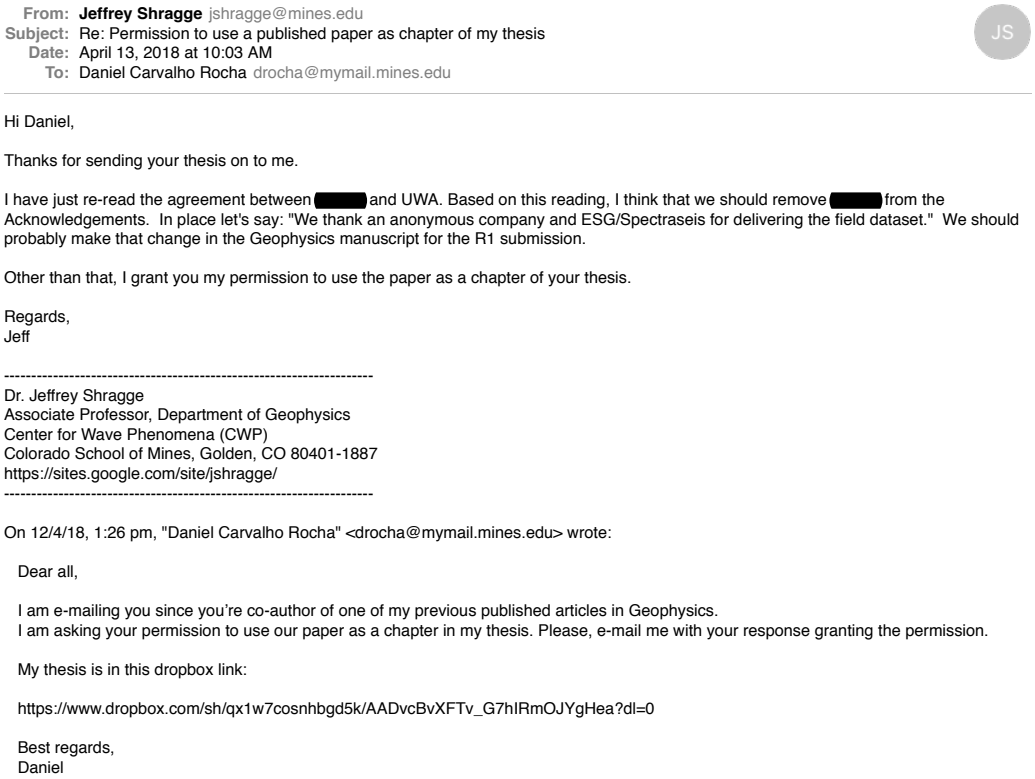

From: **Jeffrey Shragge** jshragge@mines.edu
Subject: Re: Permission to use a published paper as chapter of my thesis
Date: April 13, 2018 at 10:03 AM
To: Daniel Carvalho Rocha drocha@mymail.mines.edu

JS

Hi Daniel,

Thanks for sending your thesis on to me.

I have just re-read the agreement between [redacted] and UWA. Based on this reading, I think that we should remove [redacted] from the Acknowledgements. In place let's say: "We thank an anonymous company and ESG/Spectraseis for delivering the field dataset." We should probably make that change in the Geophysics manuscript for the R1 submission.

Other than that, I grant you my permission to use the paper as a chapter of your thesis.

Regards,
Jeff

Dr. Jeffrey Shragge
Associate Professor, Department of Geophysics
Center for Wave Phenomena (CWP)
Colorado School of Mines, Golden, CO 80401-1887
https://sites.google.com/site/jshragge/

On 12/4/18, 1:26 pm, "Daniel Carvalho Rocha" <drocha@mymail.mines.edu> wrote:

Dear all,

I am e-mailing you since you're co-author of one of my previous published articles in Geophysics.
I am asking your permission to use our paper as a chapter in my thesis. Please, e-mail me with your response granting the permission.

My thesis is in this dropbox link:

https://www.dropbox.com/sh/qx1w7cosnhbgd5k/AADvcBvXFTv_G7hIRmOJYgHea?dl=0

Best regards,
Daniel

Figure A.2: Permission for the 3D microseismic field dataset used in Chapter 3: anonymous company and ESG/Spectraseis

From: John.Kimbro@shell.com
Subject: RE: [redacted] dataset: permission to show results in Geophysics and Thesis chapter
Date: April 25, 2018 at 6:52 AM
To: drocha@mymail.mines.edu
Cc: psava@mines.edu

Daniel,

Thank you for sharing this, very nice work. It is again great to see the data being used in this way. We have no issues with the content, images or language. Thanks for asking, and good luck.

Cheers,

John

From: Daniel Carvalho Rocha [mailto:drocha@mymail.mines.edu]
Sent: Thursday, April 19, 2018 6:41 PM
To: Kimbro, John J SEPCO-PTD/E/W <John.Kimbro@shell.com>
Cc: Paul Sava <psava@mines.edu>
Subject: Re: [redacted] dataset: permission to show results in Geophysics and Thesis chapter

Dear John,

Following the same procedure as we did for the SEG abstract and CWP report, we are asking for permission to use the images of [redacted] in a Geophysics article, which will also be published as a chapter of my PhD thesis. The gallery proof of the Geophysics article is attached, but I can tell you in advance that these images are exactly the same used in our previously approved CWP report and SEG abstract.

Best regards,

Figure A.3: Permission for the 3D GOM field dataset used in Chapter 4: Shell Exploration and Production Company

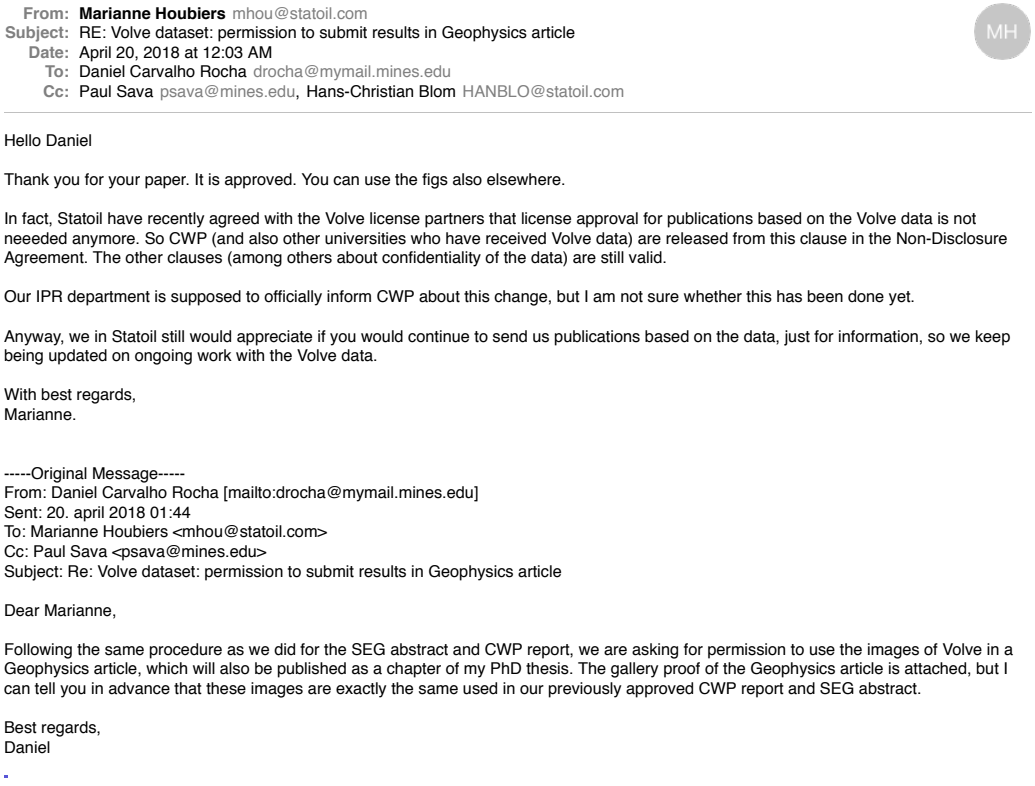

From: **Marianne Houbiers** mhou@statoil.com
Subject: RE: Volve dataset: permission to submit results in Geophysics article
Date: April 20, 2018 at 12:03 AM
To: Daniel Carvalho Rocha drocha@mymail.mines.edu
Cc: Paul Sava psava@mines.edu, Hans-Christian Blom HANBLO@statoil.com

MH

Hello Daniel

Thank you for your paper. It is approved. You can use the figs also elsewhere.

In fact, Statoil have recently agreed with the Volve license partners that license approval for publications based on the Volve data is not neeeded anymore. So CWP (and also other universities who have received Volve data) are released from this clause in the Non-Disclosure Agreement. The other clauses (among others about confidentiality of the data) are still valid.

Our IPR department is supposed to officially inform CWP about this change, but I am not sure whether this has been done yet.

Anyway, we in Statoil still would appreciate if you would continue to send us publications based on the data, just for information, so we keep being updated on ongoing work with the Volve data.

With best regards,
Marianne.

-----Original Message-----
From: Daniel Carvalho Rocha [mailto:drocha@mymail.mines.edu]
Sent: 20. april 2018 01:44
To: Marianne Houbiers <mhou@statoil.com>
Cc: Paul Sava <psava@mines.edu>
Subject: Re: Volve dataset: permission to submit results in Geophysics article

Dear Marianne,

Following the same procedure as we did for the SEG abstract and CWP report, we are asking for permission to use the images of Volve in a Geophysics article, which will also be published as a chapter of my PhD thesis. The gallery proof of the Geophysics article is attached, but I can tell you in advance that these images are exactly the same used in our previously approved CWP report and SEG abstract.

Best regards,
Daniel

Figure A.4: Permission for the 2D Volve field dataset used in Chapter 5: Statoil ASA and the Volve license partners ExxonMobil E&P Norway AS and Bayerngas Norge AS

A.3 Permission from co-authors

I include copies of the emails exchanged with my co-authors, who granted permissions to include the papers in the dissertation:

From: **Nick Tanushev** nicktan@z-terra.com
Subject: Re: Permission to use a published paper as chapter of my thesis
Date: April 13, 2018 at 5:16 AM
To: Daniel Carvalho Rocha drocha@mymail.mines.edu

NT

Hi Daniel,

You have my permission to use any of our previous work for your thesis.

Cheers,

Nick

On 04/12/2018 02:26 PM, Daniel Carvalho Rocha wrote:

> Dear all,
>
> I am e-mailing you since you're co-author of one of my previous published articles in Geophysics.
> I am asking your permission to use our paper as a chapter in my thesis. Please, e-mail me with your response granting the permission.
>
> My thesis is in this dropbox link:
>
> https://www.dropbox.com/sh/qx1w7cosnhbgd5k/AADvcBvXFTv_G7hIRmOJYgHea?dl=0
>
> Best regards,
> Daniel

Figure A.5: Permission from Nicolay Tanushev

From: **Jeffrey Shragge** jshragge@mines.edu
Subject: Re: Permission to use a published paper as chapter of my thesis
Date: April 13, 2018 at 10:03 AM
To: Daniel Carvalho Rocha drocha@mymail.mines.edu

JS

Hi Daniel,

Thanks for sending your thesis on to me.

I have just re-read the agreement between [redacted] and UWA. Based on this reading, I think that we should remove [redacted] from the Acknowledgements. In place let's say: "We thank an anonymous company and ESG/Spectraseis for delivering the field dataset." We should probably make that change in the Geophysics manuscript for the R1 submission.

Other than that, I grant you my permission to use the paper as a chapter of your thesis.

Regards,
Jeff

Dr. Jeffrey Shragge
Associate Professor, Department of Geophysics
Center for Wave Phenomena (CWP)
Colorado School of Mines, Golden, CO 80401-1887
https://sites.google.com/site/jshragge/

On 12/4/18, 1:26 pm, "Daniel Carvalho Rocha" <drocha@mymail.mines.edu> wrote:

> Dear all,
>
> I am e-mailing you since you're co-author of one of my previous published articles in Geophysics.
> I am asking your permission to use our paper as a chapter in my thesis. Please, e-mail me with your response granting the permission.
>
> My thesis is in this dropbox link:
>
> https://www.dropbox.com/sh/qx1w7cosnhbgd5k/AADvcBvXFTv_G7hIRmOJYgHea?dl=0
>
> Best regards,
> Daniel

Figure A.6: Permission from Jeffrey Shragge

From: **Ben Witten** bwitten@gmail.com
Subject: Re: Permission to use a published paper as chapter of my thesis
Date: April 12, 2018 at 3:47 PM
To: Daniel Carvalho Rocha drocha@mymail.mines.edu

BW

Daniel,

You have my permission to use our paper as a chapter in your thesis.

-Ben

On Thu, Apr 12, 2018 at 2:26 PM, Daniel Carvalho Rocha <drocha@mymail.mines.edu> wrote:

> Dear all,
>
> I am e-mailing you since you're co-author of one of my previous published articles in Geophysics.
> I am asking your permission to use our paper as a chapter in my thesis. Please, e-mail me with your response granting the permission.
>
> My thesis is in this dropbox link:
>
> https://www.dropbox.com/sh/qx1w7cosnhbgd5k/AADvcBvXFTv_G7hIRmOJYgHea?dl=0
>
> Best regards,
> Daniel

Figure A.7: Permission from Ben Witten

From: **Antoine Guitton** aguitton@mines.edu
Subject: Re: Permission to use a published paper as chapter of my thesis
Date: April 12, 2018 at 5:20 PM
To: Daniel Carvalho Rocha drocha@mymail.mines.edu

AG

Dear Daniel: you have my permission to use the Geophysics article we co-authored in your thesis.

Best regards,
Antoine

On Thu, Apr 12, 2018 at 1:26 PM, Daniel Carvalho Rocha <drocha@mymail.mines.edu> wrote:

> Dear all,
>
> I am e-mailing you since you're co-author of one of my previous published articles in Geophysics.
> I am asking your permission to use our paper as a chapter in my thesis. Please, e-mail me with your response granting the permission.
>
> My thesis is in this dropbox link:
>
> https://www.dropbox.com/sh/qx1w7cosnhbgd5k/AADvcBvXFTv_G7hIRmOJYgHea?dl=0
>
> Best regards,
> Daniel

Figure A.8: Permission from Antoine Guitton